Directing the Assembly of Nanostructures on Surfaces with Molecular Monolayers

Mohamed Amine Mezour

Department of Chemistry
McGill University
Montreal, Quebec
Canada

October 2015

A thesis submitted to McGill University in partial fulfillment of the requirements of the degree of Doctor of Philosophy

Abstract

The precise organization of nano-objects into well-defined patterns at surfaces and interfaces is of increasing importance in nanoscience research. Among the existing nanopatterning approaches, molecular self-assembly provides a highly accurate, efficient, and potentially low-cost "bottom-up" route to create complex nano-patterns with immense flexibility in terms of nanoscale building blocks. The structure and functionality of molecular building blocks define the type of interactions that are involved in the formation of the molecular pattern and in the templating process. This Thesis combines the high hierarchical order offered by physisorbed self-assembled molecular networks (SAMNs) and the enhanced stability gained from chemisorbed self-assembled monolayers (SAMs). The result is robust and/or versatile 2D molecular monolayers that can be applied to the template-directed formation of organic and inorganic nanostructures.

The first part of this Thesis explores the use of a new tridentate thiol for the formation of SAMs with long-term stability on Au(111). This design is based on a benzene ring substituted with three methylthiol groups in alternation with three alkyl chains. The molecular orientation and long-range order of these SAMs depend on the length of the alkyl chains.

Physisorbed SAMN for nanopatterning of gold nanoparticles were prepared using a *p*-dialkoxybenzene SAMN modified-HOPG substrate. The observed templating effect is based on van der Waals interactions between the alkyl chains of the SAMN and AuNP. The assembly efficiency is greatest when these chains are of similar length.

The dynamics of C_{60} assembly onto SAMs of benzenethiols (BT) and penfluorobenzenthiols (PFBT) were been studied. The electronic properties of these SAMs directly affect the growth kinetic of C_{60} overlayers.

The study of physisorbed [C_{60}]fullerene multicarboxylic acids on an Au (111) substrate identifies the important role of molecule-substrate interactions and the intermolecular hydrogen bonding in the formation of a 2D assembly. The possibility of tuning the molecule-Au interaction was demonstrated using a PFBT-modified Au substrate. The dimensionality of the resulting [C_{60}]fullerene multicarboxylic acids monolayer (1D vs 2D) was shown to depend on the number of malonic acid functionalities present.

Résumé

L'organisation précise des nanostructures sur des surfaces et des interfaces est d’une importance croissante en nanotechnologie. Parmi les différentes méthodes de nano-structuration, l’auto-assemblage des molécules présente une approche ascendante précise, efficace et moins onéreuse pour créer des nano-motifs complexes avec une grande flexibilité en composantes moléculaires. Dans cette approche, la structure et la fonctionnalité des molécules définissent le processus de nano-structuration ainsi que le type d'interactions impliquées dans la formation des motifs moléculaires. La présente thèse a pour objectif de combiner la grande flexibilité des monocouches moléculaires physisorbées (SAMNs) et la stabilité des monocouches moléculaires chimisorbées (SAM) afin de créer des nano-motifs robustes et / ou polyvalents. Ces nano-motifs moléculaires seront utilisés par la suite pour guider la nano-structuration des entités organiques et inorganiques.

La première partie de la thèse étudiée l’auto-assemblage d’une molécule thiolée et tridentée sur le Au(111) dans le but de former des SAMs avec une meilleure stabilité. Cette molécule comporte un cycle benzénique ayant des substituants méthyl thiols aux positions 1,3,5 et des chaînes alkyles aux positions 2,4,6. La caractérisation des résultantes SAMs démontre une étroite dépendance entre l’orientation et l’ordre moléculaire des SAM et la taille des chaînes alkyles.

La deuxième partie de la thèse explore la nano-structuration des nano-particules d’or sur une monocouche de *p*-dialcoxybenzene physisorbée sur le graphite. Cette étude démontre que des interactions de type van der Waals entre les chaînes du motif moléculaire et le ligand des nanoparticules d’or guident le processus de nano-structuration. De plus, cette nano-structuration est optimale lorsque ces deux chaînes sont de même longueur.

La troisième partie de la thèse analyse la dynamique du C_{60} sur une SAM de benzenethiols (BT) et de pentafluorobenzenethiols (PFBT). Nos résultats démontrent que les propriétés électroniques de ces SAMs ont une répercussion directe sur la croissance des monocouches de C_{60}. Dans la dernière partie de la thèse, l’adsorption des dérivées de fullerène (C_{60}) ayant des groupements carboxyliques sur Au (111) met en évidence le rôle important des interactions molécule-substrat et des liaisons hydrogènes intermoléculaires dans la formation et la structure de l'assemblage (1D vs 2D).

Acknowledgement

Firstly, I would like to acknowledge all people who made this dissertation possible and who contributed to the development to my overall experience as researcher.

Special thanks to my supervisors, Dr. R. Bruce Lennox, and Dr. Dmitrii F. Perepichka, for giving me the opportunity to work on this interesting project. I am thankful to them for their meticulous suggestions and astute criticism during the different stages of this dissertation. Their enthusiasm, support, and insightful guidance were of paramount importance for the success of my Ph.D study.

I am very thankful to CSACS, FQRNT and NSERC for the financial support during my Ph.D research.

My sincere thanks also to my colleagues who contributed to the different chapter of this Ph.D thesis: Iryna Perepichka, Jun Zhu, Olexandr Ivasenko, Rachelle M. Choueiri, Olexandr Voznyy and Olena Lukoyanova. Furthermore, I want to thank all present and former members of the Lennox group and Perepichka group for their various contributions.

I would also like to acknowledge the Chemistry Department staff at McGill University: Chantal Marotte for her guidance during my graduate studies, Mohini Ramkaran and Beatrice Lego for the scanning probe microscopy facilities, Nadim Saade for his assistance with mass spectrometry. Many thanks as well to Helen Campbell and Lihong Shang for the X-ray photoelectron spectroscopy.

Finally, I would like to thank my family for their continual support and encouragement throughout my studies

Author’s contribution

The main body of this Thesis consists of four chapters (Chapter 2 to Chapter 5). Chapters 2 and 3 have been published, while Chapter 4 and 5 will be submitted to peer-reviewed journals. The Supporting Information sections of the manuscripts included in this Thesis have been added as Appendices. An introduction to the field is provided in Chapter 1, and conclusions to the work are provided in Chapter 6.

In this PhD thesis, Prof Dmitrii F. Perepichka and R. Bruce Lennox provided research objectives and intellectual guidance. In Chapter 2, Dr. I. Perepichka and Dr. Oleksandr Ivasenko synthesized the tridentate molecules. I prepared and characterized SAMs of these molecules using STM, XPS and electrochemistry. STM analysis was performed in collaboration with O. Ivasenko. In Chapter 3, Dr. I. Perepichka synthesized the molecular templates, Dr. J. Zhu and I synthesized AuNPs. I performed the self-assembly study, collected and analysed STM images. In Chapter 4, I performed all the experimental studies and analysed the data. Dr. O. Voznyy did the surface energy calculations. In Chapter 5, R. M. Choueiri and Dr. O. Lukoyanova synthesized [C_{60}]fullerene multicarboxylic acids. I performed the STM study and analyzed the data.

List of Abbreviations and Acronyms

AES	Auger electron spectroscopy
AFM	atomic force microscopy
AuNPs	gold nanoparticles
BT	benzenethiol
BTMT	tridentate benzenetris(methylthiols)
CV	cyclic voltamogramm
C_{60}	fullerenes
DBA-C_{12}	hexadehydrotribenzo[12]annulene
DFT	density functional theory
Et_3-BTMT	tridentate benzenetris(methylthiols) substituted with three ethyls
E_b	binding energy
E_d	diffusion barrier
E_k	kinetic energy
E_{inter}	intermolecular interaction energy
FFT	fast Fourier transform
FWHM	full width at half-maximum
HOPG	highly oriented pyrolytic graphite
KJMA	Kolmogorov–Johnson–Mehl–Avrami
Me_3-BTMT	tridentate benzenetris(methylthiols) substituted with three methyls
ML	monolayer
NPs	nanoparticles
ODe_3-BTMT	tridentate benzenetris(methylthiols) substituted with three decyloxys
ODe_3-B	1,3,5-tris(decyloxy)benzene
PCBM	phenyl-C_{61}-butyric acid methyl ester
PFBT	pentafluorobenzenethiol
PTCDI	perylene tetracarboxylic di-imide
SAMs	self-assembled monolayers
SAMNs	self-assembled molecular networks
STM	scanning tunnelling microscopy

STS	scanning tunnelling spectroscopy
TEM	transmission electron microscopy
TMA	trimesic acid
UHV	ultra-high vacuum
UPS	ultraviolet photoelectron spectroscopy
vdW	van der Waals
XPS	X-ray photoelectron spectroscopy
0D, 1D, 2D, 3D	zero-, one-, two-, three-dimensional

Table of contents

Introduction

The ability of building blocks with chemical and structural complementarity to self-assemble into complex structures is ubiquitous in Nature. Proteins, viruses, cells are examples of advanced biological self-assembled structures at the nano- and micrometre scale.

Designing nature-inspired materials via molecular self-assembly has been a central focus in nanoscience. Consequently, a variety of nanostructures with intriguing functionalities and wide spectrum of properties have been successfully synthesized. Nanostructures with different dimensionality (0D nanoparticles, 1D chains, 2D sheets, and 3D frameworks with nanoscale cavities) were developed for potential application in catalysis, drug delivery, thin film based organic electronic devices, etc.[1-3]

Since the emergence of nanotechnology in the 1990s, molecular self-assembly on surfaces has been considered as a "next generation" nanopatterning method.[1,2,4] This highly accurate, efficient, and low-cost "bottom-up" approach provides a flexible and efficient way to create complex structures and patterns of nano-objects with sub-nanometer precision, over an extended length scale.[5,6] A plethora of molecular patterns have been created through molecular chemisorption or physisorption and explored for the templating of various nanomaterials.

Despite the exciting development of molecular self-assembly and its application in 2D templating, many challenges still remain ahead. The subtle, multifaceted, and cooperative character of molecular-substrate and intermolecular interactions that governs molecular self-assembly makes rational control of such nanopatterning challenging. In fact, many if not most of the novel molecular networks have been discovered serendipitously rather than by design. Thus, further control of these interactions is imperative for further progress toward the systematic engineering of 2D supramolecular networks in a "preprogrammed" fashion.

Depending on the nature and strength of molecule-substrate interactions, molecules might covalently bind to the substrate forming chemisorbed self-assembled monolayer (SAMs) or weakly adsorb on the substrate resulting in a physisorbed molecular network (SAMNs). The use of SAMs and SAMN in nanopatterning organic molecules is well established in literature.[1,2,4] In contrast, little efforts have been devoted to templating inorganic nanostructures (e.g. metal, semiconductors, quantum dots), although their intrinsic physical and chemical properties make them highly attractive for technological applications. For example, gold nanoparticles (AuNPs) can exhibit a range of desirable electronic, magnetic, and optical properties when templated into well-defined 2D structure.[7]

The main objective of this Thesis is to combine the high hierarchical order of physisorbed monolayers and the enhanced stability offered by chemisorbed molecules for the creation of robust or/and versatile 2D molecular networks for templating organic and inorganic nanostructures. The key milestones toward achieving this objective were: (i) Design of molecular building blocks that self-assemble on Au(111) and HOPG substrate through various molecule-substrate and intermolecular interactions; (ii) *in-situ* study of the dynamic of the assembly process and the structural properties of the resulting 2D monolayer at liquid-solid interface; (iii) investigation of the templating ability of these molecular networks for C_{60} and AuNPs.

In Chapter 1 the basic principles and the general concepts behind molecular self-assembly are introduced. Some examples of using these molecular networks in directing the assembly of organic and inorganic guest entities are then highlighted.

Chapter 2 investigates tridentate thiols for binding to an Au substrate The use of alkyl substituents with different lengths allows for tuning of the lateral structure/periodicity of the monolayer. The use of physisorbed SAMN for nanopatterning gold nanoparticles (AuNPs) is studied in Chapter 3. Specifically, a physisorbed lamellar pattern formed by adsorption of *p*-dialkoxybenzene derivatives onto HOPG is used as molecular template for AuNPs. In this study the templating effect is based on van der Waals interactions of the alkyl chains of the SAMN and AuNPs, and the assembly efficiency is shown to be greatest when these chains are of similar length. Chapter 4 explores the use of SAMs of benzenethiol and its perfluorinated derivative for controlling the adsorption of a subsequent layers of C_{60}. The electronic properties of these SAMs directly affect the growth kinetic of C_{60} overlayers. Finally, in Chapter 5, the assembly of [C_{60}]fullerene multicarboxylic acids on Au (111) and SAM-modified Au(111) demonstrates the interplay of the molecule-substrate interactions and the intermolecular hydrogen bonding in the formation of 2D assembly of fullerene derivatives. Chapter 6 outlines the results obtained in this Thesis as well as directions for future work.

Overall, these studies highlight the great potential of merging the fields of chemisorbed SAMs and self-assembled molecular networks (SAMNs) in advancing surface nanoscience and related nanotechnology applications.

Chapter 1: Self-Assembled Molecules and their Application to Nanopatterning

1.1 Mechanism of molecular self-assembly

Molecular self-assembly is defined as the spontaneous organization of molecules into aggregates by non-covalent interactions under thermodynamic equilibrium without the intervention of external forces.[1] At solid surfaces, molecular self-assembly is governed by delicate balance of molecule–molecule and molecule–substrate interactions. More specifically, molecule-substrate interactions drive the adsorption of molecules onto the substrate. They can then diffuse and reorganize into ordered structures so as to maximize intermolecular interactions. This mechanism requires a kinetic energy (E_k) of the adsorbate molecules that is sufficiently high to overcome the diffusion barrier (E_d), but not exceed the binding energy (E_b) so as to avoid desorption. On the other hand, the intermolecular interaction energy (E_{inter}) must be lower than E_b and slightly greater than E_k to ensure the formation of an ordered equilibrium structure. These conditions can be summarized as follow $E_b > E_{inter} \geq E_k > E_d$. (Fig. 1.1)

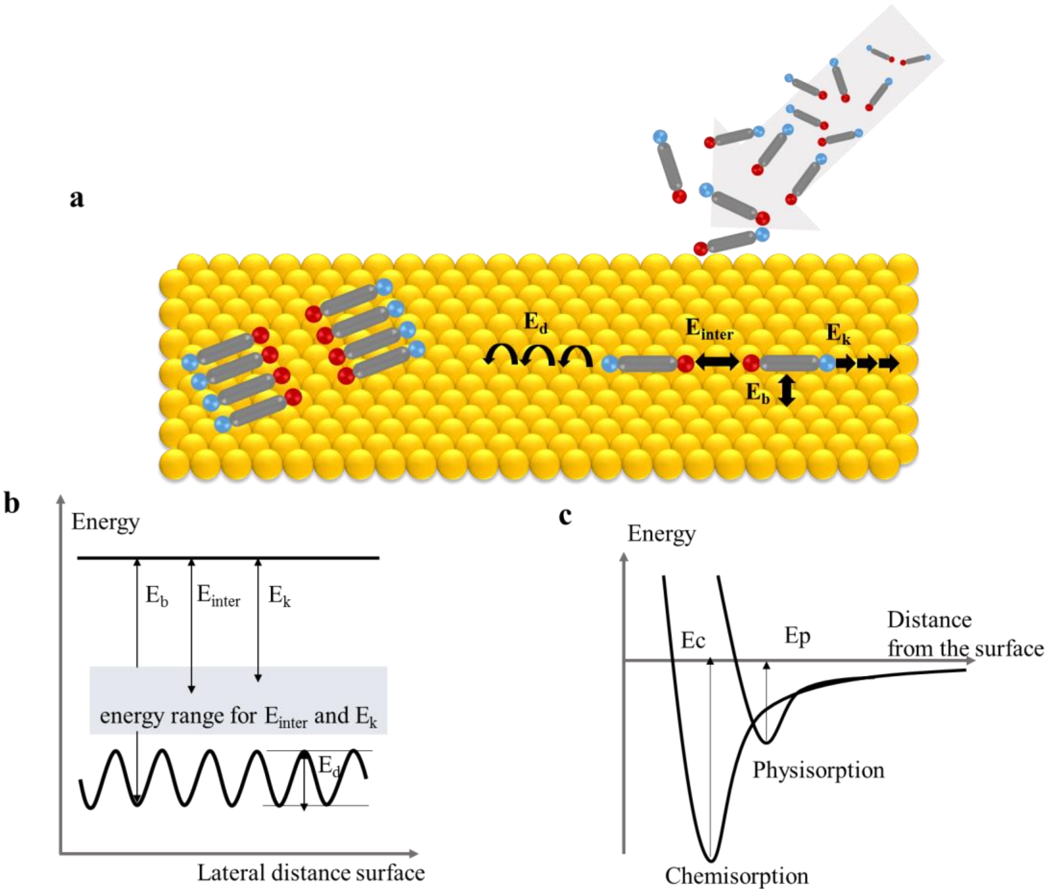

Figure 1.1. (a) Schematic representation of molecular self-assembly. E_b is the binding energy of the molecules to the surface, E_{inter} is the intermolecular interaction energy, E_k is the kinetic energy of the molecules. E_d is the diffusion barrier. (b) Energy diagram showing energy requirement for molecular self-assembly formation ($E_b > E_{inter} \geq E_k > E_d$). (c) Schematic potential energy diagram illustrating the difference between physisorbed and chemisorbed species. Adapted from ref. 8 with permission.

Two types of adsorption are commonly recognized in molecular assemblies, depending on the extent to which the electronic or bonding structure of the attached molecule is affected. Physisorption occurs when molecules adsorb onto the substrate through weak interactions (e.g. dispersion forces), without any significant change in their electronic structure. Chemisorption occurs when molecules are bound to the substrate through strong chemical interactions (covalent, metallic, and ionic). This is typically accompanied by a significant change in the electronic structure of the adsorbate as well as the surface.

1.2 Brief historical background

The last three decades have witnessed a great interest in molecular self-assembly, although the subject has fairly old roots (Fig. 1.2). At the end of 18th Century, Franklin's experiments on the calming effect of an oil film on a water surface were the first known molecular self-assembly experiment at an interface.[9] The first truly quantitative study of amphiphilic molecules monolayers was reported by Agnes Pockels in 19th century. Pockels reported direct measurements of the surface tension of a liquid and a compression-induced phase transition curve of a molecular monolayer at air-water interface in what is known today as compression isotherm.[10]

One of the major contributions to organic monolayers field was made by Irving Langmuir in 1917, who systematically measured the surface tension and surface pressure of numerous organic oils on water and provided a new understanding of monolayer structure at the molecular level, in particular the preferential orientation and ordering of molecules at interfaces.[11] Two decades later, Katharine Blodgett demonstrated that multilayer films can be synthesized by repeatedly dipping solid substrates into suitable polar liquids.[12] This constitutes the foundation of the Langmuir-Blodgett technique. This technique was later used by Timmons, Zisman and other[13] to transfer amphiphilic molecules such as fatty acids to metals and metal oxide surfaces.

Three breakthroughs in the mid 1980's completely changed the face of molecular monolayer research: (i) the invention of scanning tunnelling microscopy (STM), a tool that allows one to visualize, characterize and even manipulate single atoms and molecules on metallic surfaces,[14] (ii) the pioneering work of Nuzzo and Allara on the formation of SAMs of thiols on gold,[15] and (iii) the emergence of the 2D crystal engineering via supramolecular interactions.[16]

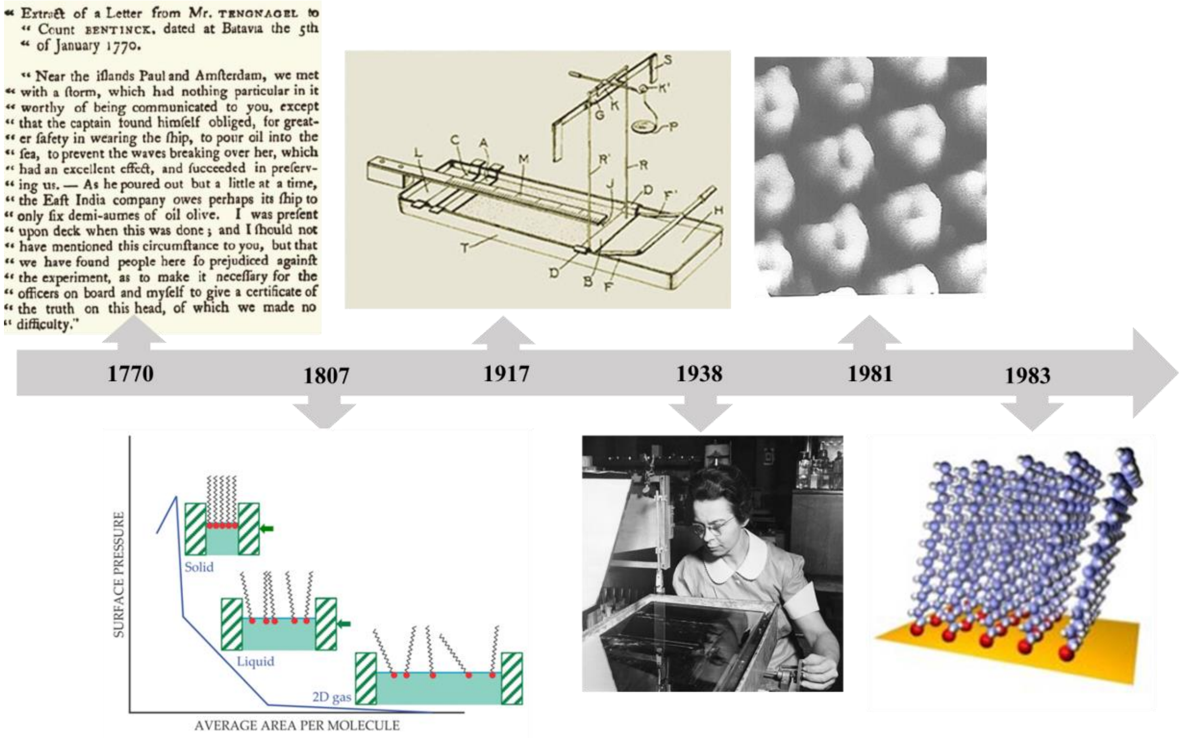

“ Extract of a Letter from Mr. TENGNAGEL to
“ Count BENTINCK, dated at Batavia the 5th
“ of January 1770.

“ Near the iſlands Paul and Amſterdam, we met “ with a ſtorm, which had nothing particular in it “ worthy of being communicated to you, except “ that the captain found himſelf obliged, for greater ſafety in wearing the ſhip, to pour oil into the “ ſea, to prevent the waves breaking over her, which “ had an excellent effect, and ſucceeded in preſerving us. — As he poured out but a little at a time, “ the Eaſt India company owes perhaps its ſhip to “ only ſix demi-aumes of oil olive. I was preſent “ upon deck when this was done; and I ſhould not “ have mentioned this circumſtance to you, but that “ we have found people here ſo prejudiced againſt “ the experiment, as to make it neceſſary for the “ officers on board and myſelf to give a certificate of “ the truth on this head, of which we made no “ difficulty.”

Figure 1.2. Timeline showing key milestone discoveries in the field of molecular self-assembly. From left to right. A letter sent to Benjamin Franklin discussing the possibility that oil could calm the high seas. A simplified compression isotherm discovered by Pockels. The instrument invented by Irving Langmuir to measure the pressure of organic oils on water. Photograph of Katharine Blodgett demonstrating an early version of the Langmuir–Blodgett experiment. First STM image of molecules showing benzene monolayer on Rh(111) substrate. Self-assembled monolayer of organothiol molecules on Au. Adapted from ref. 16,17 with permission.

1.3 Self-assembled monolayers of thiols on gold (SAMs)

1.3.1 Molecular design

A SAM is a monomolecular thin film that forms on top of an inorganic surface (metals, metal oxides and semiconductors) upon adsorption of organic molecules. SAM formation is induced by the affinity between the polar group (head group) of the organic molecule and the substrate. The molecular backbone of the organic molecule (the spacer) contributes to the organization and the structure of the resulting SAM by favoring inter-molecular interactions. The terminal functional group determines the surface properties of the SAMs (Fig. 1.3).

Different molecular designs for SAMs have been reported and summarized in many literatures reviews.[18,19] Generally, organothiols are among the most commonly used molecules for SAMs. Through the strong interaction between the thiol functional group and gold (38 - 45 kcal/mol), stable and well-ordered SAM can be formed.[19]

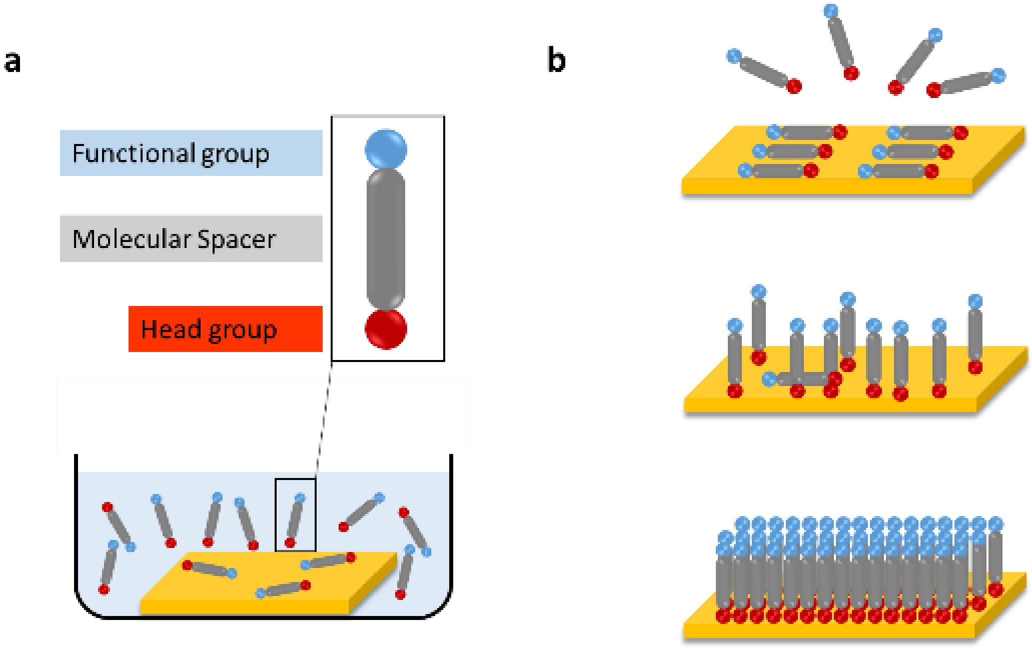

Figure 1.3. (a) SAM preparation from liquid phase and components of a SAM molecule. (b) Different steps taking place during the self-assembly of alkanethiol on Au(111). From top down: Physisorption of alkanethiol on Au(111) in a lying down configuration, reorientation of lying down molecules to a standing up arrangement, and close packing of the chemisorbed molecules.

1.3.2 Thiol SAMs preparation and mechanism of formation

SAMs are readily formed by adsorption of an organothiols (alkanethiol, disulfide, thiol acetate, etc) from either liquid or gas phase, onto metal substrate. A common experimental protocol for their formation involves immersion of a clean gold substrate in a millimolar organic solution of a thiol for a period of time ranging from a few seconds to a few days.[19-21] This protocol generally yields a reproducible homogeneous SAM. Nevertheless, the formation of a well-ordered SAM is affected by a number experimental factors including solvent, concentration, temperature, immersion time, oxygen concentration, and exposure to light.[22]

Although SAMs have been a subject of intense research for more than three decades,[15,23] their formation mechanism is still not completely understood. A simple picture of the assembly process, involves an initial physisorption step where the molecule is weakly adsorbed on the surface in a lying down configuration. This lying down configuration maximizes the interactions with the surface through multiple CH_2…Au van der Waals contacts, plus Au-S interaction. A reorientation of the adsorbed molecules occurs when the coverage exceeds a critical density.

The standing up configuration is followed by a tight packing of the chemisorbed molecules, aided by chain-chain interactions.[24,25]

The exact process of S-H scission, the fate of the hydrogen (H^+ or H_2) and the nature of the S-Au bond are still in question.[19-21] It was commonly accepted that upon adsorption on Au substrate the S-H is converted, via a dissociative adsorption pathway, to a thiolate (S^-) which forms a strong bond with Au. The hydrogen atom would then be lost via a recombinative desorption as H_2.[19,20,25,26]

$$CH_3(CH_2)_nSH + Au \rightarrow (CH_3(CH_2)_nSH)_{phys}Au \qquad (1.1)$$

$$(CH_3(CH_2)_nSH)_{phys}Au \rightarrow CH_3(CH_2)_nS\text{–}Au + 1/2H_2 \qquad (1.2)$$

However Paik et al.[27] have shown that in solution the mechanism more likely involves a sequence of electron transfers and the hydrogen desorbing as H^+.

$$CH_3(CH_2)_nSH + Au \rightarrow CH_3(CH_2)_nS\text{–}Au + H^+ + e^- \qquad (1.3)$$

Another controversial issue in SAM research is the nature and structure of the S-Au bond, even for the simple $\sqrt{3} \times \sqrt{3}$ R30° lattice. (Fig. 1.4c) Different adsorption sites have alternatively been proposed as the energetically most favoured for alkanethiol adsorption including hcp, fcc hollow, and bridge. More recently a new model considering gold reconstruction and adatom formation has been proposed.[28]

1.3.3 Thiol SAM surface structures

a) Grammar of epitaxy

The notation of Wood is commonly used to describe the registry of the adsorbates with the underlying substrate.[29] The relationship between the lengths of the basic translation vectors of the superlattice of the adsorbate a_A, b_A and those of the substrate a_S, b_S is expressed as:

$$S(hkl) - \left(\frac{a_A}{a_S} \times \frac{b_A}{b_S}\right) \times R\alpha \tag{1.4}$$

Where S is the chemical symbol of substrate, (hkl) are the Miller indices describing the crystallographic orientation of the substrate surface, $R\alpha$ and $\left(\frac{a_A}{a_S} \times \frac{b_A}{b_S}\right)$ describe the angle and ratio between the unit cell vectors of adsorbate and substrate respectively. In some cases the characters *c* and *p* are used for centred and primitive unit cells respectively.

A more general way to describe superstructures is the matrix notation proposed by Park and Madden.[30] In this notation the adsorbate vectors (a_A, b_A) are independently defined as linear combinations of (a_S , b_S) and these relationships are expressed in a matrix format.

$$M = \begin{pmatrix} M_{11} & M_{12} \\ M_{21} & M_{22} \end{pmatrix} \tag{1.5}$$

$$a_A = M_{11}a_s + M_{12}b_s \tag{1.6}$$

$$b_A = M_{21}a_s + M_{22}b_s \tag{1.7}$$

b) Structure of alkanethiols on Au(111)

Alkanethiols on an Au(111) surface are used as a well-defined system to understand in detail the structural properties of SAM. A striped phase of alkanethiols has often been observed at low molecular coverage (Θ= 0.27 ML, 1 ML=4.62×10^{14} molecules/cm^2), usually obtained either by partial desorption of the dense phase or by immersion of an Au substrate in a dilute solution of thiols for a short period of time.[31,32] This phase is described by a (*p* x √3) structure, where *p* is an integer that depends on the length of the chain (Fig. 1.4a.b). [33]

On the other hand, at high coverage (Θ= 1 ML) the molecules form a close packed phase with a (√3 × √3) R30° structure. This is characterized by a standing-up orientation of molecules with a tilt from the surface normal direction (30° - 35°) and an intermolecular separation of ~ 0.5 nm. This structure is typically characterized by a *c*(4 × 2) superlattice (Fig. 1.4c.d).[25,31]

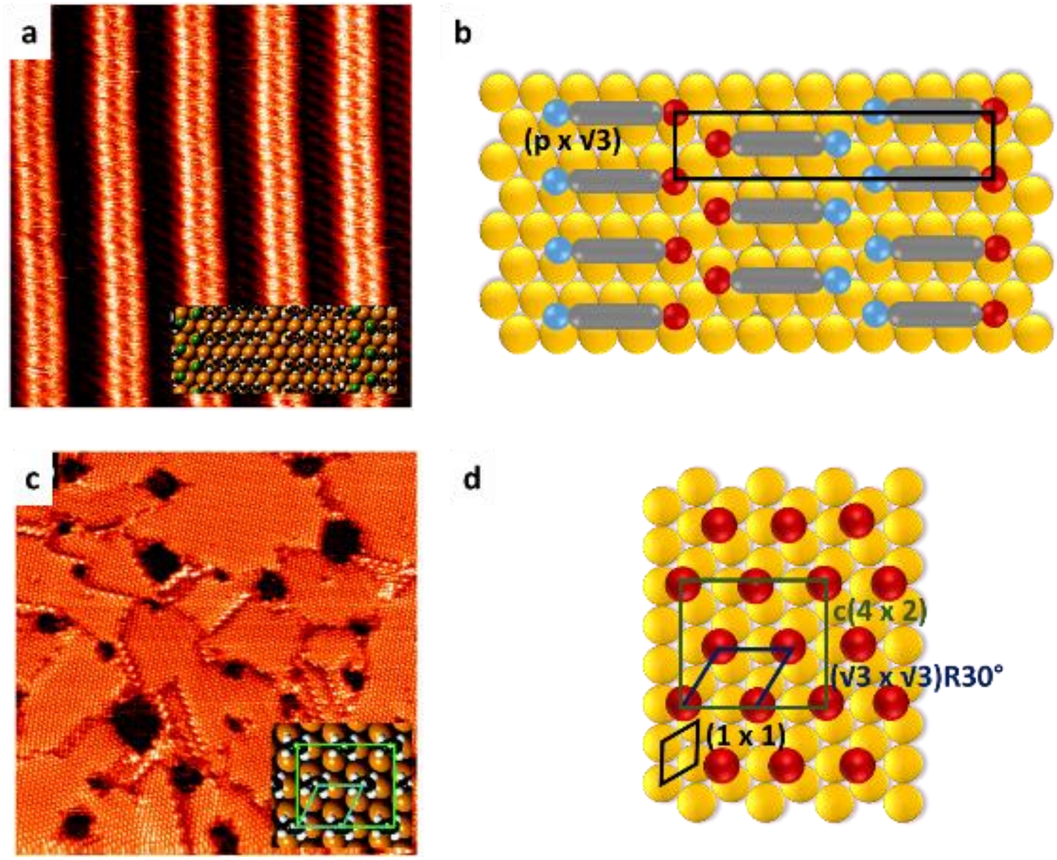

Figure 1.4. STM image (a, c) and the corresponding structural model (b, d) of the stripped (a, b) and close packed phase (c, d) of alkanethiol SAMs. Adapted from ref. 34 with permission.

c) Structure of fluorinated alkanethiols on Au(111)

Fluorinated alkanethiols are widely used for tailoring the physical and chemical properties of surfaces such as friction,[35] wettability,[36] work function[37] and capacitance.[38] In fluorinated alkanethiol SAMs, the rigid fluorocarbon tails are densely packed and form a hexagonal lattice with a nearest-neighbor distance of ∼5.8 Å (Fig. 1.5a, b). This greater lattice spacing is attributed to the large van der Waals diameter of perfluorocarbon chains (5.67 Å)[39] as compared to ~5 Å for alkyl chains. This results in a p(2 × 2) or c(7 × 7) structures with a much less tilted vertical orientation of fluorocarbon chains (16° vs normal).[40,41]

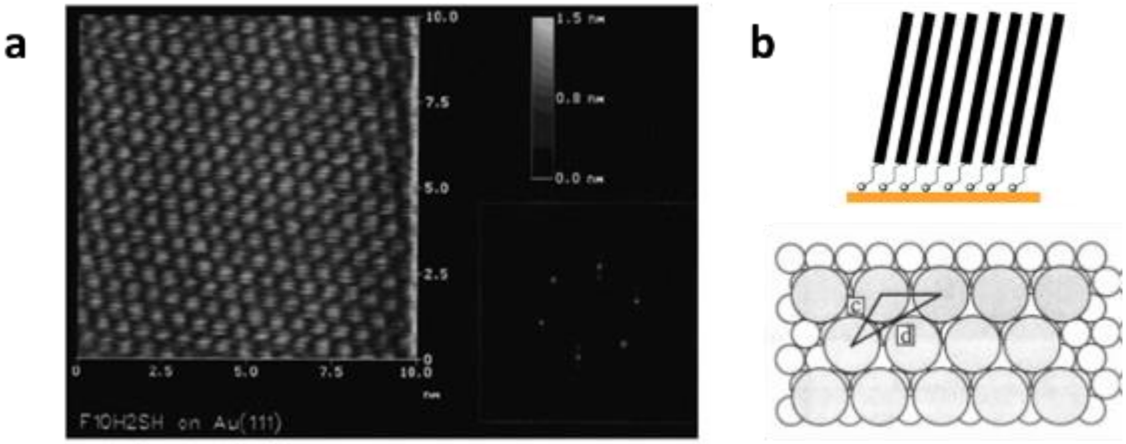

Figure 1.5. (a) AFM image of $F_{10}H_2SH$ SAM (b) schematic illustration of SAM structure. The tilt angle (θ) of fluorocarbon 16° and the c(2 × 2) lattice are shown. The AFM image and molecular model are reproduced from refs 42,40 with permission.

d) SAM of thiolated cage molecules on Au(111)

Thiolated cage molecules such as adamantanethiol and carboranethiol are other important examples of SAM formed from thiols in which the molecular backbone consists of a bulky rigid 3D structure. SAMs of these cage molecules are characterized by large molecular lattice constants relative to alkanethiols (~0.7 nm *vs.* 0.5 nm), and lesser intermolecular interactions which explains their facile displacement with other thiol molecules. The compactness and high symmetry of the cage structure, and the accessibility of different isomers allow the formation of monolayers with a variety of interesting structures and properties (Fig. 1.6).[43]

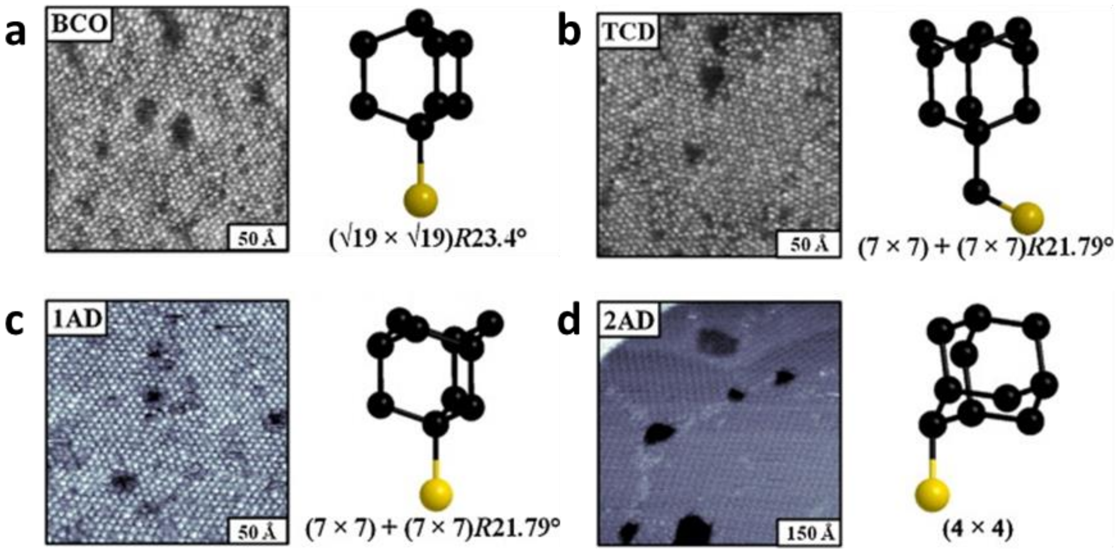

Figure 1.6. A comparison of morphologies for simple organic cage building blocks. (a) bis(bicyclo[2.2.2]octane)disulfide (BCO), (b) bis(tricyclo[3.3.1.1]decylmethyl)disulfide (TCD), (c) 1-adamantanethiol (1AD), and (d) 2-adamantanethiol (2AD). Images reproduced with permission from a) ref. 44 b) ref.45 c) ref .46 d) ref. 47 with permission.

1.3.4 Aromatic thiol SAMs

Compared to SAMs of *n*-alkanethiols, SAMs formed from aromatic thiols are characterized by strong $\pi\cdots\pi$ intermolecular interactions and enhanced electrical conductance.[48] Both of these features make them highly attractive for molecular electronic applications. A number of aromatic SAMs have been studied using various spectroscopic and microscopic techniques. The SAMs studied include phenyl **1**,[49,50] biphenyl **2**,[51,52] and terphenyl moieties **3** [53] attached to the thiol group either directly **2**,[51] via acetylene **3**,[54] or alkyl groups **4** (Fig. 1.7).[52]

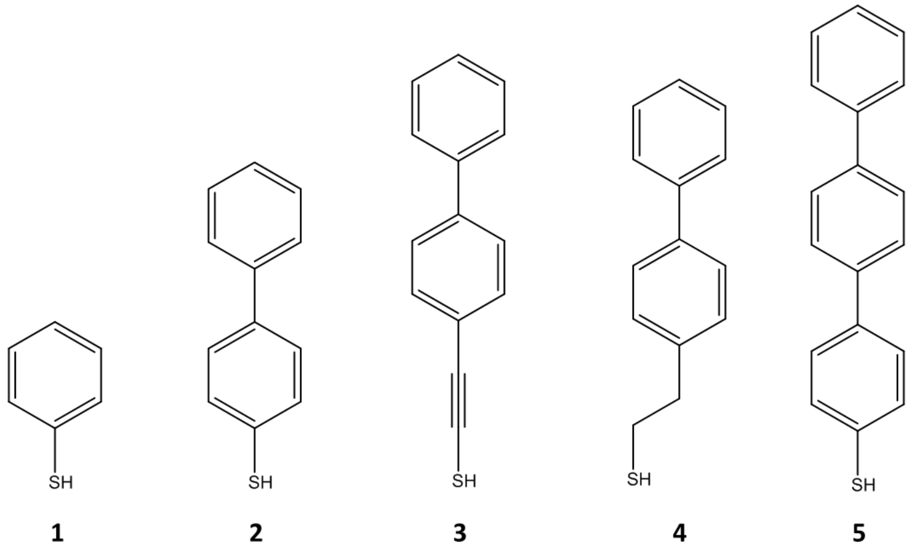

Figure 1.7. Structures of benzenethiol (**1**), biphenylthiol (**2**), biphenylethynethiol (**3**), biphenylethanethiol (**4**), and terphenylthiol (**5**).

In contrast to SAMs formed from alkanethiols, there is much less consensus regarding the two-dimensional ordering of aromatic-based thiol SAMs. This is well illustrated for benzenethiol **1** (BT) and its halogenated derivative pentafluorobenzenethiol (PFBT), two simple aromatic thiols that are widely used in the tuning of the work function of metal electrodes in organic electronic devices.[55] For example, adsorption of BT on Au(111) at room temperature results in either a completely disordered SAM[56,57] or a SAM with relatively small ordered domains (less than 15nm^2).[58] Long range ordered BT and PFBT SAMs have been observed using specific preparation conditions (incubation time of 190 h,[59] solution temperature of 75 °C,[49,50] exchange with a pre-adsorbed cyclohexanethiol SAMs[60]). These studies report different unit cells (Table 1.1) which are somewhat similar for BT SAMs and considerably different for PFBT SAMs.

Table 1.1. Structural lattice of benzenethiol (BT) and pentafluorobenzenethiol (PFBT) SAMs on Au(111) as function of preparation under different experimental conditions.

SAM condition preparation	Unit cell	Reference
Immersion in BT solution at room temperature for 18h	disordered phases	56,57
Immersion in BT solution at room temperature for 2min	$(\sqrt{13}\times\sqrt{13})R13.9^\circ$	61
Immersion in BT solution at 75 °C for 18h	$(2\times3\sqrt{2})R23^\circ$	62
BT exchange with a pre-adsorbed cyclohexanethiol SAM	$(\sqrt{13}\times2\sqrt{5})R46^\circ$	60
Computational simulation	$(2\sqrt{3}\times\sqrt{3})R30^\circ$ or $(\sqrt{3}\times\sqrt{3})R30^\circ$	63
Immersion in PFBT solution at 75 °C for 2h	$(2\times5\sqrt{13})R30^\circ$	50
Immersion in PFBT solution at room temperature for 190h	$(10\sqrt{3}\times2)$	59

1.3.5 Multidentate thiol SAMs

The stability of SAMs under ambient environmental conditions is an important consideration in achieving the full potential of SAMs for practical applications. Numerous studies have reported desorption of SAMs within a few days at ambient conditions through formation of a range of species (thiol radical,[64] sulphonate, [65]disulphide[66]). In this context, the use of multidentate ligands that bind to the substrate with several anchoring thiol groups have been particularly effective for generating SAMs with long-term stability (Fig. 1.8).[67]

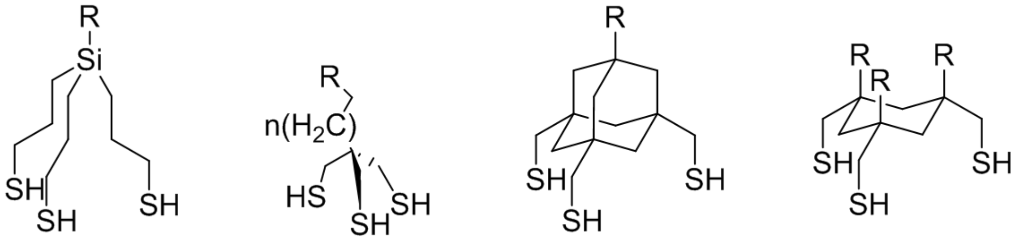

6 7 8 9

Figure 1.8. Examples of multidentate thiols used in SAM.

One of the first multidentate designs used consisted of a dendritic structure having three legs with thiol groups connected to a single branch point (**6** and **7**).[68,69] XPS measurements revealed an enhanced thermal and chemical stability of the tridentate **7** compared to its bidentate and monodentate analogs.[69] However, the systematic improvement in SAM stability is accompanied by a decrease of molecular density and ordering. More recently, a new molecular design involving the rigidity of cyclic frameworks has demonstrate a significant improvement in tridentate SAM ordering.[70] For example, a tripod-adamantane trithiol **8** has been reported for the formation of a 2D SAM with a well-ordered hexagonal packing.[70] In a related study, Lee et al. prepared tridentate SAMs using a cyclohexane ring with three thiol substituents as a framework for stable and well-ordered SAM **9**.[71] In this study, the stability and the conformational ordering of SAMs depend on the length of the alkyl chains of the tridentate adsorbate.

1.4 Physisorbed self-assembled molecular networks (SAMNs)

In contrast to SAMs, physisorbed self-assembled molecular networks (SAMNs) are formed by weakly adsorbed molecules that are sufficiently mobile to diffuse and achieve a well-ordered 2D structure. The structure of SAMN relies on a subtle balance of non-covalent intermolecular and molecule-substrate interactions.[72] The careful selection of molecular building blocks with desired functionality and geometry defines the type of supramolecular interactions involved in the formation SAMNs and their degree of complexity (Table 1.2).

Table 1.2. Classification of the typical supramolecular interactions involved in SAMN formation.[73]

Intermolecular interactions	**Energy range kcal/mol**	**Distance (Å)**	**Directionality**
Van der Waals	0.1–2	< 10	Low
Hydrogen bonding	1–15	1.5–3.5	High
Ionic	2–50	2–3	Low
π-stacking	1–15	3–4	Moderate
Dipole-dipole	10-45	2–3	High
Halogen bonding	1-45	2–3.5	High
Metal-ligand coordination	10–50	1.5–2.5	High

Van der Waals interactions and hydrogen bonding have been extensively employed for the construction of SAMN.[6] In the next sections several examples of SAMNs engineered exclusively through these two types of interactions are discussed.

1.4.1 Van der Waals Interactions

The term van der Waals (vdW) interactions generally refers to dispersion forces that arise from the weak attraction of temporary induced dipoles.[74] Also known as London forces, these interactions have been employed in the stabilization of SAMN of various molecules, notably those with large aromatic cores equipped with alkyl substituents. In this case, SAMN stability arises from two main factors (i) the large total adsorption energy of long alkane chains (on the order of ~1.5-2 kcal/mol per methylene unit on both HOPG[75] and Au (111)[76]) and (ii) the interdigitation of alkyl chains of adjacent molecules which contributes to SAMN stability with an approximate energy of interaction of ∼1 kcal/mol per methylene unit.[77] As mentioned above, vdW interactions have been widely used to drive the assembly of alkylated molecules, such as polycyclic aromatics,[78] other oligomers,[79] and polymers[80](Fig 1.9).

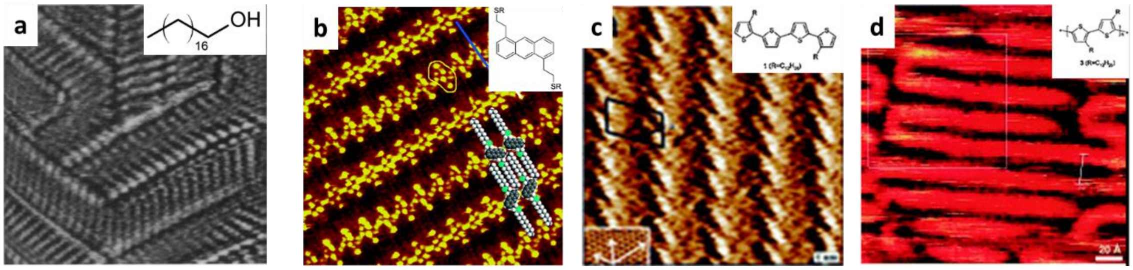

Figure 1.9. STM image of alkylated molecules stabilized on HOPG via vdW interactions. (a) SAMN of octadecanol. (b) SAMN of dialkylanthracene. (c) SAMN of dodecyl substituted quaterthiophene. (d) SAMN of poly(3-dodecylthiophene). Adapted from: a) ref. 81, b) ref. 78, c) ref . 79, d) ref. 80 with permission.

An elegant example of the complexity that can be achieved in SAMNs includes the construction of a four-component architecture of hexadehydrotribenzo[12]annulene(DBA-C_{12}), coronene, isophthalic acid and triphenylene at the solid–liquid interface of HOPG based on van der Waals interactions (Fig. 1.10).[82]

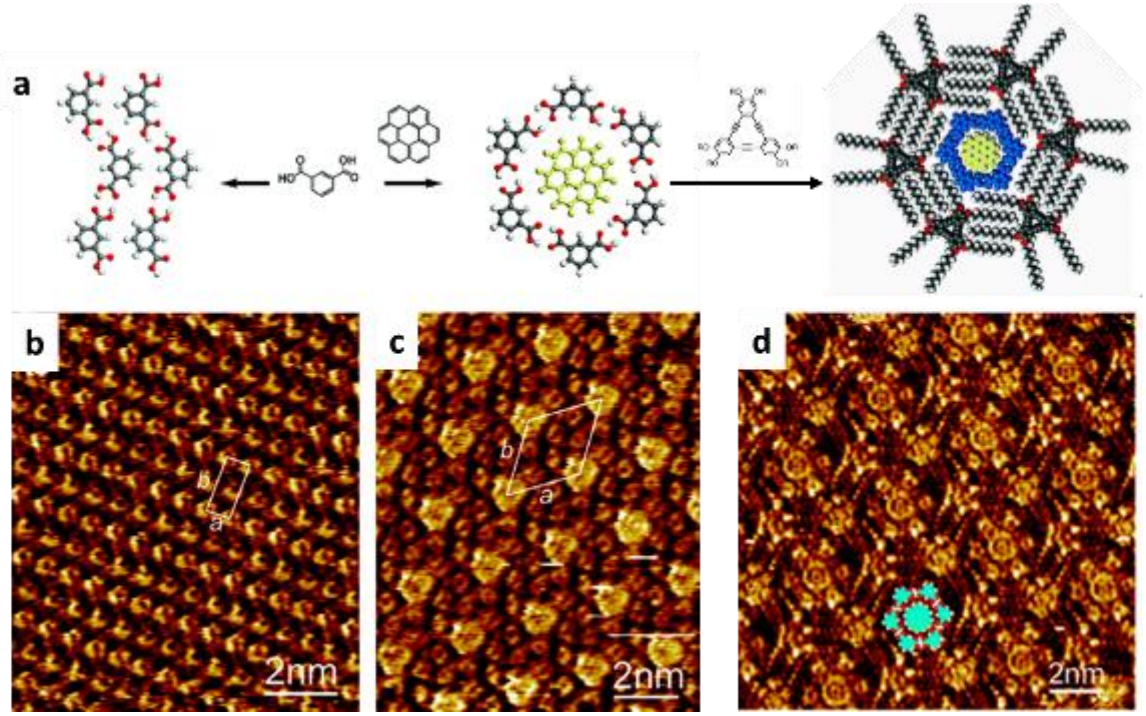

Figure 1.10. STM image of SAMN of a mixture of DBA-Cn, isophthalic acid, coronene, and triphenylene. Adapted from ref. 82 with permission.

Intermolecular vdW interactions can also be used to template other functional molecules on top of SAMN. For example, SAMN of n-$C_{50}H_{102}$ and $C_{36}H_{75}N$ have been used to template alkylated coronene[83] and porphyrin[84] respectively (Fig. 1.11).

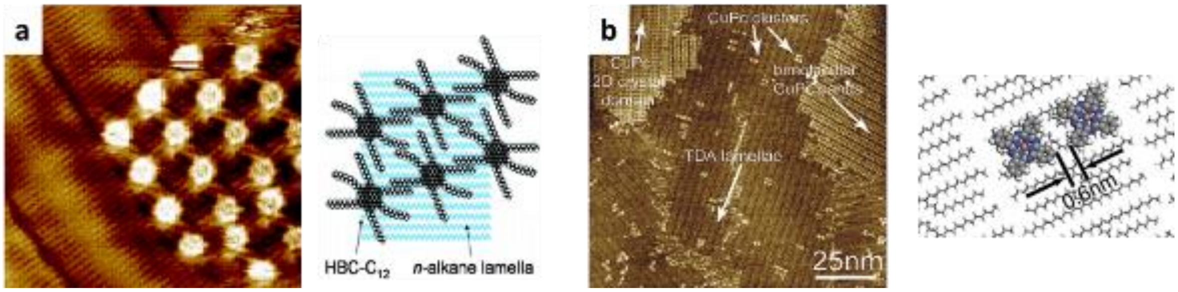

Figure 1.11. (*a*) SAMN of hexakis(n-dodecyl)-peri-hexabenzocoronene (HBC-C_{12}) on a n-alkane (n-$C_{50}H10_2$) molecular template. *(b*) SAMN of copper phthalocyanine (CuPc) on tridedycelamine (TDA) molecular template. Adapted from a) ref. 83 and b) ref. 84 with permission.

1.4.2 Hydrogen bonding

A hydrogen bond (H-bond) is defined as the attractive interaction that occurs between a positively polarized hydrogen and a negatively polarized atom.[85] Depending on the electronegativity of the atoms constituting H-bond donor and the acceptor molecules, the strength of a H-bond can range from strong (15–40 kcal mol^{-1}, *e.g.*, COOH···COO^{-}), to moderate (~5–15 kcal mol^{-1}, *e.g.*, COOH···COOH), to weak (~1–5 kcal mol^{-1}, *e.g.*, CH···O). In addition to their significant strength, H-bonds are characterized by a remarkable selectivity and directionality, which make them one of the most important supramolecular interactions used in engineering 2D SAMNs. Typical examples illustrating the role of H-bonds in SAMN formation are the well-studied benzene carboxylic acids (phthalic acid **10**; isophthalic acid **11**; terephthalic acid **12**; trimellitic acid **13**; trimesic acid (TMA) **14** ; pyromellitic acid **15**) which contain carboxylic acid functions that act as both H-bond donors and acceptors (Fig. 1.12).[86,87]

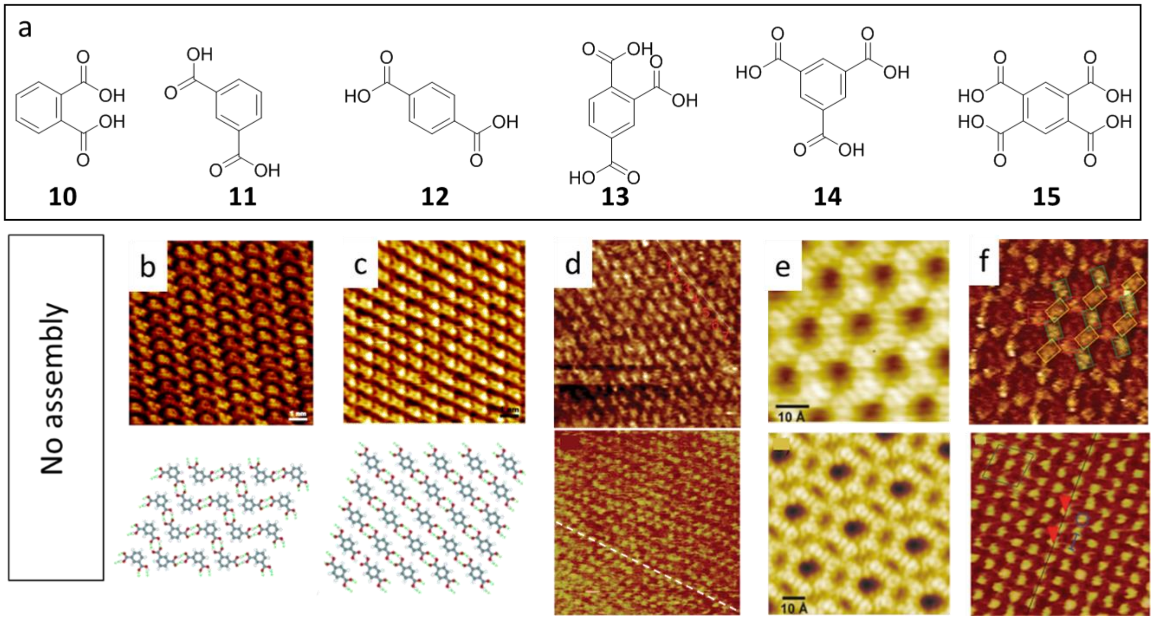

Figure 1.12. (a) Molecular structure of different benzenecarboxylic acids. (b) STM image and molecular model of isophthalic acid SAMN on HOPG. (c) STM image and molecular model of terephthalic acid SAMN on HOPG. (d) STM of trimellitic acid SAMN. (e) The "chicken-wire" and "flower" structures of TMA SAMN. (f) STM images of open and close-packed structures of pyromellitic acid. Adapted with permission from (b,c) ref. 86 (d,f) ref. 88 (e) ref. 89

Various molecular networks have been reported for these benzenecarboxylic acid derivatives, depending of the number and position of the carboxylic groups. For example, while **10** does not form SAMN because of the steric hindrance between the adjacent carboxylic groups, **11** and **12** arrange into zigzag and linear chains of molecules, respectively, that are interconnected with hydrogen bonds.[86] For **13**, a disordered dense layer has been observed because its low symmetry. [88] In **15**, the stability afforded by four acid groups involved in multiple H-bonds enables formation of either close-packed or open structures depending on the solvent type and solution concentration. [88] TMA, which has a 3-fold-symmetric hydrogen-bonding unit, forms both cyclic dimeric hydrogen bonds (denoted $R_2^2(8)$) and trimeric associations ($R_3^3(12)$) through its −COOH groups.[90] Among TMA polymorphs, two nanoporous structures, known as "chicken wire" and "flower" structures, have been extensively employed for hosting guest molecules such as coronene,[90] circulenes[91], and fullerene[92] (Fig. 1.13).

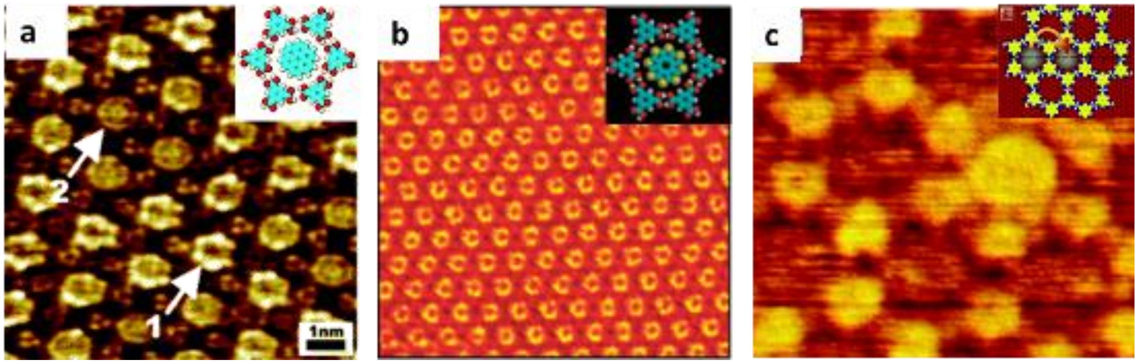

Figure 1.13. STM images of TMA **14** chicken-wire structure hosting different guest molecules. (a) coronene, (b) heterocirculene (c) fullerene. Adapted from: a) ref. 93, b) ref. 91 , c) ref. 92 with permission.

1.5 Directing the assembly of NP

Various self-assembled molecular networks with programmable shape, size and functionality, bonded by single, binary or even multi-component subunits have been developed and explored for nanopatterning applications. In this context, porous two-dimensional networks, such as those constructed using TMA[93,91,92] (Fig. 1.13), calix[8]arene[94] (Fig. 1.19c), or DBA-C_n[82] (Fig. 1.10) building blocks, are of particular interest for the precise localization and confinement of guest entities (e.g. fullerene,[92] coronene,[93] heterocirculene[91]) within their nano-cavities**.** Densely packed (non-porous) molecular networks have also been shown for templating organic molecules. For example, monolayers of alkanethiols[95] (Fig 1.18), coronene[96] (Fig. 1.19h), or pentacene[97] (Fig. 1.19f) have been used for templating fullerene; long *n*-alkane (*n*-$C_{50}H_{102}$) SAMN has been used for HBC-C_{12}[83] (Fig. 1.11a), and TDA SAMN has been shown to template porphyrin[84] (Fig. 1.11b).

In contrast to the great many achievements reported on templating organic molecules, less attention has been paid to metal nanoparticles (NPs). On the other hand, NPs have a range of electronic, magnetic and optical properties that are of great interest in many nanotechnology applications, and thus their templated assembly is of particular interest.[98] Various routes to direct NPs self-assembly have been explored, including 2D crystallization, copolymer, SAMs, and SAMN templates.

1.5.1 2D crystallization of NP assembly on a bare substrate

The 2D crystallization of NPs is one of the simplest approaches for directing the assembly of mono and multicomponent NPs.[93,99] This method was first used for producing AuNP assemblies from a monodisperse AuNPs solution,[100] then was further extended to more than a dozen of binary systems including CuAu,[101] AlB_2,[102] $MgZn_2$,[103] and Cu_3Au.[104] Maximization of the nanoparticle packing density has been proposed as the driving force for these assemblies, and only the close packed structures have been predicted to be thermodynamically stable. However, further studies highlight the complexity of NP crystallization mechanism which involves various interactions between nanoparticles, substrates and solvents such as Coulombic, van der Waals, charge-dipole, and dipole–dipole,[105] space-filling (entropic) factors,[101] drying kinetics,[102] hydrodynamic effects,[106] and diffusion processes.[107] NP assembly is greatly influenced by the size distribution of the nanoparticles. It has been reported that a successful assembly requires a polydispersity of a few percent (<3%), while no assembly is observed when the polydispersity >12%.[108] The crystallization approach has been particularly effective for generating NP supercrystals with exceptional long-range ordering whose length scales range from hundreds of nm to millimeters (Fig. 1.14).[93] However, these patterns are generally restricted to close packed hexagonal or cubic lattices, and it is often challenging to control the formation of multilayers.

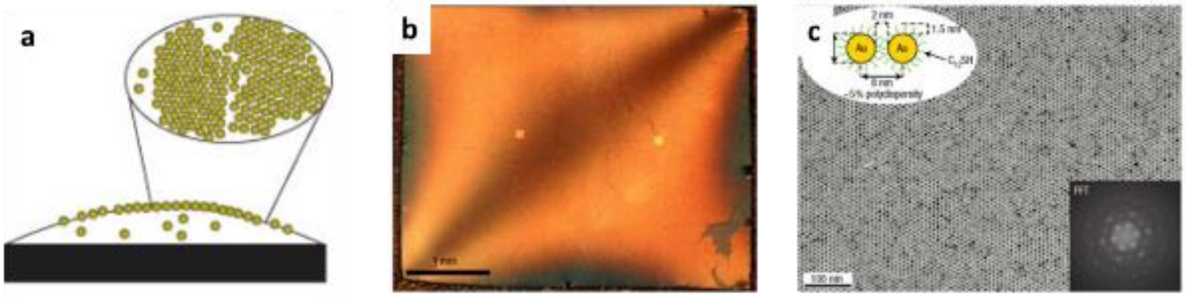

Figure 1.14. (a) Schematic diagram of the self-assembly process during solvent evaporation. (b) Top view of a fully formed, compact nanocrystal monolayer produced by drop-casting 10 µl of a solution of dodecanethiol-ligated 6-nm gold NPs onto a 3 mm × 4 mm Si_3N_4 substrate. (c) Transmission electron micrograph of a typical NP assembly. The upper left inset schematically shows the arrangement of two neighboring NPs. The lower right inset is a fast Fourier transform of the image (c). Adapted from ref. 93 with permission.

1.5.2 NP assembly using copolymer templates

A common strategy for directing the organization of inorganic nanoparticles involves surface patterning with macromolecules such as linear polymers[109] and block copolymers.[110] Block copolymers self-assemble into well-defined arrays of nanostructures that served as effective templates for obtaining nanoparticle assemblies with tunable symmetry and periodicity. Amongst the first block copolymers extensively investigated for NPs patterning are polystyrene-*block*-poly(4-vinylpyridine) (PS-*b*-P4VP) and polystyrene-*block*-poly(ethylene oxide) (PS-*b*-PEO). For example, a quasi-hexagonal close packed array of inorganic oxide semiconducting NPs has been generated using a matrix of PS-*b*-PEO film as a template (Fig. 1.15a).[111] Polystyrene-b-poly(4-vinylpyridine) (PS-*b*-P4VP) has been shown to template metal NPs by exploiting specific interactions between the P4VP block and metallic precursors (Fig. 1.15b).[112]

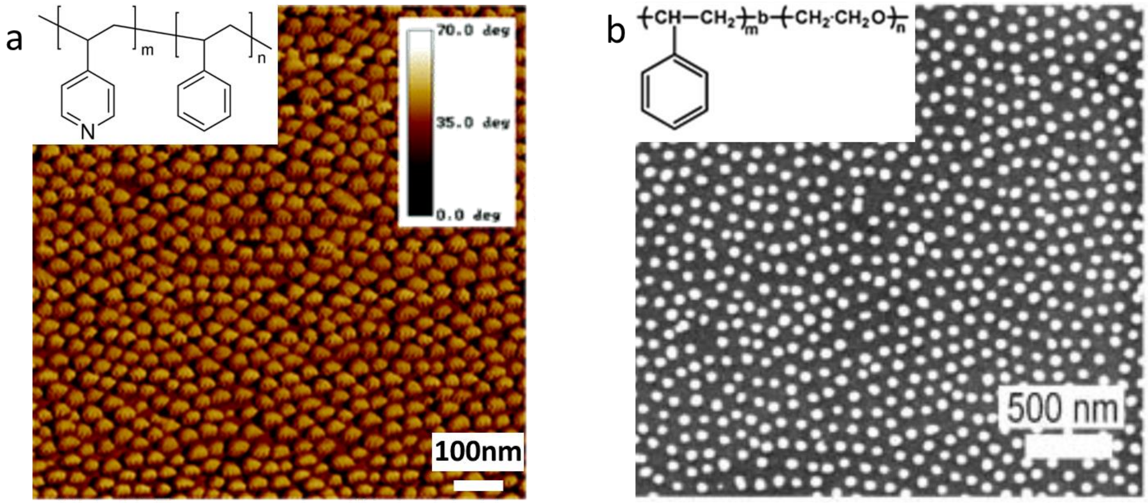

Figure 1.15. (a) Phase contrast AFM image of silica dot arrays on PS-*b*-PEO film (b) Scanning electron microscopy (SEM) images of gold nanoparticles on PS-*b*-P2VP micelles. Adapted from: a) ref. 111, b) ref. 132 with permission.

1.5.3 NP on SAM modified substrates

SAMs formed from organothiols have been used for immobilizing NPs on metal substrates. In this approach, functionalized thiol molecules are bonded to NPs either covalently or through non-covalent interactions. The covalent immobilization of NPs has typically been carried out using dithiol or aminothiol SAMs (Fig. 1.16a).[113] In both cases, NP immobilization is induced by the high affinity between SAM functional groups (SH or NH_2) and the metallic core of NPs. On the other hand, the non-covalent immobilization of NPs has been reported using various supramolecular interactions (hydrogen bonding, coordination, and vdW interactions) between the functional group of SAM and the capping ligand of NP. For example, Zirbs et al.[114] assembled NPs onto SAM through the formation of multiple hydrogen bonds between the barbituric acid containing ligand of NPs and the Hamilton-type receptors anchored as terminal groups in the SAM (Fig 1.16b). The use of coordination interactions to immobilise NPs has been demonstrated using COOH-functionalized SAMs that form a coordination complex between NPs capping ligand and a divalent metal ion (Cu^{2+}, Zn^{2+}, Ni^{2+}) (Fig. 1.16c).[115] Moreover, Vijayamohanan et al. reported the immobilization of NP from aprotic solutions through the hydrophobic interactions between alkanethiols on the AuNP and those forming the SAMs on Au (111) (Fig. 1.16d).[116] Although these studies demonstrate the efficiency of SAMs for immobilizing NPs, little to no long-range order and very limited coverage have been achieved.

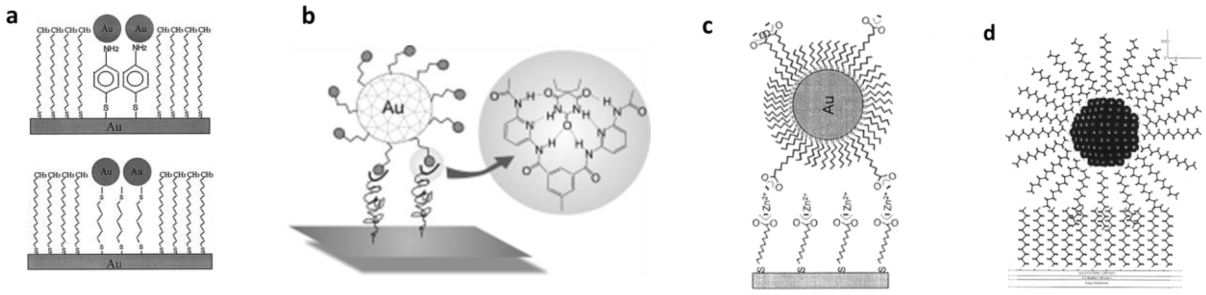

Figure 1.16. Strategies for assembling NPs onto SAMs via (a) metal-ligand interaction, (b) hydrogen bonding, (c) coordination complex, (d) vdW interaction. Adapted from: a) ref. 119 b) ref. 114 c) ref. 115 d) ref. 116 with permission.

1.5.4 NP on SAMN modified substrate

A number of studies have explored the use of SAMN for templating other molecules (see section 1.4). However little work has been reported on inorganic NP guests. The first attempt to template NP involved SAMN of a fatty acid ($C_{14}H_{29}COOH$) (Fig. 1.17a,b).[117] In this work, linearly arranged strands of octadecanethiols coated AuNPs with a periodicity of a few nanometers were formed on top of SAMN. Similarly, dodecanethiol coated NiNPs form rows on top of alkylthiol SAMN, which were attributed to favorable vdW interaction between the hydrophobic coating layer of NPs and the alkyl part of the SAMN.[118] Recently, Zimmt et al. reported the assembly of AuNPs on dialkoxyanthracene derivative SAMN modified with −COOH functional groups using ionic interactions with Cu^{2+} (Fig. 1.17c,d).[119] As for SAM templates, only a short range order and limited surface coverage have been achieved using SAMN.

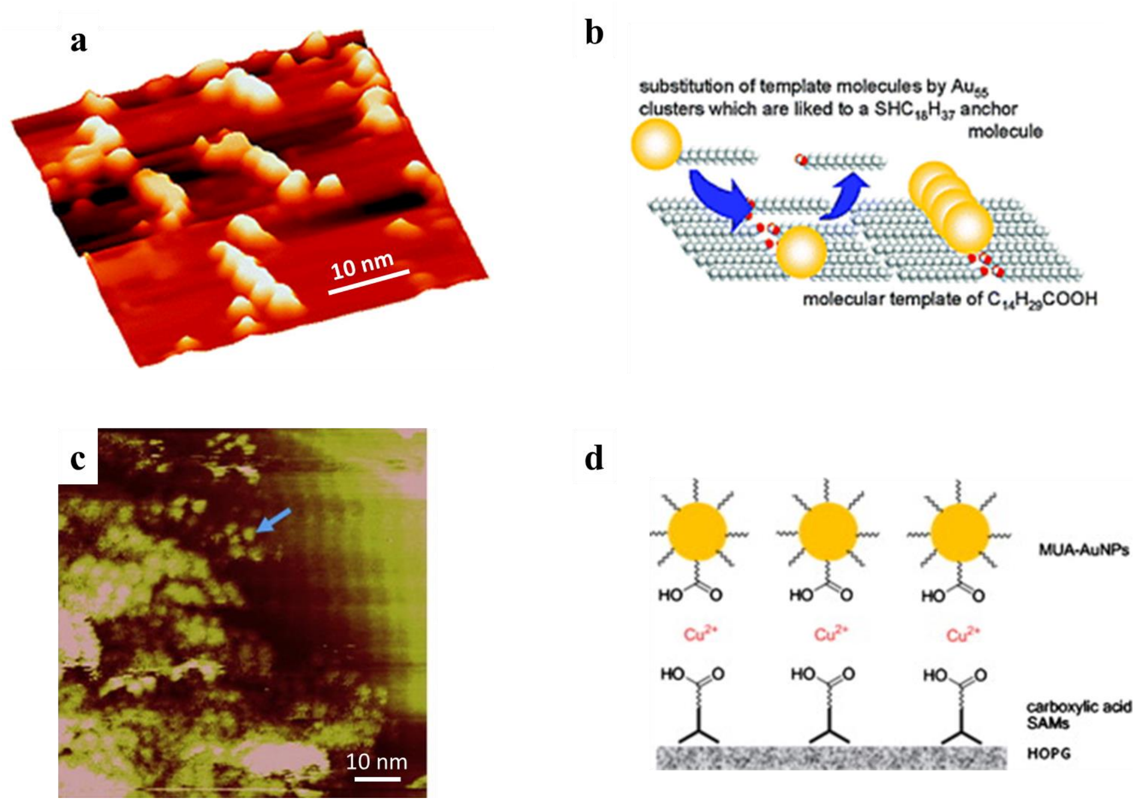

Figure 1.17. STM image and schematic representation of (a,b) $C_{18}H_{37}SH$ AuNP-stabilized by hydrophobic interactions with $C_{14}H_{29}CO_2H$ SAMN. (c,d) $C_{10}H_{20}CO_2HSH$ coated AuNP stabilized with coordination interaction with COOH of an anthracene derivative in the presence of Cu^{2+}. Adapted from a) ref. 117, b) ref. 119 with permission.

1.6 Self-assembly of C_{60} and its derivatives on surfaces

Shortly after their discovery[120] and bulk production,[121] buckminsterfullerene (C_{60}) – one of the allotropes of elemental carbon - became a popular building block in nanoscience and nanotechnology. Due to its unique shape, structural, physical, and chemical properties,[121] fullerene and its derivatives have found applications in a number of research areas including photovoltaics,[122] field effect transistor, [123] and biotechnology devices.[124] Many of these applications involve deposition of a thin film of C_{60} onto a solid support or electrode. In this context, much effort has been devoted to understanding and controlling the structural properties of the C_{60} films, especially at the interface with metals and other semiconductors. Consequently, the molecular orientation and supramolecular organization of C_{60} monolayers have been studied on a variety of substrates, including bare metal substrate, SAMN and SAMs modified substrate.

1.6.1 C_{60} on bare substrates

Since the pioneering work of Altman and Colton on thermal evaporation of C_{60} on Au,[125] C_{60} monolayers have been prepared using different methods (thermal evaporation, solution drop-casting, Langmuir Blodgett) and studied on top of various crystalline substrates ranging from metals,[126,127] to semiconductors,[128] to insulator[129] and polymers.[130] Different structures have been observed depending on the nature and strength of the interaction between C_{60} and the substrate. For example, C_{60} adopts a close-packed structure on the (111) surface of most metals (i.e. Au, Ag, Cu, Ni, and Pd).[131] On Au(111), one of the most extensively studied substrates, C_{60} adopts several structural orientations with respect to the underlying gold lattice: $(2\sqrt{3} \times 2\sqrt{3})R30°$, 38×38, $(7 \times 7)R14°$, and $(3 \times 3)R34°$ structures.[127,132] The nature of Au…C_{60} interactions has been the subject of several studies.[133-135] High-resolution angle resolved photoemission[133] and DFT calculations[134] suggest a very strong, nearly “covalent” character of this bonding with an adsorption energy as high as 50–60 kcal/mol. This is attributed to the hybridization between the d-states of the metal surface and the π-orbitals at the C_{60} cage, in addition to the significant charge transfer from the substrate to C_{60} (from 0.7 to 2 e^- per molecule).[135]

1.6.2 C_{60} on SAM modified substrates

The control of electronic coupling between C_{60} and a metal substrate opens up the possibility of tuning the molecule-surface interactions, which in turn permits the construction of nanostructured surfaces with tailored electronic properties.[136] One approach to achieve this control involves introduction of an organic monolayer at the C_{60}/Au interface. For instance vapor deposition of C_{60} onto alkanethiol SAMs showed the formation of close packed islands that were suggested to be residing on top of the SAM molecules.[95,137] Such assumption was based on the inability of resolving the internal structure of C_{60} molecules. This was explained by their free rotation as result of the weak interaction with SAM. However, other studies suggested that C_{60} molecules penetrate SAMs of octanethiol[95] and 11-phenoxyundecanethiol[138] by forming islands (chains, hexagonal and cubic close packed domains) that are intermixed with the thiol molecules (Fig. 1.18a,b).

Furthermore, deposition of C_{60} onto the striped phase of alkanethiols shows the formation of one-dimensional chains of fullerene. The 1D striped structures of alkanethiols allows the accommodation of two C_{60} molecules at the S termini of the flat lying down alkanethiols (Fig. 1.18c).[139]

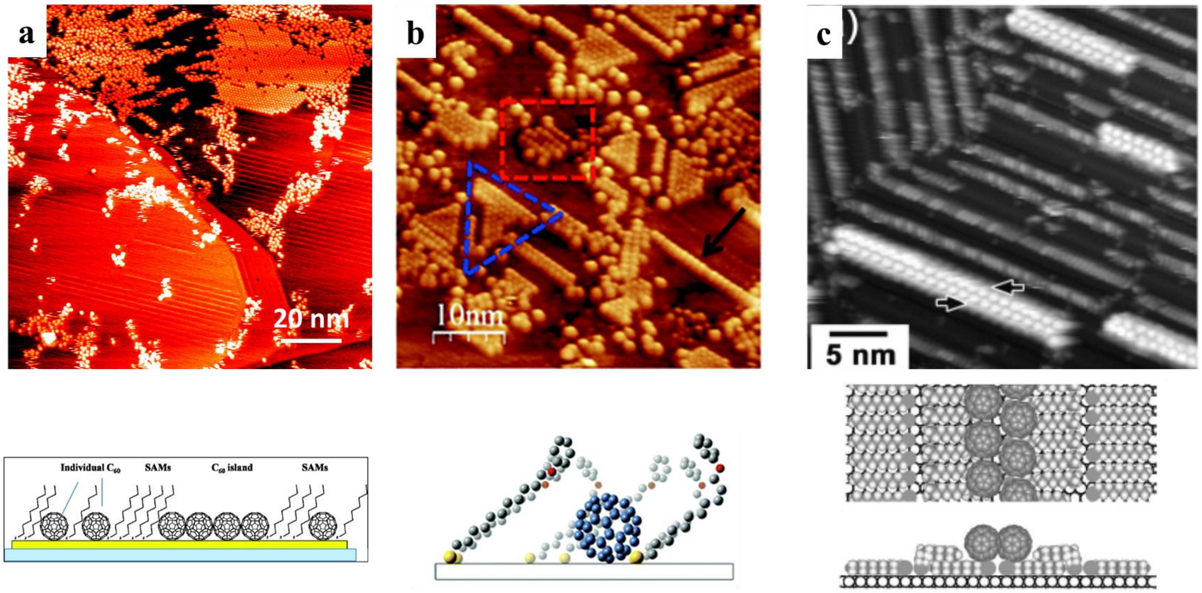

Figure 1.18. STM image and schematic presentation of C_{60} molecules deposited on SAMs of (a) octanethiol, (b) 11-phenoxyundecanethiol, (c) the striped phase of alkanethiol. Adapted from: a) ref. 95, b) ref. 138, c) ref. 139 with permission.

1.6.3 C_{60} on SAMN modified substrate

As mentioned above, fullerenes generally self-assemble into close packed arrays when deposited on bare or SAM-modified metals. More complex fullerene architectures have been created by pre-patterning the substrate with SAMN that accommodate individual C_{60} molecules either through host-guest interactions via a porous network (Fig. 1.19a-d) or the donor-acceptor interactions (Fig. 1.19e-h) with SAMN of electron donating molecules. The host-guest interactions have been reported using various porous SAMN of oligothiophene,[140,141] benzene di- and tricarboxylic acids,[142] calix[8]arene,[94] perylenetetracarboxydiimide (PTCDI)-melamine.[143] In some of these systems, fullerenes play a more complex role rather than a simple passive occupation of the voids within the SAMN. Indeed, C_{60} molecules were shown to promote the structural transformation of the host framework as well as inducing the growth of a second layer of host molecules.[144] Donor-acceptor interactions of C_{60} have been reported for SAMN of polyaromatic donor molecules such as porphyrin,[145] perylene,[146] coronene,[96] pentacene[97], and α-sexithiophene.[147] These donor–acceptor systems are of great interest in the development of organic electronic devices.[148] For example, they are used in organic heterojunction solar cells.[149]

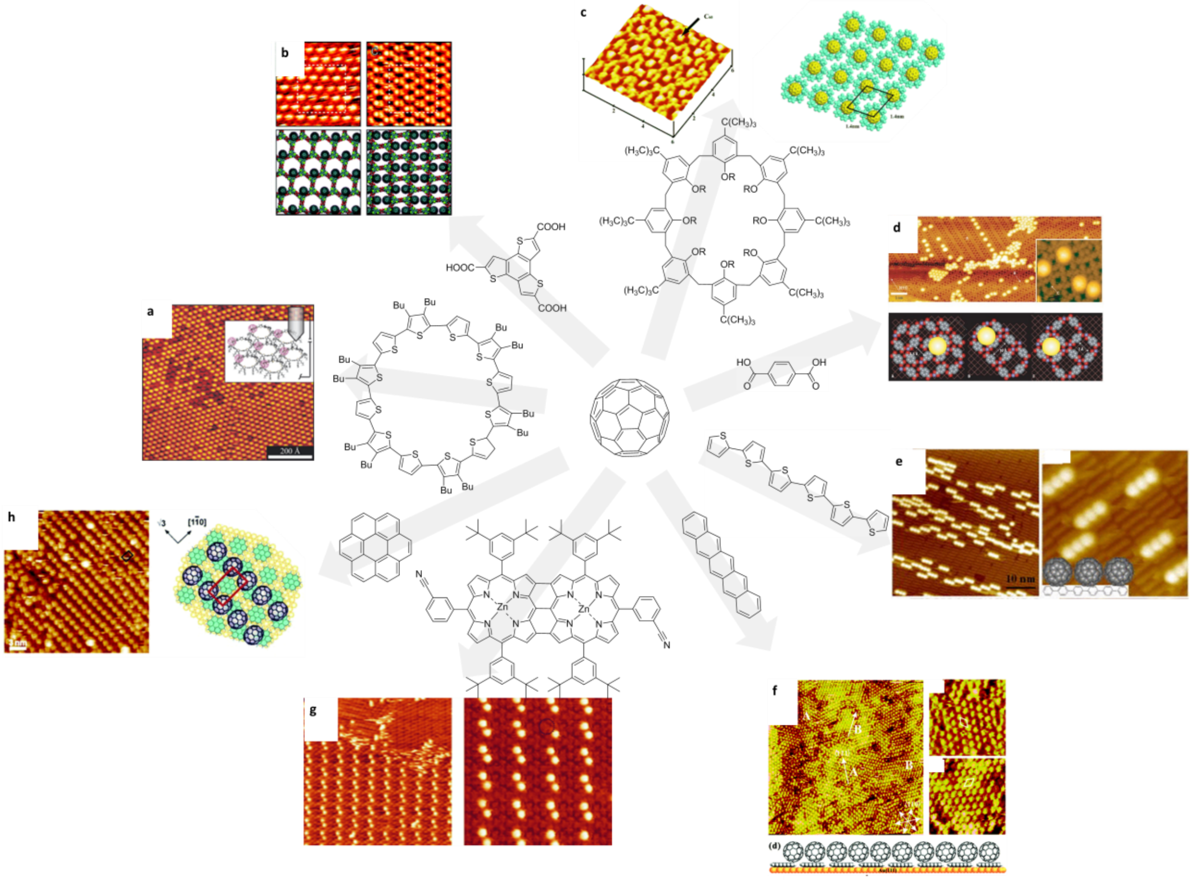

Figure 1.19. C_{60} assembly stabilized through (a-d) host-guest interactions and (e-h) acceptor-donor interactions. C_{60} on SAMN of (a) oligothiophene, (b) tricarboxylic acid, (c) calix[8]arene, (d) dicarboxylic acid, (e) α-sexithiophene, (f) pentacene, (g) porphyrin, (h) coronene. Adapter from: a) ref. 140,141, b) ref. 141, c) ref. 94, d) ref. 142, e) ref. 147, f) ref. 97, g) ref. 145, h) ref. 96 with permission.

1.6.4 Self-assembly of functionalized C_{60}

Many applications involving fullerene molecules require their chemical modification with specific functional groups. A variety of fullerene derivatives have thus been synthesized and self-assembled on metal substrate. For example, Ecija et al studied monolayers of phenyl-C_{61}-butyric acid methyl ester (PCBM) on Au(111) in UHV environment (Fig. 1.20a).[150] The authors show a coverage-dependent transition of the self-assembly of PCBM. At low coverage, the fullerenes were present predominantly as monomers. At higher coverages, rows of PCBM dimers and tetramers were observed and attributed to the weak hydrogen bonding interaction between the ester groups of adjacent molecules. Deposition of a fullerene malonic acid (C_{61}-$(CO_2H)_2$) adlayer on Au(111) yields a (3.1 × 3.1)R5° structure which was attributed to hydrogen bonds forming between COOH groups of adjacent fullerene molecules (Fig.1. 20b).[151] The self-assembly of a fullerene that bears long alkyl chains leads to the formation of rows of molecular dimers due to the vdW interactions between the alkyl chains of adjacent molecules (Fig. 1.20c).[152] Chen et al. examined four fullerene derivatives with functional groups of varying size and different intermolecular interaction types on Au(111) (Fig. 1.20d-f). They observed a $(2\sqrt{3} \times 2\sqrt{3})R30°$ structure for C_{60} with small functional groups and a multilayered disordered structure for C_{60} derivatized with bulky substituents.[153]

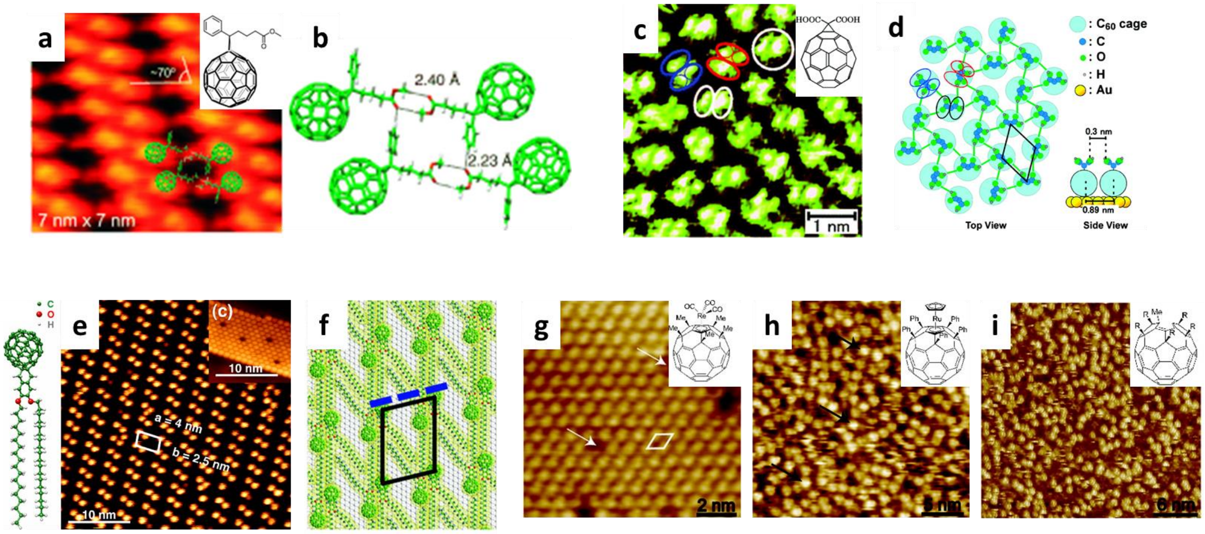

Figure 1.20. (a) High resolution STM and the corresponding molecular model of phenyl-C_{61}-butyric acid methyl ester (PCBM) arranged in dimeric rows connected by an array of weak hydrogen bonds. (b) High resolution STM image and top view molecular model of an ordered C_{60} malonic acid adlayer on Au(111). (c) STM image and molecular model of a self-assembled monolayer of alkylated C_{60} on Ag(111). (d), (e), and (f) STM image of functionalized C_{60} molecules with different size of functional groups. Adapted from a) ref. 150, b) ref. 151, c) ref. 152, d) ref. 153 with permission.

The above examples illustrate the considerable effort devoted to understanding and controlling the assembly of C_{60} and C_{60} derivatives on various substrates. Overall, the assembly of non-functionalized C_{60} is governed by molecule-substrate interactions. For functionalized C_{60}, the nature of the functional groups plays a determinant role in the resulting assembly. For example, relatively robust and complex nanostructures of C_{60} derivatives might be formed through the use of directional supramolecular interactions such hydrogen bonding as will be shown in Chapter 5.

1.7 Characterization techniques

The remarkable evolution in surface analysis techniques, which began with the development of electron-based spectroscopy techniques, Auger electron spectroscopy (AES), X-ray photoelectron spectroscopy (XPS), ultraviolet photoelectron spectroscopy (UPS), in the early 1950s and continued with the invention of scanning probe techniques (STM, AFM) in mid 1980s, have greatly contributed to our present knowledge of organic monolayers on solid surfaces. Generally, in order to obtain a complete picture of organic monolayers (including structure, mechanism of adsorption, stability) the use of several complementary techniques is required. The following sections provide a brief description of XPS, STM, and electrochemical methods employed in this Thesis research.

1.7.1 X ray photoelectron spectroscopy

XPS is one of the most widely used techniques for the analysis of solid surface (1-5 nm thin film) (Fig1. 21). Its utility lies in the accurate quantification of elements as well as the determination of their chemical environment.[154] XPS is based on the irradiation of a sample under vacuum conditions with a monochromatic beam of photons, generally generated from AlK_α (1486.6 eV) or MgK_α (1253.6 eV) sources. The incident X-rays cause the ejection of core-level electron from sample atoms. The kinetic energy of the photoemitted electron is a function of its binding energy which is characteristic of the element from which it was emitted and its chemical environment. The binding energy of the core electron is given by the Einstein relationship:

$$E_b = h\nu - E_k - \varphi \tag{1.4}$$

Where hν is the X-ray photon energy; E_k is the kinetic energy of the photoelectron, and φ is the work function induced by the analyzer (about 4~5eV).

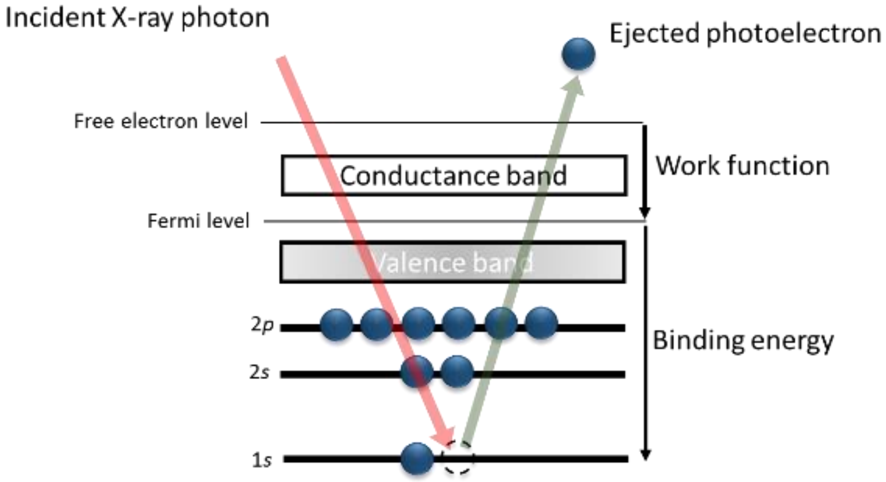

Figure 1.21. Schematic representation of XPS principle.

XPS has been extensively used for the characterization of thiol-based SAMs (Fig. 1.22).[22,155,156] The S2p binding energy (E_b) provides the key evidence for S-Au bond formation.[115] The S2p spectrum consists of ($2p_{3/2}$) and ($2p_{1/2}$) peaks with an intensity ratio of 2:1. Typical $S_{2p3/2}$ BE values for an unbound alkanethiol (and dialkyldisulfide) are between 163 and 164 eV. After chemisorption of these molecules onto the gold surface the $S2p_{3/2}$ E_b decreases to 162 eV,[156] which is attributed to the formation of a gold−thiolate bond. In contrast, when sulfur bound to elements with high electronegativity such as oxygen the E_b of $S2p_{3/2}$ shifts toward higher values. For example, the $S2p_{3/2}$ peak of the oxidized thiol species (sulfonates) occurs at 167−168 eV.[157] An additional peak is also observed at 161 eV for thiol-based SAMs, in either the initial stage of monolayer growth or after annealing. The origin of this peak is not well understood; some studies assign it to either atomic sulfur on Au (formed by scission of the C-S bond), or differently adsorbed molecular constituents (e.g. adsorption of a thiolate at high coordination sites such as a kink site on the gold surface).[158]

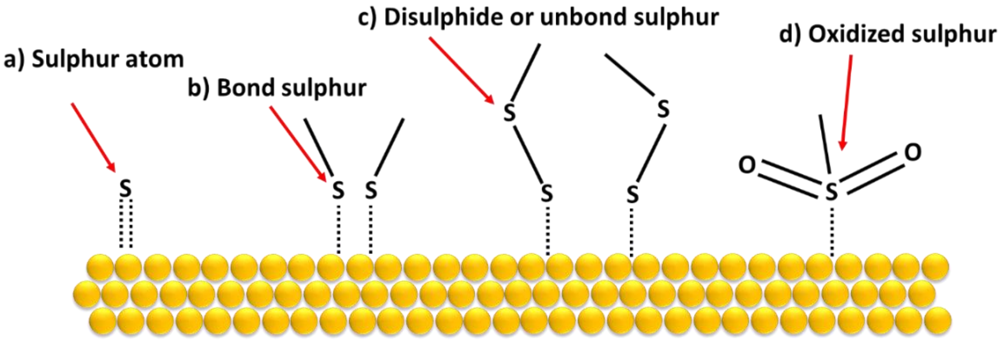

Figure 1.22. Schematic representation of four types of sulphur atom typically observed in the XPS S2p spectrum of thiol SAMs on Au(111). a) Atomic sulfur or another bound sulfur with a binding energy of 161 eV, b) bond sulfur at 162 eV, (c) unbond sulfur at 163-164 eV, (d) oxidized sulphur at 168 eV. Adapted from ref. 159 with permission.

1.7.2 Scanning tunneling microscopy

Scanning tunneling microscopy (STM) is a powerful scanning probe technique that exploits quantum-mechanical electron tunnelling between the tip and the sample to sense the topography and the electronic properties of the sample at an atomic level. Invented by Binnig and Rohrer in 1981, STM has revolutionized the field of nanotechnology, presenting the first tool with the ability to image, characterize and even manipulate single atoms and molecules on metallic surfaces.[160]

The principle of STM is based on bringing a sharp metallic tip very close (0.3–1 nm) to a conducting surface so that the wave functions of the tip and surface overlap sufficiently to allow the flow of a distance-dependent tunneling current under applied bias voltage. A tunneling current (~0.1 to 10 nA) is then measured at a convenient operating voltage (~10 mV–1 V). This tunneling current exhibits an exponential decay with an increase of the gap z according to equation:

$$G \propto A \exp(-\alpha z) \tag{1.5}$$

Where α is the decay constant of the material, z is the tip–sample separation, and A is a constant.

An STM can be operated in either a constant current mode or a constant height mode. In constant current imaging, the tip-sample separation is controlled by a current feedback loop that allows a constant current map of the surface. This mode is characterized by a slow speed but is more suitable for relatively rough surface. Alternatively, in constant height mode the feedback is turned off, the tip is scanned across a surface at (near) constant height and the current is recorded yielding a locally changing tunneling current map. This mode is more advantageous at high scanning frequencies (up to 10 KHz) and for atomically flat surfaces as otherwise a tip crash would be inevitable.

As shown in Figure 1.23, the main components of an STM apparatus include a sharp probe tip, made by the mechanical cutting or electrochemical etching of a metallic wire. A coarse positioning unit is used for large displacements of the tip from the initial position to within the tunneling range (few Å). A piezoelectric scanner allows the fine tuning of the vertical and lateral movement of the tip. A vibration isolation stage and electronics with sufficient sensitivity for a significant increase of resolution and stability of the measurements, even under unfavourable lab conditions.

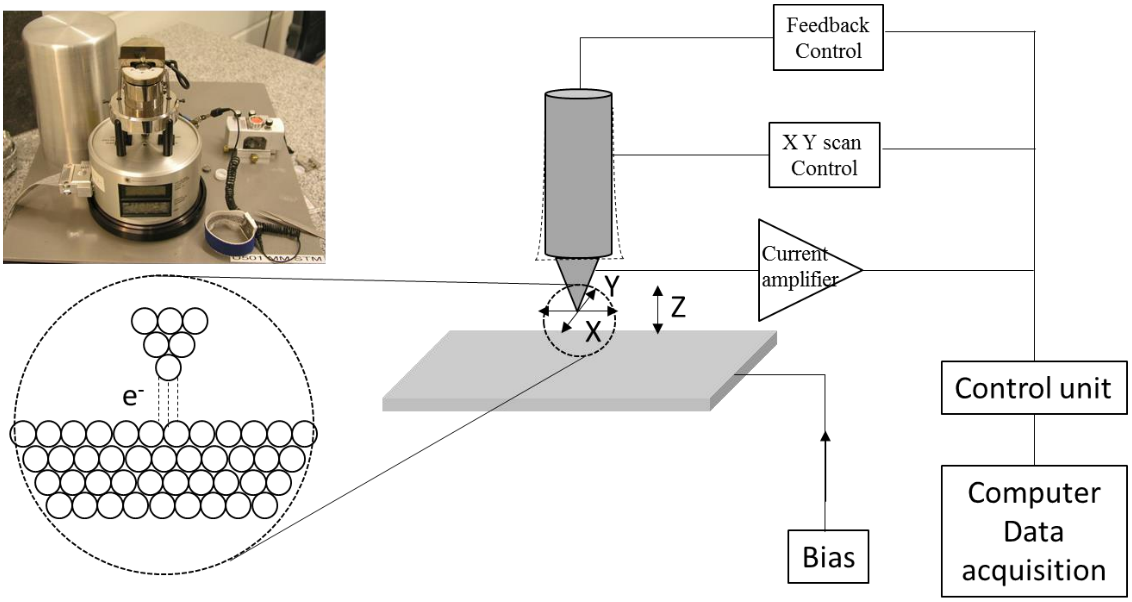

Figure 1.23. Schematic diagram of the working principle of an STM, microscopic view of tip-sample interface is shown in the circle. Image of the Veeco Multimode 8 instrument is shown in the top left corner.

An STM experiment can be carried out in ultrahigh vacuum conditions (UHV) as well as in ambient air or liquid environments. The first experiments on molecular adlayers were carried out under UHV on metal surfaces.[16] The UHV environment has been particularly attractive for two reasons. First, a UHV environment increases the signal-to-noise ratio by eliminating the sample-air-tip interactions allowing to achieve unprecedentedly high resolution STM images and reliable current vs voltage (I-V) curves in scanning tunnelling spectroscopy (STS).

Secondly, such an environment extends STM studies to a large number of metal (copper, platinum…) and semiconductors substrates, not accessible in pure form under ambient conditions. On the other hand, performing STM at a liquid-solid interface does not require a complex and expensive infrastructure as for UHV conditions. Moreover, the liquid phase acts as a reservoir of dissolved species which can contribute to the dynamic of molecular assembly and promotes the repair of defects. In this Thesis, all the STM experiments were performed at liquid-solid interface.

1.7.3 Cyclic voltammetry

Cyclic voltammetry is one of the most commonly used electrochemical techniques for studying different aspects of redox processes such as the kinetics of electron transfer, the reversibility of reactions, the presence of intermediates, and the stability of products in redox reactions.[161]

In cyclic voltammetry the working electrode potential is scanned linearly back and forth between two potentials, V1 and V2, while the current is recorded (Fig. 1.24). The resulting curves are called voltammograms. A voltammogram provides the measured current between the working electrode and the reference electrode versus the applied potential between the working and reference electrode.

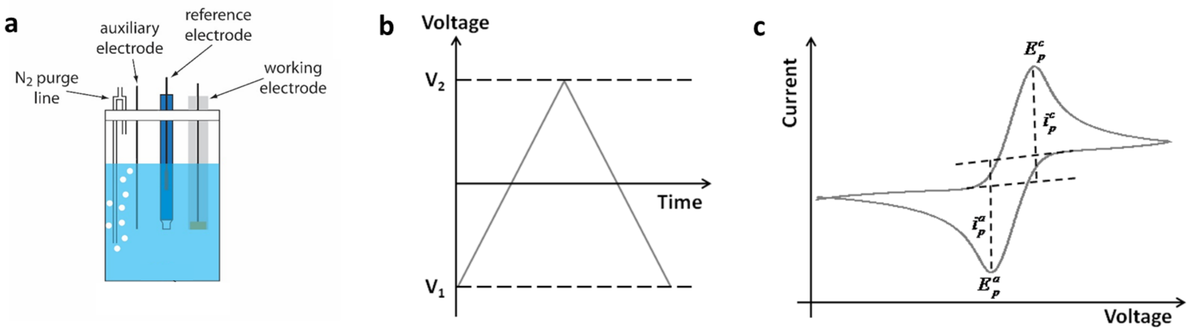

Figure 1.24. Setup of an electrochemical cell. Cyclic voltammetry waveform (b) and typical cyclic voltammogram (CV). $E_p^{\ c}$ ($E_p^{\ a}$) and $i_p^{\ c}$ ($i_p^{\ a}$) are the potentials and currents at cathodic (anodic) peaks, respectively.

Cyclic voltammetry is a common technique used for characterizing organothiol SAMs. The CV of thiol SAMs on Au(111) in strongly alkaline electrolytes exhibits a cathodic wave due to the charge produced by reductive desorption of thiolate (Fig. 1.25):[162]

$$\text{Au-SR} + 1e^{-} \rightarrow \text{Au}(0) + \text{RS}^{-} \quad (1.6)$$

This desorption process can be used to determine the surface concentration of a SAM adlayer, Γ_{m} (mol/cm^2), following Faraday's law:

$$\Gamma_{\mathrm{m}} = Q/ZnFA \quad (1.7)$$

where Q (μC) is the passed charge (determined from the CVs by integrating the area under the reduction peak), Z is the number of electrons involved in the redox reaction, n is the number of moles of reactants, F is Faraday's constant (96 487 C mol^{-1}) and A is the active area of the electrode ($A = A_g \times \gamma$(cm^2)), with A_g (cm^2) being the geometric area and γ being the roughness factor of the electrode. A typical coverage density of a well packed alkanethiol on Au(111) determined via CV is 7.8×10^{-10} mol/cm^2, corresponding to the close packed (√3 x √3) R30 lattice.[163]

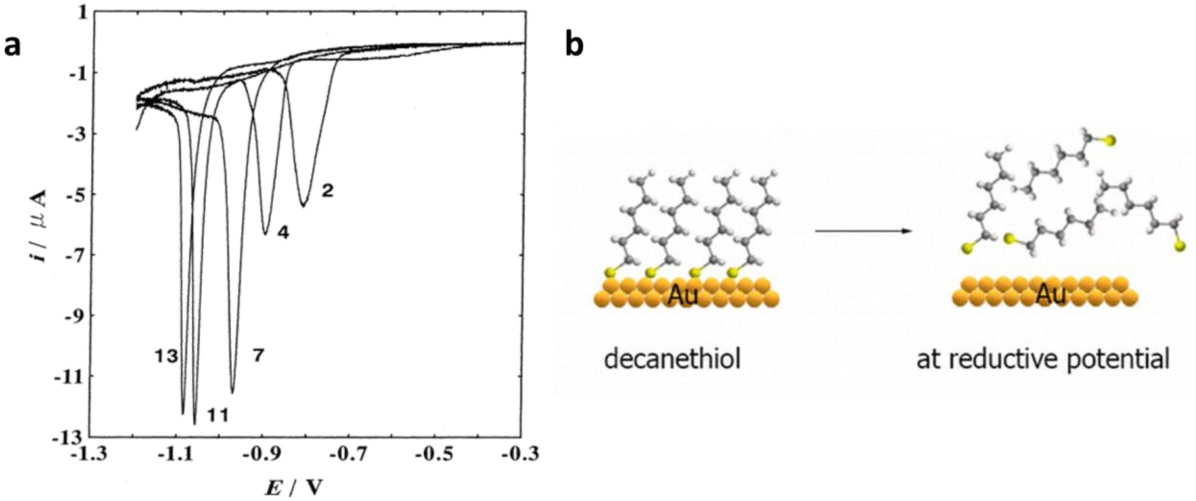

Figure 1.25. (a) Cyclic voltammograms of the reductive desorption of self-assembled monolayers composed of n-alkanethiolates on Au(111) recorded in 0.5 M KOH solution. The number of methylene units is indicated at each curve. (b) Schematic presentation for hexanethiol desorption. Adapted from: a) ref. 164, b) ref. 165 with permission.

The potential of the cathodic stripping peaks is a function of the strength of the metal–sulfur bond and the interchain interaction, the accessibility of the metal–sulfur bond to cations from the solution, the presence of any intermediate or weakly adsorbed states, and surface crystallography.[166]

1.8 Summary

Patterning surfaces at the nanoscale is of great interest in many nanotechnology applications. Among the bottom-up strategies, self-assembly provides a promising route to create complex nanostructures with immense flexibility in terms of nanoscale building blocks and properties. The structure and functionality of molecular building blocks define the type of interactions that are involved in the formation of the molecular pattern and in the whole templating process.

In chemisorbed monolayers, namely alkanethiols SAMs on gold, molecules are covalently attached to a gold substrate through S-Au bond. The widespread use of SAMs in practical applications depends largely on their long-term stability. In this context, SAMs with enhanced stability have been reported using multidentate thiols that have several groups anchored to the substrate. In molecular electronics, aromatic thiols have been particularly attractive, especially their fluorinated derivatives because of their ability to tune the work function of electrode devices.

On the other hand, physisorbed monolayers represent an elegant and versatile approach to achieve structurally complex nanostructures with specific shape, composition, and functionality. Physisorbed monolayers are generally governed by a subtle interplay of supramolecular interactions between molecules and substrate and between molecules themselves. Particular attention has been given to hydrogen bonding and van der Waals interactions due to their extensive use in the creation of complex architectures of physisorbed monolayers.

A number of these SAMs and SAMNs have been used for nanopatterning applications. While most of the work has been carried out on molecular guests, little attention has been paid to templating inorganic nanostructures. In the following chapters several examples of chemisorptive and physisorptive self-assembled monolayers are formed and explored for templating gold nanoparticles (AuNPs) and C_{60} molecules.

References

[1]. Whitesides, G.; Mathias, J.; Seto, C. Molecular Self-Assembly and Nanochemistry: A Chemical Strategy for the Synthesis of Nanostructures. *Science* **1991**, *254*, 1312-1319.

[2]. Whitesides, G. M.; Grzybowski, B. Self-Assembly at All Scales. *Science* **2002**, *295*, 2418-2421.

[3]. Whitesides, G. M.; Kriebel, J. K.; Love, J. C. Molecular Engineering of Surfaces Using Self-Assembled Monolayers. *Sci. Prog.* **2005**, *88*, 17-48.

[4]. Spatz, J. P. Nano- and Micropatterning by Organic–Inorganic Templating of Hierarchical Self-Assembled Structures. *Angew. Chem. Int. Ed.* **2002**, *41*, 3359-3362; Hamley, I. W. Nanotechnology with Soft Materials. *Angew. Chem. Int. Ed.* **2003**, *42*, 1692-1712.

[5]. De Feyter, S.; De Schryver, F. C. Two-Dimensional Supramolecular Self-Assembly Probed by Scanning Tunneling Microscopy. *Chem. Soc. Rev.* **2003**, *32*, 139-150.

[6]. Ciesielski, A.; Palma, C.-A.; Bonini, M.; Samorì, P. Towards Supramolecular Engineering of Functional Nanomaterials: Pre-Programming Multi-Component 2d Self-Assembly at Solid-Liquid Interfaces. *Adv. Mater.* **2010**, *22*, 3506-3520.

[7]. Nie, Z.; Petukhova, A.; Kumacheva, E. Properties and Emerging Applications of Self-Assembled Structures Made from Inorganic Nanoparticles. *Nat. Nanotechnol.* **2010**, *5*, 15-25.

[8]. Kühnle, A. Self-Assembly of Organic Molecules at Metal Surfaces. *Curr. Opin. Colloid Interface Sci.* **2009**, *14*, 157-168.

[9]. Franklin, B. Of the Stilling of Waves by Means of Oil. *Philos. Trans. R. Soc. London* **1774**, *64*, 445-460.

[10]. Pockels, A. Surface Tension [4]. *Nature* **1891**, *43*, 437-439.

[11]. Langmuir, I. The Constitution and Fundamental Properties of Solids and Liquids. II. Liquids.1. *J. Am. Chem. Soc.* **1917**, *39*, 1848-1906.

[12]. Blodgett, K. B. Films Built by Depositing Successive Monomolecular Layers on a Solid Surface. *J. Am. Chem. Soc.* **1935**, *57*, 1007-1022.; Blodgett, K. B.; Langmuir, I. Built-up Films of Barium Stearate and Their Optical Properties. *Phys. Rev.* **1937**, *51*, 964-982.

[13]. Timmons, C. O.; Zisman, W. A. Investigation of Fatty Acid Monolayers on Metals by Contact Potential Measurements1. *J. Phys. Chem.* **1965**, *69*, 984-990; Levine, O.; Zisman, W. A. Physical Properties of Monolayers Adsorbed at the Solid–Air Interface. I. Friction and Wettability of Aliphatic Polar Compounds and Effect of Halogenation. *J. Phys. Chem.* **1957**, *61*, 1068-1077.

[14]. Binnig, G.; Rohrer, H.; Gerber, C.; Weibel, E. Tunneling through a Controllable Vacuum Gap. *Appl. Phys. Lett.* **1982**, *40*, 178-180; Binnig, G.; Rohrer, H.; Gerber, C.; Weibel, E. 7 × 7 Reconstruction on Si(111) Resolved in Real Space. *Phys. Rev. Lett.* **1983**, *50*, 120-123.

[15]. Nuzzo, R. G.; Allara, D. L. Adsorption of Bifunctional Organic Disulfides on Gold Surfaces. *J. Am. Chem. Soc.* **1983**, *105*, 4481-4483.

[16]. Ohtani, H.; Wilson, R. J.; Chiang, S.; Mate, C. M. Scanning Tunneling Microscopy Observations of Benzene Molecules on the Rh(111)-(3 × 3) (C_6H_6 + 2CO) Surface. *Phys. Rev. Lett.* **1988**, *60*, 2398-2401.

[17]. Greene, J. E. Organic Thin Films: From Monolayers on Liquids to Multilayers on Solids. *Phys. Today* **2014**, *67*, 43-48; Eigler, D. M.; Schweizer, E. K. Positioning Single Atoms with a Scanning Tunnelling Microscope. *Nature* **1990**, *344*, 524-526.

[18]. Ulman, A. Formation and Structure of Self-Assembled Monolayers. *Chem. Rev.* **1996**, *96*, 1533-1554; Gooding, J. J.; Mearns, F.; Yang, W.; Liu, J. Self-Assembled Monolayers into the 21st Century: Recent Advances and Applications. *Electroanalysis* **2003**, *15*, 81-96; Onclin, S.; Ravoo, B. J.; Reinhoudt, D. N. Engineering Silicon Oxide Surfaces Using Self-Assembled Monolayers. *Angew. Chem. Int. Ed.* **2005**, *44*, 6282-6304.

[19]. Love, J. C.; Estroff, L. A.; Kriebel, J. K.; Nuzzo, R. G.; Whitesides, G. M. Self-Assembled Monolayers of Thiolates on Metals as a Form of Nanotechnology. *Chem. Rev.* **2005**, *105*, 1103-1169.

[20]. Vericat, C.; Vela, M. E.; Benitez, G.; Carro, P.; Salvarezza, R. C. Self-Assembled Monolayers of Thiols and Dithiols on Gold: New Challenges for a Well-Known System. *Chem. Soc. Rev.* **2010**, *39*, 1805-1834.

[21]. Vericat, C.; Vela, M. E.; Corthey, G.; Pensa, E.; Cortes, E.; Fonticelli, M. H.; Ibanez, F.; Benitez, G. E.; Carro, P.; Salvarezza, R. C. Self-Assembled Monolayers of Thiolates on Metals: A Review Article on Sulfur-Metal Chemistry and Surface Structures. *RSC Adv.* **2014**, *4*, 27730-27754.

[22]. Bain, C. D.; Troughton, E. B.; Tao, Y. T.; Evall, J.; Whitesides, G. M.; Nuzzo, R. G. Formation of Monolayer Films by the Spontaneous Assembly of Organic Thiols from Solution onto Gold. *J. Am. Chem. Soc.* **1989**, *111*, 321-335.

[23]. Porter, M. D.; Bright, T. B.; Allara, D. L.; Chidsey, C. E. D. Spontaneously Organized Molecular Assemblies. 4. Structural Characterization of N-Alkyl Thiol Monolayers on Gold by Optical Ellipsometry, Infrared Spectroscopy, and Electrochemistry. *J. Am. Chem. Soc.* **1987**, *109*, 3559-3568.

[24]. Narasimhan, S.; Vanderbilt, D. Elastic Stress Domains and the Herringbone Reconstruction on Au(111). *Phys. Rev. Lett.* **1992**, *69*, 1564-1567; Xu, S.; Cruchon-Dupeyrat, S. J. N.; Garno, J. C.; Liu, G. Y.; Jennings, G. K.; Yong, T. H.; Laibinis, P. E. In Situ Studies of Thiol Self-Assembly on Gold from Solution Using Atomic Force Microscopy. *J. Chem. Phys.* **1998**, *108*, 5002-5012; Yamada, R.; Uosaki, K. In Situ Scanning Tunneling Microscopy Observation of the Self-Assembly Process of Alkanethiols on Gold(111) in Solution. *Langmuir* **1998**, *14*, 855-861.

[25]. Poirier, G. E.; Pylant, E. D. The Self-Assembly Mechanism of Alkanethiols on Au(111). *Science* **1996**, *272*, 1145-1148.

[26]. Nuzzo, R. G.; Zegarski, B. R.; Dubois, L. H. Fundamental Studies of the Chemisorption of Organosulfur Compounds on Gold(111). Implications for Molecular Self-Assembly on Gold Surfaces. *J. Am. Chem. Soc.* **1987**, *109*, 733-740; Dilimon, V. S.; Rajalingam, S.; Delhalle, J.; Mekhalif, Z. Self-Assembly Mechanism of Thiol, Dithiol, Dithiocarboxylic Acid, Disulfide and Diselenide on Gold: An Electrochemical Impedance Study. *PCCP* **2013**, *15*, 16648-16656.

[27]. Eu, S.; Paik, W. K. Self-Assembly Process of Organosulfur Molecular Layers on Gold Electrode: An in Situ Ellipsometric and Electrochemical Study. *Chem. Lett.* **1998**, 405-406; Paik, W.-k.; Eu, S.; Lee, K.; Chon, S.; Kim, M. Electrochemical Reactions in Adsorption of Organosulfur Molecules on Gold and Silver: Potential Dependent Adsorption. *Langmuir* **2000**, *16*, 10198-10205; Chon, S.; Paik, W. K. Adsorption of Self-Assembling Sulfur Compounds through Electrochemical Reactions: Effects of Potential, Acid and Oxidizing Agents. *PCCP* **2001**, *3*, 3405-3410.

[28]. Hakkinen, H. The Gold-Sulfur Interface at the Nanoscale. *Nat. Chem.* **2012**, *4*, 443-455.

[29]. Wood, E. A. Vocabulary of Surface Crystallography. *J. Appl. Phys.* **1964**, *35*, 1306-1312.

[30]. Park, R. L.; Madden Jr, H. H. Annealing Changes on the (100) Surface of Palladium and Their Effect on Co Adsorption. *Surf. Sci.* **1968**, *11*, 188-202.

[31]. Poirier, G. E.; Tarlov, M. J.; Rushmeier, H. E. Two-Dimensional Liquid Phase and the Px.Sqroot.3 Phase of Alkanethiol Self-Assembled Monolayers on Au(111). *Langmuir* **1994**, *10*, 3383-3386.

[32]. Staub, R.; Toerker, M.; Fritz, T.; Schmitz-Hübsch, T.; Sellam, F.; Leo, K. Flat Lying Pin-Stripe Phase of Decanethiol Self-Assembled Monolayers on Au(111). *Langmuir* **1998**, *14*, 6693-6698.

[33]. Camillone, N.; Leung, T. Y. B.; Schwartz, P.; Eisenberger, P.; Scoles, G. Chain Length Dependence of the Striped Phases of Alkanethiol Monolayers Self-Assembled on Au(111): An Atomic Beam Diffraction Study. *Langmuir* **1996**, *12*, 2737-2746.

[34]. Guo, Q.; Li, F. Self-Assembled Alkanethiol Monolayers on Gold Surfaces: Resolving the Complex Structure at the Interface by Stm. *PCCP* **2014**, *16*, 19074-19090.

[35]. Pujari, S. P.; Spruijt, E.; Cohen Stuart, M. A.; Van Rijn, C. J. M.; Paulusse, J. M. J.; Zuilhof, H. Ultralow Adhesion and Friction of Fluoro-Hydro Alkyne-Derived Self-Assembled Monolayers on H-Terminated Si(111). *Langmuir* **2012**, *28*, 17690-17700.

[36]. Weinstein, R. D.; Moriarty, J.; Cushnie, E.; Colorado Jr, R.; Lee, T. R.; Patel, M.; Alesi, W. R.; Jennings, G. K. Structure, Wettability, and Electrochemical Barrier Properties of Self-Assembled Monolayers Prepared from Partially Fluorinated Hexadecanethiols. *J. Phys. Chem. B* **2003**, *107*, 11626-11632.

[37]. Pujari, S. P.; Van Andel, E.; Yaffe, O.; Cahen, D.; Weidner, T.; Van Rijn, C. J. M.; Zuilhof, H. Mono-Fluorinated Alkyne-Derived Sams on Oxide-Free Si(111) Surfaces: Preparation, Characterization and Tuning of the Si Workfunction. *Langmuir* **2013**, *29*, 570-580.

[38]. Ma, H.; Yip, H. L.; Huang, F.; Jen, A. K. Y. Interface Engineering for Organic Electronics. *Adv. Funct. Mater.* **2010**, *20*, 1371-1388.

[39]. Tsao, M. W.; Hoffmann, C. L.; Rabolt, J. F.; Johnson, H. E.; Castner, D. G.; Erdelen, C.; Ringsdorf, H. Studies of Molecular Orientation and Order in Self-Assembled Semifluorinated N-Alkanethiols: Single and Dual Component Mixtures. *Langmuir* **1997**, *13*, 4317-4322.

[40]. Alves, C. A.; Porter, M. D. Atomic Force Microscopic Characterization of a Fluorinated Alkanethiolate Monolayer at Gold and Correlations to Electrochemical and Infrared Reflection Spectroscopic Structural Descriptions. *Langmuir* **1993**, *9*, 3507-3512.

[41]. Chidsey, C. E. D.; Loiacono, D. N. Chemical Functionality in Self-Assembled Monolayers: Structural and Electrochemical Properties. *Langmuir* **1990**, *6*, 682-691; Liu, G. Y.; Fenter, P.; Chidsey, C. E. D.; Ogletree, D. F.; Eisenberger, P.; Salmeron, M. An Unexpected Packing of Fluorinated N-Alkane Thiols on Au(111): A Combined Atomic Force Microscopy and X-Ray Diffraction Study. *J. Chem. Phys.* **1994**, *101*, 4301-4306.

[42]. Tamada, K.; Ishida, T.; Knoll, W.; Fukushima, H.; Colorado, R.; Graupe, M.; Shmakova, O. E.; Lee, T. R. Molecular Packing of Semifluorinated Alkanethiol Self-Assembled Monolayers on Gold: Influence of Alkyl Spacer Length. *Langmuir* **2001**, *17*, 1913-1921.

[43]. Hohman, J. N.; Claridge, S. A.; Kim, M.; Weiss, P. S. Cage Molecules for Self-Assembly. *Mater. Sci. Eng. R-Rep.***2010**, *70*, 188-208.

[44]. Dameron, A. A.; Charles, L. F.; Weiss, P. S. Structures and Displacement of 1-Adamantanethiol Self-Assembled Monolayers on Au{111}. *J. Am. Chem. Soc.* **2005**, *127*, 8697-8704.

[45]. Fujii, S.; Akiba, U.; Fujihira, M. Geometry for Self-Assembling of Spherical Hydrocarbon Cages with Methane Thiolates on Au(111). *J. Am. Chem. Soc.* **2002**, *124*, 13629-13635.

[46]. Fujii, S.; Akiba, U.; Fujihira, M. Novel Self-Assembled Monolayers of Disulfides with Bicyclo[2.2.2]Octane Moieties on Au(111). *Chem. Commun.* **2001**, 1688-1689.

[47]. Kim, M.; Hohman, J. N.; Morin, E. I.; Daniel, T. A.; Weiss, P. S. Self-Assembled Monolayers of 2-Adamantanethiol on Au{111}: Control of Structure and Displacement. *J. Chem. Phys. A* **2009**, *113*, 3895-3903.

[48]. Reed, M. A.; Zhou, C.; Muller, C. J.; Burgin, T. P.; Tour, J. M. Conductance of a Molecular Junction. *Science* **1997**, *278*, 252-254; Salomon, A.; Cahen, D.; Lindsay, S.; Tomfohr, J.; Engelkes, V. B.; Frisbie, C. D. Comparison of Electronic Transport Measurements on Organic Molecules. *Adv. Mater.* **2003**, *15*, 1881-1890.

[49]. Kang, H.; Park, T.; Choi, I.; Lee, Y.; Ito, E.; Hara, M.; Noh, J. Formation of Large Ordered Domains in Benzenethiol Self-Assembled Monolayers on Au(1 1 1) Observed by Scanning Tunneling Microscopy. *Ultramicroscopy* **2009**, *109*, 1011-1014.

[50]. Kang, H.; Lee, N.-S.; Ito, E.; Hara, M.; Noh, J. Formation and Superlattice of Long-Range-Ordered Self-Assembled Monolayers of Pentafluorobenzenethiols on Au(111). *Langmuir* **2010**, *26*, 2983-2985.

[51]. Leung, T. Y. B.; Schwartz, P.; Scoles, G.; Schreiber, F.; Ulman, A. Structure and Growth of 4-Methyl-4′-Mercaptobiphenyl Monolayers on Au(111): A Surface Diffraction Study. *Surf. Sci.* **2000**, *458*, 34-52.

[52]. Azzam, W.; Cyganik, P.; Witte, G.; Buck, M.; Wöll, C. Pronounced Odd−Even Changes in the Molecular Arrangement and Packing Density of Biphenyl-Based Thiol Sams: A Combined Stm and Leed Study. *Langmuir* **2003**, *19*, 8262-8270; Zharnikov, M.; Frey, S.; Rong, H.; Yang, Y. J.; Heister, K.; Buck, M.; Grunze, M. The Effect of Sulfur-Metal Bonding on the Structure of Self-Assembled Monolayers. *PCCP* **2000**, *2*, 3359-3362.

[53]. Sabatani, E.; Cohen-Boulakia, J.; Bruening, M.; Rubinstein, I. Thioaromatic Monolayers on Gold: A New Family of Self-Assembling Monolayers. *Langmuir* **1993**, *9*, 2974-2981; Ishida, T.; Mizutani, W.; Azehara, H.; Sato, F.; Choi, N.; Akiba, U.; Fujihira, M.; Tokumoto, H. Adsorption Processes of Self-Assembled Monolayers Made from Terphenyl Thiols. *Langmuir* **2001**, *17*, 7459-7463.

[54]. Tour, J. M.; Jones, L.; Pearson, D. L.; Lamba, J. J. S.; Burgin, T. P.; Whitesides, G. M.; Allara, D. L.; Parikh, A. N.; Atre, S. Self-Assembled Monolayers and Multilayers of Conjugated Thiols, .Alpha.,.Omega.-Dithiols, and Thioacetyl-Containing Adsorbates. Understanding Attachments between Potential Molecular Wires and Gold Surfaces. *J. Am. Chem. Soc.* **1995**, *117*, 9529-9534.

[55]. Chong, L.-W.; Lee, Y.-L.; Wen, T.-C.; Guo, T.-F. Self-Assembled Monolayer-Modified Ag Anode for Top-Emitting Polymer Light-Emitting Diodes. *Appl. Phys. Lett.* **2006**, *89*, 233513; Hong, J.-P.; Park, A.-Y.; Lee, S.; Kang, J.; Shin, N.; Yoon, D. Y. Tuning of Ag Work Functions by Self-Assembled Monolayers of Aromatic Thiols for an Efficient Hole Injection for Solution Processed Triisopropylsilylethynyl Pentacene Organic Thin Film Transistors. *Appl. Phys. Lett.* **2008**, *92*, 143311.

[56]. Yang, G.; Liu, G.-y. New Insights for Self-Assembled Monolayers of Organothiols on Au(111) Revealed by Scanning Tunneling Microscopy. *J. Phys. Chem. B* **2003**, *107*, 8746-8759.

[57]. Tao, Y.-T.; Wu, C.-C.; Eu, J.-Y.; Lin, W.-L.; Wu, K.-C.; Chen, C.-h. Structure Evolution of Aromatic-Derivatized Thiol Monolayers on Evaporated Gold. *Langmuir* **1997**, *13*, 4018-4023.

[58]. Kang, H.; Noh, J. Influence of Thiol Molecular Backbone Structure on the Formation and Reductive Desorption of Self-Assembled Aromatic and Alicyclic Thiol Monolayers on Au(111) Surface. *Bull. Korean Chem. Soc.* **2013**, *34*, 1383-1387.

[59]. Azzam, W.; Bashir, A.; Ulrich Biedermann, P.; Rohwerder, M. Formation of Highly Ordered and Orientated Gold Islands: Effect of Immersion Time on the Molecular Adlayer Structure of Pentafluorobenzenethiols (PFBT) Sams on Au(111). *Langmuir* **2012**, *28*, 10192-10208.

[60]. Kang, H.; Lee, H.; Kang, Y.; Hara, M.; Noh, J. Two-Dimensional Ordering of Benzenethiol Self-Assembled Monolayers Guided by Displacement of Cyclohexanethiols on Au(111). *Chem. Commun.* **2008**, 5197-5199.

[61]. Wan, L.-J.; Terashima, M.; Noda, H.; Osawa, M. Molecular Orientation and Ordered Structure of Benzenethiol Adsorbed on Gold(111). *J. Phys. Chem. B* **2000**, *104*, 3563-3569.

[62]. Käfer, D.; Bashir, A.; Witte, G. Interplay of Anchoring and Ordering in Aromatic Self-Assembled Monolayers. *J. Phys. Chem. C* **2007**, *111*, 10546-10551.

[63]. Jung, H. H.; Won, Y. D.; Shin, S.; Kim, K. Molecular Dynamics Simulation of Benzenethiolate and Benzyl Mercaptide on Au(111). *Langmuir* **1999**, *15*, 1147-1154.

[64]. Kondoh, H.; Kodama, C.; Nozoye, H. Structure-Dependent Change of Desorption Species from N-Alkanethiol Monolayers Adsorbed on Au(111): Desorption of Thiolate Radicals from Low-Density Structures. *J. Phys. Chem. B* **1998**, *102*, 2310-2312.

[65]. Schoenfisch, M. H.; Pemberton, J. E. Air Stability of Alkanethiol Self-Assembled Monolayers on Silver and Gold Surfaces. *J. Am. Chem. Soc.* **1998**, *120*, 4502-4513.

[66]. Vericat, C.; Benitez, G. A.; Grumelli, D. E.; Vela, M. E.; Salvarezza, R. C. Thiol-Capped Gold: From Planar to Irregular Surfaces. *J. Phys.: Condens. Matter* **2008**, *20*, 184004.

[67]. Chinwangso, P.; Jamison, A. C.; Lee, T. R. Multidentate Adsorbates for Self-Assembled Monolayer Films. *Acc. Chem. Res.* **2011**, *44*, 511-519.

[68]. Whitesell, J. K.; Chang, H. K. Directionally Aligned Helical Peptides on Surfaces. *Science* **1993**, *261*, 73-76.

[69]. Park, J.-S.; Vo, A. N.; Barriet, D.; Shon, Y.-S.; Lee, T. R. Systematic Control of the Packing Density of Self-Assembled Monolayers Using Bidentate and Tridentate Chelating Alkanethiols. *Langmuir* **2005**, *21*, 2902-2911.

[70]. Kitagawa, T.; Idomoto, Y.; Matsubara, H.; Hobara, D.; Kakiuchi, T.; Okazaki, T.; Komatsu, K. Rigid Molecular Tripod with an Adamantane Framework and Thiol Legs. Synthesis and Observation of an Ordered Monolayer on Au(111). *J. Org. Chem.* **2006**, *71*, 1362-1369; Kitagawa, T.; Matsubara, H.; Komatsu, K.; Hirai, K.; Okazaki, T.; Hase, T. Ideal Redox Behavior of the High-Density Self-Assembled Monolayer of a Molecular Tripod on a Au(111) Surface with a Terminal Ferrocene Group. *Langmuir* **2013**, *29*, 4275-4282.

[71]. Singhana, B.; Jamison, A. C.; Hoang, J.; Lee, T. R. Self-Assembled Monolayer Films Derived from Tridentate Cyclohexyl Adsorbates with Alkyl Tailgroups of Increasing Chain Length. *Langmuir* **2013**, *29*, 14108-14116; Singhana, B.; Rittikulsittichai, S.; Lee, T. R. Tridentate Adsorbates with Cyclohexyl Headgroups Assembled on Gold. *Langmuir* **2013**, *29*, 561-569.

[72]. Kudernac, T.; Lei, S.; Elemans, J. A. A. W.; De Feyter, S. Two-Dimensional Supramolecular Self-Assembly: Nanoporous Networks on Surfaces. *Chem. Soc. Rev.* **2009**, *38*, 402-421.

[73]. Barth, J. V. Molecular Architectonic on Metal Surfaces. *Annu. Rev. Phys. Chem.* **2007**, *58*, 375-407.

[74]. Margenau, H. Van Der Waals Forces. *Rev. Mod. Phys.* **1939**, *11*, 1-35; Israelachvili, J. N.: 6 - Van Der Waals Forces. In *Intermolecular and Surface Forces (Third Edition)*; Israelachvili, J. N., Ed.; Academic Press: San Diego, 2011; pp 107-132.

[75]. Gellman, A. J.; Paserba, K. R. Kinetics and Mechanism of Oligomer Desorption from Surfaces: N-Alkanes on Graphite. *J. Phys. Chem. B* **2002**, *106*, 13231-13241.

[76]. Wetterer, S. M.; Lavrich, D. J.; Cummings, T.; Bernasek, S. L.; Scoles, G. Energetics and Kinetics of the Physisorption of Hydrocarbons on Au(111). *J. Phys. Chem. B* **1998**, *102*, 9266-9275.

[77]. Samorí, P.; Fechtenkötter, A.; Jäckel, F.; Böhme, T.; Müllen, K.; Rabe, J. P. Supramolecular Staircase Via Self-Assembly of Disklike Molecules at the Solid−Liquid Interface. *J. Am. Chem. Soc.* **2001**, *123*, 11462-11467.

[78]. Wei, Y.; Kannappan, K.; Flynn, G. W.; Zimmt, M. B. Scanning Tunneling Microscopy of Prochiral Anthracene Derivatives on Graphite: Chain Length Effects on Monolayer Morphology. *J. Am. Chem. Soc.* **2004**, *126*, 5318-5322.

[79]. Mena-Osteritz, E. Superstructures of Self-Organizing Thiophenes. *Adv. Mater.* **2002**, *14*, 609-616.

[80]. Mena-Osteritz, E.; Meyer, A.; Langeveld-Voss, B. M. W.; Janssen, R. A. J.; Meijer, E. W.; Bäuerle, P. Two-Dimensional Crystals of Poly(3-Alkyl- Thiophene)S: Direct Visualization of Polymer Folds in Submolecular Resolution. *Angew. Chem. Int. Ed.* **2000**, *39*, 2679-2684.

[81]. Rabe, J. P.; Buchholz, S. Commensurability and Mobility in Two-Dimensional Molecular Patterns on Graphite. *Science* **1991**, *253*, 424-427.

[82]. Adisoejoso, J.; Tahara, K.; Okuhata, S.; Lei, S.; Tobe, Y.; De Feyter, S. Two-Dimensional Crystal Engineering: A Four-Component Architecture at a Liquid–Solid Interface. *Angew. Chem. Int. Ed.* **2009**, *48*, 7353-7357.

[83]. Piot, L.; Marchenko, A.; Wu, J.; Müllen, K.; Fichou, D. Structural Evolution of Hexa-Peri-Hexabenzocoronene Adlayers in Heteroepitaxy on N-Pentacontane Template Monolayers. *J. Am. Chem. Soc.* **2005**, *127*, 16245-16250.

[84]. Lei, S.; Wang, C.; Wan, L.; Bai, C. Site Selective Adsorption and Templated Assembling: Effects of Organic−Organic Heterogeneous Interface Studied by Scanning Tunneling Microscopy. *J. Phys. Chem. B* **2004**, *108*, 1173-1175.

[85]. Ivasenko, O.; Perepichka, D. F. Mastering Fundamentals of Supramolecular Design with Carboxylic Acids. Common Lessons from X-Ray Crystallography and Scanning Tunneling Microscopy. *Chem. Soc. Rev.* **2011**, *40*, 191-206.

[86]. Lackinger, M.; Griessl, S.; Markert, T.; Jamitzky, F.; Heckl, W. M. Self-Assembly of Benzene−Dicarboxylic Acid Isomers at the Liquid Solid Interface: Steric Aspects of Hydrogen Bonding. *J. Phys. Chem. B* **2004**, *108*, 13652-13655.

[87]. MacLeod, J. M.; Ben Chaouch, Z.; Perepichka, D. F.; Rosei, F. Two-Dimensional Self-Assembly of a Symmetry-Reduced Tricarboxylic Acid. *Langmuir* **2013**, *29*, 7318-7324.

[88]. Florio, G. M.; Stiso, K. A.; Campanelli, J. S. Surface Patterning of Benzenecarboxylic Acids: Influence of Structure, Solvent, and Concentration on Molecular Self-Assembly. *J. Phys. Chem. C* **2012**, *116*, 18160-18174.

[89]. Lackinger, M.; Griessl, S.; Heckl, W. M.; Hietschold, M.; Flynn, G. W. Self-Assembly of Trimesic Acid at the Liquid−Solid Interfacea Study of Solvent-Induced Polymorphism. *Langmuir* **2005**, *21*, 4984-4988.

[90]. Griessl, S. J. H.; Lackinger, M.; Jamitzky, F.; Markert, T.; Hietschold, M.; Heckl, W. M. Incorporation and Manipulation of Coronene in an Organic Template Structure. *Langmuir* **2004**, *20*, 9403-9407.

[91]. Ivasenko, O.; MacLeod, J. M.; Chernichenko, K. Y.; Balenkova, E. S.; Shpanchenko, R. V.; Nenajdenko, V. G.; Rosei, F.; Perepichka, D. F. Supramolecular Assembly of Heterocirculenes in 2d and 3d. *Chem. Commun.* **2009**, 1192-1194.

[92]. Griessl, S. J. H.; Lackinger, M.; Jamitzky, F.; Markert, T.; Hietschold, M.; Heckl, W. M. Room-Temperature Scanning Tunneling Microscopy Manipulation of Single C_{60} Molecules at the Liquid−Solid Interface: Playing Nanosoccer. *J. Phys. Chem. B* **2004**, *108*, 11556-11560.

[93]. Bigioni, T. P.; Lin, X.-M.; Nguyen, T. T.; Corwin, E. I.; Witten, T. A.; Jaeger, H. M. Kinetically Driven Self Assembly of Highly Ordered Nanoparticle Monolayers. *Nat Mater.* **2006**, *5*, 265-270.

[94]. Pan, G.-B.; Liu, J.-M.; Zhang, H.-M.; Wan, L.-J.; Zheng, Q.-Y.; Bai, C.-L. Configurations of a Calix[8]Arene and a C_{60}/Calix[8]Arene Complex on a Au(111) Surface. *Angew. Chem. Int. Ed.* **2003**, *42*, 2747-2751.

[95]. Li, F.; Tang, L.; Zhou, W.; Guo, Q. Formation of Confined C_{60} Islands within Octanethiol Self-Assembled Monolayers on Au(111). *J. Phys. Chem. C* **2009**, *113*, 17899-17903.

[96]. Yoshimoto, S.; Tsutsumi, E.; Narita, R.; Murata, Y.; Murata, M.; Fujiwara, K.; Komatsu, K.; Ito, O.; Itaya, K. Epitaxial Supramolecular Assembly of Fullerenes Formed by Using a Coronene Template on a Au(111) Surface in Solution. *J. Am. Chem. Soc.* **2007**, *129*, 4366-4376.

[97]. Yang, Y.-C.; Chang, C.-H.; Lee, Y.-L. Complexation of Fullerenes on a Pentacene-Modified Au(111) Surface. *Chem. Mater.* **2007**, *19*, 6126-6130.

[98]. Daniel, M.-C.; Astruc, D. Gold Nanoparticles: Assembly, Supramolecular Chemistry, Quantum-Size-Related Properties, and Applications toward Biology, Catalysis, and Nanotechnology. *Chem. Rev.* **2004**, *104*, 293-346; Pelaz, B.; Jaber, S.; de Aberasturi, D. J.; Wulf, V.; Aida, T.; de la Fuente, J. M.; Feldmann,

J.; Gaub, H. E.; Josephson, L.; Kagan, C. R.; Kotov, N. A.; Liz-Marzán, L. M.; Mattoussi, H.; Mulvaney, P.; Murray, C. B.; Rogach, A. L.; Weiss, P. S.; Willner, I.; Parak, W. J. The State of Nanoparticle-Based Nanoscience and Biotechnology: Progress, Promises, and Challenges. *ACS Nano* **2012**, *6*, 8468-8483.

[99]. Sperling, R. A.; Parak, W. J.: Surface Modification, Functionalization and Bioconjugation of Colloidal Inorganic Nanoparticles, **2010**; Vol. 368.

[100]. Kiely, C. J.; Fink, J.; Brust, M.; Bethell, D.; Schiffrin, D. J. Spontaneous Ordering of Bimodal Ensembles of Nanoscopic Gold Clusters. *Nature* **1998**, *396*, 444-446.

[101]. Shevchenko, E. V.; Talapin, D. V.; Kotov, N. A.; O'Brien, S.; Murray, C. B. Structural Diversity in Binary Nanoparticle Superlattices. *Nature* **2006**, *439*, 55-59.

[102]. Redl, F. X.; Cho, K. S.; Murray, C. B.; O'Brien, S. Three-Dimensional Binary Superlattices of Magnetic Nanocrystals and Semiconductor Quantum Dots. *Nature* **2003**, *423*, 968-971.

[103]. Chen, Z.; O'Brien, S. Structure Direction of Ii-Vi Semiconductor Quantum Dot Binary Nanoparticle Superlattices by Tuning Radius Ratio. *ACS Nano* **2008**, *2*, 1219-1229.

[104]. Shevchenko, E. V.; Talapin, D. V.; Murray, C. B.; O'Brien, S. Structural Characterization of Self-Assembled Multifunctional Binary Nanoparticle Superlattices. *J. Am. Chem. Soc.* **2006**, *128*, 3620-3637.

[105]. Korgel, B. A.; Fitzmaurice, D. Small-Angle X-Ray-Scattering Study of Silver-Nanocrystal Disorder-Order Phase Transitions. *Phys. Rev. B Condens. Matter Mater. Phys.* **1999**, *59*, 14191-14201.

[106]. Maillard, M.; Motte, L.; Ngo, A. T.; Pileni, M. P. Rings and Hexagons Made of Nanocrystals: A Marangoni Effect. *J. Phys. Chem. B* **2000**, *104*, 11871-11877.

[107]. Ge, G.; Brus, L. E. Fast Surface Diffusion of Large Disk-Shaped Nanocrystal Aggregates. *Nano Lett.* **2001**, *1*, 219-222.

[108]. Prasad, B. L. V.; Sorensen, C. M.; Klabunde, K. J. Gold Nanoparticle Superlattices. *Chem. Soc. Rev.* **2008**, *37*, 1871-1883.

[109]. Shenhar, R.; Norsten, T. B.; Rotello, V. M. Polymer-Mediated Nanoparticle Assembly: Structural Control and Applications. *Adv. Mater.* **2005**, *17*, 657-669.

[110]. Chiu, J. J.; Kim, B. J.; Kramer, E. J.; Pine, D. J. Control of Nanoparticle Location in Block Copolymers. *J. Am. Chem. Soc.* **2005**, *127*, 5036-5037.

[111]. Kim, D. H.; Kim, S. H.; Lavery, K.; Russell, T. P. Inorganic Nanodots from Thin Films of Block Copolymers. *Nano Lett.* **2004**, *4*, 1841-1844.

[112]. Glass, R.; Arnold, M.; Blümmel, J.; Küller, A.; Moller, M.; Spatz, J. P. Micro-Nanostructured Interfaces Fabricated by the Use of Inorganic Block Copolymer Micellar Monolayers as Negative Resist for Electron-Beam Lithography. *Adv. Funct. Mater.* **2003**, *13*, 569-575; Lohmueller, T.; Bock, E.; Spatz, J. P. Synthesis of Quasi-Hexagonal Ordered Arrays of Metallic Nanoparticles with Tuneable Particle Size. *Adv. Mater.* **2008**, *20*, 2297-2302.

[113]. He, H. X.; Zhang, H.; Li, Q. G.; Zhu, T.; Li, S. F. Y.; Liu, Z. F. Fabrication of Designed Architectures of Au Nanoparticles on Solid Substrate with Printed Self-Assembled Monolayers as Templates. *Langmuir* **2000**, *16*, 3846-3851; Ma, H.; Zin, M. T.; Zareie, M. H.; Kang, M.-S.; Kang, S.-H.; Kim, K.-S.; Reed, B. W.; Behar, C. T.; Sarikaya, M.; Jen, A. K. Y. Assembly of Nanomaterials through Highly Ordered Self-Assembled Monolayers and Peptide-Organic Hybrid Conjugates as Templates. *J. Nanosci. Nanotechnol.* **2007**, *7*, 2549-2566.

[114]. Zirbs, R.; Kienberger, F.; Hinterdorfer, P.; Binder, W. H. Directed Assembly of Au Nanoparticles onto Planar Surfaces Via Multiple Hydrogen Bonds. *Langmuir* **2005**, *21*, 8414-8421.

[115]. Zamborini, F. P.; Hicks, J. F.; Murray, R. W. Quantized Double Layer Charging of Nanoparticle Films Assembled Using Carboxylate/(Cu^{2+} or Zn^{2+})/Carboxylate Bridges. *J. Am. Chem. Soc.* **2000**, *122*, 4514-4515; Templeton, A. C.; Zamborini, F. P.; Wuelfing, W. P.; Murray, R. W. Controlled and Reversible Formation of Nanoparticle Aggregates and Films Using Cu2+−Carboxylate Chemistry. *Langmuir* **2000**, *16*, 6682-6688.

[116]. Aslam, M.; Mulla, I. S.; Vijayamohanan, K. Hydrophobic Organization of Monolayer-Protected Au Clusters on Thiol-Functionalized Au(111) Surfaces. *Langmuir* **2001**, *17*, 7487-7493.

[117]. Hoeppener, S.; Chi, L.; Fuchs, H. Formation of Au55 Strands on a Molecular Template at the Solid-Liquid Interface. *Nano Lett.* **2002**, *2*, 459-463.

[118]. Lei, S. B.; Wang, C.; Yin, S. X.; Wan, L. J.; Bai, C. L. Assembling Nanometer Nickel Particles into Ordered Arrays. *ChemPhysChem* **2003**, *4*, 1114-1117.

[119]. Wei, X.; Tong, W.; Fidler, V.; Zimmt, M. B. Reactive Capture of Gold Nanoparticles by Strongly Physisorbed Monolayers on Graphite. *J. Colloid Interface Sci.* **2012**, *387*, 221-227.

[120]. Kroto, H. W.; Heath, J. R.; O'Brien, S. C.; Curl, R. F.; Smalley, R. E. C_{60}: Buckminsterfullerene. *Nature* **1985**, *318*, 162-163.

[121]. Kratschmer, W.; Lamb, L. D.; Fostiropoulos, K.; Huffman, D. R. Solid C_{60}: A New Form of Carbon. *Nature* **1990**, *347*, 354-358.

[122]. Clarke, T. M.; Durrant, J. R. Charge Photogeneration in Organic Solar Cells. *Chem. Rev.* **2010**, *110*, 6736-6767; Günes, S.; Neugebauer, H.; Sariciftci, N. S. Conjugated Polymer-Based Organic Solar Cells. *Chem. Rev.* **2007**, *107*, 1324-1338.

[123]. Dodabalapur, A.; Katz, H. E.; Torsi, L.; Haddon, R. C. Organic Heterostructure Field-Effect Transistors. *Science* **1995**, *269*, 1560-1562; Wang, C.; Dong, H.; Hu, W.; Liu, Y.; Zhu, D. Semiconducting Pi-Conjugated Systems in Field-Effect Transistors: A Material Odyssey of Organic Electronics. *Chem. Rev.* **2012**, *112*, 2208-2267.

[124]. Goyal, R. N.; Gupta, V. K.; Bachheti, N.; Sharma, R. A. Electrochemical Sensor for the Determination of Dopamine in Presence of High Concentration of Ascorbic Acid Using a Fullerene-C_{60}

Coated Gold Electrode. *Electroanalysis* **2008**, *20*, 757-764; Nakamura, E.; Isobe, H. Functionalized Fullerenes in Water. The First 10 Years of Their Chemistry, Biology, and Nanoscience. *Acc. Chem. Res.* **2003**, *36*, 807-815.

[125]. Altman, E. I.; Colton, R. J. Determination of the Orientation of C_{60} Adsorbed on Au(111) and Ag(111). *Phys.Rev.B* **1993**, *48*, 18244-18249; Altman, E. I.; Colton, R. J. Interaction of C_{60} with the Au(111) 23×√3 Reconstruction. *J. Vac. Sci. Technol. B* **1994**, *12*, 1906-1909.

[126]. Gimzewski, J. K.; Modesti, S.; David, T.; Schlittler, R. R. Scanning Tunneling Microscopy of Ordered C_{60} and C_{70} Layers on Au(111), Cu(111), Ag(110), and Au(110) Surfaces. *J. Vac. Sci. Technol. B* **1994**, *12*; Altman, E. I.; Colton, R. J. The Interaction of C_{60} with Noble Metal Surfaces. *Surf. Sci.* **1993**, *295*, 13-33.

[127]. Altman, E. I.; Colton, R. J. Nucleation, Growth, and Structure of Fullerene Films on Au(111). *Surf. Sci.* **1992**, *279*, 49-67.

[128]. Hou, J. G.; Jinlong, Y.; Haiqian, W.; Qunxiang, L.; Changgan, Z.; Hai, L.; Wang, B.; Chen, D. M.; Qingshi, Z. Identifying Molecular Orientation of Individual C_{60} on a Si(111)-(7 × 7) Surface. *Phys. Rev. Lett.* **1999**, *83*, 3001-3004; Yao, X.; Ruskell, T. G.; Workman, R. K.; Sarid, D.; Chen, D. Scanning Tunneling Microscopy and Spectroscopy of Individual C_{60} Molecules on Si(100)-(2 × 1) Surfaces. *Surf. Sci.* **1996**, *366*, L743-L749; Li, Y. Z.; Patrin, J. C.; Chander, M.; Weaver, J. H.; Chibante, L. P. F.; Smalley, R. E. Ordered Overlayers of C_{60} on Gaas(110) Studied with Scanning Tunneling Microscopy. *Science* **1991**, *252*, 547-548.

[129]. Burke, S. A.; Mativetsky, J. M.; Hoffmann, R.; Grutter, P. Nucleation and Submonolayer Growth of C_{60} on KBr. *Phys. Rev. Lett.* **2005**, *94*, 096102.

[130]. Ren, S.; Yang, S.; Zhao, Y. Preparation and Tribological Studies of C_{60} Thin Film Chemisorbed on a Functional Polymer Surface. *Langmuir* **2004**, *20*, 3601-3605; Porath, D.; Levi, Y.; Tarabiah, M.; Millo, O. Tunneling Spectroscopy of Isolated C_{60} Molecules in the Presence of Charging Effects. *Phys. Rev. B Condens. Matter Mater. Phys.* **1997**, *56*, 9829-9833.

[131]. Katsonis, N.; Marchenko, A.; Fichou, D. Dynamics and Spectroscopy of Single C_{60} Molecules Adsorbed on Au(111) at the Liquid/Solid Interface. *Synth. Met.* **2003**, *137*, 1453-1455; Uemura, S.; Samori, P.; Kunitake, M.; Hirayama, C.; Rabe, J. P. Crystalline C_{60} Monolayers at the Solid-Organic Solution Interface. *J. Mater. Chem.* **2002**, *12*, 3366-3367; Mirkin, C. A.; Caldwell, W. B. Thin Film, Fullerene-Based Materials. *Tetrahedron* **1996**, *52*, 5113-5130.

[132]. Gardener, J. A.; Briggs, G. A. D.; Castell, M. R. Scanning Tunneling Microscopy Studies of C_{60} Monolayers on Au(111). *Phys. Rev. B Condens. Matter Mater. Phys.* **2009**, *80*; Zhang, X.; Yin, F.; Palmer, R. E.; Guo, Q. The C_{60}/Au(1 1 1) Interface at Room Temperature: A Scanning Tunnelling Microscopy Study. *Surf. Sci.* **2008**, *602*, 885-892; Schull, G.; Berndt, R. Orientationally Ordered (7×7)

Superstructure of C_{60} on Au(111). *Phys. Rev. Lett.* **2007**, *99*; Gardener, J. A.; Briggs, G. A. D.; Castell, M. R. Scanning Tunneling Microscopy Studies of C_{60} Monolayers on Au(111). *Phys. Rev. B* **2009**, *80*, 235434.

[133]. Tamai, A.; Seitsonen, A. P.; Baumberger, F.; Hengsberger, M.; Shen, Z. X.; Greber, T.; Osterwalder, J. Electronic Structure at the C_{60}/Metal Interface: An Angle-Resolved Photoemission and First-Principles Study. *Phys.Rev.B* **2008**, *77*, 075134.

[134]. Wang, L. L.; Cheng, H. P. Density Functional Study of the Adsorption of a C_{60} Monolayer on Ag(111) and Au(111) Surfaces. *Phys. Rev. B Condens. Matter Mater. Phys.* **2004**, *69*, 165417-165411-165417-165412.

[135]. Fernández Torrente, I.; Franke, K. J.; Ignacio Pascual, J. Spectroscopy of C_{60} Single Molecules: The Role of Screening on Energy Level Alignment. *J. Phys. Condens. Mater* **2008**, *20*; Lu, X.; Grobis, M.; Khoo, K. H.; Louie, S. G.; Crommie, M. F. Charge Transfer and Screening in Individual C_{60} Molecules on Metal Substrates: A Scanning Tunneling Spectroscopy and Theoretical Study. *Phys. Rev. B Condens. Matter Mater. Phys.* **2004**, *70*, 15418-1-115418-8; Rogero, C.; Pascual, J. I.; Gómez-Herrero, J.; Baró, A. M. Resolution of Site-Specific Bonding Properties of C_{60} Adsorbed on Au(111). *J. Chem. Phys.* **2002**, *116*, 832-836.

[136]. Bonifazi, D.; Enger, O.; Diederich, F. Supramolecular [60]Fullerene Chemistry on Surfaces. *Chem. Soc. Rev.* **2007**, *36*, 390-414.

[137]. Hou, J. G.; Jinlong, Y.; Haiqian, W.; Qunxiang, L.; Changgan, Z.; Lanfeng, Y.; Bing, W.; Chen, D. M.; Qingshi, Z. Surface Science: Topology of Two-Dimensional C_{60} Domains. *Nature* **2001**, *409*, 304-305; Zeng, C.; Wang, H.; Wang, B.; Yang, J.; Hou, J. G. Negative Differential-Resistance Device Involving Two C_{60} Molecules. *Appl. Phys. Lett.* **2000**, *77*, 3595-3597.

[138]. Nakayama, M.; Kautz, N. A.; Wang, T.; Sibener, S. J. Formation of Rectangular Packing and One-Dimensional Lines of C_{60} on 11-Phenoxyundecanethiol Self-Assembled Monolayers on Au(111). *Langmuir* **2012**, *28*, 4694-4701.

[139]. Zeng, C.; Wang, B.; Li, B.; Wang, H.; Hou, J. G. Self-Assembly of One-Dimensional Molecular and Atomic Chains Using Striped Alkanethiol Structures as Templates. *Appl. Phys. Lett.* **2001**, *79*, 1685-1687.

[140]. Mena-Osteritz, E.; Bäuerle, P. Complexation of C_{60} on a Cyclothiophene Monolayer Template. *Adv. Mater.* **2006**, *18*, 447-451.

[141]. MacLeod, J. M.; Ivasenko, O.; Fu, C.; Taerum, T.; Rosei, F.; Perepichka, D. F. Supramolecular Ordering in Oligothiophene−Fullerene Monolayers. *J. Am. Chem. Soc.* **2009**, *131*, 16844-16850.

[142]. Stepanow, S.; Lingenfelder, M.; Dmitriev, A.; Spillmann, H.; Delvigne, E.; Lin, N.; Deng, X.; Cai, C.; Barth, J. V.; Kern, K. Steering Molecular Organization and Host-Guest Interactions Using Two-Dimensional Nanoporous Coordination Systems. *Nat Mater* **2004**, *3*, 229-233.

[143]. Theobald, J. A.; Oxtoby, N. S.; Phillips, M. A.; Champness, N. R.; Beton, P. H. Controlling Molecular Deposition and Layer Structure with Supramolecular Surface Assemblies. *Nature* **2003**, *424*, 1029-1031.

[144]. Li, M.; Deng, K.; Lei, S.-B.; Yang, Y.-L.; Wang, T.-S.; Shen, Y.-T.; Wang, C.-R.; Zeng, Q.-D.; Wang, C. Site-Selective Fabrication of Two-Dimensional Fullerene Arrays by Using a Supramolecular Template at the Liquid-Solid Interface. *Angew. Chem. Int. Ed.* **2008**, *47*, 6717-6721; Blunt, M. O.; Russell, J. C.; Gimenez-LopezMaria del, C.; Taleb, N.; Lin, X.; Schröder, M.; Champness, N. R.; Beton, P. H. Guest-Induced Growth of a Surface-Based Supramolecular Bilayer. *Nat Chem* **2011**, *3*, 74-78.

[145]. Bonifazi, D.; Spillmann, H.; Kiebele, A.; de Wild, M.; Seiler, P.; Cheng, F.; Güntherodt, H.-J.; Jung, T.; Diederich, F. Supramolecular Patterned Surfaces Driven by Cooperative Assembly of C_{60} and Porphyrins on Metal Substrates. *Angew. Chem. Int. Ed.* **2004**, *43*, 4759-4763.

[146]. Yoshimoto, S.; Tsutsumi, E.; Fujii, O.; Narita, R.; Itaya, K. Effect of Underlying Coronene and Perylene Adlayers for [60]Fullerene Molecular Assembly. *Chem. Commun.* **2005**, 1188-1190.

[147]. Chen, W.; Zhang, H. L.; Huang, H.; Chen, L.; Wee, A. T. S. Self-Assembled Organic Donor/Acceptor Nanojunction Arrays. *Appl. Phys. Lett.* **2008**, *92*, 193301.

[148]. Zhang, J. L.; Zhong, S.; Zhong, J. Q.; Niu, T. C.; Hu, W. P.; Wee, A. T. S.; Chen, W. Rational Design of Two-Dimensional Molecular Donor-Acceptor Nanostructure Arrays. *Nanoscale* **2015**, *7*, 4306-4324.

[149]. Yu, G.; Gao, J.; Hummelen, J. C.; Wudl, F.; Heeger, A. J. Polymer Photovoltaic Cells: Enhanced Efficiencies Via a Network of Internal Donor-Acceptor Heterojunctions. *Science* **1995**, *270*, 1789-1791; Sun, Y.; Welch, G. C.; Leong, W. L.; Takacs, C. J.; Bazan, G. C.; Heeger, A. J. Solution-Processed Small-Molecule Solar Cells with 6.7% Efficiency. *Nat Mater* **2012**, *11*, 44-48.

[150]. Écija, D.; Otero, R.; Sánchez, L.; Gallego, J. M.; Wang, Y.; Alcamí, M.; Martín, F.; Martín, N.; Miranda, R. Crossover Site-Selectivity in the Adsorption of the Fullerene Derivative Pcbm on Au(111). *Angew. Chem. Int. Ed.* **2007**, *46*, 7874-7877.

[151]. Matsumoto, M.; Inukai, J.; Yoshimoto, S.; Takeyama, Y.; Ito, O.; Itaya, K. Two-Dimensional Network Formation in the C_{60} Malonic Acid Adlayer on Au(111). *J. Phys. Chem. C* **2007**, *111*, 13297-13300.

[152]. Diaconescu, B.; Yang, T.; Berber, S.; Jazdzyk, M.; Miller, G. P.; Tománek, D.; Pohl, K. Molecular Self-Assembly of Functionalized Fullerenes on a Metal Surface. *Phys. Rev. Lett.* **2009**, *102*, 056102; Nakanishi, T.; Miyashita, N.; Michinobu, T.; Wakayama, Y.; Tsuruoka, T.; Ariga, K.; Kurth, D. G.

Perfectly Straight Nanowires of Fullerenes Bearing Long Alkyl Chains on Graphite. *J. Am. Chem. Soc.* **2006**, *128*, 6328-6329.

[153]. Chen, T.; Pan, G.-B.; Yan, H.-J.; Wan, L.-J.; Matsuo, Y.; Nakamura, E. Substituent-Dependent Ordering of Adlayer Structures of Fullerene Derivatives Adsorbed on Au(111): A Scanning Tunneling Microscopy Study. *J. Phys. Chem. C* **2010**, *114*, 3170-3174.

[154]. Sherwood, P. M. A.: Data Analysis in X-Ray Photoelectron Spectroscopy, 1983; Wagner, J. M.: X-Ray Photoelectron Spectroscopy, **2011**.

[155]. Bain, C. D.; Biebuyck, H. A.; Whitesides, G. M. Comparison of Self-Assembled Monolayers on Gold: Coadsorption of Thiols and Disulfides. *Langmuir* **1989**, *5*, 723-727.

[156]. Castner, D. G.; Hinds, K.; Grainger, D. W. X-Ray Photoelectron Spectroscopy Sulfur 2p Study of Organic Thiol and Bisulfide Binding Interactions with Gold Surfaces. *Langmuir* **1996**, *12*, 5083-5086.

[157]. Lee, M. T.; Hsueh, C. C.; Freund, M. S.; Ferguson, G. S. Air Oxidation of Self-Assembled Monolayers on Polycrystalline Gold: The Role of the Gold Substrate. *Langmuir* **1998**, *14*, 6419-6423.

[158]. Ishida, T.; Choi, N.; Mizutani, W.; Tokumoto, H.; Kojima, I.; Azehara, H.; Hokari, H.; Akiba, U.; Fujihira, M. High-Resolution X-Ray Photoelectron Spectra of Organosulfur Monolayers on Au(111): S(2p) Spectral Dependence on Molecular Species. *Langmuir* **1999**, *15*, 6799-6806; Ishida, T.; Hara, M.; Kojima, I.; Tsuneda, S.; Nishida, N.; Sasabe, H.; Knoll, W. High Resolution X-Ray Photoelectron Spectroscopy Measurements of Octadecanethiol Self-Assembled Monolayers on Au(111). *Langmuir* **1998**, *14*, 2092-2096.

[159]. Ishida, T.; Choi, N.; Mizutani, W.; Tokumoto, H.; Kojima, I.; Azehara, H.; Hokari, H.; Akiba, U.; Fujihira, M. High-Resolution X-Ray Photoelectron Spectra of Organosulfur Monolayers on Au(111): S(2p) Spectral Dependence on Molecular Species. *Langmuir* **1999**, *15*, 6799-6806.

[160]. Chen, C. J.: Introduction to Scanning Tunneling Microscopy: Second Edition, **2007**; Kalinin, S.; Gruverman, A.: Scanning Probe Microscopy, **2007**; Vol. 2.

[161]. Bard, A. J.; Faulkner, L. R.: Electrochemical Methods: Fundamentals and Applications; Wiley, **2000**.

[162]. Badia, A.; Lennox, R. B.; Reven, L. A Dynamic View of Self-Assembled Monolayers. *Acc. Chem. Res.* **2000**, *33*, 475-481; Yang, D. F.; Wilde, C. P.; Morin, M. Electrochemical Desorption and Adsorption of Nonyl Mercaptan at Gold Single Crystal Electrode Surfaces. *Langmuir* **1996**, *12*, 6570-6577; Zhong, C. J.; Porter, M. D. Fine Structure in the Voltammetric Desorption Curves of Alkanethiolate Monolayers Chemisorbed at Gold. *J. Electroanal. Chem.* **1997**, *425*, 147-153; Zhong, C. J.; Zak, J.; Porter, M. D. Voltammetric Reductive Desorption Characteristics of Alkanethiolate Monolayers at Single Crystal Au(111) and (110) Electrode Surfaces. *J. Electroanal. Chem.* **1997**, *421*, 9-13.

[163]. Widrig, C. A.; Chung, C.; Porter, M. D. The Electrochemical Desorption of N-Alkanethiol Monolayers from Polycrystalline Au and Ag Electrodes. *Journal of Electroanalytical Chemistry and Interfacial Electrochemistry* **1991**, *310*, 335-359.

[164]. Kakiuchi, T.; Usui, H.; Hobara, D.; Yamamoto, M. Voltammetric Properties of the Reductive Desorption of Alkanethiol Self-Assembled Monolayers from a Metal Surface. *Langmuir* **2002**, *18*, 5231-5238.

[165]. Jacob, J. D. C.; Lee, T. R.; Baldelli, S. In Situ Vibrational Study of the Reductive Desorption of Alkanethiol Monolayers on Gold by Sum Frequency Generation Spectroscopy. *J. Phys. Chem. C* **2014**, *118*, 29126-29134.

[166]. Finklea, H. O.: Self-Assembled Monolayers on Electrodes. In *Encyclopedia of Analytical Chemistry*; John Wiley & Sons, Ltd, 2006; Hatchett, D. W.; Uibel, R. H.; Stevenson, K. J.; Harris, J. M.; White, H. S. Electrochemical Measurement of the Free Energy of Adsorption of N-Alkanethiolates at Ag(111). *J. Am. Chem. Soc.* **1998**, *120*, 1062-1069.

Chapter 2: Tridentate Benzylthiols on Gold(111): Control of Self-Assembly Geometry

After describing the principles of molecular self-assembly, Chapter 1 has highlighted the differences between physisorbed self-assembled molecular networks (SAMNs) that allows efficient control of molecular arrangement and chemisorbed self-assembled monolayers (SAMs) that enable a comparatively strong binding to the surface but whose 2D supramolecular structure is difficult to control. The formation of chemisorbed monolayer with using new trithiol ligand molecules is explored in Chapter 2, with an objective of exploring the possibility of controlling the lateral order in the SAMs and increase their stability for the future use as molecular templates. This design is based on a benzene ring substituted with three methylthiol groups in alternation with three alkyl chains of various length. SAM characterization using STM, XPS and electrochemistry revealed a direct dependence of the SAMs properties on the size of the alkyl chains substituents. Furthermore, the balance between intermolecular and molecule–substrate interactions have been determinant for the packing, orientation, and stability of the tridentate thiol monolayer.

Adapted with permission from:

M. A. Mezour, I. I. Perepichka, O. Ivasenko, R. B. Lennox, and D. F. Perepichka. Tridentate Benzylthiols on Au(111): Control of Self-Assembly Geometry. *Nanoscale*, 2015, 7, 5014-5022, DOI: 10.1039/C4NR07207C. Copyright, 2015, the Royal Society of Chemistry.

I am the principle author of this article and as such collected the majority of the data presented, performed the analyses and composed the manuscript. Dr. O. Ivasenko contributed to the interpretation of STM images and synthesized Me_3-BTMT. Dr. I. Perepichka synthesized Et_3-BTMT, ODe_3-BTMT and ODe_3-B.

2.1 Abstract

A set of hexasubstituted benzene derivatives with three thiol groups in the 1, 3, 5 positions and varied alkyl substituents in the 2, 4, 6 positions (Me_3-BTMT, Et_3-BTMT, ODe_3-BTMT) has been synthesized and self-assembled on Au(111). The resulting self-assembled monolayers (SAMs) are characterized by scanning tunneling microscopy (STM), X-ray photoelectron spectroscopy (XPS), and electrochemistry. The molecular orientation and long-range order are affected by the "gear effect" of the hexasubstituted benzene ring and van der Waals interactions between the physisorbed alkyl chains drive. Me_3-BTMT adopts a standing up orientation which results in a high molecular areal density but also the lowest degree of chemisorption (1 to 2 Au-S bonds per molecule). In contrast, Et_3-BTMT favors a lying down orientation with a greater number of surface-bonded thiol groups (2 to 3) per molecule which is due to the preferred all-"anti" conformation of this molecule. Finally, ODe_3-BTMT adsorbs mainly in a lying down orientation, forming the SAM with the highest degree of chemisorption (all thiol groups are gold-bonded) and the lowest molecular areal density.

2.2 Introduction

Thiol-based self-assembled monolayers have been widely used to tailor the interfacial properties of gold and other metals for applications in diverse fields such as corrosion inhibition,[1] organic and molecular electronic devices,[2,3,4] switches,[5,6] biomolecular adhesion,[7] chemosensors,[8,9] and biosensors.[10]

A number of these applications depend on the long-term stability of the component.[11] Although the Au-S gold bond is moderate in strength (38–48 kcal/mol),[12] formation of a disulphide bond by the departing ligands provides an energetically feasible desorption mechanism.[13] In thiol-free solution thiol-based SAMs can desorb to a significant extent within a few days.[14] In the presence of air the desorption is further facilitated by oxidation of the thiol groups.[15]

Several strategies have been employed to enhance SAMs stability, by strengthening the molecule-substrate interactions and/or the lateral interactions between adsorbates. The use of multidentate ligands with several anchoring thiol groups is one of the most effective methods for generating SAMs with long-term stability.[16,17] Such an approach has been successfully employed using different molecular architectures, as illustrated in Fig. 2.1.[18,19,20,21,22,23,24,25,26,27]

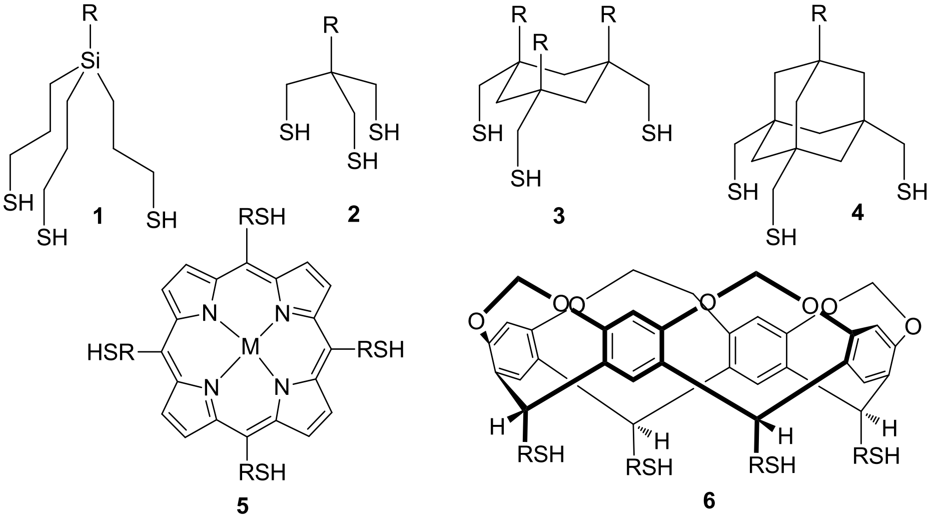

Figure. 2.1. Structure of multidentate thiol

These multidentate thiols are frequently applied to the design of functional SAMs, in molecular electronics and related applications.[28,29,30,31] For example, **1** and **2** motifs have been used for carrying various functional units, including large (bio)macromolecules: fluophores,[32] porphyrins,[29] fullerenes,[30] DNA,[33] etc. However, controlling molecular orientation in multidentate thiols is often difficult and the resulting SAMs are generally much less ordered than those based on monodentate thiol.[21] An incomplete bonding of the thiol groups has been shown by X-ray photoelectron spectroscopy (XPS) in many cases for **1** and **2**.[34,35] In the case of porphyrin tetrathiol derivatives **5**, only one or two thiol groups are typically attached to the gold surface.[26,36,37] This is often detrimental not only for the stability but also for the order of the SAM, as having the "free" thiol group makes the SAM vulnerable to multilayer formation (through disulfide cross-links), oxidation, and other defects. The uncontrolled molecular orientation affects the desired functional characteristics of the SAMs; eg, the impossibility of achieving flat-lying fully bonded conformation in case of porphyrin **5** negatively impacts the photo-electrochemical and electro-catalytic properties of its SAMs.[26,36,37] Together with the slower dynamics of the multidentate thiol, such partial binding might also be responsible for the lower lateral order in their SAMs. A significant control of the molecular orientation was, nevertheless, achieved using rigid non-aromatic adamantane and cyclohexane cores (**3** and **4)** which can provide complete Au-S bonding and long-range order in the SAMs.[22,25]

In this work, we explore a new, synthetically versatile, molecular motif of tridentate thiols suitable for formation of SAMs. Such design, based on a single rigid aromatic core with three "legs" is advantageous for at least four reasons. First, it allows controlling molecular conformation by exploiting the steric gearing and conformational constraints of the hexasubstituted benzene.[38] Second, the desorption pathways involving the formation of disulfides are disfavored due to the rigidity of the aromatic ring.[39] Third, the flat-lying aromatic ring allows to dramatically reduce the thickness (to ~0.5 nm) of the monolayer comparing to any other thiol-based SAMs, which should lead to enhanced electronic interactions of the surface with the environment (electron tunneling, sensing, *etc*). Finally, intermolecular interactions of substituents on the benzene core (*eg*, long alkyl chains) could allow tuning the lateral structure/periodicity of the monolayer, merging aspects of the fields of chemisorbed SAMs and self-assembled molecular networks (SAMNs).[40,41,42]

Herein, we report three new tridentate benzenetris(methylthiols) (BTMT), substituted with methyl, ethyl and decyloxy groups (Me_3-BTMT, Et_3-BTMT, ODe_3-BTMT) (Fig. 2.2) and explore their self-assembly behavior on Au(111) surface. A comparative characterization of these SAMs, carried out using XPS, electrochemistry, and STM, provides insight into their relative SAM formation properties.

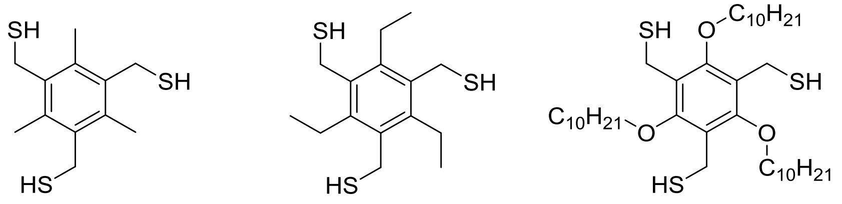

Me_3-BTMT $Ph(Me)_3(CH_2SH)_3$

Et_3-BTMT $Ph(Et)_3(CH_2SH)_3$

ODe_3-BTMT $Ph(ODe)_3(CH_2SH)_3$

Figure 2.2. Structure of tridentate benzylthiols

2.3 Results and discussions

Hexasubstituted benzene derivatives have been widely used as synthetically accessible scaffolds for building molecular hosts in supramolecular systems.[38,43,44] Conformational control in this system results from the pre-organized *syn*-geometry of substituents in 1, 3, 5 (as well as

2, 4, 6) positions brought about by a thermodynamic preference for an *anti* orientation of the neighboring substituents, which minimizes steric interactions.[45] While such preorganization has been extensively exploited in supramolecular templates, to our knowledge no studies on its use in molecular self-assembly on surfaces have been reported. We speculated that such conformational control might improve the ordering in tridentate SAMs by forcing the orientation of each thiol anchor toward the surface. Accordingly, we have synthesized three new benzenetris(methylthiols) with three alkyl groups (methyl, ethyl, and decyloxy) substituents (Scheme 2.1).

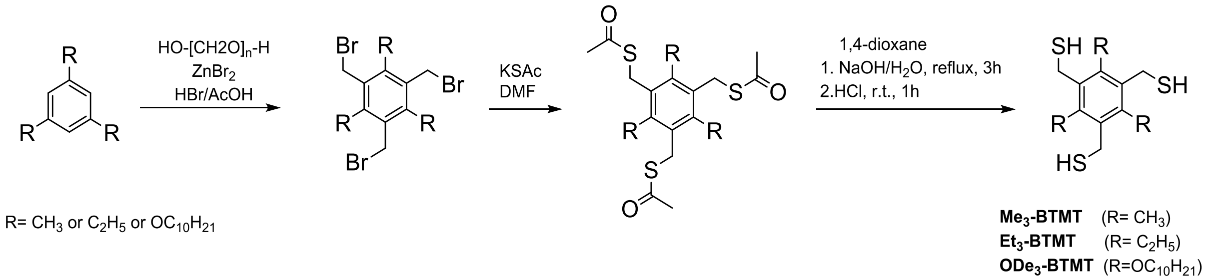

Scheme 2.1. Synthesis of tridentate benzylthiols.

Density functional theory (DFT) calculations at the B3LYP/6-31G(d) level were performed on Me_3-BTMT, Et_3-BTMT and ODe_3-BTMT to evaluate the energetic preference for the *syn* vs *anti* conformation (Fig. 2.3). For Me_3-BTMT, the *anti* conformation (with thiol groups on the opposite side of the ring) is slightly preferred by 0.9 kcal/mol, which is likely due to weak dipole-dipole interactions of the thiol groups. In contrast Et_3-BTMT shows a preference of the *syn* conformer by 2.2 kcal/mol, in where the steric repulsion with the bulkier ethyl groups is minimized. This corresponds to ca. 99% of molecules adopting the *syn* conformation at room temperature. For ODe_3-BTMT, the *syn* isomer is also favored but by only 0.6 kcal/mol. We note that in all three cases the calculated energetic preferences are 1-2 orders of magnitude smaller than the total energy of chemisorption. However this not all means they are inconsequential, since the difference between various chemisorption geometries (*lying down* or *standing up*) is also much smaller than the total adsorption energy.

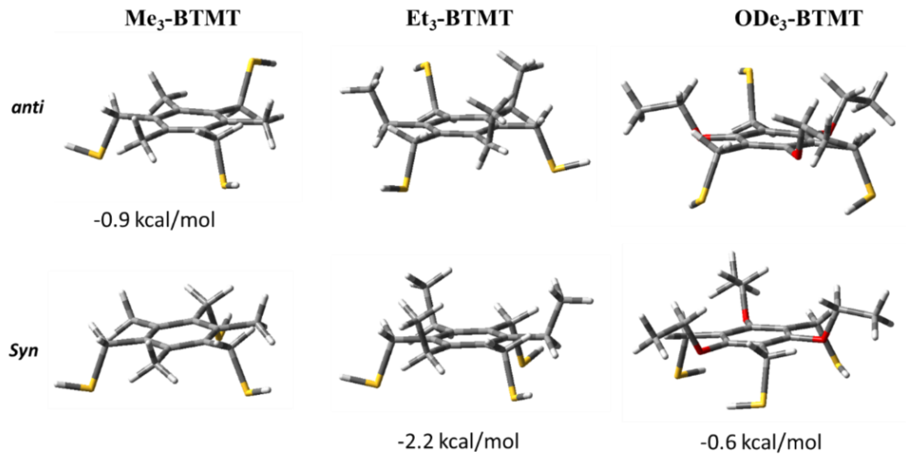

Figure 2.3. Relative stabilization energies (B3LYP/6-31G(d)) of *syn* and *anti* conformations of Me_3-BTMT, Et_3-BTMT and OEt_3-BTMT (a model of ODe_3-BTMT). *Syn*/*anti* refers to the orientation of one CH_2SH group relative to the other two.

2.3.1 STM characterization

STM provides direct insights into local structures of molecular monolayers on conductive surfaces and has been frequently used for the analysis of thiol assemblies on Au(111).[46] STM images of Me_3-BTMT and Et_3-BTMT SAMs (Fig. 2.4) exhibit rather disordered structures, as compared to the 2D crystalline SAMs (Fig. 2.SI1) formed under identical conditions by 1-octanethiol (C_8SH), used as a reference throughout this study. A partial ordering is, however, manifested as rows of bright protrusion, particularly for Me_3-BTMT. The separation between these rows (~1.3 nm) corresponds well to the lateral size of the molecule plus the van der Waals (vdW) spacing (Fig. 2.SI2). Although 2D FFT (Fig. 2.4g) shows a weak indication of long-range ordering, the quality of the data does not allow extracting reliable unit cell parameters. Therefore, a pair correlation analysis of the observed bright protrusions has been performed via the nearest three-point contacts (Fig. 2.SI3). This procedure provides both the average intermolecular distances and the relative orientation of two contacts emanating from the same origin (an angle of a “local unit cell”). The resulting histograms of the nearest neighbor distances for Me_3-BTMT shows a bimodal distribution with preferred distances at ~0.5 nm and ~1.2 nm (Fig. 2.4c). The longer of the two distances corresponds to the separation between the aforementioned rows, while the shorter one can be attributed to the preferentially spacing along the rows. The latter is significantly smaller than the lateral size of the molecules in a *lying down* orientation on the surface. However, it is consistent with the molecules *standing up* and closely packed in the rows of co-aligned benzene rings, with possible π-stacking interaction (Fig. 2.4e).

The pair correlation analysis[47,48] (see also Fig. 2.SI3) for the SAM of Et_3-BTMT (Fig.2. 4d) shows the most frequently observed intermolecular contacts at ~1.0 nm which is consistent with the tentative model of flat-lying molecules (Fig.2.4f). A minor peak at ~0.6 nm in the distribution histogram suggests some occurrence of vertically oriented molecules, as tentatively presented by the model in Fig. 2.4h. Thus, the discussed above conformational effect of the ethyl groups and the possible hindrance to π-stacking of the vertically oriented molecules seem to favor, albeit not fully enforce, the *lying down* assembly of the Et_3-BTMT. A co-existence of the two self-assembly modes may well be responsible for the generally less-ordered STM appearance of the Et_3-BTMT SAM.

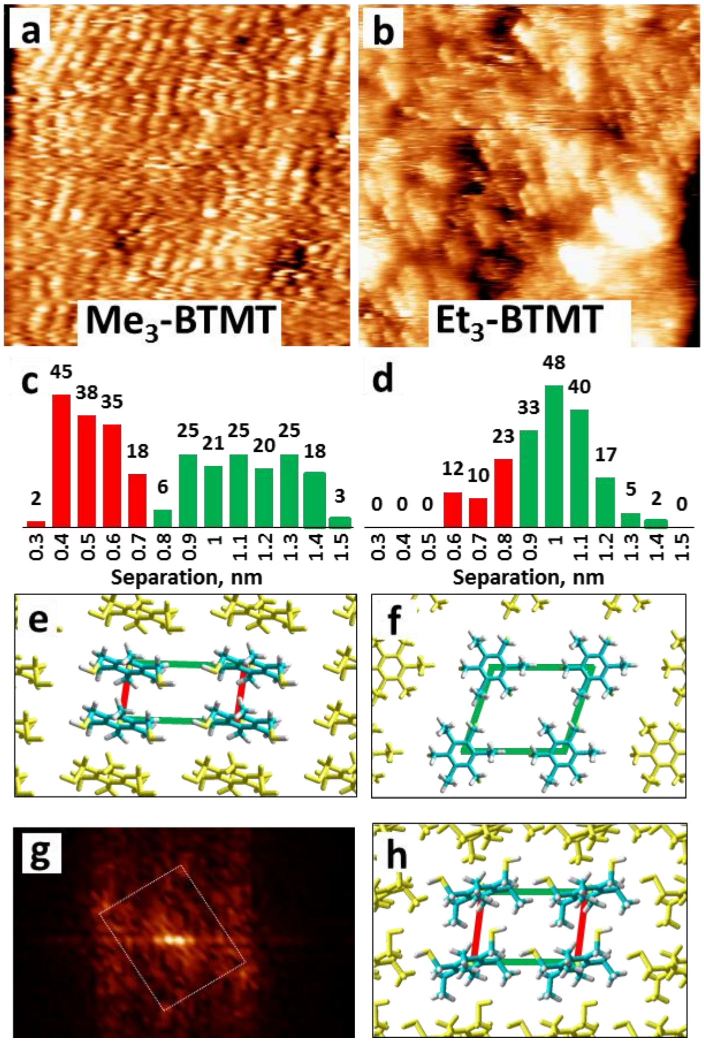

Figure 2.4. Representative 25×25 nm STM images of SAMs formed by Me$_3$-BTMT (a) and Et$_3$-BTMT (b); scanning parameters: (a) V_t = 800 mV, I_t = 0.2 nA; (e) V_t = 600 mV, I_t = 0.3 nA). (c), (d) Corresponding histograms of the nearest neighbor distances; the red bars correspond to intermolecular separations that are only possible for *standing up* molecules; green bars represent distances at which the neighboring molecules can either lie down or stand up on the surface. Tentative models for close-packed assembly of '*standing up*' Me$_3$-BTMT (e) and Et$_3$-BTMT (h) and '*lying down*' Et$_3$-BTMT (f). (g) Fast Fourier transform (FFT) image of (a).

To further promote the *lying down* orientation, the trithiol ODe$_3$-BTMT was equipped with three long dodecyl chains which were expected to engage in multiple van der Waals interactions with the surface and between themselves. Fig. 2.5 shows STM images of SAMs of ODe$_3$-BTMT and of its non-thiolated analog ODe$_3$-B. The defining role of the alkyl chain interactions is apparent from the assembly of ODe$_3$-B which forms a well-ordered 2D periodic lattice with an oblique unit cell (a = 1.4 ± 0.1 nm; b = 2.3 ± 0.2 nm; α = 78 ± 6°). The high-resolution image of this assembly clearly shows the orientation of the alkyl chains (Fig. 2.5c). Measurements of the area available for adsorption of alkyl side chains, together with the number of visualized alkyl chains, suggest that two interdigitated alkyl chains are adsorbed on the surface, while the third one protrudes into the solution (as observed earlier for similar molecules).[49]

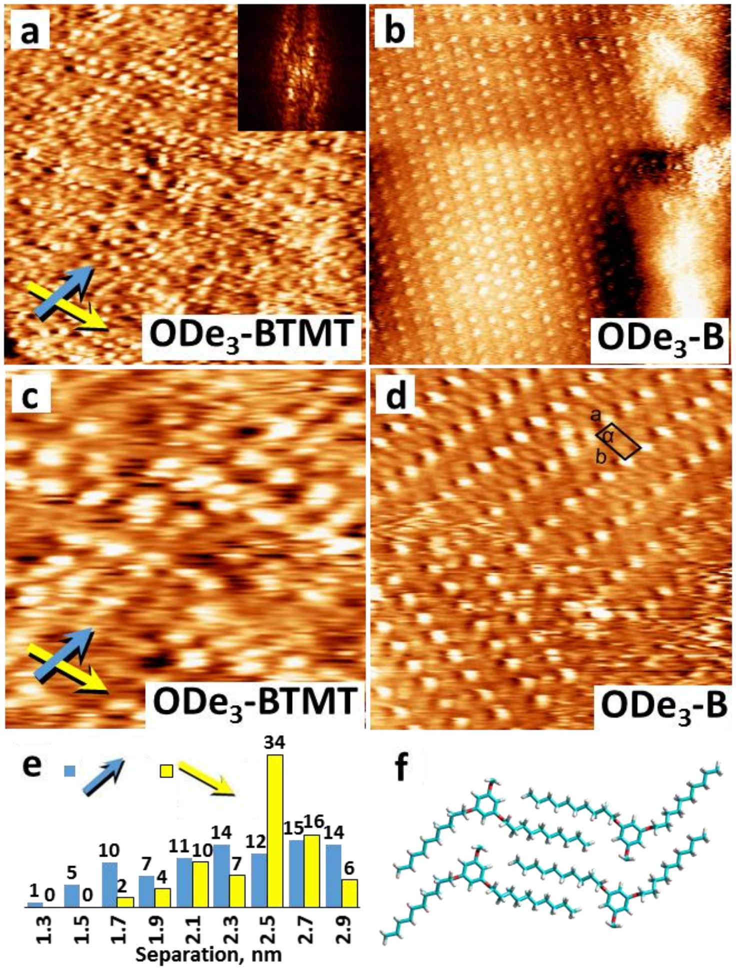

Figure 2.5. Representative STM images of SAMs formed by ODe_3-BTMT (a,c) and ODe_3-B (b,d). Image size and scanning parameters: (a) 77×77 nm, V_b = 300 mV, I_t = 0.15 nA; (b) 40×40 nm, V_b = 800 mV, I_t = 0.08 nA; (c) 25×25 nm, V_b = 300 mV, I_t = 0.15 nA; (d) 25×25 nm, V_b = 800 mV, I_t = 0.08 nA. An inset in (a) shows fast Fourier transform (FFT) image of the STM micrograph. (e) A histograms of the nearest neighbor distance of ODe_3-BTMT along (yellow bars) and across (blue bars) the apparent one-dimensional rows (marked with the yellow arrow in (a) and (c). (f) Tentative models for self-assembly of ODe_3-B. For clarity, the alkyl chains pointing into the solution face are not shown.

The SAM of the corresponding trithiol ODe_3-BTMT is significantly less ordered than that of the physisorbed ODe_3-B, and contrary to Me_3-BTMT and Et_3-BTMT, there are no sub-nanometer nearest neighbor separation in ODe_3-BTMT. The average three-point contact (*a*=1.7±0.5 nm, *b*=2.5±0.5 nm, α =75°±20°, SI3) is similar but slightly larger than the unit cell parameters of the parent ODe_3-B suggesting a similar adsorption geometry.

2.3.2 XPS characterization of tridentate benzylthiols

XPS has been widely used for the characterization of thiol-based SAMs. The binding energy (BE) of the S2p signal provides clear evidence for S-Au bond formation. XPS S2p spectra of the C_8SH, Me_3-BTMT, Et_3-BTMT and ODe_3-BTMT SAMs are presented in Fig. 2.6. Consistent with the literature, the S2p spectrum of C_8SH shows a well resolved doublet with a BE of 162.0 eV ($S2p_{3/2}$ peak).[50] The Me_3-BTMT, Et_3-BTMT and ODe_3-BTMT SAMs show broad S2p peaks best fitted as two doublets at 162.0 eV and 163.0 eV (for $S2p_{3/2}$ peaks) assigned to Au-bonded and non-bonded sulphur, respectively. No oxidized sulphur is detected at higher binding energy values (>166 eV[50]).

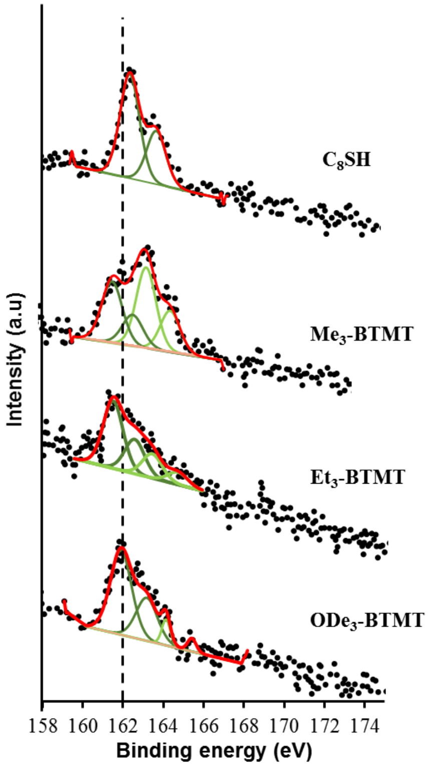

Figure 2.6. X-ray photoelectron spectra and their deconvoluted components of the four SAMs studied, formed by 18 h immersion of Au/mica slides in 0.1mM DMF solutions of the corresponding thiols.

Compared to the SAM of C_8SH, where all sulphurs are bound to gold (100%), the trithiols reveal a mixture of bonded and nonbonded sulphur (Table 2.1). The lowest degree of sulphur binding (~44%) was observed for Me_3-BTMT, while Et_3-BTMT and ODe_3-BTMT shows a higher bound/non-bound thiol with the values of ~73% and ~90% respectively.

Table 2.1. A summary of XPS and electrochemical analysis of C_8SH, Me_3-BTMT, Et_3-BTMT and ODe_3-BTMT SAMs on Au.

		C_8SH	**Me_3-BTMT**	**Et_3-BTMT**	**ODe_3-BTMT**
S_b/S_T (%)[a]		100	44	73	90
S_T/Au[b]		4.2×10^{-3}	7.5×10^{-3}	5.6×10^{-3}	4.2×10^{-3}
Cycle 1	E[c] (V vs Ag/AgCl)	−0.88	−0.83	−0.86	−1
	Q_c (μC/cm^2) [d]	33.1	31.6	24.2	14.5
	Γ (mol/cm^2) [e]	3.4×10^{-10}	2.6×10^{-10}	1.1×10^{-10}	0.6×10^{-10}
	A’ (nm^2) [f]	0.5	0.7	1.6	2.8
	fwhm (mV) [g]	37	46	113	120
Cycle 2	E_{red} (V vs Ag/AgCl)	−0.84	−0.85	−0.89	−0.92
	Q_c (μC/cm^2)	15.4	13.9	11.8	13.6
	Q_{c2}/Q_{c1}	0.47	0.44	0.49	0.94

(a) XPS ratio of bound sulfur to total sulfur (b) XPS ratio of total sulfur to gold (c) desorption peak potential, (d) desorption charge density, (e) electrochemical surface concentration, (f) area per molecule (deduced from Γ), and (g) full width at half-maximum of a desorption wave.

The ratio of the peak areas of bound/non-bound sulphur might be related to the conformation of tridentate molecules forming the SAMs. The observed ratio suggests that Me_3-BTMT molecules are most likely attached to the gold substrate in a standing-up configuration, which allows for only one of three thiol groups to bind to the surface. On the other hand, Et_3-BTMT involves both the lying down and standing-up conformations, resulting in ca. two thiol groups per molecule being bound to the gold surface. This difference can be explained by the large energetic preference of all thiol groups in Et_3-BTMT to adopt the *syn* conformation (Fig. 2.3), which facilitates their binding with the surface. In addition, the bulkier ethyl substituents can inhibit the π…π interactions between the aromatic cores that are the likely source of stabilization of the standing-up conformation of the Me_3-BTMT case, as suggested by STM measurements.

Interestingly, ODe_3-BTMT does not show a large preference for the co-facial *syn* position of its thiol groups, and exhibits the lowest extent of non-bound sulphur. This most likely should be attributed to the large preference of these molecules to adsorb in a lying down orientation on the surface, so as to maximize the vdW interactions of the alkoxy chains with the gold and between themselves.

The analysis of the ratio of the S2p and Au4f peak intensity (Table 2.1) shows a decrease of the molecular surface density upon increasing the size from Me to Et to ODe. This trend is also in agreement with the footprint of the different conformations of these tridentate molecules. Indeed, ODe_3-BTMT shows the lowest surface density, followed by Et_3-BTMT (both in a lying down conformation) and finally Me_3-BTMT which adopts standing-up conformation. For C_8SH, the lower sulfur to gold ratio could be explained by attenuation of the photoelectrons by standing up alkyl chain (which leads to a relative enhancement of the Au signal from defective areas of the SAM[51]).

2.3.3 Electrochemical desorption of tridentate benzylthiols

Further information concerning the strength of the intermolecular interaction, degree of molecular order, and surface density of SAMs was acquired by electrochemical desorption experiments. Fig. 2.7 shows consecutive cyclic voltammograms (CV) of C_8SH, Me_3-BTMT, Et_3-BTMT and ODe_3-BTMT coated gold electrodes. The CVs were recorded by repetitive scanning of the potential of the SAM-modified gold electrode from 0 to –1.3 V at 0.02 V/s in aqueous KOH solution (0.5 M). On cathodic sweep, all SAMs exhibit an irreversible reduction wave between E_{red} −0.83 and −1 V vs Ag/AgCl indicative of S–Au bond cleavage.[52] Significant differences in the shape and position of the desorption peaks as well as the quantity of reductive charge for the four SAMs were observed (Table 2.1).

The shape and the location of the desorption peak is strongly affected by the state of the monolayer, including factors such as the packing density and the magnitude of the lateral interactions between the adsorbed molecules.[53,54] As shown in Fig. 2.7, desorption of a C_8SH SAM results in a narrow symmetric cathodic peak at –0.88 V. With respect to the C_8SH SAM, the reduction peaks of Me_3-BTMT, Et_3-BTMT SAMs were observed at less negative potentials, at –0.83 V and –0.86 V, respectively, while ODe_3-BTMT SAM reveals a peak at a more negative potential (around –1 V). The shift toward more negative potential was previously correlated with the electrochemical stability of the SAM.[53] The following trend in SAM stability is thus suggested: ODe_3-BTMT > C_8SH > Et_3-BTMT > Me_3-BTMT. The apparent electrochemical stability of C_8SH is thus higher than that of Et_3-BTMT although the latter forms at least twice as many thiol-gold bonds with the surface. This observation highlights that both chemisorptive (Au-S) bonding and vdW intermolecular interactions are (equally) important contributors to the stability of thiol-based monolayers.[12,53]

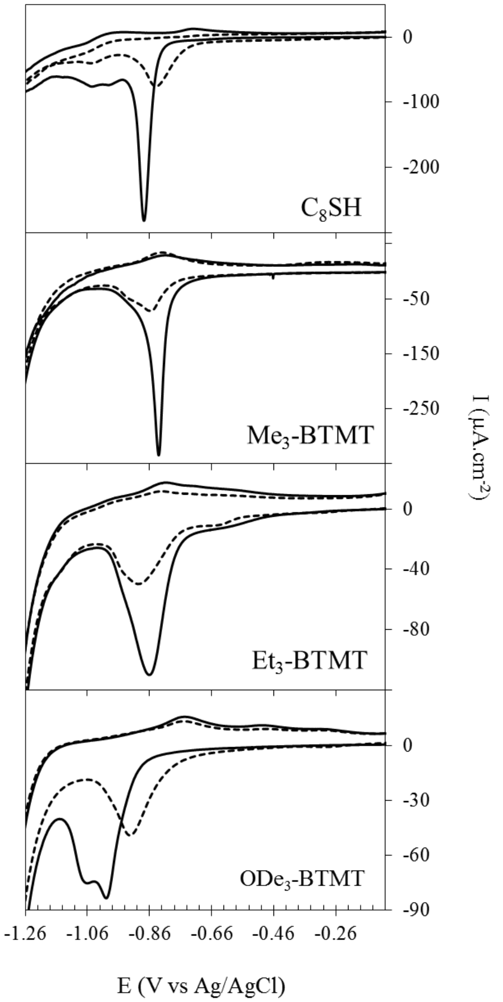

Figure 2.7. Cyclic voltammograms of the reductive desorption of the four SAMs on gold working electrode in 0.5 M KOH. The first (solid line) and the second cycles (dashed line) are shown. Scan rate 0.02 V/s.

On the other hand, C_8SH and Me_3-BTMT show full width at half-maximum (fwhm) values of 37 mV and 46 mV respectively, while broader peaks are observed for Et_3-BTMT and ODe_3-BTMT, with fwhm of 113 and 124 mV respectively. A very small fwhm was previously explained by the extensive intermolecular interactions within the SAMs of n-alkanethiols. For aromatic trithiols SAMs, the relative sharpness of the reductive peak of Me_3-BTMT could be a confirmation of the suggested earlier standing up orientation of this molecule, which can engage in intermolecular π-interactions. On the other hand, the larger fwhm of Et_3-BTMT and ODe_3-BTMT is consistent with each adopting a lying down orientation on gold surface.

Integration of the reductive desorption peak of C_8SH yields a charge density (Q_c) of 33 µC/cm^2. This is smaller than theoretical value but consistent with other reports for gold surfaces prepared by analogous procedure (cleaning with piranha solution).[55,56] Electrochemical desorption of Me_3-BTMT, Et_3-BTMT and ODe_3-BTMT is associated with the charge densities of 32 µC/cm^2, 24 µC/cm^2 and 15 µC/cm^2 respectively. The charge density was then converted to a surface concentration value assuming 1.3 electron per molecule for Me_3-BTMT, 2.2 for Et_3-BTMT and 2.7 for ODe_3-BTMT as per the XPS-derived ratios of bound to nonbound sulphur, Table 2.1. These calculations lead to surface concentrations of 3.6×10^{-10} mol/cm^2, 1.1×10^{-10} mol/cm^2 and 0.6×10^{-10} mol/cm^2, and molecular footprint areas of 0.7 nm^2, 1.6 nm^2 and 2.8 nm^2 for Me_3-BTMT, Et_3-BTMT, and ODe_3-BTMT, respectively. These values are in agreement with the XPS and STM data: as the size of the substituent increases the constituent molecules occupy a greater area in the respective SAMs.

In each of the four SAMs, upon reversing the scan direction, weak broad anodic (oxidation) peaks arise, characteristic of re-adsorption of the non-diffused thiolate. In the second CV cycle (Fig. 2.7, dashed curve), the oxidatively re-adsorbed thiols are again desorbed. Significant differences in the shape and position of the desorption peaks and in the quantity of reductive charges between the first and second cycle were observed, reflecting the change of the adsorbed state of the molecules.

For C_8SH, the integration of second reduction peak shows that 45% of the desorbed thiols molecules subsequently re-adsorb on an anodic scan. Similar redeposition efficiencies are measured for both Me_3-BTMT (44%) and Et_3-BTMT (49%). In contrast, ODe_3-BTMT undergoes much more extensive readsorption (95%). This is likely related to the lesser solubility of ODe_3-BTMT thiolate vs Me_3-BTMT and Et_3-BTMT in the aqueous electrolyte. Such behavior has been previously reported for $C_{16}SH$ and explained by the formation of micelles of amphiphilic $C_{16}S^-$ at the electrode-electrolyte interface, which significantly lowers the diffusion coefficient.[57]

The reduction potential of the second voltammetric sweep undergoes a shift of +40 mV in the case of C_8SH, –20 mV for Me_3-BTMT, –30mV for Et_3-BTMT, and +80 mV for ODe_3-BTMT. This positive shift, frequently observed in alkanethiol desorption,[53,55] is attributed to the higher ionic permeability of the less ordered SAM that is formed during the oxidative readsorption. On the other hand, the formation of disulfide bridges between the free thiols of neighboring molecules within the SAM during the oxidative readsorption might explain the negative shift observed for Me_3-BTMT and Et_3-BTMT.[58,59]

Overall, the electrochemical data are thus consistent with a standing up organization of Me_3-BTMT and a lying down conformation of Et_3-BTMT and ODe_3-BTMT.[60] The standing up orientation yields a SAM with high molecular density, greater intermolecular interactions and the possibility of formation of a disulphide bonds. The lying down orientation of ODe_3-BTMT and to a lesser extent Et_3-BTMT (whose SAM also includes some standing-up molecules) yields a lower surface coverage and weaker intermolecular interactions.

2.4 Conclusions

A set of new tridentate molecules based on a benzene ring substituted with three methylthiol groups in alternation with three alkyl chains were synthesized and their self-assembly on Au(111) was studied. STM characterization of the resulting SAMs revealed a locally ordered arrangement of bright protrusions attributable to individual molecules. XPS and electrochemistry results establish that the surface density and orientation of these molecules depend on the size of their substituents. SAMs of Me_3-BTMT exhibit the higher molecular density of the three molecules studied and the lowest ratio of bound/non-bound thiol. This suggests a preference for the standing-up orientation for this molecule. For Et_3-BTMT, the bulkier ethyl substituents favors a lying down orientation on the surface, yielding a SAM with a higher degree of chemisorption (>70% of thiol groups are bonded to gold). Finally, ODe_3-BTMT, predominantly adsorbs in a lying down orientation, with almost all its thiol groups bonded to the gold substrate. This orientation is driven mainly by the vdW interactions between the alkoxy chains and the gold, and between themselves. Overall, the balance between intermolecular and molecule–substrate interactions appear to determine the packing, orientation, and stability of the monolayer of tridentate thiols.

2.5 Experimental section

Preparation of the SAMs. Au(111) substrates with atomically flat terraces were prepared by thermal evaporation of gold onto freshly cleaved mica sheets preheated at 450 °C under a pressure of 10^{-7}-10^{-8} Pa.[61] Au/Cr/glass and Au/Cr/Si substrates were purchased from Emtron Hybrids (Yaphank, NY).The SAMs of C_8SH, Me_3-BTMT, Et_3-BTMT and ODe_3-BTMT SAMs were prepared by immersing the Au/mica (for STM measurements), Au/Cr/glass and Au/Cr/Si substrates (for other measurements) in a 0.1 mM DMF (ACS reagent) solution of the corresponding thiols under Ar atmosphere at room temperature for 18 hours. After SAM formation, the samples were thoroughly rinsed with pure DMF to remove physisorbed molecules and dried under a stream of ultrapure N_2.

Cyclic voltammetry (CV). Prior to SAM deposition, the gold electrodes were dipped into a freshly prepared piranha solution (concentrated H_2SO_4: 30% H_2O_2 = 3:1) for 5 min (caution: "piranha solution" reacts violently with organic materials and should be handled very carefully), rinsed with copious quantities of Milli-Q water, and dried under an N_2 stream. This was immediately followed by electrochemical polishing performed by repetitive CV cycles in 0.5 M H_2SO_4 solution from −0.4 to +1.5 V at 0.1 V/s, until reproducible voltammograms were obtained.

The electrode roughness factor γ was determined by integrating the charge of the reduction peak of the gold oxide.[62,63] Assuming a theoretical value[63] (Q_{O2}) of 400 $\mu C/cm^2$ for a monolayer of chemisorbed oxygen on a polycrystalline gold electrode and a geometric area (A_g) of the Au electrode of 3.2×10^{-3} cm^2, the Au electrode roughness factor was determined to be $\gamma = 1.3\pm 0.1$ ($\gamma = Qc/(A_g\times Q_{O2})$), where Qc is the charge of the reduction peak of gold oxide (μC)).

Cyclic voltammograms were acquired using a CHI 760C workstation (CH Instruments Inc, Austin, TX). The three-electrode electrochemical cell consisted of a modified Au electrode, a Pt wire counter electrode, and an Ag/AgCl reference electrode. The reductive desorption of the SAMs was performed in 0.5 M KOH solution, purged with high purity Ar for 15 min prior to measurements. The reductive desorption voltammograms were recorded by cycling the potential between 0.1 to −1.3 V at 0.02 V/s. The surface concentration of the adlayer, Γ_m (mol/cm^2) was obtained from Faraday's law: $\Gamma_m = Q/ZnFA$, where Q (μC) is the passed charge determined from the CVs by integrating the area under the reduction peak, Z is the number of electrons involved in the redox reaction, n is the number of moles of reactants, F is Faraday’s constant and A is the active area of gold electrode ($A=Ag\times\gamma$ (cm^2)).

Scanning tunneling microscopy (STM). STM measurements were performed under ambient conditions using either a NanoSurf EasyScan 2 or Multimode8^{TM} equipped with a Nanoscope^{TM} V controller (Bruker, Santa Barbara, CA) and Nanoscope 8.15r3 software. The STM tips were mechanically cut from Pt/Ir wire (80/20, diameter 0.25 mm, Nanoscience). All STM-images were obtained in the constant current mode using an A scanner and low current STM converter by applying a tunneling current I_{set} of 70 to 250 pA and a sample bias V_{set} of 500 to 1400 mV. Calibration of the piezoelectric positioners was verified by atomic resolution imaging of graphite. The raw images were processed from WSxM5.0 software[64] through 2D-FFT and line profiles.

X-Ray photoelectron spectroscopy (XPS). XPS spectra were recorded on a ThermoFisher Scientific K-alpha instrument equipped with a monochromatic Al Kα X-ray source (1486.6 eV). Spectral energies were calibrated by setting the binding energy of Au $4f_{7/2}$ (84.0 eV). The peak-fitting procedure was performed using the Thermo Avantage software (version 4.60).

References

---

[1] Scherer, J.; Vogt, M. R.; Magnussen, O. M.; Behm, R. J. Corrosion of Alkanethiol-Covered Cu(100) Surfaces in Hydrochloric Acid Solution Studied by in-Situ Scanning Tunneling Microscopy. *Langmuir* **1997**, *13*, 7045− 7051.

[2] Song, H.; Reed, M. A.; Lee, T. Single Molecule Electronic Devices *Adv. Mater*. **2011**, *23*, 1583− 1608.

[3] De Boer, B.; Meng, H.; Perepichka, D. F.; Zheng, J.; Frank, M. M.; Chabal, Y. J.; Bao, Z. Synthesis and Characterization of Conjugated Mono- and Dithiol Oligomers and Characterization of their Self-Assembled Monolayers. *Langmuir* **2003**, *19*, 4272– 4284.

[4] Halik, M.; Hirsch, A. The Potential of Molecular Self-Assembled Monolayers in Organic Electronic Devices. *Adv. Mater*. **2011**, *23*, 2689− 2695.

5 Arramel, T. C. Pijper, T. Kudernac, N. Katsonis, M. van der Maas, B. L. Feringa and B. J. van Wees, Reversible light induced conductance switching of asymmetric diarylethenes on gold: Surface and electronic studies. *Nanoscale* **2013**, 5, 9277−9282.

[6] Masillamani, A. P.; Osella, S.; Liscio, A.; Fenwick, O.; Reinders, F.; Mayor, M.; Palermo, V.; Cornil, J.; Samori, P.Light-induced reversible modification of the work function of a new perfluorinated biphenyl azobenzene chemisorbed on Au (111). *Nanoscale* **2014**, 6, 8969–8977.

---

[7] Deng, L.; Mrksich, M.; Whitesides. G.M.; Self-Assembled Monolayers of Alkanethiolates Presenting Tri(propylenesulfoxide) Groups Resist the Adsorption of Protein. *J. Am. Chem. Soc.* **1996**, *118*, 5136–5137.

[8] Gooding, J. J.; Mearns, F.; Yang, W.; Liu, J. Self-Assembled Monolayers into the 21st Century: Recent Advances and Applications. *Electroanalysis* **2003**, *15*, 81– 96.

[9] Tabard-Cossa, V.; Godin, M.; Burgess, I.J.; Monga, T.; Lennox, R.B.; Grütter, P. Microcantilever-Based Sensors: Effect of Morphology, Adhesion, and Cleanliness of the Sensing Surface on Surface Stress. *Anal. Chem.* **2007**, *79*, 8136– 8143.

[10] Chaki, N. K.; Vijayamohanan. Self-assembled Mmonolayers as a Tunable Platform for Biosensor Applications. *Biosens. Bioelectron*. **2002**, *17*, 1− 12.

[11] Vericat, C.; Vela, M. E.; Benitez, G.; Carro, P.; Salvarezza, R. C. Self-assembled Monolayers of Thiols and Dithiols on Gold: New Challenges for a Well-known System. *Chem. Soc. Rev.* **2010**. *39*, 1805– 1834.

[12] Love, J. C.; Estroff, L. A.; Kriebel, J. K.; Nuzzo, R. G.; Whitesides, G. M. Self-Assembled Monolayers of Thiolates on Metals as a Form of Nanotechnology. *Chem. Rev.* **2005**. *105*, 1103– 1170.

[13] Nuzzo, R. G.; Zegarski, B. R.; Dubois, L. H. Fundamental Studies of the Chemisorption of Organosulfur Compounds on Gold(111). Implications for Molecular Self-Assembly on Gold Surfaces. *J. Am. Chem. Soc*. **1987**, *109*, 733− 740.

[14] Schlenoff, J. B.; Li, M.; Ly, H. Stability and Self-Exchange in Alkanethiol Monolayers. *J. Am. Chem. Soc*. **1995**, *117*, 12528− 12536.

[15] Schoenfisch, M. H.; Pemberton, J. E. Air Stability of Alkanethiol Self-Assembled Monolayers on Silver and Gold. *J. Am. Chem. Soc*. **1998**, *120*, 4501– 4513.

[16] Chinwangso, P.; Jamison, A. C.; Lee, T. R. Multidentate Adsorbates for Self-Assembled Monolayer Films. *Acc. Chem. Res.* **2011**, *44*, 511− 519.

[17] Miller, M. S.; San Juan, R. R.; Ferrato, M. M. Carmichael, T. B. The unusual self-organization of dialkyldithiophosphinic acid self-assembled monolayers on ultrasmooth gold. *J. Am. Chem. Soc*. **2013**, 136, 4212–4222.

[18] Whitesell, J. K.; Chang, H. K. Directionally Aligned Helical Peptides on Surfaces. *Science* **1993**, *261*, 73– 76.

[19] Yao, Y.; Tour, J. M. Facile Convergent Route to Molecular Caltrops. *J. Org. Chem.* **1999**, *64*, 1968–1971.

[20] Jian, H.; Tour, J. M. En Route to Surface-Bound Electric Field-Driven Molecular Motors. *J. Org. Chem.* **2003**, *68*, 5091– 5103.

---

[21] Park, J.-S.; Vo, A. N.; Barriet, D.; Shon, Y.-S.; Lee, T. R. Systematic Control of the Packing Density of Self-Assembled Monolayers Using Bidentate and Tridentate Chelating Alkanethiols. *Langmuir* **2005**, *21*, 2902– 2911.

[22] Kitagawa, T.; Idomoto, Y.; Matsubara, H.; Hobara, D.; Kakiuchi, T.; Okazaki, T.; Komatsu, K. Rigid Molecular Tripod with an Adamantane Framework and Thiol Legs. Synthesis and Observation of an Ordered Monolayer on Au(111). *J. Org. Chem.* **2006**, *71*, 1362− 1369.

[23] Katano, S.; Kim, Y.; Matsubara, H.; Kitagawa, T.; Kawai, M. Hierarchical Chiral Framework Based on a Rigid Adamantane Tripod on Au(111). *J. Am. Chem. Soc.* **2007**, *129*, 2511– 2515.

[24] Singhana, B.; Rittikulsittichai, S.; Lee, T.R. Tridentate Adsorbates with Cyclohexyl Headgroups Assembled on Gold. *Langmuir* **2013**, *29*, 561− 569.

[25] Singhana, B.; Jamison, A.C.; Hoang, J.; Lee, T.R. Self-Assembled Monolayer Films Derived from Tridentate Cyclohexyl Adsorbates with Alkyl Tailgroups of Increasing Chain Length. *Langmuir* **2013**, *29*, 14108− 14116.

[26] Hutchison, J. E.; Postlethwaite, T. A.; Murray, R. W. Molecular Films of Thiol-Derivatized Tetraphenylporphyrins on Gold: Film Formation and Electrocatalytic Dioxygen Reduction. *Langmuir* **1993**, *9*, 3277– 3283.

[27] Thoden van Velzen, E. U.; Engbersen, J. F. J.; de Lange, P. J.; Mahy, J. W. G.; Reinhoudt, D.N. Self-Assembled Monolayers of Resorcin[4]arene Tetrasulfides on Gold. *J. Am. Chem. Soc.* **1995**, *117*, 6853–6862

[28] Zhu, L.; Tang, H.; Harima, Y.; Yamashita, K.; Hirayama, D.; Aso, Y.; Otsubo, T. Electrochemical Properties of Self-Assembled Monolayers of Tripod-Shaped Molecules and their Applications to Organic Light-Emitting Diodes. *Chem. Commun*. **2001**, 1830– 1831.

[29] Wei, L.; Tiznado, H.; Liu, G.; Padmaja, K.; Lindsey, J.S.; Zaera, F.; Bocian, D.F. Adsorption Characteristics of Tripodal Thiol-Functionalized Porphyrins on Gold. *J. Phys. Chem. B.* **2005**, *109*, 23963– 23971.

[30] Shirai, Y.; Cheng, L.; Chen, B.; Tour, J.M. Characterization of Self-Assembled Monolayers of Fullerene Derivatives on Gold Surfaces: Implications for Device Evaluations. *J. Am. Chem. Soc*. **2006**, *128*, 13479– 13489

[31] Kitagawa, T.; Matsubara, H.; Komatsu, K.; Hirai, K.; Okazaki, T.; Hase, T. Ideal Redox Behavior of the High-Density Self-Assembled Monolayer of a Molecular Tripod on a Au(111) Surface with a Terminal Ferrocene Group. *Langmuir* **2013**, *29*, 4275–4282.

[32] Fox, M. A.; Whitesell, J. K.; McKerrow, A.J. Fluorescence and Redox Activity of Probes Anchored through an Aminotrithiol to Polycrystalline Gold. *Langmuir* **1998**, *14*, 816– 820.

---

[33] Phares, N.; White, R.J.; Plaxco, K.W. Improving the Stability and Sensing of Electrochemical Biosensors by Employing Trithiol-Anchoring Groups in a Six-Carbon Self-Assembled Monolayer. *Anal. Chem*. **2009**, *81*, 1095–1100.

[34] Yasseri, A. A.; Syomin, D.; Malinovskii, V. L.; Loewe, R. S.; Lindsey, J. S.; Zaera, F.; Bocian, D. F. Characterization of Self-Assembled Monolayers of Porphyrins Bearing Multiple Thiol-Derivatized Rigid-Rod Tethers. *J. Am. Chem. Soc*. **2004**, *126*, 11944− 11953.

[35] Moore, A. M.; Dameron, A. A.; Mantooth, B. A.; Smith, R. K.; Fuchs, D. J.; Ciszek, J. W.; Maya, F.; Yao, Y.; Tour, J. M.; Weiss, P. S. Molecular Engineering and Measurements To Test Hypothesized Mechanisms in Single Molecule Conductance Switching. *J. Am. Chem. Soc.*, **2006**, *128* , 1959–1967

[36] Shimazu, K,; Takechi, M; Fujii, H.; Suzuki, M.; Saiki, H.; Yoshimura, T.; Uosaki, K. Formation and Characterization of Thiol-Derivatized Zinc (II) Porphyrin Monolayers on Gold. *Thin Solid Films*. **1996**, *273*, 250− 253.

[37] Watcharinyanon, S.; Puglia, C.; Gothelid, E.; Backvall, J. E.; Moons, E.; Johansson, L. S. O. Molecular Orientation of Thiol-Derivatized Tetraphenylporphyrin on Gold Studied by XPS and NEXAFS. *Surf. Sci*. **2009**, *603*, 1026– 1033.

[38] Hennrich, G.; Anslyn, E.V. 1,3,5-2,4,6-Functionalized, Facially Segregated Benzenes–Exploitation of Sterically Predisposed Systems in Supramolecular Chemistry. *Chem. Eur. J.* **2002**, *8*, 2218– 2224.

[39] Burns, J. A.; Whitesides, G. M. Predicting the Stability of Cyclic Disulfides by Molecular Modeling: Effective Concentrations in Thiol-Disulfide Interchange and the Design of Strongly Reducing Dithiols. *J. Am. Chem. Soc.* **1990**, *112*, 6296– 6303.

[40] Mali, K. S.; Adisoejoso, J.; Ghijsens , E.; De Cat, I.; De Feyter, S. Exploring the complexity of supramolecular interactions for patterning at the liquid-solid interface. *Acc. Chem. Res*. **2012**, 45 1309–1320.

[41] Ciesielski, A.; Palma, C. A.; Bonini, M.; Samorì, P. Towards Supramolecular Engineering of Functional Nanomaterials: Pre-Programming Multi-Component 2D Self-Assembly at Solid-Liquid Interfaces. *Adv. Mater.* **2010**, *22*, 3506– 3520.

[42] Xue, Y.; Zimmt, M. B. Patterned monolayer self-assembly programmed by side chain shape: Four-component gratings. *J. Am. Chem. Soc*. **2012**, 134, 4513–4516.

[43] Sarwar, M.G.; Dragisic, B.; Sagoo, S.; Taylor, M.S. Document a Tridenatet Halogen-Bonding Receptor for Binding of Halide Anions. *Angew. Chem. Int. Ed.* **2010**, *49*, 1674– 1677.

[44] Sather, A.C; Berryman ,O.B.; Rebek Jr, J. Selective Recognition and Extraction of the Uranyl Ion. *J. Am. Chem. Soc.* **2010**, *132*, 13572– 13574.

[45] Wang, X.; Hof, F. (How) Does 1,3,5-Triethylbenzene Scaffolding Work? Analyzing the Abilities of 1,3,5-Triethylbenzeneand 1,3,5-Trimethylbenzene-Based Scaffolds to Preorganize the Binding

---

Elements of Supramolecular Hosts and to Improve Binding of Targets. *Beilstein. J. Org. Chem.* **2012**, *8*, 1– 10.

[46] Poirier, G. E. Characterization of Organosulfur Molecular Monolayers on Au(111) using Scanning Tunneling Microscopy. *Chem. Rev.* **1997**, *97*, 1117– 1128.

[47] Martin, J. E.; Wilcoxon, J. P.; Odinek, J.; Provencio, P. Control of the interparticle spacing in gold nanoparticle superlattices. *J. Phys. Chem. B,* **2000**,104, 9475–9486.

[48] Merte, L. R.; Bechstein, R.; Peng, G. W.; Rieboldt, F.; Farberow, C. A.; Zeuthen, H.; Knudsen, J.; Laegsgaard, E.; Wendt, S.; Mavrikakis, M.; Besenbacher, F. Water clustering on nanostructured iron oxide films. *Nat. Commun*. **2014**, 5, 4193.

[49] Tahara, K.; Lei, S.; Adisoejoso, J.; De Feyter, S.; Tobe, Y. Supramolecular Surface-Confined Architectures Created by Self-Assembly of Triangular Phenylene–Ethynylene Macrocycles *via* Van der Waals Interaction. *Chem. Commun.* **2010**, *46*, 8507– 8525.

[50] Castner, D. G.; Hinds, K.; Grainger, D. W. X-ray Photoelectron Spectroscopy Sulfur 2p Study of Organic Thiol and Disulfide Binding Interactions with Gold Surfaces. *Langmuir* **1996**, *12*, 5083− 5086.

[51] Bain, C. D.; Evall, J.; Whitesides, G. M. Formation of Monolayers by the Coadsorption of Thiols on Gold: Variation in the Head Group, Tail Group, and Solvent. *J. Am. Chem. Soc.* **1989**, *111*, 7155– 7164.

[52] Widrig, C. A.; Chung, C.; Porter, M. D. the Electrochemical Desorption of n-Alkanethiol Monolayers from Polycrystalline Au and Ag Electrodes. *J. Electroanal. Chem*. **1991,** *310*, 335– 359.

[53] Kakiuchi, T.; Usui, H.; Hobara, D.; Yamamoto, M. Voltammetric Properties of the Reductive Desorption of Alkanethiol Self-Assembled Monolayers from a Metal Surface. *Langmuir* **2002**, *18*, 5231–5238.

[54] Liu, Y.-F.; Lee, Y.-L. Adsorption characteristics of OH-terminated alkanethiol and arenethiol on Au(111) surfaces. *Nanoscale* **2012**, 4, 2093–2100.

[55] Feng, F.; Niu, T.; You, X.; Wan, Z.; Kong, Q.; Bi, S. Studies on the Effect of Electrode Pretreatment on the Coverage of Self-Assembled Monolayers of Dodecanethiol on Gold by Electrochemical Reductive Desorption Determination. *Analyst* **2011**, *136*, 5058– 5063.

[56] Tkac, J.; Davis, J. J. An Optimised Electrode Pre-Treatment for SAM Formation on Polycrystalline Gold. *J. Electroanal. Chem*. **2008**, *621*, 117– 120.

[57] Yang, D. F.; Wilde, C. P.; Morin, M. Studies of the Electrochemical Removal and Efficient Re-formation of a Monolayer of Hexadecanethiol Self-Assembled at an Au(111) Single Crystal in Aqueous Solutions. *Langmuir* **1997**, *13*, 243– 249.

[58] Rifai, S.; Morin, M. Isomeric Effect on the Oxidative Formation of Bilayers of Benzenedimethanethiol on Au(111). *J. Electroanal. Chem.* **2003**, *550*, 277– 289.

---

[59] Cometto, F. P.; Calderón, C.A.; Euti, E. M.; Jacquelín, D. K.; Pérez, M. A.; Patrito, E. M.; Macagno, V. A. Electrochemical Study of Adlayers of A, Ω-alkanedithiols on Au(1 1 1): Influence of the Forming Solution, Chain Length and Treatment with Mild Reducing Agents. *J. Electroanal. Chem*. **2011**, *661*, 90– 99.

[60] Ellipsometric measurements are in agreement with the suggested structure of the SAMs, yielding film thickness of 0.8 ± 0.4 nm for Et_3-BTMT and 1.1 ± 0.3 nm for Me_3-BTMT, although the observed (and expected) differences are smaller than the uncertainty of the method.

[61] Dishner, M. H.; Ivey, M. M.; Gorer, S.; Hemminger, J. C.; Feher, F. J. Preparation of Gold Thin Films by Epitaxial Growth on Mica and the Effect of Fame Annealing. *J. Vac. Sci. Technol.* A. **1998**, *16*, 3295–3300.

[62] Hoogvliet, J.C.; Dijksma, M.; Kamp, B.; Van Bennekom, W.P. Electrochemical Pretreatment of Polycrystalline Gold Electrodes to Produce a Reproducible Surface Roughness for Self-Assembly: A Study in Phosphate Buffer pH 7.4. *Anal. Chem.* **2000**, *72*, 2016– 2021.

[63] Trasatti. S.; Petrii, O.A. Real Surface Area Measurements in Electrochemistry. *Pure & Appl. Chem.* **1991**, *63*, 711– 734.

[64] Horcas, I.; Fernandez, R.; Gomez-Rodriguez, J. M.; Colchero, J.; Gomez-Herrero, J.; Baro, A. M.WSxM: A Software for Scanning Probe Microscopy and a Tool for Nanotechnology. *Rev. Sci. Instrum.* **2007**, *78*, 1– 8.

Appendix X

STM: image processing and analysis

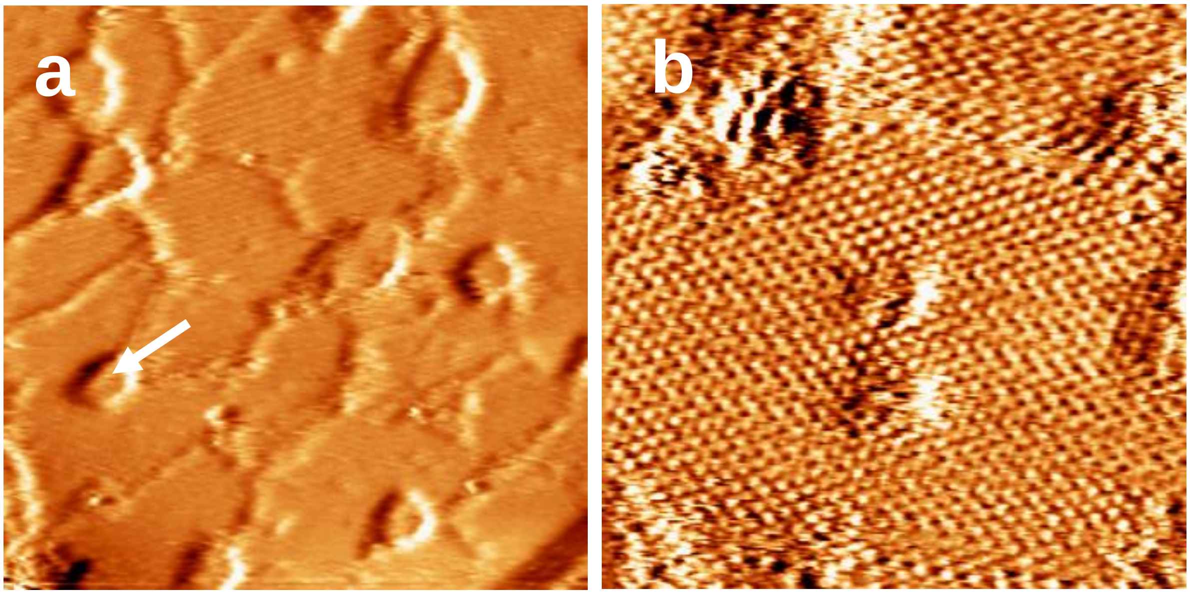

Figure 2.SI1. STM images of 1-octanethiol deposited from 0.1M DMF solution. (a) Low resolution and (b) high resolution STM images (a): 59×59 nm; (b):20×20 nm; V_t = 700 mV, I_t = 0.1 nA of C_8SH SAMs on Au(111). The white arrow in figure (a) indicates an etch pit in C_8SH SAMs.

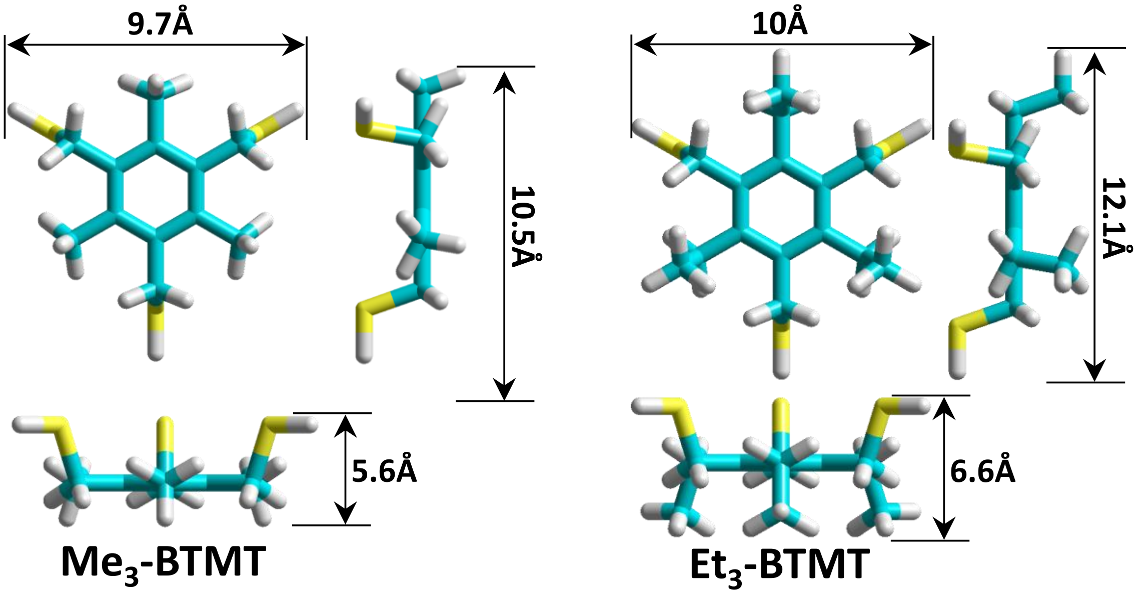

Figure 2.SI2. DFT (B3LYP/6-31G(d)) calculated molecular dimensions of Me_3-BTMT and Et_3-BTMT.

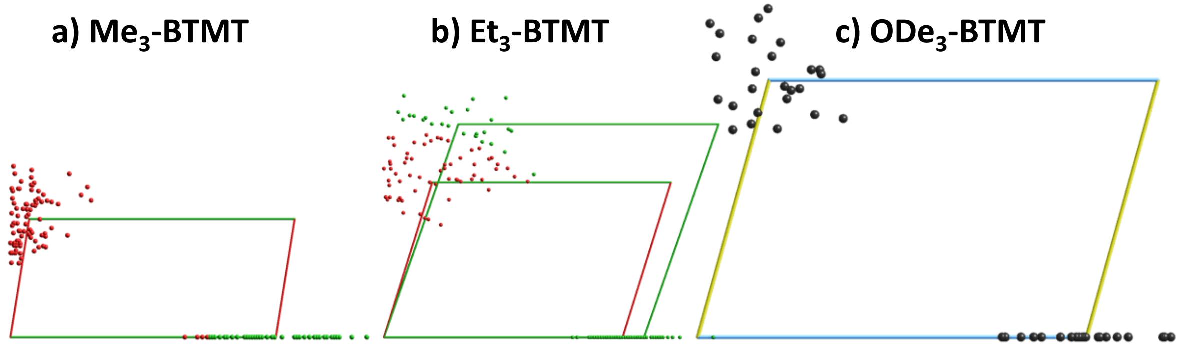

Figure 2.SI3. Pair correlation analysis of the nearest three-point contacts determined for monolayers of: a) Me_3-BTMT, b) Et_3-BTMT and 3) ODe_3-BTMT. Relative orientations of all possible trios of molecules (manually determined from high-contrast spots in STM images) was plotted in the same coordinates, providing both the average intermolecular distances and the relative orientation of two contacts emanating from the same origin (an angle of a "local unit cell"). Intermolecular separations larger than 1.6 nm (for Me_3-BTMT and Et_3-BTMT) and 3 nm (for ODe_3-BTMT) were excluded from the analysis. The red color for molecular positions and "unit cell" vectors bars correspond to intermolecular separations that are only possible for *standing up* orientation of molecules (<0.9 nm for Me_3-BTMT and <1.0 nm for Et_3-BTMT). Green color for molecular separations and average "unit cell vectors" represent distances at which the neighboring molecules can either lie down or stand up on the surface. The other colors do not bear any internal assignment. Average "unit cells" were: (a) a=0.5±0.2 nm, b=1.1±0.4 nm, α =80°±10°; (b) a=0.7±0.2 nm, b=1.0±0.3 nm, α=73°±20°; a=0.9±0.2 nm, b=1.1±0.3 nm, α =75°±20°; (c) a=1.7±0.5 nm, b=2.5±0.5 nm, α =75°±20°.

Synthesis.

1,3,5-Trimethyl-2,4,6-tris(chloromethyl)benzene. To a one-neck round-bottom flask equipped with a stir bar were added mesitylene (21.6 g, 0.18 mol), paraformaldehyde (32.4 g, 1.08 mol), concentrated hydrochloric acid (156 g, 1.58 mol) and sodium chloride (5.61 g, 0.10 mol). A cooler condenser was connected to the flask, and the mixture was refluxed for 12 h under vigorous stirred. After cooling down to r.t., the liquid part was decanted, and another portions of paraformaldehyde (32.4 g, 1.08 mol), concentrated hydrochloric acid (156 g, 1.58 mol), sodium chloride (5.61 g, 0.10 mol), and zinc chloride (24.6 g, 0.18 mol) were added to the reaction mass. The mixture was refluxed for another 24 h under vigorous stirring. After cooling to room temperature, the precipitate was filtered and washed a several times with water and concentrated under reduced pressure. The crude material was recrystallized from dichloromethane/toluene mixture to give the desired product (22.8 g, 48%) with NMR spectral data identical to that previously reported.[1]

*1,3,5-Trimethyl-2,4,6-tris(S-acetylthiomethyl)benzene.*1,3,5-trimethyl-2,4,6-tris(chloromethyl)benzene (1.0 g, mol) and potassium thioacetate (3.0 g, mol) were dissolved in DMF (10 mL) and stirred at r.t. for 4 h. The reaction mixture was poured into water (100 mL), resulting in significant precipitation. The solid material was collected by filtration, washed with H_2O (200 mL), and dried under reduced pressure to give the desired product as yellow powder (1.42 g, 98%). ^1H NMR (300 MHz, DMSO-d6): δ = 4.15 (6H, s), 2.36 (9H, s), 2.20 (9H, s).

1,3,5-Trimethyl-2,4,6-tris(hydrothiomethyl)benzene [Me_3-BTMT]. In a flame-annealed round-bottom flask equipped with a stir bar, 1,3,5-trimethyl-2,4,6-tris(S-acetylthiomethyl)benzene (1 equiv.) was dissolved in a nitrogen-purged 1,4-dioxane. Aqueous solution of sodium hydroxide (5.5 equiv.) was added dropwise to the above solution under N_2 atmosphere, and the mixture was refluxed for 2 h. After cooling to r.t., 2M HCl (6.5 equiv.) was added dropwise to the reaction mixture, and the mixture was stirred at r.t. under nitrogen for another 1 h. N_2-purged H_2O was added, and the product was extracted with chloroform. The organic layer was washed with H_2O until neutral pH, and dried over $MgSO_4$. The desired product was obtained in quantitative yield and with NMR spectral data identical to that reported earlier.[1]

1,3,5-Triethyl-2,4,6-tris(bromomethyl)benzene. To a 250 mL one-neck round-bottom flask equipped with a stir bar were added 1,3,5-triethylbenzene (3.93 g, 24 mmol), paraformaldehyde (8.75 g, 292 mmol), zinc bromide (9.69 g, 43 mmol), and 33% wt hydrogen bromide solution in acetic acid (55 mL; 0.3 mol). A cooler condenser was connected to the flask, and the mixture was heated to 100°C for 22 h under vigorous stirred. The mixture dissolved completely once heated, and in 3 h no precipitate was observed. Overnight heating resulted in formation of a precipitate, indicating that the reaction has completed. After cooling to room temperature, the precipitate was filtered and washed several times with water (400 mL). To remove possible zinc residues, the crude product was suspended in 1.5 M HCl (14 mL conc. HCl in 100 mL H_2O) and kept under stirring for 30 min. The solid product was filtered, washed with water until the wash solution had a neutral pH, then resuspended in 0.5 M aqueous $NaHCO_3$ (5.336 g in 100 mL H_2O) and kept stirred for 20 min. The material was filtered, washed with H_2O until neutral pH, and dried under reduced pressure to give the desired product as a white powder (9.99 g, 93%). m.p.=168–169°C. ^1H NMR (400 MHz, $CDCl_3$): δ = 4.58 (6H, s), 2.94 (6H, q, J = 7.6 Hz), 1.35 (9H, t, J = 7.6 Hz). ^{13}C NMR (75 MHz, $CDCl_3$): δ = 144.97, 132.63, 28.56, 22.73, 15.62.

1,3,5-Triethyl-2,4,6-tris(S-acetylthiomethyl)benzene. In a 250 mL one-neck round-bottom flask equipped with a stir bar, potassium thioacetate (9.09 g, 80 mmol) was dissolved in dimethylformamide (100 mL). 1,3,5-Triethyl-2,4,6-tris(bromomethyl)benzene (4.95 g, 11 mmol) was added to this solution and stirred at room temperature under N_2 for 3 h. The reaction mixture was poured into water (200 mL) and the resulting precipitate was collected by filtration, washed with H_2O, and dried under reduced pressure to give the pure product as a white powder (4.74 g, 99%). m.p.=148–149°C. ^{1}H NMR (400 MHz, $CDCl_3$): δ = 4.17 (6H, s), 2.60 (6H, q, J = 7.6 Hz), 2.36 (9H, s), 1.22 (9H, t, J = 7.6 Hz). ^{13}C NMR (75 MHz, $CDCl_3$): δ = 196.03, 143.15, 130.24, 30.32, 28.42, 23.29, 15.68. m/z (ESI^+ HRMS) for $C_{21}H_{30}O_3S_3$: 449.1249 $(M+Na)^+$, found 449.1240.

1,3,5-Triethyl-2,4,6-tris(hydrothiomethyl)benzene) [Et_3-BTMT]. 1,4-Dioxane and distilled H_2O were purged with bubbling Ar before use. In a 100 mL two-neck round-bottom flask equipped with a stir bar, 1,3,5-Triethyl-2,4,6-tris(S-acetylthiomethyl)benzene (0.716 g, 1.68 mmol) was dissolved in 1,4-dioxane (50 mL). The flask was equipped with a condenser and a rubber septum, and the system was flushed with Ar gas for ~30 min. Sodium hydroxide (0.393 g, 9.82 mmol) was dissolved in H_2O (3 mL) and added dropwise to the solution at r.t. The mixture was refluxed under Ar for 3 h, then cooled to r.t. 2M HCl (5 mL, 10.0 mmol) was added dropwise, and the mixture was stirred at r.t. for 1 h under Ar. H_2O was added, and the product was extracted with chloroform. The organic layer was washed with H_2O several times and dried over $MgSO_4$, followed by filtration and solvent evaporation to give the desired product as a white powder (0.504 g, 100%). ^{1}H NMR (400 MHz, $CDCl_3$): δ = 3.76 (6H, d, J = 6.4 Hz), 2.86 (6H, q, J = 7.6 Hz), 1.70 (3H, t, J = 6.2 Hz), 1.27 (9H, t, J = 7.6 Hz). ^{13}C NMR (75 MHz, $CDCl_3$): δ = 140.21, 135.48, 22.81, 22.77, 16.12.

1,3,5-Tris(acetyloxy)benzene. Acetic anhydride (70 mL, 0.7 mol) was added to a solution of phloroglucinol dihydrate (11.89 g, 73 mmol) in pyridine (50 mL) at r.t. under vigorous stirring. [Note: exothermic reaction!] In 1.5 h, ice (ca. 400 mL) was added to the reaction mixture resulting in formation of precipitate, and stirring continued for another 1 h to destroy the excess Ac_2O. The resulting solid material was filtered, washed with H_2O, and dried under reduced pressure to afford 1,3,5-tris(acetyloxy)benzene (17.01 g) as a light gray powder. Yield: 93%. m.p.=105–106°C. ^{1}H NMR (300 MHz, $CDCl_3$): δ = 6.84 (3H, s), 2.28 (9H, s). ^{13}C NMR (75 MHz, CDCl3): δ = 168.56, 151.07, 112.75, 21.08.

1,3,5-Tris(decyloxy)benzene.

In a 500 mL one-neck round-bottom flask equipped with a stir bar, 1-bromodecane (40 mL, 190 mmol) was added to a solution of 1,3,5-tris(acetyloxy)benzene (13.4 g, 50 mmol) in DMF (150 mL) at -5°C under vigorous stirring. 60% NaH in mineral oil (17.9 g, 440 mmol) was added in one portion, and the reaction mixture was stirred for 20 min, followed by addition of H_2O (6 mL, 330 mmol) at -5°C dropwise over a period of 1 h. [Note: because of released H_2, it is important to use a relatively large volume flask as used here.] The reaction mixture was allowed to slowly warm to heat to r.t and kept under vigorous stirring overnight. After 21 h, the reaction mixture was heated to 50°C and stirred for another 2 h. Brine was added, and the product was extracted into ethyl acetate. The organic layer was washed with H_2O and concentrated under reduced pressure to afford a crude product consisting of target material and excess of 1-bromodecane, which was removed by distillation using Büchi Glass Oven B-585 under reduced pressure (0.25 mbar) at 100°C. The residue from the reaction flask was filtered through silica gel using hexane as an eluent, affording 1,3,5-tris(decyloxy)benzene (16.21 g) as a light yellow liquid. Yield: 56%. The compound contains an impurity of mineral oil (from NaH) and can be used as is in further synthesis. For analytical purposes, it was purified by column chromatography (SiO2; hexane – hexane/CH_2Cl_2 (2:1) gradient). ^{1}H NMR (300 MHz, $CDCl_3$): δ = 6.06 (3H, s), 3.90 (6H, t, J = 6.6 Hz), 1.75 (6H, p), 1.52–1.20 (42H, m), 0.88 (9H, t, J = 6.6 Hz). ^{13}C NMR (75 MHz, CDCl3): δ = 160.93, 93.72, 67.99, 31.91, 29.59, 29.57, 29.39, 29.33, 29.25, 26.06, 22.69, 14.13. m/z (ESI^{+} HRMS) for $C_{36}H_{66}O_3$: 547.50847 $(M+H)^+$, found 547.50915.

1,3,5-Tris(decyloxy)-2,4,6-tris(bromomethyl)benzene. To a 100 mL one-neck round-bottom flask equipped with a stir bar were added 1,3,5-tris(decyloxy)benzene (2.97 g, 5.43 mmol), paraformaldehyde (2.57 g, 85.7 mmol), zinc bromide (2.30 g, 10.2 mmol), and 33% wt hydrogen bromide solution in acetic acid (20 mL; 110 mmol). A condenser was connected to the flask, and the mixture was heated to 55°C for 91 h under vigorous stirring. Higher temperature (~70°C) resulted in loss of alkoxy groups, and a lower temperature (~35°C) is insufficient to complete the reaction. The reaction mass was cooled to room temperature, H_2O was added, and the product was extracted to ethyl acetate. The organic layer was washed with H_2O until the wash solution was at neutral pH, dried over $MgSO_4$, filtered and concentrated under reduced pressure. The crude product was purified by column chromatography on silica using hexane and dichloromethane to afford the desired product as a colorless oil (0.71 g, 16%). ^{1}H NMR (300 MHz, $CDCl_3$): δ = 4.58 (6H, s), 4.25 (6H, t, J = 6.9 Hz), 1.93 (6H, p, J = 6.9 Hz), 1.6–1.2 (42H, m), 0.89 (9H, t, J = 6.8 Hz). ^{13}C NMR (75 MHz, $CDCl_3$): δ = 159.50, 123.15, 75.04, 31.91, 30.31, 29.61, 29.58, 29.50, 29.34, 25.82, 23.11, 22.71, 14.15.

1,3,5-Tris(decyloxy)-2,4,6-tris(S-acetylthiomethyl)benzene. In a 10 mL one-neck round-bottom flask equipped with a stir bar, potassium thioacetate (97 mg, 0.85 mmol) was dissolved in dimethylformamide (1 mL) and mixed with 1,3,5-tris(decyloxy)-2,4,6-tris(bromomethyl)benzene (71 mg, 0.09 mmol) dissolved in dimethylformamide (1 mL). The reaction mixture was stirred at room temperature for 2 days. H_2O was added, and the product was extracted to chloroform. The organic layer was washed with H_2O a few times, dried over $MgSO_4$, filtered and concentrated under reduced pressure to afford the desired product as a yellow oil (51 mg, 75%). ^{1}H NMR (300 MHz, $CDCl_3$): δ = 4.17 (6H, s), 3.79 (6H, t, J = 6.8 Hz), 2.33 (9H, s), 1.80 (6H, p), 1.51–1.21 (42H, m), 0.88 (9H, t). ^{13}C NMR (75 MHz, $CDCl_3$): δ = 195.37, 157.84, 120.37, 75.40, 31.92, 30.24, 30.22, 29.62, 29.58, 29.52, 29.35, 25.89, 23.41, 22.70, 14.14. m/z (ESI^{+} MS) for $C_{45}H_{78}O_6S_3$: 833.4858 $(M+Na)^+$, found 833.4852.

1,3,5-Tris(decyloxy)-2,4,6-tris(hydrothiomethyl)benzene [ODe_3-BTMT]. 1,4-Dioxane and distilled H_2O were degassed with bubbling Ar before use. In a 100 mL two-neck round-bottom flask equipped with a stir bar, 1,3,5-tris(decyloxy)-2,4,6-tris(S-acetylthiomethyl)benzene (0.90 g, 1.1 mmol) was dissolved in 1,4-dioxane (15 mL). The flask was equipped with a condenser and a rubber septum, and the system was flushed with N_2 for ~30 min. 2.9 M aqueous sodium hydroxide (2.3 mL, 6.6 mmol) was added dropwise to the reaction at r.t. The mixture was refluxed under N_2 for 2 h, then cooled to r.t. 2M HCl (3.8 mL, 7.6 mmol) was added dropwise, and the mixture was stirred at r.t. for 1 h under nitrogen. H_2O was added, and the product was extracted with dichloromethane. The organic layer was washed with H_2O several times and dried over $MgSO_4$, followed by filtration and solvent evaporation to yield the desired product as a light yellow oil (0.64 g, 84%). ^{1}H NMR (300 MHz, $CDCl_3$): δ = 3.95 (6H, t, J = 6.6), 3.69 (6H, d, J = 7.8 Hz), 2.23 (3H, t, J = 7.8 Hz), 1.86 (6H, p, J = 7.2 Hz), 1.6–1.2 (42H, m), 0.89 (9H, t, J = 6.5 Hz). ^{13}C NMR (75 MHz, $CDCl_3$): δ = 155.49, 125.73, 75.15, 31.87, 30.44, 29.57, 29.55, 29.49, 29.30, 26.03, 22.66, 18.18, 14.10. m/z (APCI^{-} HRMS) for $C_{39}H_{72}O_3S_3$: 683.45708 $(M-H)^-$, found 683.45550.

Spectral data.

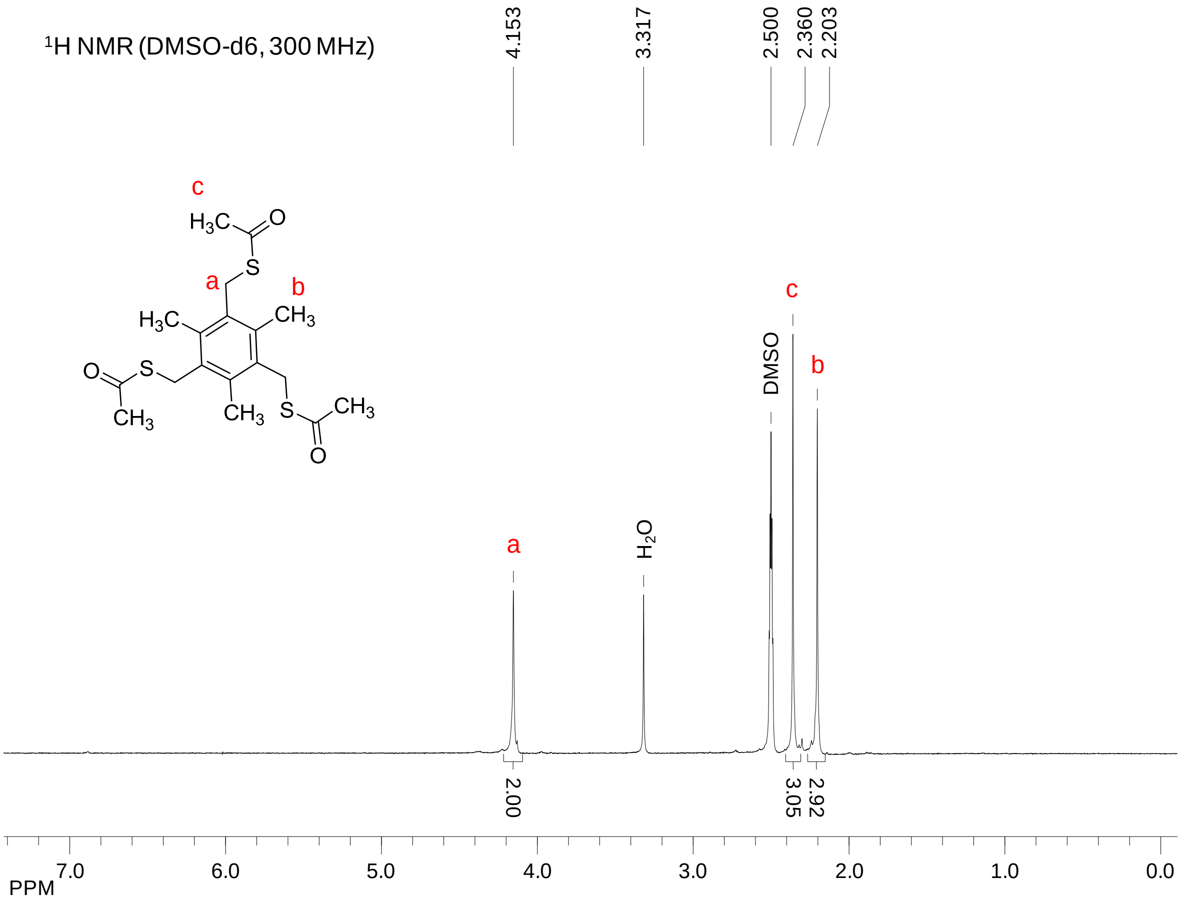

Figure 2.SI4. ^{1}H NMR spectrum of 1,3,5-trimethyl-2,4,6-tris(S-acetylthiomethyl)benzene.

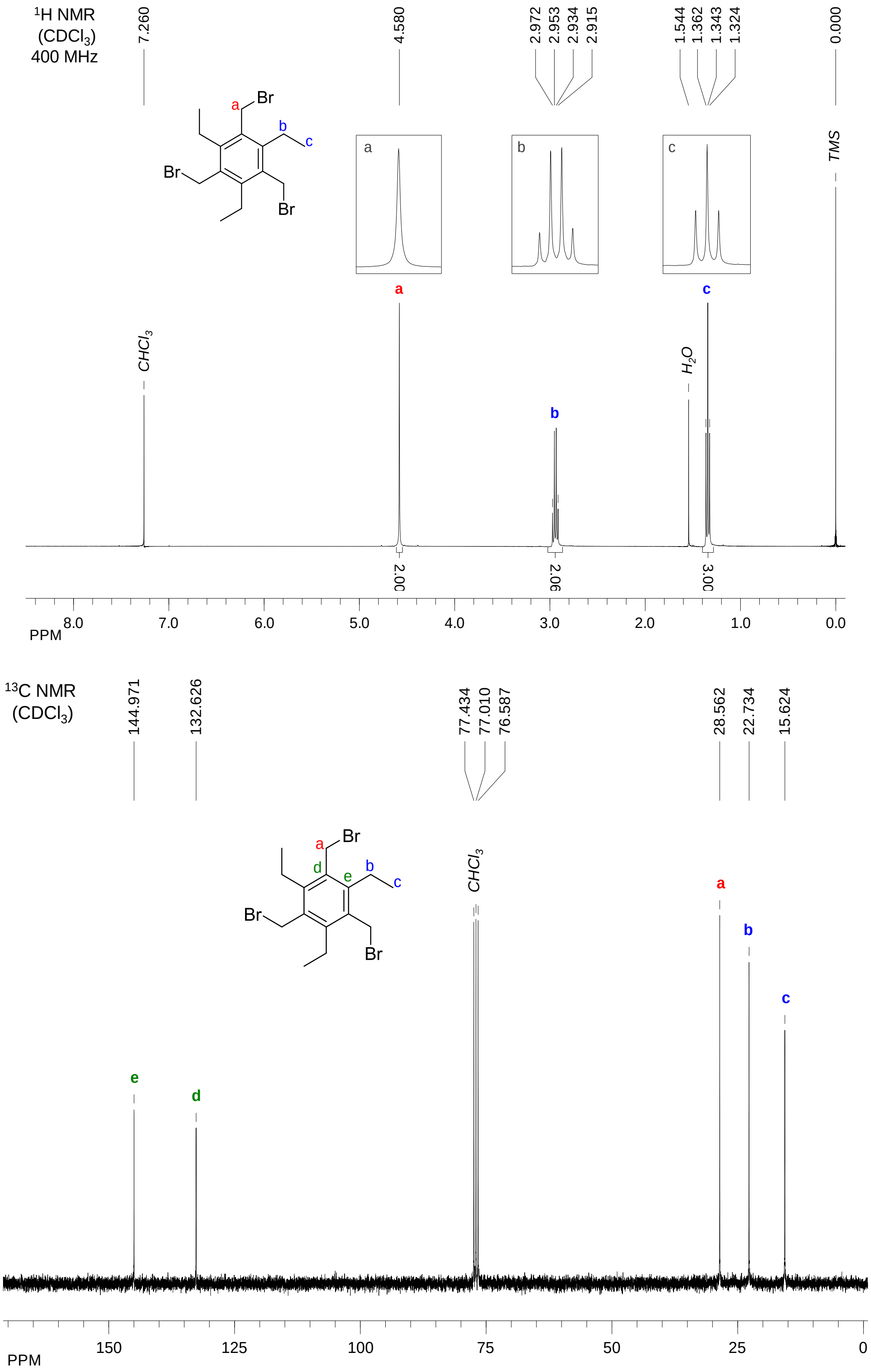

Figure 2.SI5. ^{1}H (top) and ^{13}C (bottom) NMR spectra of 1,3,5-triethyl-2,4,6-tris(bromomethyl)benzene.

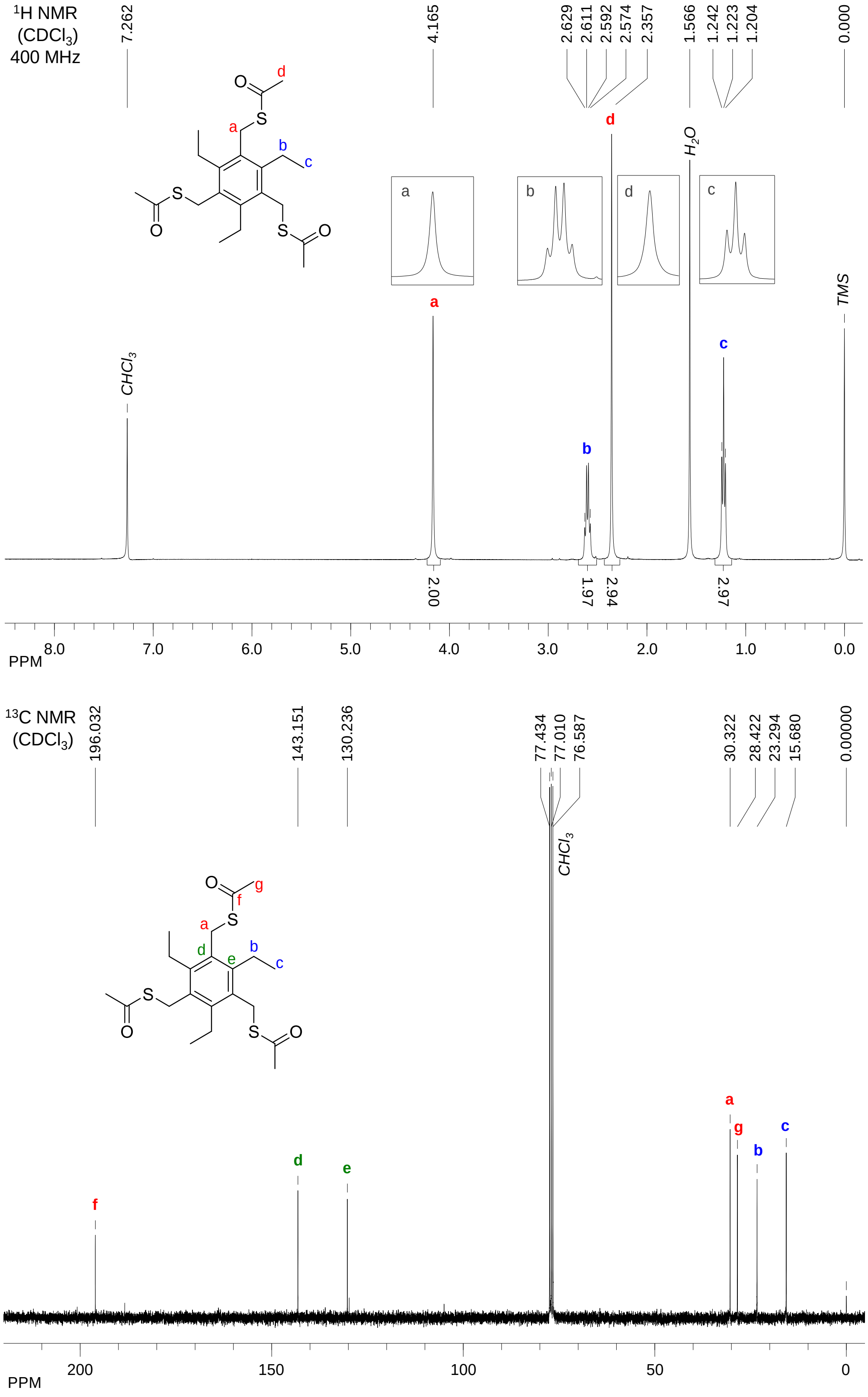

Figure 2.SI6. ^{1}H (top) and ^{13}C (bottom) NMR spectra of 1,3,5-triethyl-2,4,6-tris(S-acetylthiomethyl)benzene.

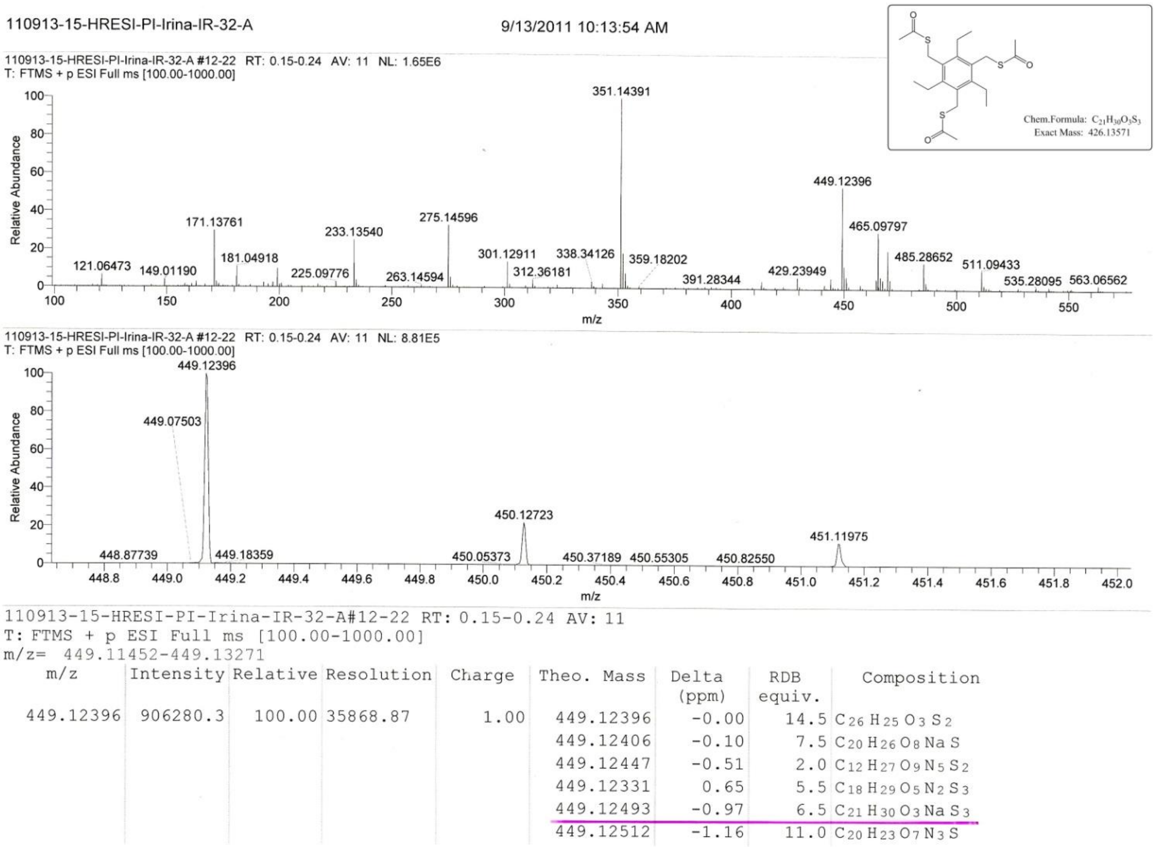

```
110913-15-HRESI-PI-Irina-IR-32-A#12-22 RT: 0.15-0.24 AV: 11
T: FTMS + p ESI Full ms [100.00-1000.00]
m/z= 449.11452-449.13271
   m/z     Intensity Relative Resolution  Charge  Theo. Mass   Delta    RDB      Composition
                                                               (ppm)   equiv.
 449.12396  906280.3    100.00 35868.87     1.00   449.12396   -0.00     14.5 C26 H25 O3 S2
                                                   449.12406   -0.10      7.5 C20 H26 O8 Na S
                                                   449.12447   -0.51      2.0 C12 H27 O9 N5 S2
                                                   449.12331    0.65      5.5 C18 H29 O5 N2 S3
                                                   449.12493   -0.97      6.5 C21 H30 O3 Na S3
                                                   449.12512   -1.16     11.0 C20 H23 O7 N3 S
```

Figure 2.SI7. Mass spectrum of 1,3,5-triethyl-2,4,6-tris(S-acetylthiomethyl)benzene.

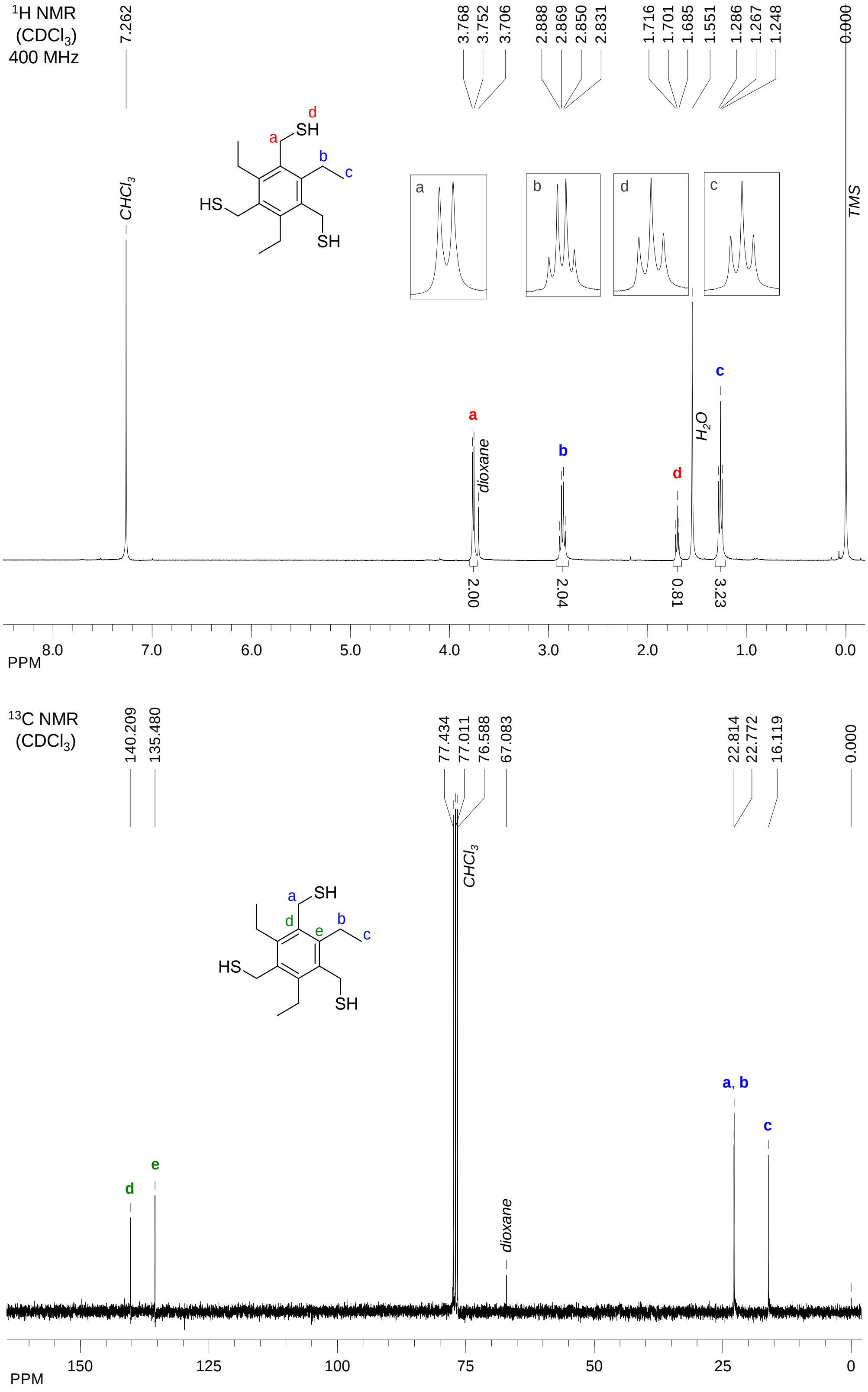

Figure 2.SI8. ^{1}H (top) and ^{13}C (bottom) NMR spectra of 1,3,5-triethyl-2,4,6-tris(hydrothiomethyl)benzene) [Et$_3$-BTMT].

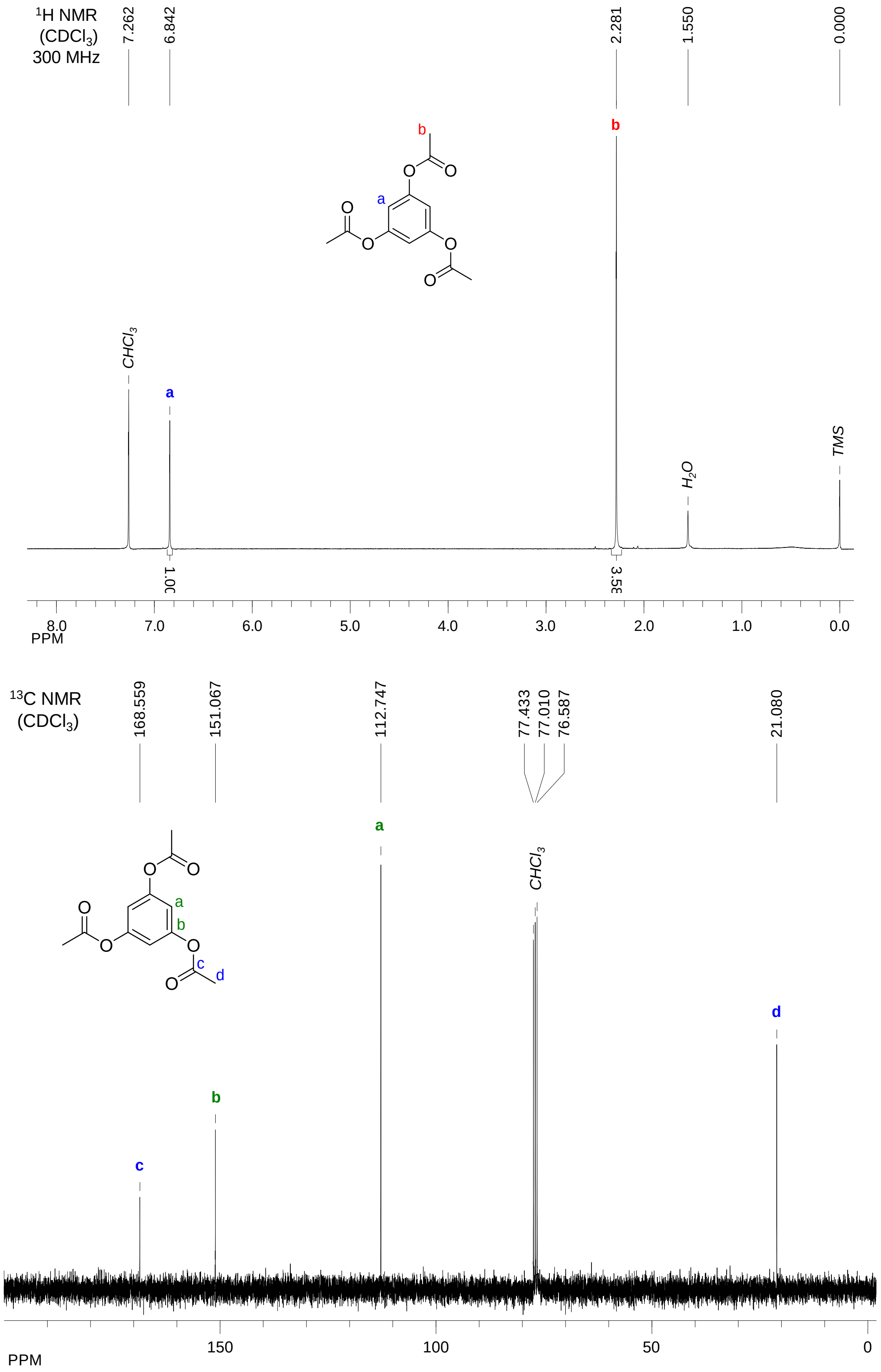

Figure 2.SI9. ^{1}H (top) and ^{13}C (bottom) NMR spectra of 1,3,5-tris(acetyloxy)benzene.

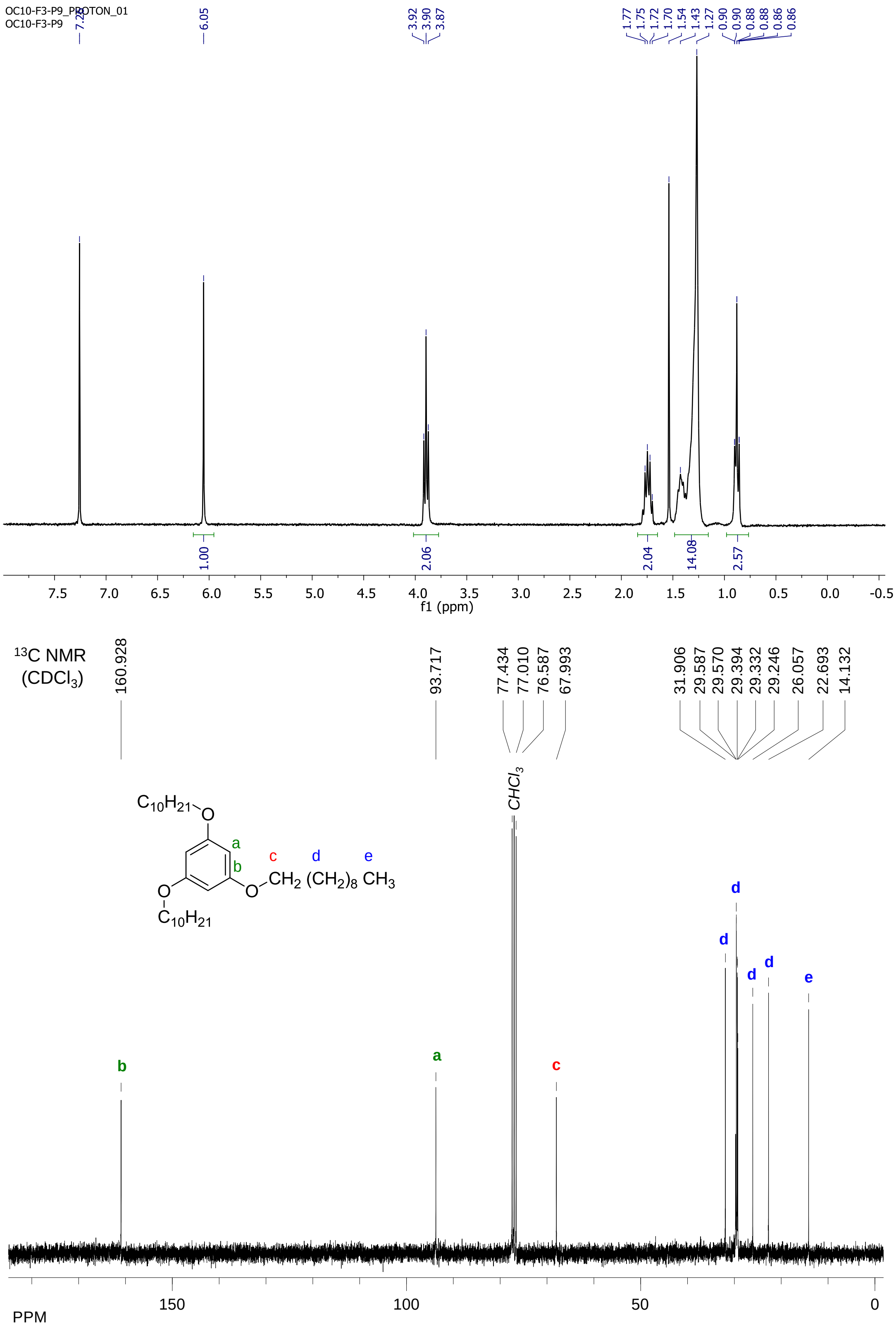

Figure 2.SI10. ^{1}H (top) and ^{13}C (bottom) NMR spectra of 1,3,5-tris(decyloxy)benzene.

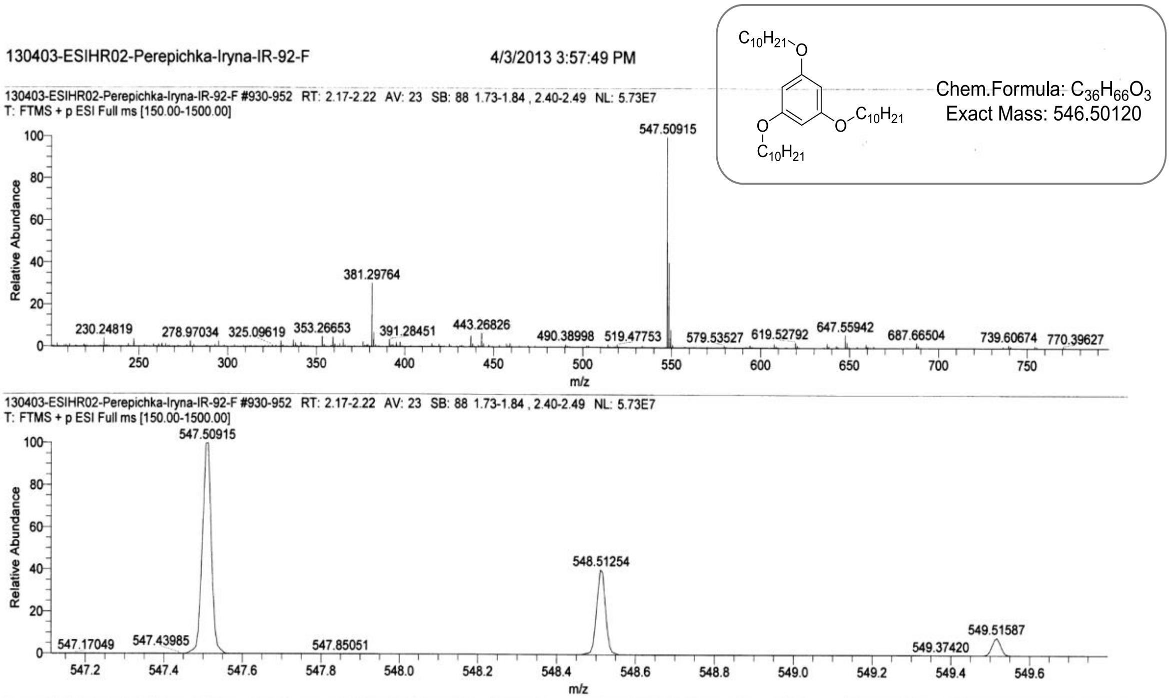

130403-ESIHR02-Perepichka-Iryna-IR-92-F#930-952 RT: 2.17-2.22 AV: 23
SB: 88 1.73-1.84 , 2.40-2.49
T: FTMS + p ESI Full ms [150.00-1500.00]
m/z= 547.46123-547.54844

m/z	Intensity	Relative	Resolution	Charge	Theo. Mass	Delta (ppm)	RDB equiv.	Composition
547.50915	59559136.0	100.00	22331.33	1.00	547.50847	0.68	3.5	$C_{36}H_{67}O_3$
					547.51115	-2.00	8.0	$C_{39}H_{65}N$
					547.50713	2.02	4.0	$C_{34}H_{65}O_2N_3$
					547.50445	4.70	-0.5	$C_{31}H_{67}O_5N_2$
					547.50311	6.04	0.0	$C_{29}H_{65}O_4N_5$

Figure 2.SI11. Mass spectrum of 1,3,5-tris(decyloxy)benzene.

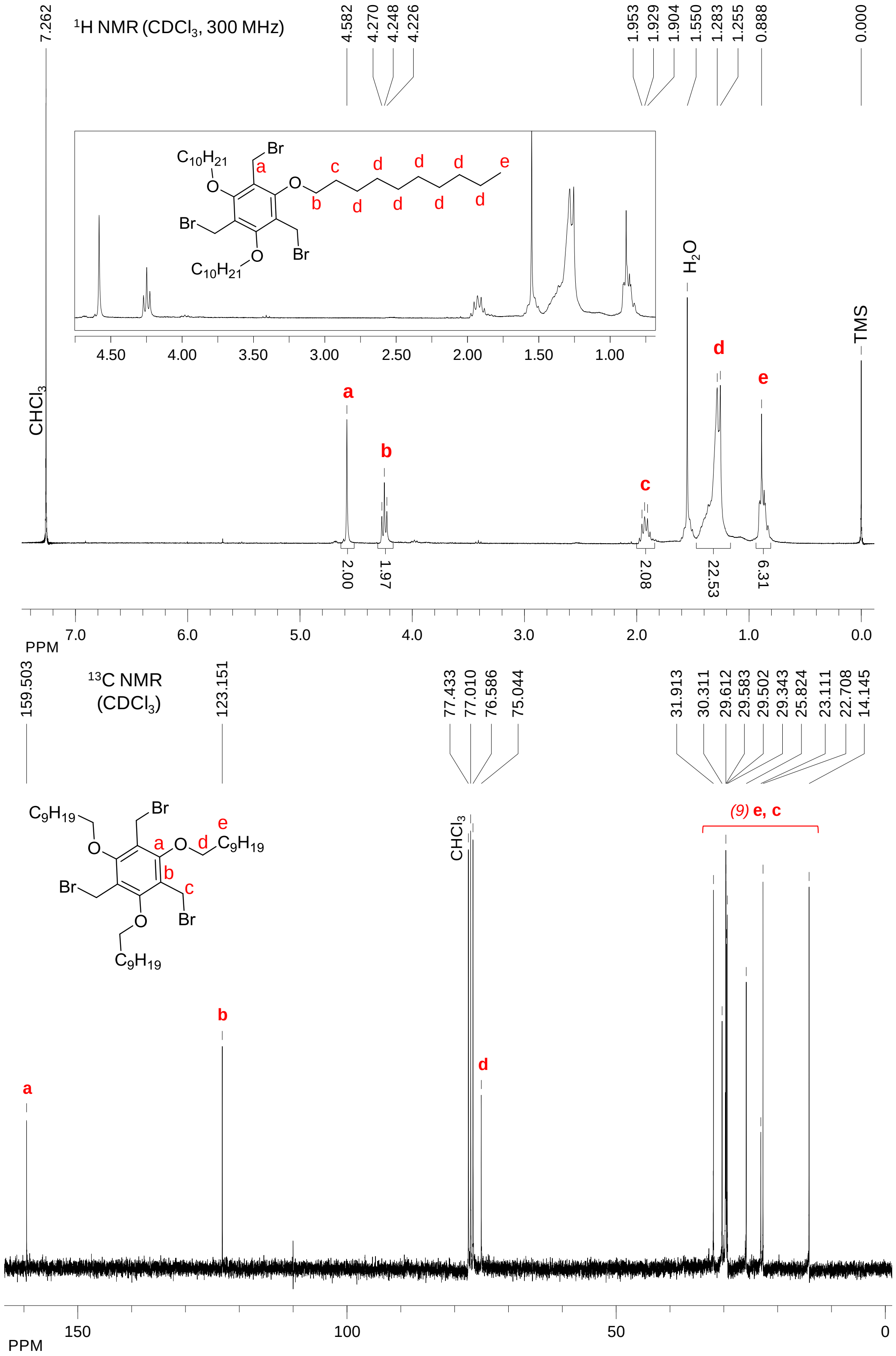

Figure 2.SI12. ^{1}H (top) and ^{13}C (bottom) NMR spectra of 1,3,5-tris(decyloxy)-2,4,6-tris(bromomethyl)benzene.

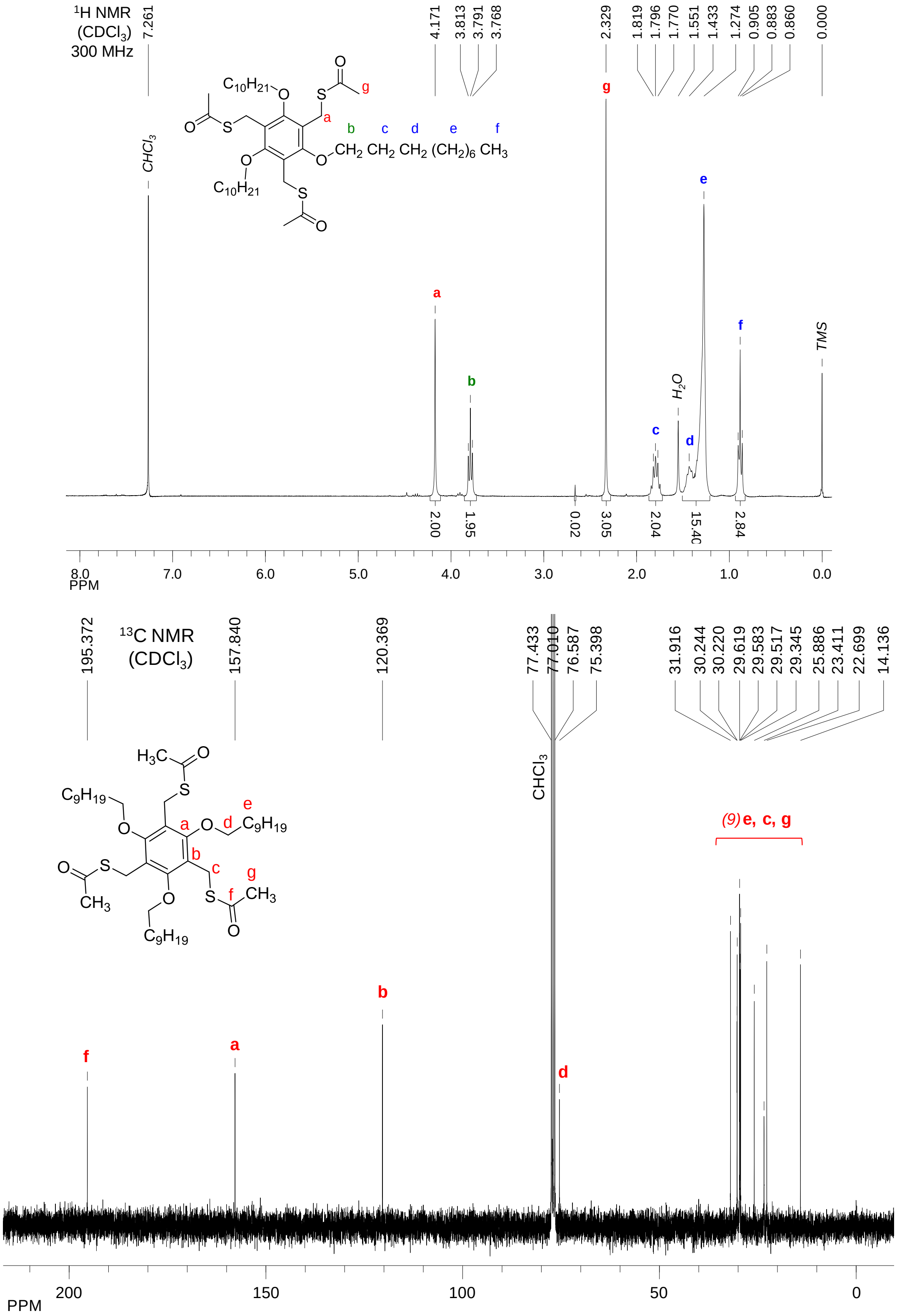

Figure 2.SI13. ^{1}H (top) and ^{13}C (bottom) NMR spectra of 1,3,5-tris(decyloxy)-2,4,6-tris(S-acetylthiomethyl)benzene.

Acquisition Parameter

Source Type	ESI	Ion Polarity	Positive	Set Nebulizer	0.6 Bar
Focus	Active	Set Capillary	4500 V	Set Dry Heater	180 °C
Scan Begin	100 m/z	Set End Plate Offset	-500 V	Set Dry Gas	4.0 l/min
Scan End	1000 m/z	Set Collision Cell RF	600.0 Vpp	Set Divert Valve	Source

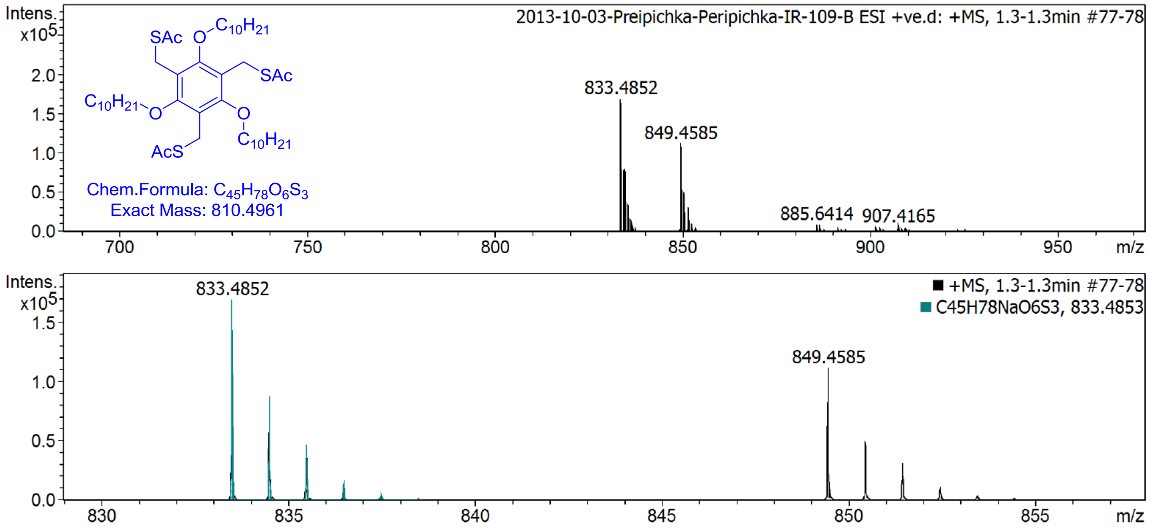

Meas. m/z	#	Ion Formula	m/z	err [ppm]	mSigma	# Sigma	Score	rdb	e¯ Conf	N-Rule
833.4852	1	C45H78NaO6S3	833.4853	-0.1	38.6	1	100.00	6.5	even	ok
	2	C38H78N6NaO4S4	833.4860	0.9	40.7	2	68.24	2.5	even	ok
849.4585	1	C42H70KN10S3	849.4579	0.8	43.9	1	86.13	12.5	even	ok
	2	C45H78KO6S3	849.4592	0.8	44.3	2	100.00	6.5	even	ok

Figure 2.SI14. Mass spectrum of 1,3,5-tris(decyloxy)-2,4,6-tris(S-acetylthiomethyl)benzene.

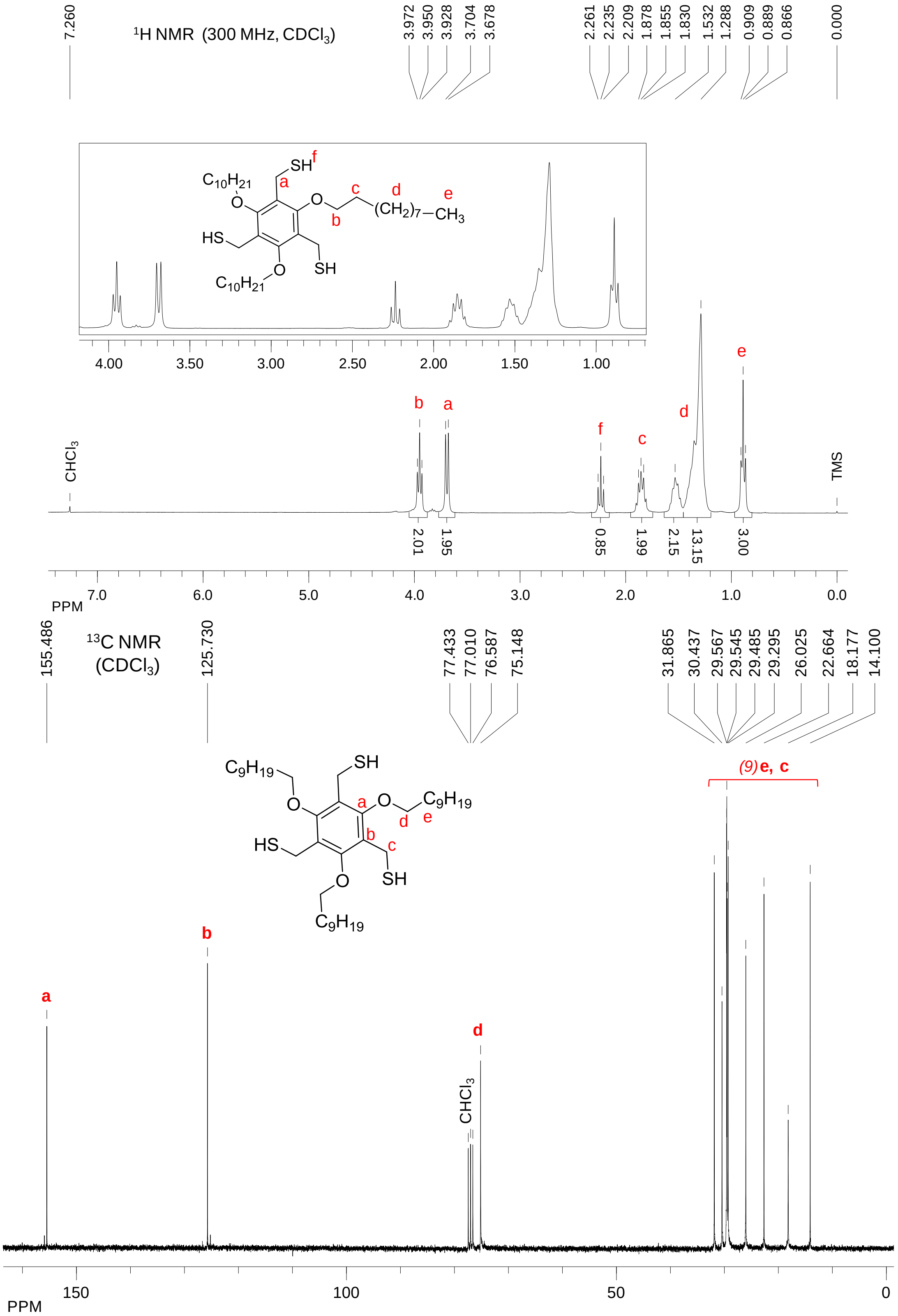

Figure 2.SI15. ^{1}H (top) and ^{13}C (bottom) NMR spectra of 1,3,5-tris(decyloxy)-2,4,6-tris(hydrothiomethyl)benzene [ODe$_3$-BTMT].

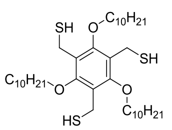

Chem.Formula: $C_{39}H_{72}O_3S_3$
Exact Mass: 684.46436

130516-08HRAPCI-Perepichka-Iryna-IR99 5/16/2013 6:25:16 PM

130516-08HRAPCI-Perepichka-Iryna-IR99 #233-247 RT: 0.69-0.73 AV: 15 NL: 3.18E6
T: FTMS - p APCI corona Full ms [266.70-4000.00]

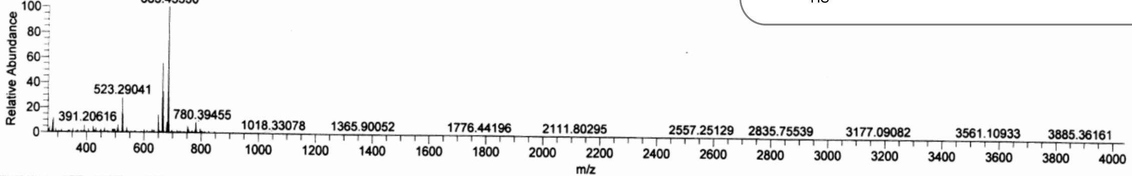

m/z	Intensity	Relative	Resolution	Charge	Theo. Mass	Delta (ppm)	RDB equiv.	Composition
683.45550	3184846.3	100.00	20599.29	1.00	683.45708	-2.32	4.5	$C_{39}H_{71}O_3S_3$
					683.45371	2.61	9.5	$C_{42}H_{67}O_3S_2$

130516-08HRAPCI-Perepichka-Iryna-IR99 #233-247 RT: 0.69-0.73 AV: 15 NL: 1.52E4
T: FTMS - p APCI corona Full ms [266.70-4000.00]

(traces of dimer)

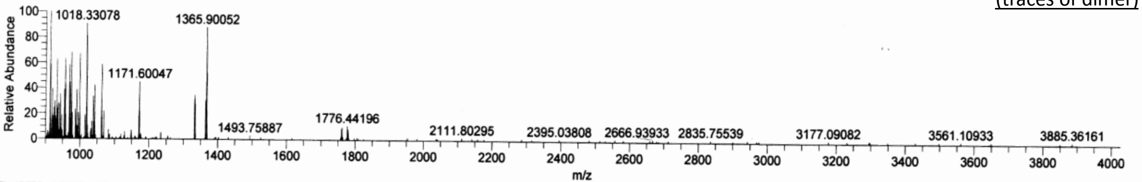

m/z	Intensity	Relative	Resolution	Charge	Theo. Mass	Delta (ppm)	RDB equiv.	Composition
1365.90052	13374.0	100.00	15018.20	1.00	1365.89992	0.44	17.5	$C_{85}H_{137}OS_6$
					1365.89905	1.08	18.5	$C_{84}H_{133}O_6S_4$
					1365.90242	-1.39	13.5	$C_{81}H_{137}O_6S_5$
					1365.90579	-3.86	8.5	$C_{78}H_{141}O_6S_6$

Figure 2.SI16. Mass spectrum of 1,3,5-tris(decyloxy)-2,4,6-tris(hydrothiomethyl)benzene.

Chapter 3: Directing the Assembly of Gold Nanoparticles with Two-Dimensional Molecular Networks

As shown in the Chapter 1, physisorbed molecular networks (SAMNs) with a broad variety of architectures have been developed and explored as molecular templates for various molecular guests. However, their use in templating nanostructured inorganic materials has been rarely explored. In this Chapter, we demonstrate a unique capability of a *p*-dialkoxybenzene derivatives SAMNs in the precise organization of nanoparticles. Interestingly, we found that van der Waals interactions alone, between the alkyl chains of the AuNP and the molecular templates, provide sufficient energy to enable a templated assembly of the AuNP. The assembly efficiency is greatest when these chains are of similar length. These results highlight the potential application of SAMN for directing the assembly of inorganic nanomaterials (metal nanoparticles, quantum dots, etc.)

Adapted with permission from:
M. A. Mezour, I. I. Perepichka, J. Zhu, R. B. Lennox, and D. F. Perepichka. Directing the Assembly of Gold Nanoparticles with Two-Dimensional Molecular Networks. *ACS Nano,* 2014, 8, 2214–2222, **DOI:** 10.1021/nn405357j. Copyright, 2014, the American Chemical Society.

I am the principal author of this article. I collected and analyzed STM data and edited the manuscript. Dr. I. Perepichka synthesized and characterized all molecules used in this study. Dr. Jun Zhu and I synthesized AuNPs.

3.1 Abstract

Lamellar patterns resulting from the adsorption of p-dialkoxybenzene derivatives on HOPG have been investigated as molecular templates for directing the assembly of thiol-capped gold nanoparticles (AuNP). STM characterization at the liquid–solid interface reveals the periodic arrangement of AuNP on top of the self-assembled molecular network (SAMN), leading to the formation of a 2D superlattice spanning hundreds of nanometers can be readily assembled with this sample template process in epitaxial relation to the SAMN. The resulting superlattices are notably non-centrosymmetric and thus differ from the close-packed superlattices formed by spherical nanoparticles during evaporative drying. The templating effect is based on van der Waals interactions of the alkyl chains of the SAMN and AuNP, and the assembly efficiency is greatest when these chains are of similar length.

3.2 Introduction

The precise organization of nano-objects into well-defined patterns at surfaces and interfaces offers a versatile approach to the development of technologically important materials and devices.[1] Among the various existing nanopatterning methods,[2,3] self-assembly has gained increasing attention as a highly accurate, efficient, and low-cost "bottom-up" approach.[4,5,6] Molecular self-assembly in particular provides a flexible and efficient way to create complex structures and patterns with sub-nanometer precision over an extended length scale.[7,8] Using supramolecular chemistry "tools" (*i.e.* hydrogen bonding, van der Waals (vdW) interactions, π–π stacking, metal coordination), self-assembled molecular networks (SAMN) with a broad variety of architectures have been developed and explored as molecular templates. For example, SAMN of porous, lamellar, and polymeric nanostructures have been reported to template various molecular guests, such as fullerenes, [9,10,11] flat polyaromatic hydrocarbons, [12,13,14] and other large macrocyclic molecules.[15,16,17]

Nanoparticles (NP) can exhibit a range of desirable electronic, magnetic and optical properties, and thus their templated assembly is of particular interest.[18,19] Various routes to direct NP self-assembly have been explored, including Langmuir-Blodgett deposition,[20] interfacial assembly,[21] and droplet evaporation.[22] However in most cases, organization of NP is restricted to the formation of close packed lattices as the particle-particle interactions dominate particle-substrate interactions. Structurally complex arrays of NP can be obtained employing macromolecules as templates including DNA,[23] linear polymers,[24] and block copolymers.[25,26] While remarkable and oftentimes useful, these templates are synthetically complex and the resulting NP arrays are limited in size (as in DNA-driven assemblies) or in long-range order (and in block-copolymer driven assemblies). In this context, the high reproducibility, versatility and precision offered by SAMN makes them an intriguing means for templating nanoparticles assemblies with tunable periodicity and long range order.

Little however is known about NP assembly on SAMN. To our knowledge, these studies are limited to (i) AuNP assembly on fatty acids SAMN,[27] (ii) NiNP assembly on long alkane and alkylthiol SAMN on HOPG[28] (both attributed to vdW interactions), and (iii) AuNP assembly on a dialkoxyanthracene derivative SAMN modified with -COOH functional group and ionic interactions with Cu^{2+}.[29] Although the existing reports demonstrate the viability NP adsorption on a SAMN template, little to no long-range order and very limited coverage has been achieved to date.

Herein, we explored the use of simple *p*-dialkoxybenzene derivatives as templates for directing the two-dimensional assembly of thiol-capped AuNP from solution. Using scanning tunneling microscopy (STM) at a solid–liquid interface, we show that AuNP assemble on lamellar SAMN to create long range-order 2D structures whose periodicities and lattice directions are commensurate with those of the SAMN template. The aforementioned assembly is driven by vdW interactions between the alkyl chains on AuNP surface and in SAMN, and the efficiency of assembly is highest when the alkyl chains of each are of similar lengths.

3.3 Results

3.3.1 Self-assembly of molecular network of PhC10

Our design of molecular building blocks was based on the requirements of predictable long-range self-assembly, the possibility for tuning the periodicity of the resulting molecular template, and a provision for specific interactions with nanoparticles. *p*-Dialkoxybenzene derivatives are among the simplest and most synthetically versatile compounds fulfilling these requirements (Scheme 3.1). Two alkoxy chains provide for strong vdW stabilization of the 2D molecular pattern at an HOPG surface.[30,31,32] The periodicity of such a pattern can be controlled by the length of the alkyl groups (decyl *vs*. octadecyl). The aromatic core enables facile introduction of various functionalities, such as thiol sites for potential binding to AuNP (while the use of free dithiols in air is problematic due to oxidative polymerization, acetyl-protected thiols have also been shown to form dense-packed RS-Au monolayers).[33]

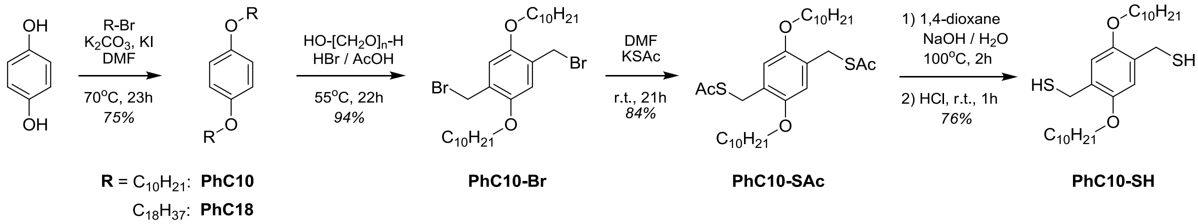

Scheme 3.1. Synthesis of template-forming molecules.

Deposition of PhC10-SAc from a tetradecane solution onto the HOPG surface results in the spontaneous formation of a stable monolayer of PhC10-SAc molecules. Within a few minutes after deposition, scanning tunneling microscopy (STM) imaging at the solid–liquid interface reveals that the surface is covered with a lamellar structure of alternating bright and dark stripes. These correspond to the aromatic core and alkyl chains, respectively, in accord with previous observations in similar SAMN (Fig. 3.1).[30,31,32]

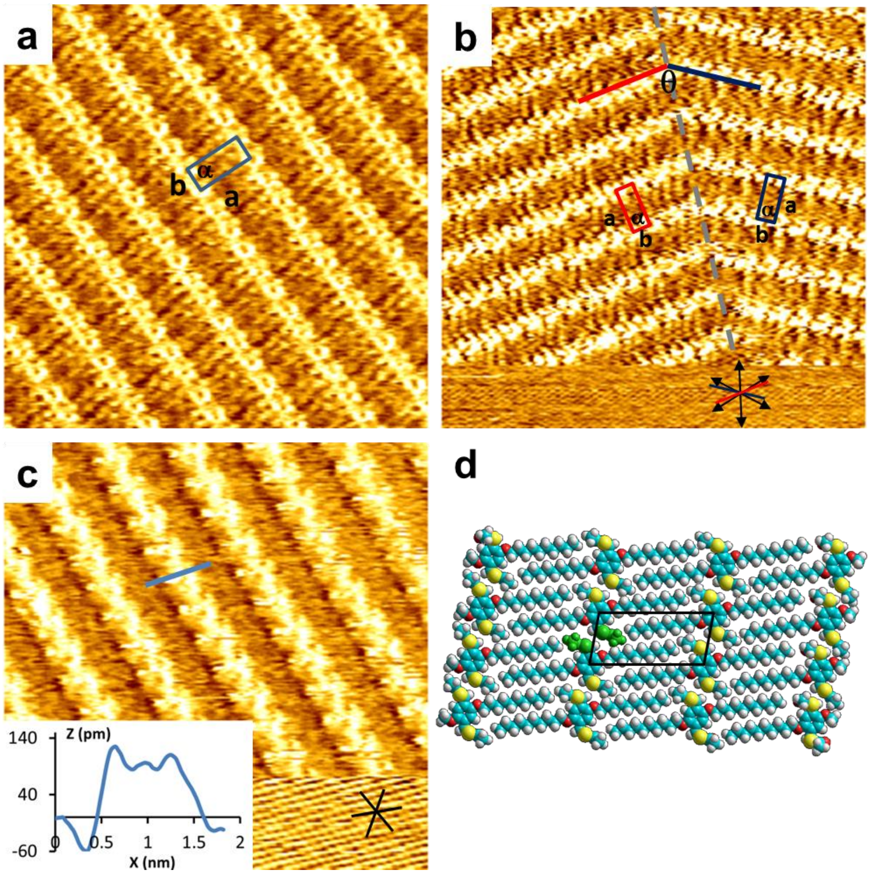

Figure 3.1. (a) Representative STM image (14×14 nm^2; V_b = 700 mV, I_t = 0.2 nA) of PhC10-SAc showing the unit cell: a = 2.1 ± 0.1nm; b = 1.0 ± 0.1nm, α = 86 ± 1°. (b) STM image (21×21 nm^2) showing two domains of PhC10-SAc (V_b = 1373 mV, I_t = 0.2 nA) simultaneously resolved with the underlying HOPG (V_b = 50 mV, I_t = 0.2 nA). The black arrows indicate the principal symmetry axes of graphite <–1100>. The red and blue lines indicate the lamellar directions. (c) Smaller scale STM image (12×12 nm^2; V_b = 700 mV, I_t = 0.09 nA (for SAMN) and V_b = 25 mV, I_t = 0.09 nA for HOPG) reveals out-of-plane substituents in the benzene ring (inset: cross-sectional profile corresponding to blue line). (d) Molecular mechanics model of the 2D packing of PhC10-SAc on a graphene sheet; optimized unit cell parameters: a = 2.1 nm; b = 0.93 nm, α = 81°. The green atom identifies the upright position of the acetylthiol group.

The SAMN contains one molecule per rectangular unit cell (a = 2.1 ± 0.1nm, b = 1.0 ± 0.1 nm, and α = 85 ± 1°, plane group $p2$), with the lamellae width (2.1 ± 0.1 nm) defined by fully extended and interdigitated decyloxy substituents. This packing, frequently reported for the assembly of alkylated aromatic molecules on HOPG,[30,31,32] is driven mainly by the attractive lateral interaction between alkoxy chains and the in-registry adsorption of alkoxy chains along one of the main axes of the HOPG lattice.

Larger scale images reveal that the adjacent domains within the PhC10-SAc monolayer are always oriented at angle of Θ = 148 ± 3° with respect to one another (Fig.3.1b and Fig.3. SI1).

Such an orientational effect is generally associated with co-alignment of alkyl chains of neighboring domains and a chiral unit cell. It can be used to deduce the angle γ between the alkyl chains and the direction of the lamellae (unit cell axis *a*): $\gamma = \Theta/2 = 74 \pm 2°$ (see Fig.3.SI2). Simultaneous imaging of the SAMN and the underlying HOPG lattice (Fig.3.b,c) demonstrates an epitaxial relationship between the two. The lamellae of PhC10-SAc SAMN are oriented with respect to the nearest main crystallographic axis of HOPG, at the angles of 14 ± 2° (Fig. 3.1b). These angles originate from the mentioned above tilt γ of the alkyl chains within the unit cell of the SAMN (74° – 60°).

The aromatic cores in PhC10-SAc SAMN were not atomically resolved. The fuzzy image of the aromatic cores can be attributed to the conformational freedom of the thioacetyl groups, which protrude out of the plane of the monolayer. This behavior was previously reported for molecules bearing out-of-plane substituents.[34] At certain tunneling conditions, it was possible to resolve pairs of bright spots on the sides of bright lamellae (Fig. 3.1c). Their location and spacing (~0.75 nm) are in good agreement with the position of the acetyl groups predicted by the molecular model (Fig. 3.1d). The calculated unit cell parameters (a = 2.1 nm; b = 0.93 nm, α = 81°) are in in agreement with the experimental values.

A similar SAMN could also be prepared with the deprotected dithiols PhC10-SH (Fig. 3.SI3). However, the spacing of molecules along the lamellae is less uniform and the STM imaging is more difficult to reproduce, suggesting that the anticipated oxidative cross-linking of the thiol groups (*via* disulfide bridge) might have occurred.

3.3.2 Assembly of AuNP on PhC10-SAc modified HOPG

In order to explore the potential of SAMN to template the assembly of nanomaterials, gold nanoparticles (AuNP) stabilized by a dodecanethiol ligand shell (C12SH) were synthesized by the Brust-Schiffrin method.[35] The nanoparticles were purified by repeated (10×) washing with ethanol to remove the excess free thiol ligand and the quaternary ammonium salt (used as the phase transfer reagent), dried in vacuum, and re-dissolved in tetradecane for the STM investigation at liquid-solid interface. The template-directed assembly of AuNP was carried out on samples with a typical mean size of 1.9 ± 0.3 nm (Fig. 3.SI4). The size distribution of nanoparticles is known to be critical for their self-assembly into ordered arrays,[36] Indeed, higher polydispersity AuNP samples (3 ± 1 nm) were not successful in the self-assembly experiments described below (Figure 3.SI5).

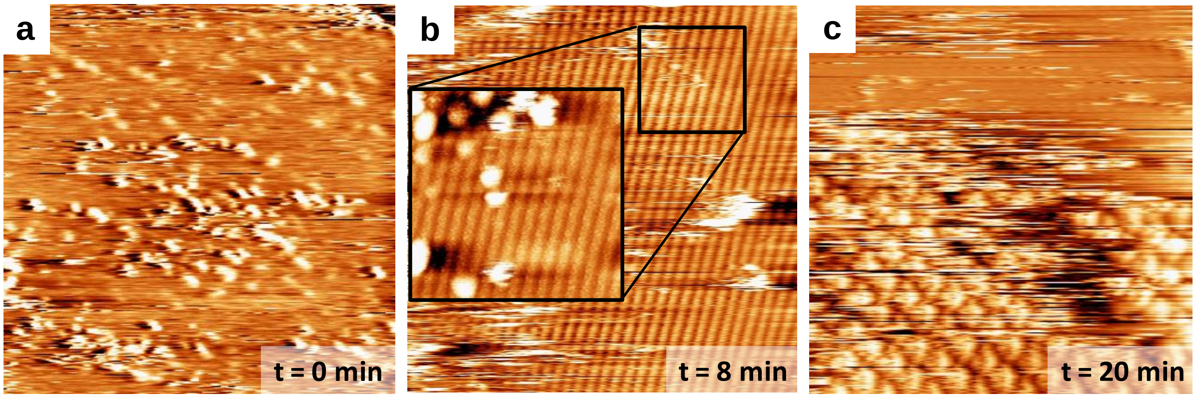

Figure. 3.2. STM images of AuNP-C12SH assembly on top of HOPG before and after adding PhC10-SAc. (a) Representative STM image (130×130 nm^2; V_b = 800 mV, I_t = 0.1 nA) of C12-AuNP at tetradecane/HOPG interface. (b, c) STM images (80×80 nm^2 and 50×50 nm^2; V_b = 800 mV, I_t = 0.08 nA) of AuNP at tetradecane/PhC10-SAc/HOPG interface after 8 and 20 minutes of time scanning respectively.

Adsorption of thiol-capped AuNP on top of bare HOPG using a simple immersion procedure was reported to lead to inhomogeneous, disordered aggregates.[37,38] Our control experiments involving deposition of tetradecane solutions of AuNP onto HOPG did not lead to any self-assembly and only scattered, disordered aggregates of nanoparticles were observed (Fig. 3.2a). However, within a few minutes after adding PhC10-SAc, the characteristic periodic lamellar structure of PhC10-SAc was formed (Fig. 3.2b). This was shortly followed by the appearance of small domains of bright protrusions attributable to ordered AuNP assemblies (Fig. 3.2c). Higher quality STM images were typically obtained by adding AuNP after the complete formation of PhC10-SAc SAMN.

Within *ca*. 20 minutes after placing a drop of saturated tetradecane solution of AuNP onto the PhC10-SAc modified HOPG, large domains of a AuNP superlattice are clearly observed with STM (Fig. 3.3). Individual AuNP are resolved as bright circular protrusions arranged in a 2D periodic lattice with an oblique unit cell with (a = 6.1 ± 0.2 nm, b = 4.1 ± 0.1 nm, α = 67 ± 1°) that contains two nanoparticles. The observed unit cell is distinctly different from the close-packed arrangements of spherical particles which form a hexagonal lattice on surfaces.[39,40] Note that the size uniformity of the assembled AuNP arrays displayed in the STM images (Fig. 3.3 and below) is substantially better than that of the entire AuNP sample as assessed by TEM (3.SI4). This highlights the role of the dynamic equilibrium at the solid liquid interface in selecting the nanoparticles of optimal size during the self-assembly process.

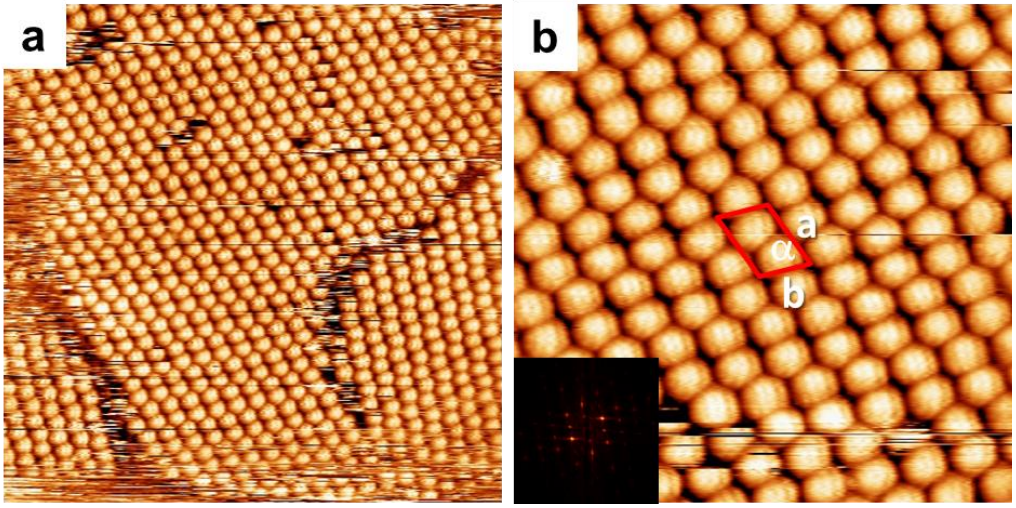

Figure 3.3. (a) Large scale and (b) high resolution STM images (100×100 nm^2 and 40×40 nm^2; V_b = 700 mV, I_t = 0.1 nA) of AuNP-C12SH at tetradecane/PhC10-SAc modified HOPG interface. Unit cell parameters: a = 6.1 ± 0.2 nm, b = 4.1 ± 0.1 nm, α= 67 ± 1°. Inset: FFT of image (b).

Simultaneous imaging of the molecular network and the AuNP superlattice gives additional insight to the templating effect of the SAMN in directing the AuNP assembly (Fig. 3.4a,b). The STM images reveal co-alignment of the close-packed axis of the AuNP domain with the lamellae axis of the PhC10-SAc SAMN (marked by black arrows in Fig. 3.4a), which highlights the template/overlayer relationships between them. This templating effect is also supported by the agreement (within experimental error) of the angles between the domain of the AuNPs assembly (154 ± 4°) and the domains of the PhC10-SAc SAMN (148 ± 2°).

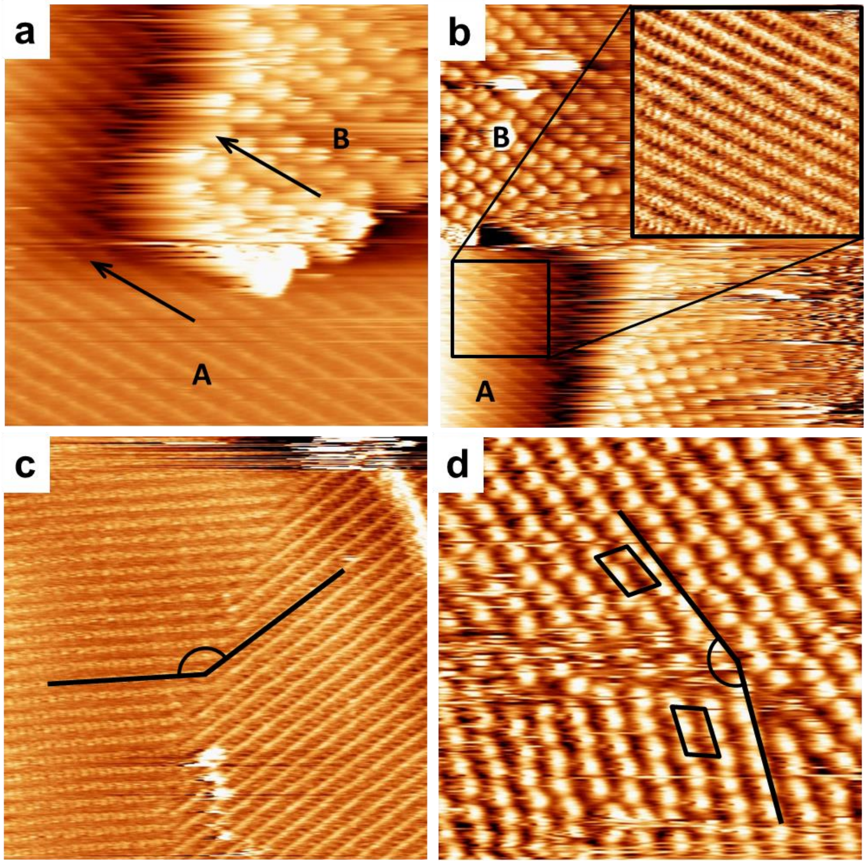

Figure 3.4. (a, b) STM images (a: 60×60 nm^2, V_b = 800 mV, I_t = 0.1 nA; b: 50×50 nm^2 , V_b = 800 mV, I_t = 0.3 nA) showing domains of PhC10-SAc (region A) and AuNP-C12SH (region B) simultaneously. The inset in (b) corresponds to a (29×29 nm^2) zoom of the molecular network of PhC10-SAc. The black arrows in (a) indicate a parallel orientation of the PhC10-SAc lamellae and AuNP rows. (c) STM image (52×52 nm^2; V_b = 800 mV, I_t = 0.1 nA) of PhC10-SAc domains oriented at 148 ± 3°. (d) STM image (80×80 nm^2; V_b = 800 mV, I_t = 0.09 nA) of AuNP domains oriented at 154 ± 4°.

From the above experiments we conclude that the PhC10-SAc molecular adlayer acts as a sticky template and that the structural information of the underlying monolayer is transferred to the AuNP assembly.

3.3.3 Self-assembly of AuNP on non-thiolated PhC10 SAMN

The thiol functionality of Ph10-SAc was initially viewed to be a means to “graft” the AuNP on SAMN. It was therefore important to verify whether the presence of thioacetyl groups in the template structure is essential for directing AuNP self-assembly. For this purpose, we repeated the experiments with 1,4-di(decyloxy)benzene (PhC10) which produces similar SAMN but lacks thiol substituents.

Deposition of a tetradecane solution of PhC10 onto HOPG (Fig. 3.5a) leads to a slightly narrower lamellar structure compared to that of PhC10-SAc (Fig. 3.5c), consistent with the absence of AcS substituents. The unit cell parameters are: a = 1.8 ± 0.1 nm, b = 1.00 ± 0.1 nm, and α = 80 ± 1°. Addition of a tetradecane solution of AuNP on top of this SAMN creates well-ordered domains of AuNP spanning many hundreds of nanometers (Fig. 3.SI 7). High resolution STM images (Fig. 3.5d) allow for identification of rows of the aligned AuNP and measurement of the unit cell (a = 6.1 ± 0.2 nm, b = 3.9 ± 0.1 nm, α = 73 ± 2°). This unit cell is only slightly smaller than that obtained on PhC10-SAc template; the difference is at the edge of the uncertainty range of the measurements (see SI) but is expected based on periodicities of the two SAMNs. On the other hand, the fact that similar AuNP superlattices were obtained on both PhC10-SAc and PhC10 templates strongly suggests that the self-assembly of AuNP is driven by vdW interactions between the alkyl chains of the AuNP and the molecular template.

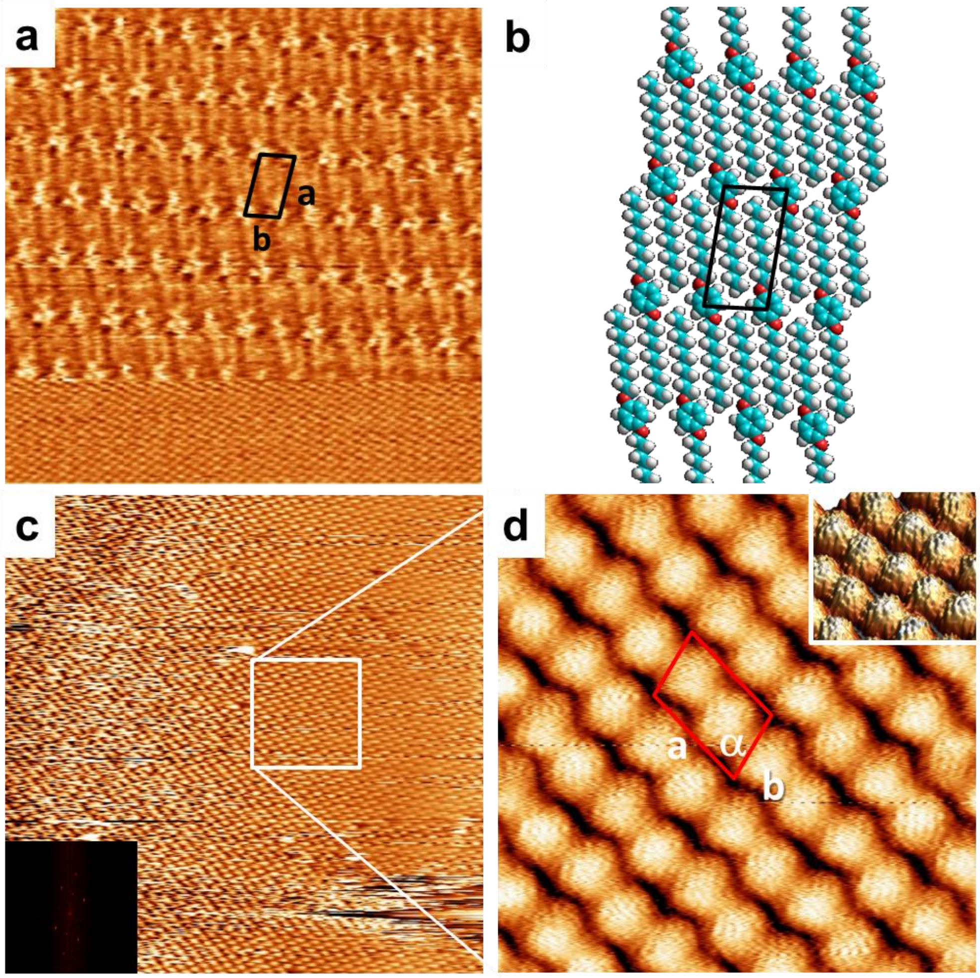

Figure 3.5. (a) Typical high-resolution STM image (13.7×13.7 nm^2) simultaneously showing the SAMN of PhC10 molecules (V_b = 500 mV, I_t = 0.2 nA) and the underneath HOPG lattice (V_b = 50 mV, I_t = 0.2 nA). Unit cell parameters: a = 1.8 ± 0.1 nm, b = 1.00 ± 0.1 nm, α = 80 ± 1°. (b) Molecular mechanics model of the 2D packing of PhC10 on a graphene sheet, optimized unit cell parameters: a = 1.78 nm; b = 0.91 nm, α = 83°. (c) Large scale STM image (72.5×72.5 nm^2, V_b = 500 mV, I_t = 0.1 nA) of AuNP at tetradecane/PhC10 modified HOPG interface. Inset: corresponding FFT image. (d) High resolution STM image (25×25 nm^2, V_b = 500 mV, I_t = 0.1 nA) showing rows of well aligned C12-AuNP. Unit cell parameters: a = 6.1 ± 0.2 nm, b = 3.9 ± 0.1 nm, α = 73 ± 2°. Inset: 3D image of AuNP assembly showing the protrusions on AuNP.

It is interesting to note that close packed assemblies of AuNP on the SAMN-modified surface enables facile STM resolution of fine features on the AuNP surface (Fig. 3.5d). These dots form ripples that are separated by ~0.6 nm; a value close to the expected distance between the terminal CH_3 groups of the ligands (see Fig. 3.SI9 for other scanning directions and speed). Similar features were observed by Stellacci and coworkers for thiol-protected AuNP immobilized on non-patterned surfaces,[41] but only when two dissimilar, presumably phase-separated, thiols were used (octanethiol-protected AuNP also showed dots separated by ~0.6 nm,[42] but no ripples). The nature of these ripples has been debated in the literature[43,44] and, while it is outside the scope of this paper, we hope that our observations may shed further light on this question.

3.3.4 Self-assembly of AuNP on PhC18 SAMN

The length of the alkoxy substituents in the molecular template was extended in order to explore the possible control over the spacing of AuNP. Similar to PhC10 and PhC10-SAc, 1,4-bis(octadecyloxy)benzene (PhC18) self-assembles to form a lamellar pattern ($a = 2.7 \pm 0.1$ nm, $b = 1.0 \pm 0.1$nm, $\alpha = 85 \pm 2°$, Fig. 3.6). The lamella width (2.7 ± 0.1 nm) is larger than that of PhC10 SAMN (1.75 nm), but is still smaller than the diameter of the coated AuNP (3.2 to 4 nm). Depositing a drop of a tetradecane AuNP solution onto the PhC18 modified HOPG results in the adsorption of only a small number of AuNP on top of the molecular template. At this low density of adsorption, the STM image (Fig. 3.6d) clearly shows that AuNP are preferentially centered on top of the aromatic units (bright features of the lamellae) of the SAMN.

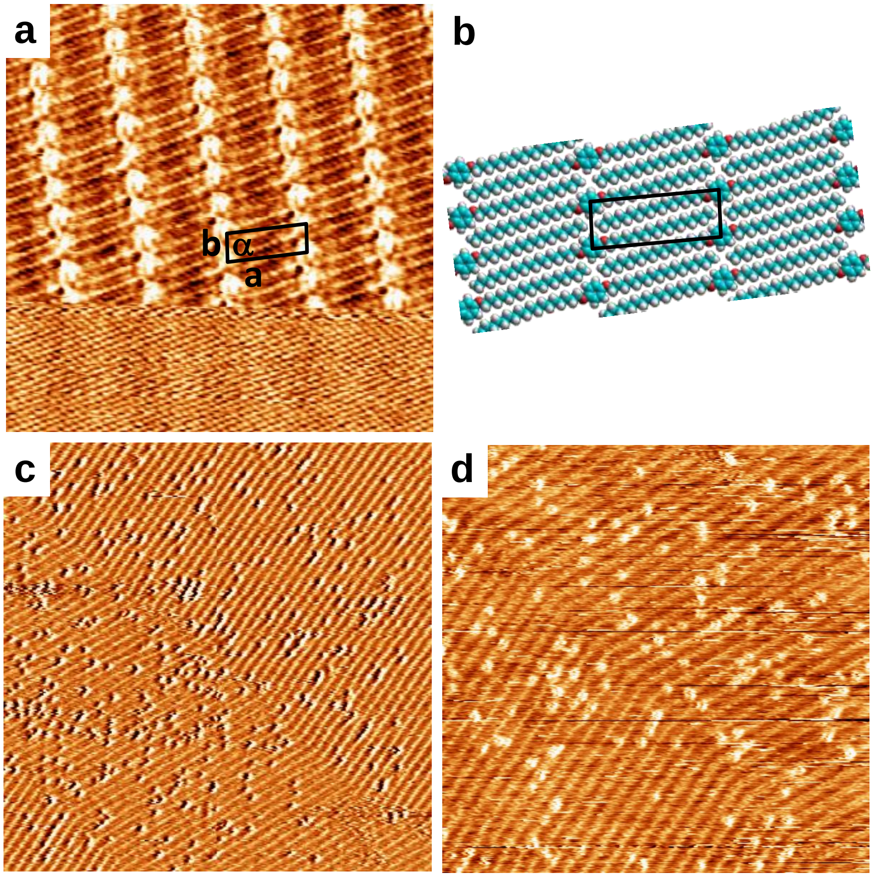

Figure 3.6. (a) High-resolution STM image (14.5×14.5 nm^2) showing the SAMN of PhC18 molecules (V_b = 700 mV, I_t = 0.25 nA) and the underneath HOPG lattice (V_b = 50 mV, I_t = 0.25 nA) simultaneously. Unit cell parameters: a = 2.7 ± 0.1 nm; b = 1.0 ± 0.1nm, α = 85 ± 2°. (b) Molecular mechanics model for the 2D packing of PhC18 on a graphene sheet, optimized unit cell parameters: a = 2.72 nm; b = 0.93 nm, α = 87°. (c, d) STM images (c: 200×200 nm^2, V_b = 900 mV, I_t = 0.1 nA; d: 93.5×93.5 nm^2, V_b = 1000 mV, I_t = 0.5 nA) of AuNP at tetradecane/PhC10-SAc modified HOPG interface.

The efficiency of AuNP templating by PhC18 was very low compared to PhC10 and PhC10-SAc SAMN. Such a difference can be attributed to the mismatch between the length of AuNP ligand (dodecylthiol) and the octadecyloxy chains of PhC18, which limits the vdW interactions between the particles transversal to the lamellae direction. Using AuNP with the longer octadecanethiol (C18SH) ligand shell on the same PhC18 SAMN significantly increases the density of nanoparticle assemblies, albeit with limited long-range order (SI13).

3.4 Discussion

It is important to note that the self-assembly at the solid-liquid interface described here is very different from evaporation-driven crystallization reported for various (metal, semiconductor, polymer) nanoparticles.[45,46] The latter is defined almost exclusively by maximizing the interparticle interactions and thus produces close-packed lattices. In contrast, the self-assembly at the liquid-solid interface is dominated by particle-surface interactions; it is generally self-limiting to a single monolayer and can produce other (non-close-packed) lattices. STM characterization under such conditions allows one to follow the dynamics of the AuNP assembly (Fig. 3.2 and 3.SI8) and to achieve high resolution on the underlying HOPG substrate, molecular templates, and AuNP superlattice.

The defining role of the molecular templates (SAMN) is obvious from the fact that no ordered structures are obtained on HOPG in their absence. As seen from the low-coverage images (Fig. 3.6), the AuNP are centered preferentially on top of the aromatic rows of the SAMN, allowing AuNP alkyl chains to interact with the aliphatic lamellae, thereby maximizing vdW interactions. As a result, AuNP assemble along the lamellae of the SAMN. When the periodicity of the SAMN matches the radius of the AuNP (including the ligands), an additional interaction arises from the vdW contacts of neighboring AuNP rows. This significantly increases the efficiency of self-assembly and large AuNP superlattices are formed on the surface, in an epitaxial relationship with the underlying template (eg, Fig. 3.5 and 3.SI7).

The presence of strongly binding functional groups in the SAMN (such as thiols) is not necessary for effective immobilization of AuNP and can actually be counter-productive in achieving highly-ordered self-assembled structures. Indeed, acetylthiol-containing PhC10-SAc SAMN yield a poorer quality of AuNP superlattices (smaller domains, more defects) compared to simple PhC10 SAMN.

Fig. 3.7 shows a schematic illustration of AuNP assembly on top of SAMN, reflecting these observations. The center-to-center interparticle spacing ($D\mathrm{nn}$) between the AuNP along the SAMN lamellae ($D\mathrm{nn}^{\parallel} = 3.1 \pm 0.1$ nm for PhC10-SAc and PhC10) is consistently shorter than that across the SAMN lamellae ($D\mathrm{nn}^{\perp} = 4.1 \pm 0.1$ nm for PhC10-SAc and 3.9 ± 0.1 nm for PhC10). Giving that the metal core diameter of AuNP is 1.9 ± 0.3 nm (measured by TEM, Fig. 3.SI4), this yields a separation between the metal cores of $D\mathrm{cc}^{\parallel} \sim 1.2$ nm and $D\mathrm{cc}^{\perp} \sim 2$ nm, along and across the PhC10 lamellae, respectively. The derived thickness of the AuNP ligand shell along the lamellae ($1/2\ D\mathrm{cc}^{\parallel} \sim 0.6$ nm) is significantly smaller than the length of a fully extended dodecanthiol (L~1.6 nm).[47] The thiol ligands must adopt some *gauche* conformations along the chain and bundle to enable such separation between the particles. This is expected considering the curved surface of

AuNP and is in good agreement with the shell thickness of 0.58 nm obtained from a molecular dynamic simulation of the monolayer of dodecanthiol-protected AuNP on SAMN-free HOPG.[48] Across the lamellae the apparent thickness of the shell (1/2 $D\text{cc}^{\perp}$ ~1.0 nm) is nearly twice as large but still is smaller than the length of the fully extended dodecanethiol ligand. This could be explained by a partial interdigitation of the fully extended ligand chains. The difference between the AuNP interactions in both directions is likely dictated by the asymmetry of the underlying SAMN template. Along the lamellae, the AuNP adopt a close-packed arrangement so as to maximize the interparticle vdW interactions. Transverse to the lamellae, the thiol ligands are most likely to be fully extended, which maximizes the vdW interactions with the alkyl chains of the template. The periodicity of the SAMN template controls the nanoparticle separation in the transverse direction ($D\text{cc}^{\perp}$). When $D\text{cc}^{\perp}$ matches the thickness of two (partially interpenetrated) AuNP ligand shells, the interparticle vdW interactions are maximized and stable well-ordered assemblies are obtained. Otherwise, more fluid, less dense and thus less ordered assemblies can result. The former is manifested in C12SH-AuNP on PhC10 templates (Fig. 3.4), while the latter is observed for C12SH-AuNP on PhC18 (Fig. 3.5) and C8SH-AuNP on PhC10 templates (SI11).

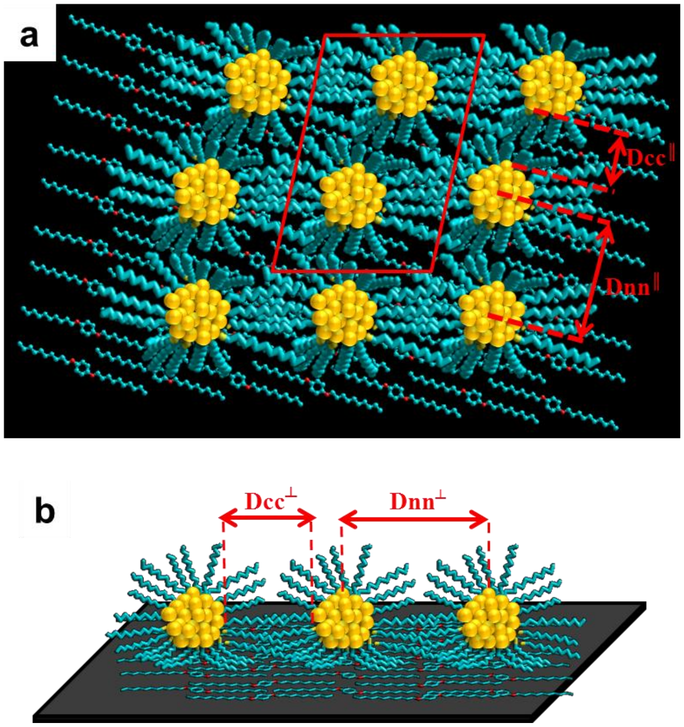

Figure 3.7. Schematic illustration of AuNP assembly on PhC10 modified HOPG. (a) and (b)Top and side view respectively. Dnn is the interparticle distance (centre to centre distance). Dcc is the spacing between two adjacent nanoclusters which is equal to twice the thickness of the AuNP ligand.

3.5 Conclusions

In summary, we have demonstrated that periodic two-dimensional AuNP assemblies can be formed at the liquid–solid interface by prepatterning the surface (HOPG) with a self-assembled molecular network. The lamellar molecular adlayer acts as a sticky template enabling the adsorption of AuNP. Notably, the structural information of the monolayer is transferred to the AuNP assembly, which leads to superlattices with non-centrosymmetric unit cell. This templating effect is primarily driven by van der Waals interactions between the alkyl chains of NP ligands and those of the underlying molecular template. When the length of the alkoxy chains of the molecular template matches that of the AuNP ligand, the enhanced inter-particle interactions leads to ordered assemblies that span hundreds of nanometers. When these conditions are not met, periodic assemblies of AuNP are not observed, despite the same chemical nature of the AuNP/SAMN interactions. Achieving the efficient 2D-templating effect at a solid-liquid interface thus creates a rational means to direct the self-organization of a variety of nanomaterials (metal nanoparticles, quantum dots, etc) under dynamic equilibrium conditions. The resulting immobilization of AuNP in the ordered monolayer on HOPG enables high-resolution STM imaging of the internal structure of AuNP in the liquid environment.

3.6 Experimental section

Synthesis.

1,4-di(decyloxy)benzene **[PhC10]**. A 1 L three-neck round-bottom flask was equipped with a stirring bar, a thermometer, a cooler condenser, a rubber septum; and was flushed with Ar. 1-Bromodecane (72 mL, 0.35 mol), potassium iodide (5.86 g, 35.3 mmol) and potassium carbonate (50.9 g, 0.37 mol) were added to the solution of hydroquinone (15.1 g, 137 mmol) in Ar-purged DMF (220 mL). The reaction mixture was heated to 70°C for 24 h under an argon atmosphere. After cooling to room temperature (results in the formation of a precipitate), distilled H_2O (500 mL) was added to the reaction mixture, and the solid material was isolated by filtration. Recrystallization from 2-propanol (800 mL) afforded colourless flakes of PhC10 (40.0 g, 75%). m.p. = 68–69°C. ^{1}H NMR ($CDCl_3$): $\delta = 6.82$ (4H, s), 3.89 (4H, t, $J = 6.5$ Hz), 1.75 (4H, p, $J = 7$

Hz), 1.49–1.38 (4H, m), 1.38–1.21 (24H, m), 0.88 (6H, t, *J* = 7 Hz). ^{13}C NMR ($CDCl_3$): δ = 153.16, 115.35, 68.64, 31.90, 29.60, 29.57, 29.43, 29.41, 29.33, 26.07, 22.69, 14.14.

1,4-di(decyloxy)-2,5-bis(bromomethyl)benzene **[PhC10-Br]**. In a 250 mL one-neck round-bottom flask equipped with a stirring bar, 1,4-di(decyloxy)benzene (4.30 g, 11.0 mmol) and paraformaldehyde (1.008 g, 33.6 mmol) were suspended in glacial acetic acid (40 mL), followed by addition of 33% wt hydrogen bromide solution in acetic acid (10 mL, 55 mmol). The flask was equipped with a cooler condenser, and the reaction mixture was heated to 55°C for 22 h under vigorous stirring. [*Note: temperature rise above 70°C results in formation of by-products.*] The reaction mixture was cooled to room temperature and poured into distilled H_2O. The solid material was collected by filtration, washed with H_2O to neutral pH, and dried under reduced pressure to afford PhC10-Br as white powder (5.96 g, 94%). m.p.= 89–90°C. ^{1}H NMR ($CDCl_3$): δ = 6.85 (2H, s), 4.53 (4H, s), 3.98 (4H, t, *J* = 6.5 Hz), 1.81 (4H, p, *J* = 7 Hz), 1.56–1.43 (4H, m), 1.43–1,21 (24H, m), 0.88 (6H, t, *J* = 7 Hz). ^{13}C NMR ($CDCl_3$): δ = 150.65, 127.50, 114.63, 69.00, 31.91, 29.60, 29.57, 29.37, 29.34, 28.78, 26.09, 22.69, 14.13.

1,4-di(decyloxy)-2,5-bis(S-acetylthiomethyl)benzene **[PhC10-SAc]**. In a 250 mL one-neck round-bottom flask equipped with a stirring bar, potassium thioacetate (2.99 g, 26.1 mmol) was dissolved in DMF (70 mL), and 1,4-di(decyloxy)-2,5-bis(bromomethyl)benzene (3.01 g, 5.22 mmol) was added to this solution. The reaction mixture was stirred at room temperature under nitrogen for 21 h. The suspension was poured into distilled H_2O, and the crude material was collected by filtration. Recrystallization from ethyl acetate (40 mL) afforded PhC10-SAc as a white cotton-like solid (2.50 g, 84%). m.p.= 78–79°C. ^{1}H NMR ($CDCl_3$): δ = 6.83 (2H, s), 4.08 (4H, s), 3.92 (4H, t, *J* = 6.5 Hz), 2.31 (6H, s), 1.75 (4H, p, *J* = 7 Hz), 1.51–1.39 (4H, m), 1.39–1.22 (24H, m), 0.88 (6H, t, *J* = 7 Hz). ^{13}C NMR ($CDCl_3$): δ = 195.90, 150.36, 125.89, 114.00, 68.73, 31.92, 30.37, 29.62, 29.58, 29.39, 29.36, 28.55, 26.11, 22.70, 14.14. *m/z* (ESI^{+} HRMS): calc. for $C_{32}H_{54}O_4S_2Na$: 589.3356, found 589.3350 $(M+Na)^{+}$.

1,4-bis(decyloxy)-2,5-bis(hydrothiomethyl)benzene **[PhC10-SH].** 1,4-Dioxane and distilled H_2O were degassed with bubbling nitrogen before use. In a 100 mL two-neck round-bottom flask equipped with a stirring bar, 1,4-bis(decyloxy)-2,5-bis(S-acetylthiomethyl)benzene 7 (0.31 g, 0.54 mmol) was dissolved in 1,4-dioxane (22 mL). The flask was equipped with a cooler condenser and a rubber septa, and the system was flushed with nitrogen. 3.1 M aqueous solution of sodium hydroxide (0.7 mL, 2 mmol) was added dropwise to the above solution, and the reaction mixture was refluxed for 2 h. After cooling to room temperature, 2.0 M HCl (1.3 mL, 2.6 mmol) was added dropwise, and the mixture was stirred at r.t. for 1 h under N_2. H_2O was added, and the product was extracted into ethyl ether. Organic layer was washed with H_2O for a few times and dried over $MgSO_4$ followed by filtration and solvent evaporation to give PhC10-SH as white powder (0.20 g, 76%). δ = 6.78 (2H, s), 3.96 (4H, t, *J* = 6.5 Hz), 3.73 (4H, d, *J* = 7.8 Hz), 1.96 (2H, t, *J* = 8.1 Hz), 1.80 (4H, p, *J* = 7 Hz), 1.53–1.41 (4H, m), 1.41–1.22 (24H, m), 0.88 (6H, t, *J* = 6.5 Hz). *m/z* (ESI$^-$ HRMS): calc. for $C_{28}H_{49}O_2S_2$: 481.3180, found 481.3183 $(M–H)^-$. [*Note: The product contains ca. 3% (by ^{1}H NMR) of disulfide dimer, that is also visible as q weak signal in HRMS spectra: m/z (ESI$^-$ HRMS): calc. for $C_{56}H_{98}O_4S_4$: 961.6270, found 961.6298 $(M–H)^-$*]

1,4-di(octadecyloxy)benzene **[PhC18]** was synthesized following the similar procedure as described for synthesis of PhC10. A 1 L two-neck round-bottom flask was equipped with a stirring bar, a condenser, a rubber septum; and was flushed with N_2. Hydroquinone (6.66 g, 60.5 mmol), 1-bromooctadecane (48.60 g, 145.7 mmol), potassium carbonate (21.30 g 154.1 mmol), potassium iodide (2.17 g, 13.1 mmol) and Ar-purged DMF (250 mL) were mixed together and stirred at 55°C for 3 days under a nitrogen atmosphere. After cooling to room temperature, distilled H_2O (600 mL) was added to the reaction mixture, and solid material was isolated by filtration. To remove excess of 1-bromooctadecane, the crude product was suspended in hot acetone and filtered. Recrystallization from 2-propanol (ca. 20 mL/g) afforded PhC18 as light gray powder (26.80 g, 72%). m.p.= 88–89°C. ^{1}H NMR ($CDCl_3$): δ = 6.82 (4H, s), 3.89 (4H, t, *J* = 6.5 Hz), 1.75 (4H, p, *J* = 7 Hz), 1.50–1.20 (30H, m), 0.88 (6H, t, *J* = 7 Hz). ^{13}C NMR ($CDCl_3$): δ = 153.17, 115.36, 68.65, 31.94, 29.71, 29.67, 29.62, 29.60, 29.44, 29.41, 29.38, 26.07, 22.71, 14.14.

Dodecanethiol protected gold nanoparticles **(C12-AuNP)** were synthesized by the Brust-Schiffrin method described elsewhere.[35] Hydrogen tetrachloroaurate (III) trihydrate (0.050 mg, 0.13 mmol) was dissolved in distilled water (8 mL) and then mixed with tetraoctylammonium bromide (0.382 g, 0.70 mmol) in toluene (25 mL). The mixture was stirred at room temperature for 30 minutes to facilitate the phase transfer of the $AuCl_4^-$ into the toluene layer. The aqeous layer was then discarded. The organic layer was cooled to 0°C. Dodecanethiol (0.077 g, 0.39 mmol) was added to the solution *via* a micropipette and allowed to stir for ten minutes. A fresh solution of sodium borohydride (0.055 g, 1.45 mmol) in water (8 mL) was added to the rapidly stirring reaction mixture over 5 seconds. The colour of solution became dark-red instantly. The mixture was allowed to warm to room temperature and left under stirring overnight (~18 hours). The aqueous layer was removed and the toluene layer was washed with distilled water (3×20 mL) and dried over $MgSO_4$, followed by filtration and solvent removal under reduced pressure. Crude AuNP were suspended in 50 mL of 95% ethanol and placed in the freezer overnight. The supernatant was decanted, and the AuNP precipitate was washed with 95% ethanol (10×15 mL). The average size of obtained AuNP is 1.9 ± 0.3 nm (see Fig. 3.SI1).

STM imaging. All STM experiments were performed using a Digital Instruments Inc. (Veeco) NanoScope V. The STM tips were mechanically cut from Pt/Ir wire (80/20, diameter 0.25 mm, Nanoscience). PhC10-SAc, PhC10, PhC18 molecules and AuNP were dissolved in teradecane (Sigma-Aldrich, ≥99.8%), and used directly without further purification. The physisorbed monolayrer was formed spontaneously after deposition of 10 to 15 μl of *saturated* tetradecane solution of PhC10-SAc, PhC10 and PhC18 molecules onto freshly cleaved HOPG (grade SPI-2, SPI Supplies). The nanoparticles superlattice was formed at liquid–solid interface by applying a volume of 10 to 15 μl of AuNP solution onto the organic monolayer modified HOPG. The experimental time (1-3 hours) was always shorter than the evaporation of solvent from HOPG (> 10 hours; b.p. of tetradecane is 252-254 °C).

All STM-images were obtained in the constant current mode by applying a tunneling current I_{set} of 70 to 250 pA and a sample bias V_{set} of 500 to 1400 mV. The raw images were processed from WSxM5.0 and SPIP 6.0.3 software. The calibration of the STM images of the molecular networks was performed through 2D-FFT using the underlying graphite lattice unit cell. The drift in images of AuNP assembly was minimized by a repetitive scanning up and down until the unit cell parameters became independent of the scanning directions.

Molecular modelling. The geometry optimization of the molecular networks of PhC10-SAc, PhC10 and PhC18 were performed using HyperChem 8.0 software (from Hypercube Inc.), applying the MM+ force field with Polak–Ribiere gradient optimization algorithm and a root mean square (RMS) gradient convergence criteria of 0.001 kcal $Å^{-1}$ mol^{-1}.

PhC10-SAc, PhC10 and PhC18 assemblies on graphite were simulated using a single layer of graphene covered with a monolayer of 16 molecules. Assemblies of PhC10-SAc, PhC10 and PhC18 molecules were placed on the graphene sheet, in geometries approximating the observed unit cell, and allowed to fully relax (while the graphene atoms positions were fully contstrained).

References

---

[1]. Nie, Z.; Petukhova, A.; Kumacheva, E. Properties and Emerging Applications of Self-assembled Structures Made from Inorganic Nanoparticles. *Nat Nanotechnol***.** **2010**, *5*, 15–25.

[2]. Piner, R. D.; Zhu, J.; Xu, F.; Hong, S.; Mirkin, C. A. Dip-Pen Nanolithography. *Science* **1999**, *283*, 661–663.

[3]. Liu, S.; Maoz, R.; Sagiv, J. Planned Nanostructures of Colloidal Gold *via* Self-assembly on Hierarchically Assembled Organic Bilayer Template Patterns with *in-situ* Generated Terminal Amino Functionality. *Nano Lett.* **2004**, *4*, 845–851.

[4]. Whitesides, G.M.; Grzybowski, B. Self-assembly at All Scales. *Science* **2002**, *295*, 2418–2421.

[5]. Hamley, I. W. Nanotechnology with Soft Materials. *Angew. Chem. Int. Ed.* **2003**, *42*, 1692–1712.

[6]. Lei, Y.;Yang, S.;Wu, M.; Wilde, G. Surface Patterning Using Templates: Concept, Properties and Device Applications. *Chem. Soc. Rev.* **2011**, *40*, 1247–1258.

[7]. De Feyter, S., De Schryver, F.C. Two-dimensional Supramolecular Self-Assembly Probed by Scanning Tunneling Microscopy. *Chem. Soc. Rev.* **2003**, *32*, 139–150.

[8]. Ciesielski**,** A.; Palma**,** C.-A.; Bonini**,** M.; Samori**,** P. Towards Supramolecular Engineering of Functional Nanomaterials: Pre-Programming Multi-Component 2D Self-Assembly at Solid–Liquid Interfaces. *Adv. Mater.* **2010**, *22*, 3506–3520.

[9]. Mena-Osteritz. E.; Bäuerle. P. Complexation of C_{60} on a Cyclothiophene Monolayer Template. *Adv. Mater.* **2006**, *18*, 447–451.

[10]. Li, M.; Deng, K.; Lei, S. B.; Yang, Y. L.; Wang, T. S.; Shen, Y. T.;Wang, C. R.; Zeng, Q. D.; Wang, C. Site-selective Fabrication of Two-Dimensional Fullerene Arrays by Using a Supramolecular Template at the Liquid–Solid Interface. *Angew. Chem. Int. Ed.* **2008**, *47*, 6717–6721.

[11]. MacLeod, J. M.; Ivasenko, O.; Fu, C.; Taerum, T.; Rosei, F.; Perepichka, D. F. Supramolecular Ordering in Oligothiophene–Fullerene Monolayers. *J. Am. Chem. Soc.* **2009**, *131*, 16844–16850.

[12]. Griessl, S. J. H.; Lackinger, M.; Jamitzky, F.; Markert, T.; Hietschold, M.; Heckl, W. M. Incorporation and Manipulation of Coronene in an Organic Template Structure. *Langmuir* **2004**, *20*, 9403–9407.

[13]. Schull, G.; Douillard, L.; Fiorini-Debuisschert, C.; Charra, F.; Mathevet, F.; Kreher, D.; Attias, A. J. Single-molecule Dynamics in a Self-Assembled 2D Molecular Sieve. *Nano Lett.* **2006**, *6*, 1360–1363.

[14]. Adisoejoso, J.; Tahara, K.; Okuhata, S.; Lei, S.; Tobe, Y.; De Feyter, S. Two-Dimensional Crystal Engineering: a Four-Component Architecture at a Liquid–Solid Interface. *Angew. Chem. Int. Ed.* **2009**, *48*, 7353–7357.

---

[15]. Lu, J.; Lei, S. B.; Zeng, Q. D.; Kang, S. Z.; Wang, C.; Wan, L. J.; Bai, C. L. Template-Induced Inclusion Structures with Copper (II) Phthalocyanine and Coronene as Guests in Two-Dimensional Hydrogen-Bonded Host Networks. *J. Phys. Chem. B* **2004**, *108*, 5161–5165.

[16]. Ivasenko, O.; MacLeod, J. M.; Chernichenko, K. Yu.; Balenkova, E. S.; Shpanchenko, R. V.; Nenajdenko, V. G.; Rosei, F.; Perepichka, D. F. Supramolecular Assembly of Heterocirculenes in 2D and 3D. *Chem. Commun.* **2009**, 1192–1194.

[17]. Den Boer, D.; Habets, T.; Coenen, M.J.J.; Van Der Maas, M.; Peters, T.P.J.; Crossley, M.J.; Khoury, T.; Rowan, A.E.; Nolte, R.J.M.; Speller, S.; Elemans, J.A.A.W. Controlled Templating of Porphyrins by a Molecular Command Layer. *Langmuir* **2011**, *27*, 2644–2651.

[18]. Daniel, M. C.; Astruc, D. Gold Nanoparticles: Assembly, Supramolecular Chemistry, Quantum-Size-Related Properties, and Applications Toward Biology, Catalysis, and Nanotechnology. *Chem. Rev.* **2004**, *104*, 293–346.

[19]. Pelaz, B.; Jaber, S.; De Aberasturi, D.J.; Wulf, V.; Aida, T.; De La Fuente, J.M.; Feldmann, J.; Gaub, H.E.; Josephson, L.; Kagan, C.R.; Kotov, N.A.; Liz-Marzán, L.M.; Mattoussi, H.; Mulvaney, P.; Murray, C.B.; Rogach, A.L.; Weiss, P.S.; Willner, I.; Parak, W.J. The State of Nanoparticle-Based Nanoscience and Biotechnology: Progress, Promises, and Challenges. *ACS Nano* **2012**, *6*, 8468–8483.

[20]. Acharya, S.; Hill, J.P.; Ariga, K. Soft Langmuir-Blodgett Technique for Hard Nanomaterials. *Adv. Mater.* **2009**, *21*, 2959–2981.

[21]. Rao, C. N. R.; Kalyanikutty, K. P. The Liquid–Liquid Interface as a Medium to Generate Nanocrystalline Films of Inorganic Materials. *Acc. Chem. Res.* **2008**, *41*, 489–499.

[22]. Bigioni, T. P.; Lin, X.-M.; Nguyen, T. T.; Corwin, E. I.; Witten, T. A.; Jaeger, H. M. Kinetically Driven Self Assembly of Highly Ordered Nanoparticle Monolayers. *Nat. Mater.* **2006**, *5*, 265–270.

[23]. Aldaye, F. A.; Palmer, A. L.; Sleiman, H. F. Assembling Materials with DNA as the Guide. *Science* **2008**, *321*, 1795–1799.

[24]. Shenhar, R.; Norsten, T. B.; Rotello, V. M. Polymer-Mediated Nanoparticles Assembly: Structural Control and Applications. *Adv. Mater.* **2005**, *17*, 657–669.

[25]. Chiu, J. J.; Kim, B. J.; Kramer, E. J.; Pine, D. J. Control of Nanoparticle Location in Block Copolymers. *J. Am. Chem. Soc.* **2005**, *127*, 5036–5037.

[26]. Perepichka, I. I.; Ximin, C.; Bazuin, C. G. Nanopatterning of Substrates by Self-Assembly in Supramolecular Block Copolymer Monolayer Films. *Sci. China, Chem.* **2013**, *56*, 48–55.

[27]. Hoeppener, S.; Chi, L.; Fuchs, H. Formation of Au55 Strands on a Molecular Template at the Solid−Liquid Interface. *Nano Lett.* **2002**, *2*, 459–463.

[28]. Lei, S. B.; Wang, C.; Yin, S. X.; Wan, L. J.; Bai, C. L. Assembling Nanometer Nickel Particles into Ordered Arrays. *Chem. Phys. Chem.* **2003**, *4*, 1114–1117.

---

[29]. Wei, X.; Tong, W.; Fidler, V.; Zimmt, M. B. Reactive Capture of Gold Nanoparticles by Strongly Physisorbed Monolayers on Graphite. *J. Colloid Interf. Sci*. **2012**, *387*, 221–227.

[30]. Hansen, T.; Itoua, S.; Kamounah, F. S.; Christensen, J. B.; Bjørnholm, T.; Schaumburg, K.; Bechgaard, K.; Wilkes. S. B. STM Investigations of Physisorbed Monolayers of Dialkoxy-Substituted Aromatics. *J. Mater. Chem.* **1999**, *9*, 1107–1113.

[31]. Shao, X.; Luo, X.; Hu, X.; Wu, K. Solvent Effect on Self-Assembled Structures of 3,8-Bis-Hexadecyloxy-Benzo[*C*]Cinnoline on Highly Oriented Pyrolytic Graphite. *J. Phys. Chem. B* **2006**, *110*, 1288–1293.

[32]. Wei, Y.; Tong, W.; Zimmt, M. B. Self-Assembly of Patterned Monolayers with Nanometer Features: Molecular Selection Based on Dipole Interactions and Chain Length. *J. Am. Chem. Soc.* **2008**, *130*, 3399–3405.

[33]. Tour, J. M.; Jones II, L.; Pearson, D. L.; Lamba, J. J. S.; Burgin, T. P.; Whitesides, G. M.; Allara, D. L.; Parikh, A. N.; Atre, S. Self-Assembled Monolayers and Multilayers of Conjugated Thiols, Alpha,Omega-Dithiols, and Thioacetyl-Containing Adsorbates. Understanding Attachments Between Potential Molecular Wires and Gold Surfaces. *J. Am. Chem. Soc.* **1995**, *117*, 9529–9534.

[34]. Elemans, J. A. A. W.; de Cat, I.; Xu, H.; de Feyter, S. Two-Dimensional Chirality at Liquid–Solid Interfaces. *Chem. Soc. Rev.* **2009**, *38*, 722–736.

[35]. Brust, M.; Walker, M.; Bethell, D.; Schiffrin, D. J.; Whyman, R. J. Synthesis of Thiol-Derivatized Gold Nanoparticles in a Two-Phase Liquid−Liquid System. *J. Chem. Soc., Chem. Commun.* **1994**, 801−802.

[36]. Auer, S.; Frenkel, D. Suppression of Crystal Nucleation in Polydisperse Colloids due to Increase of the Surface Free Energy. *Nature* **2001**, *413*, 711–713.

[37]. Grumelli, D.; Vericat, C.; Benitez, G.; Vela, M. E.; Salvarezza, R. C.; Giovanetti, L.J.; Ramallo-Lopez, J. M.; Requejo, F. G.; Craievich, A. F.; Shon, Y. S. Thiol-Capped Gold Nanoparticles on Graphite: Spontaneous Adsorption and Electrochemically Induced Release. *J. Phys. Chem. C* **2007**, *111*, 7179–7184.

[38]. Orive, A. G.; Grumelli, D.; Vericat. C.; Ramallo-López, J.M.; Giovanetti, L.; Benitez, G.; Azcárate, J. C.; Corthey, G.; Fonticelli, M. H.; Requejo, F. G.; Hernández Creus, A.; Salvarezza, R.C. "Naked" Gold Nanoparticles Supported on HOPG: Melanin Functionalization and Catalytic Activity. *Nanoscale* **2011**, *3*, 1708–1716.

[39]. Talapin**,** D. V.; Shevchenko**,** E. V.; Murray**,** C. B.; Titov**,** A. V.; Kral**,** P. Dipole−Dipole Interactions in Nanoparticle Superlattices. *Nano Lett.* **2007**, *7*, 1213–1219.

[40]. Prasad, B. L. V.; Sorensen, C. M.; Klabunde, K. J. Gold Nanoparticle Superlattices. *Chem. Soc. Rev.* **2008**, *37*, 1871–1883.

---

[41]. Jackson, A. M.; Hu, Y.; Silva, P. J.; Stellacci, F. From Homoligand- to Mixed-Ligand Monolayer-Protected Metal Nanoparticles: a Scanning Tunneling Microscopy Investigation. *J. Am. Chem. Soc.* **2006**, *128*, 11135–11149.

[42]. Ong, Q. K.; Reguera, J.; Silva, P. J.; Moglianetti, M.; Harkness, K.; Longobardi, M.; Mali, K. S.; Renner, C.; De Feyter, S.; Stellacci, F. High-Resolution Scanning Tunneling Microscopy Characterization of Mixed Monolayer Protected Gold Nanoparticles. *ACS Nano* 2013, *7* ,8529–8539.

[43] Cesbron, Y., Shaw, C.P., Birchall, J.P., Free, P., Lévy, R. Stripy Nanoparticles Revisited. *Small* **2012**, *8*, 3714–3719.

[44] Yu, M., Stellacci, F. Response to "Stripy Nanoparticles Revisited". *Small* **2012**, *8*, 3720-3726.

[45]. Claridge, S. A.; Castleman, A. W.; Khanna, S. N.; Murray, C. B.; Sen, A.; Weiss, P. S. Cluster-Assembled Materials. *ACS Nano* **2009**, *3*, 244–255.

[46]. Nie, Z.; Petukhova, A.; Kumacheva, E. Properties and Emerging Applications of Self-Assembled Structures Made from Inorganic Nanoparticles. *Nat. Nanotechnol.* **2010**, *5*, 15–25.

[47]. Whetten, R. L.; Shafigullin, M. N.; Khoury, J. T.; Schaaff, T. G.; Vezmar, I.; Alvarez, M. M.; Wilkinson, A. Crystal Structures of Molecular Gold Nanocrystal Arrays. *Acc. Chem. Res.* **1999**, *32*, 397−406.

[48]. Luedtke, W. D.; Landman. U. Structure, Dynamics, and Thermodynamics of Passivated Gold Nanocrystallites and their Assemblies. *J. Phys. Chem.* **1996**, *100*, 13323–13329.

Appendix Y

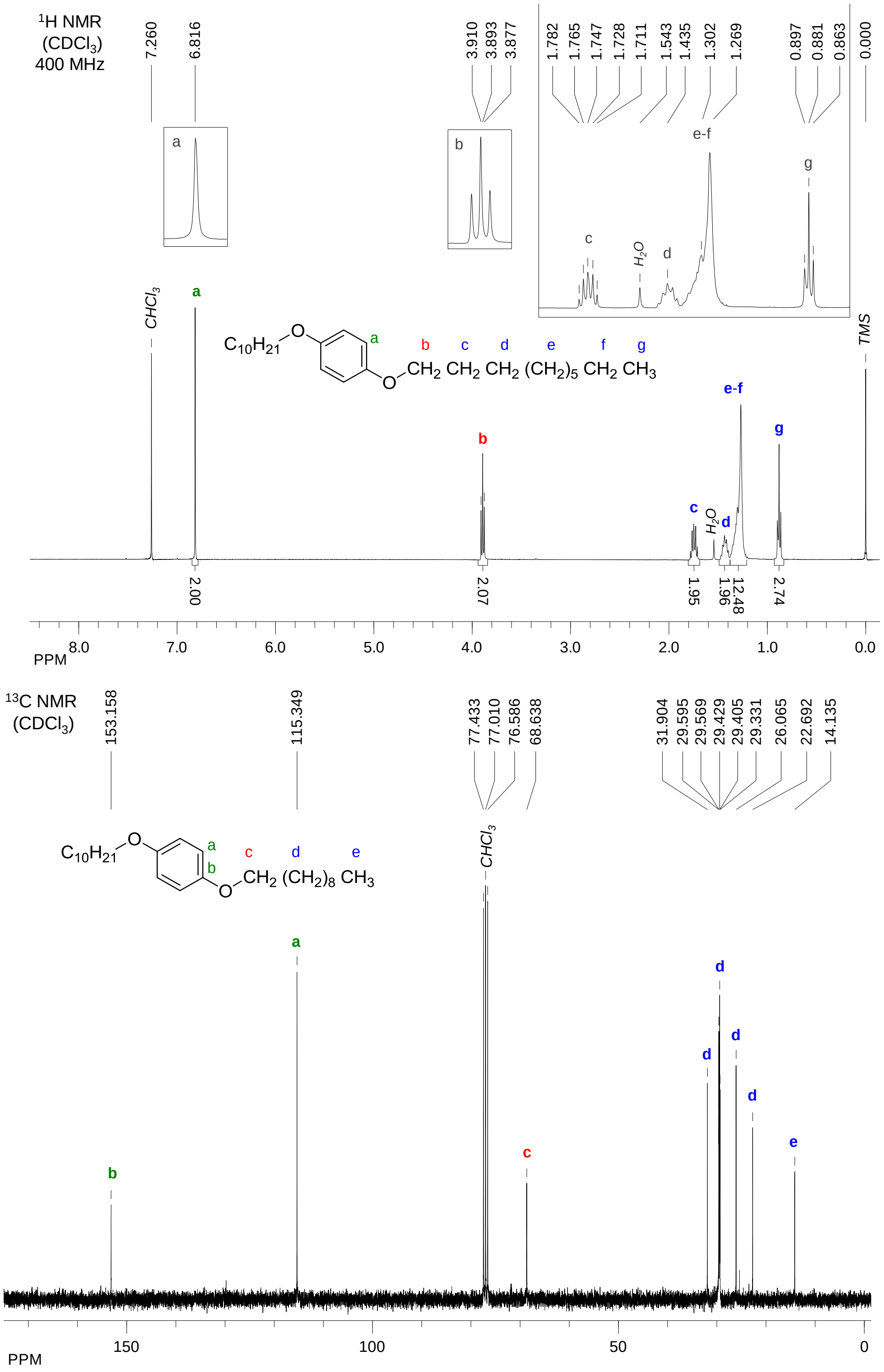

^{1}H (top) and ^{13}C (bottom) NMR spectra of 1,4-di(decyloxy)benzene [PhC10].

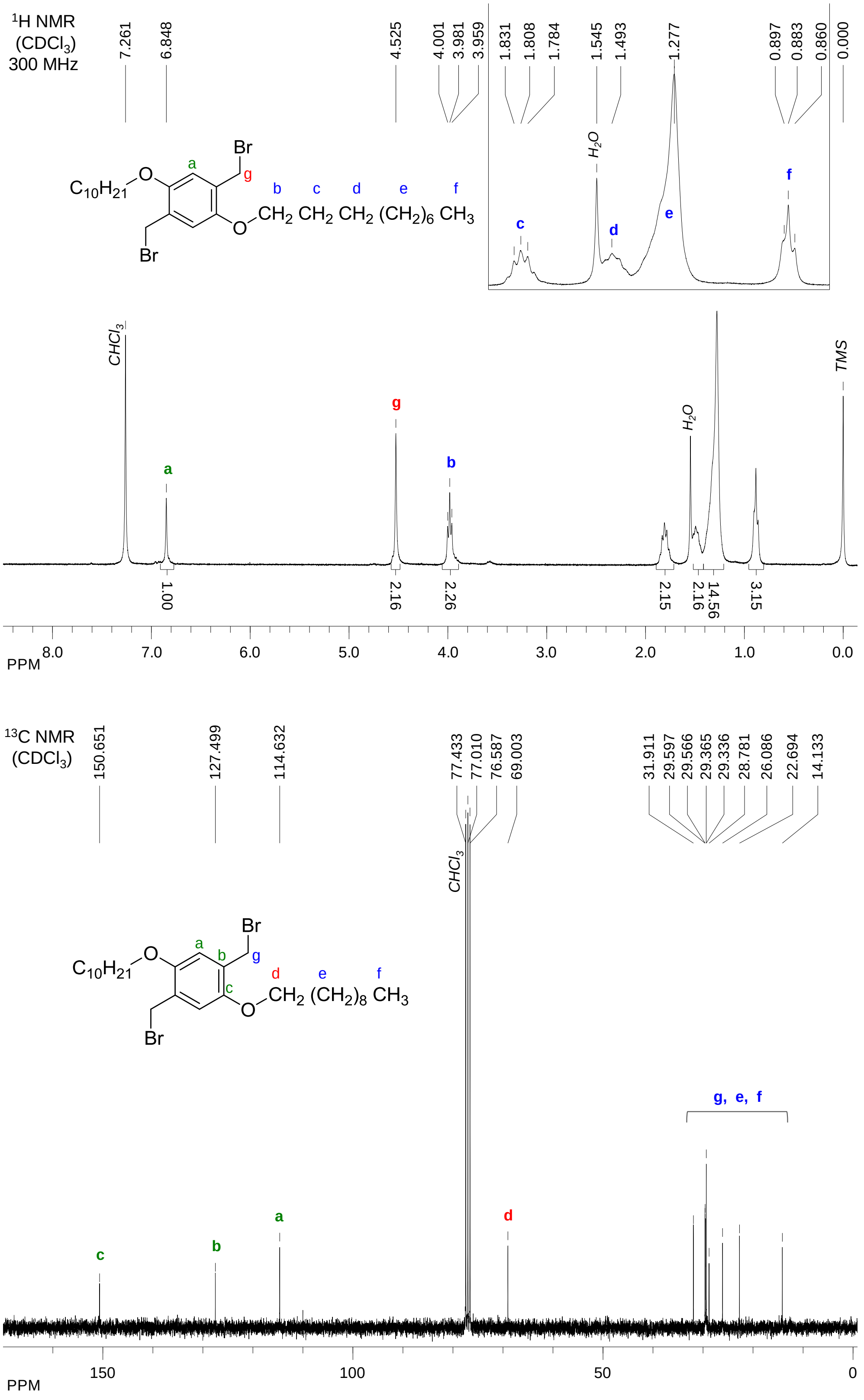

^{1}H (top) and ^{13}C (bottom) NMR spectra of 1,4-di(decyloxy)-2,5-bis(bromomethyl)benzene [PhC10-Br].

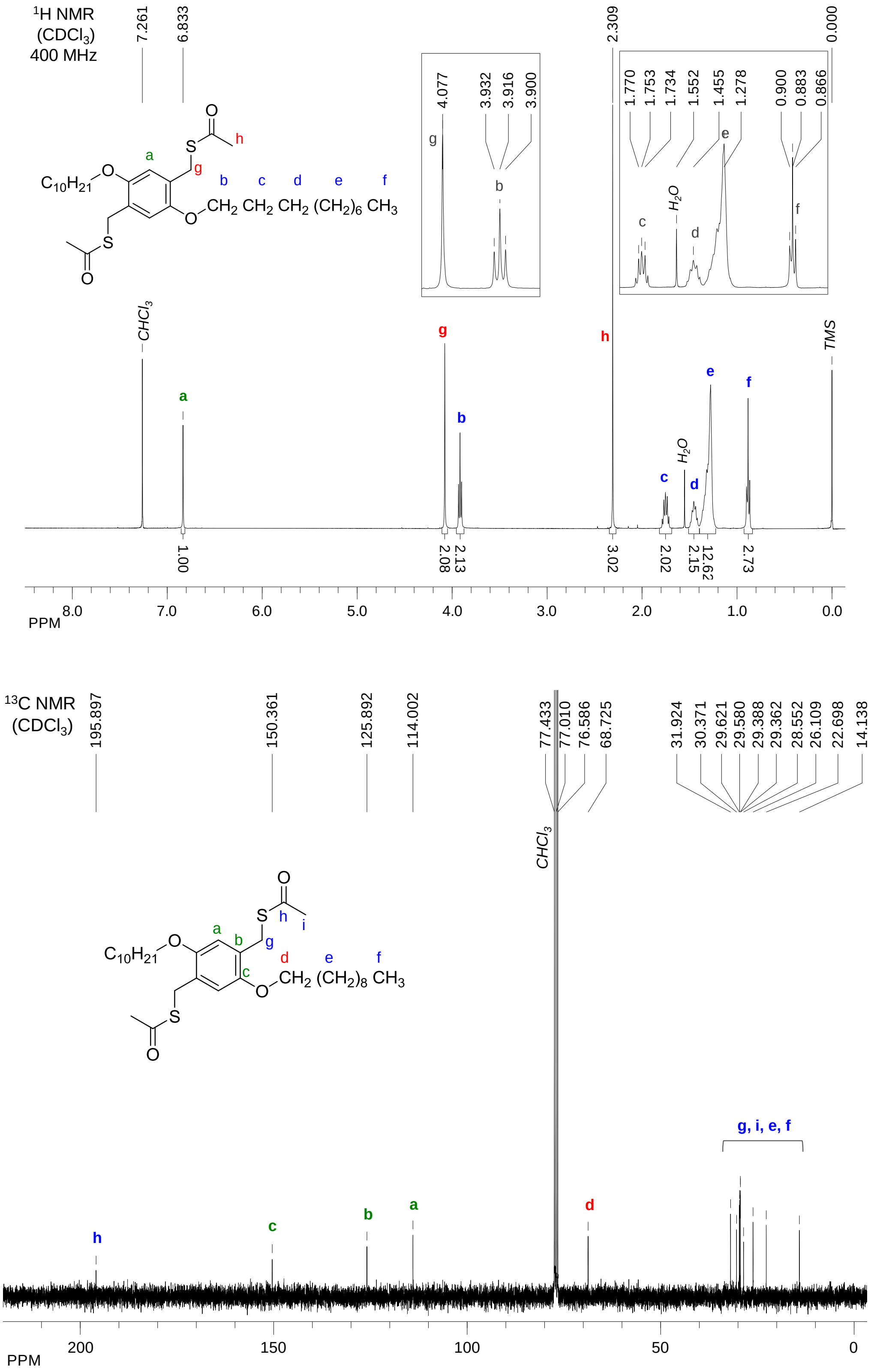

^{1}H (top) and ^{13}C (bottom) NMR spectra of 1,4-di(decyloxy)-2,5-bis(S-acetylthiomethyl)benzene [PhC10-SAc].

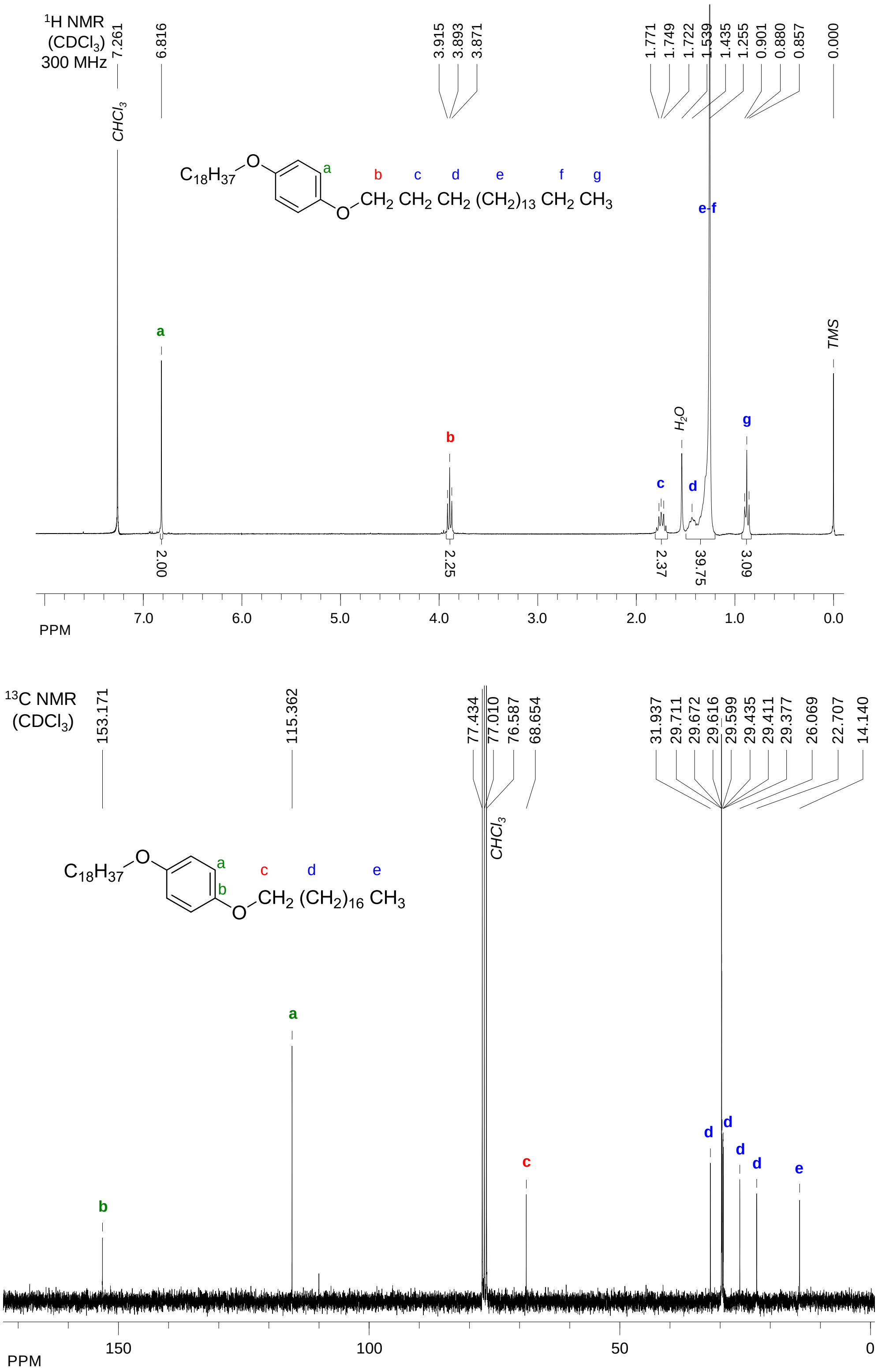

^{1}H (top) and ^{13}C (bottom) NMR spectra of 1,4-di(octadecyloxy)benzene [PhC18].

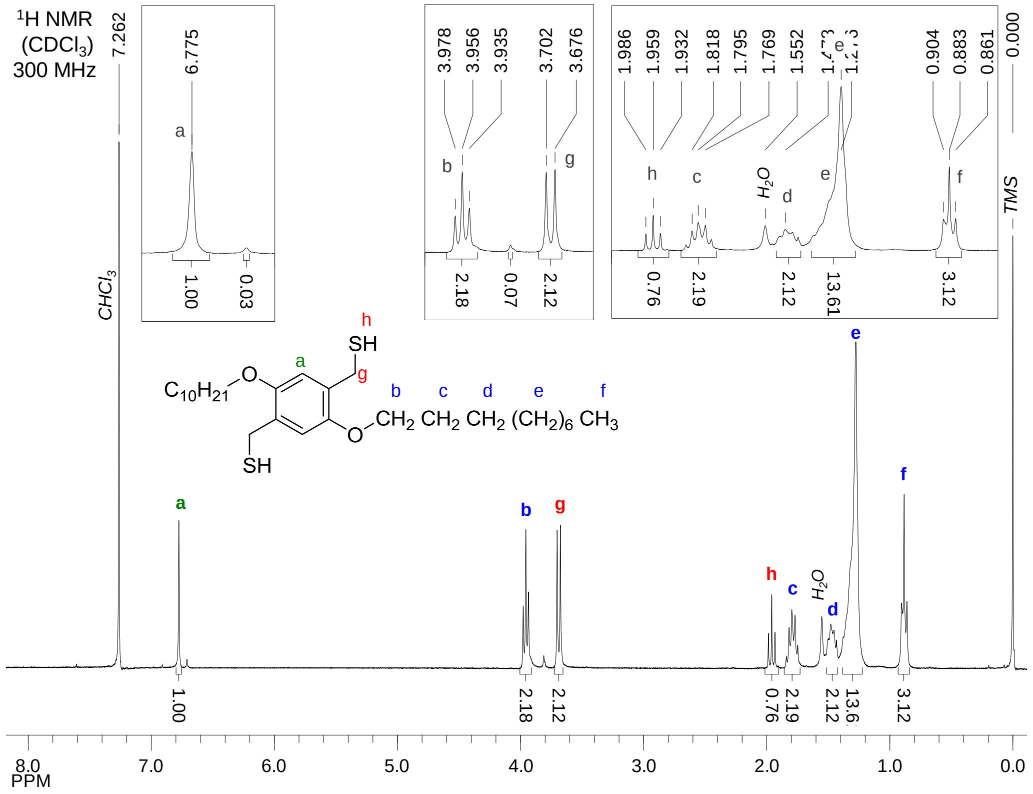

^{1}H NMR spectrum of 1,4-di(decyloxy)-2,5-bis(hydrothiomethyl)benzene [PhC10-SH].

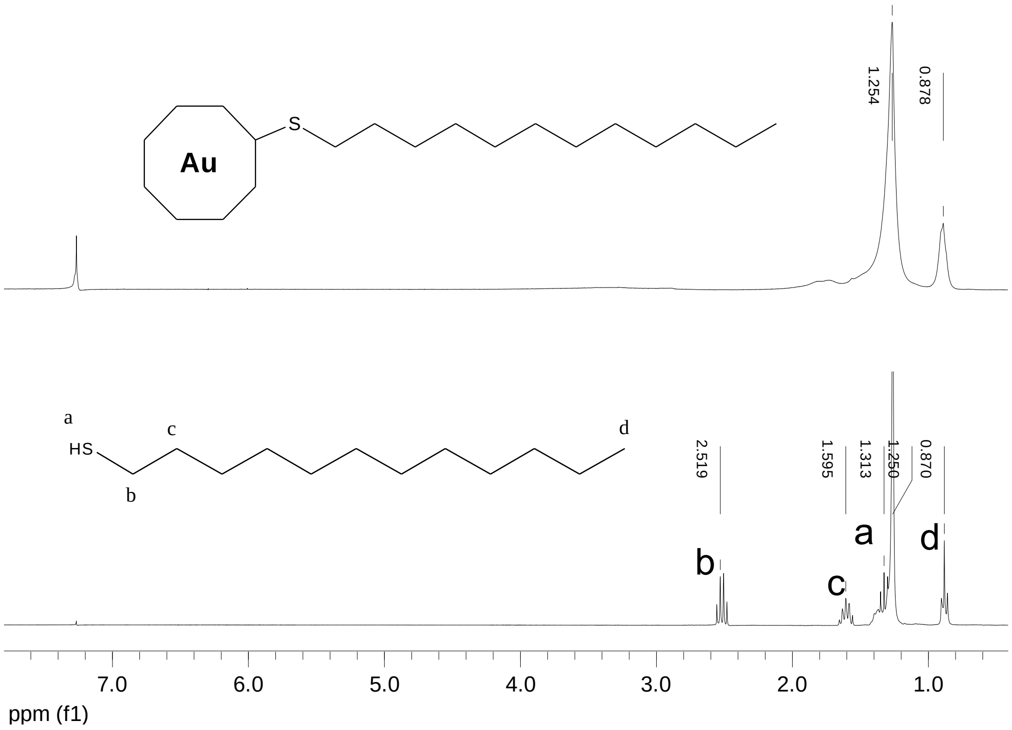

^{1}H NMR spectra of C12-AuNP and dodecanethiol (used as a protecting ligand). Disappearance of characteristic peak [b] in C12-AuNP spectrum points to absence of free ligands in AuNP solution.

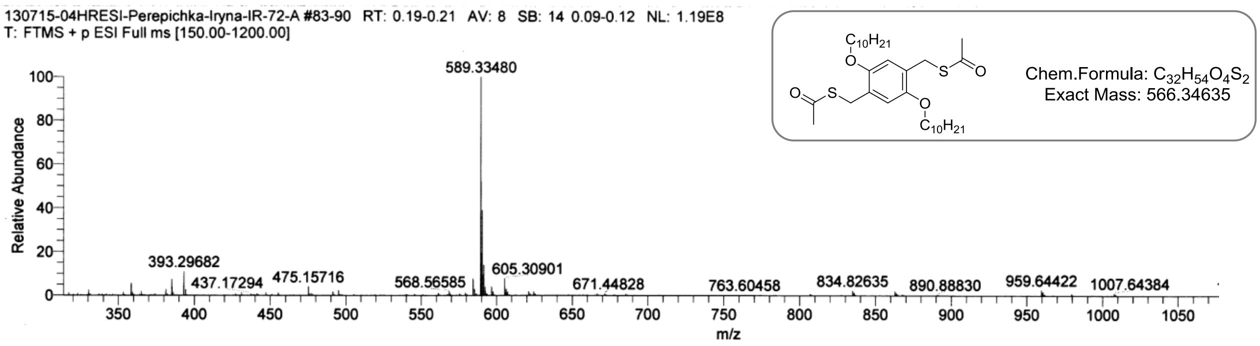

```
130715-04HRESI-Perepichka-Iryna-IR-72-A#120-129 RT: 0.29-0.31 AV: 10
SB: 9 0.32-0.34
T: FTMS + p ESI Full ms [150.00-1200.00]
m/z= 589.30329-589.36396
     m/z      Intensity  Relative Resolution  Charge  Theo. Mass   Delta     RDB     Composition
                                                                   (ppm)    equiv.
  589.33500  56435160.0   100.00 25545.10      1.00   589.33488    0.21     15.0 C38 H48 O N Na S
                                                      589.33470    0.51      6.5 C31 H50 O9 Na
                                                      589.33461    0.67     13.5 C37 H49 O4 S
                                                      589.33557   -0.96      5.5 C32 H54 O4 Na S2
                                                      589.33396    1.78      4.5 C29 H53 O6 N2 S2
```

Mass spectrum of 1,4-di(decyloxy)-2,5-bis(S-acetylthiomethyl)benzene [PhC10-SAc].

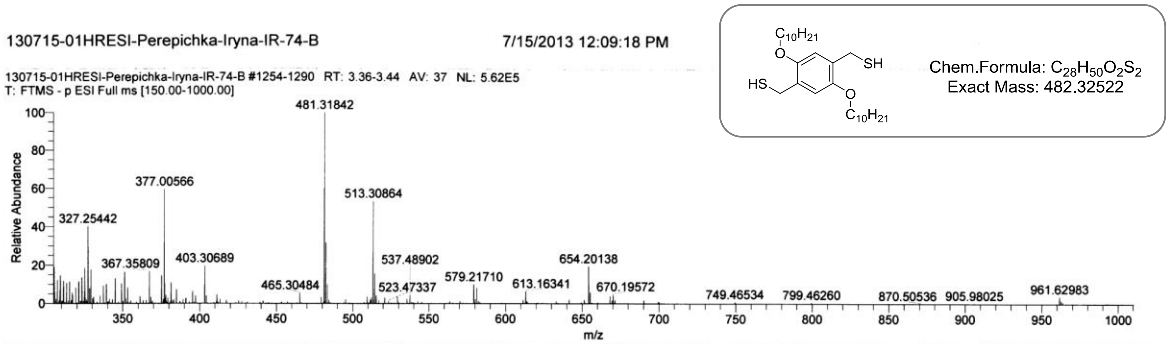

```
130715-01HRESI-Perepichka-Iryna-IR-74-B#1279-1295 RT: 3.42-3.46 AV: 17
T: FTMS - p ESI Full ms [150.00-1000.00]
m/z= 481.29515-481.34617
     m/z   Intensity Relative Resolution  Charge  Theo. Mass   Delta    RDB     Composition
                                                               (ppm)   equiv.
  481.31829  390464.1  100.00 23849.80      1.00   481.31795    0.71     4.5 C28 H49 O2 S2
                                                   481.31976   -3.06    10.0 C30 H43 O4 N
```

```
130715-01HRESI-Perepichka-Iryna-IR-74-B#1279-1295 RT: 3.42-3.46 AV: 17
T: FTMS - p ESI Full ms [150.00-1000.00]
m/z= 961.56420-961.68983
     m/z   Intensity Relative Resolution  Charge  Theo. Mass   Delta    RDB     Composition
                                                               (ppm)   equiv.
  961.62906   14180.2  100.00 17968.27      1.00   961.63020   -1.18    13.0 C59 H95 O N S4
                                                   961.62752    1.61     8.5 C56 H97 O4 S4
```

Mass spectrum of1,4-di(decyloxy)-2,5-bis(hydrothiomethyl)benzene [PhC10-SH].

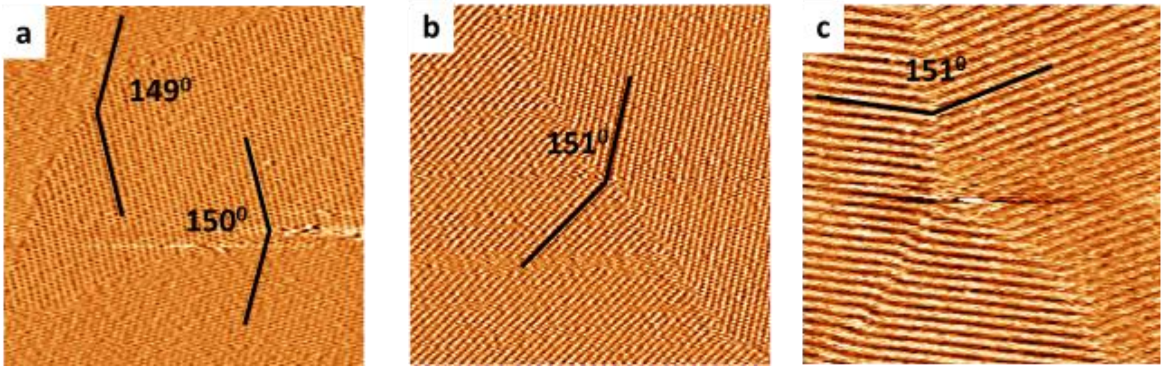

Figure 3.S1. STM of PhC10-SAc domains at tetradecane/HOPG interface: (a) 120×120 nm^2, V_b = 900 mV, I_t = 0.05 nA; (b) 120×120 nm^2, V_b = 1600 mV, I_t = 0.18 nA; (c) 80×80 nm^2, V_b = 900 mV, I_t = 0.15 nA.

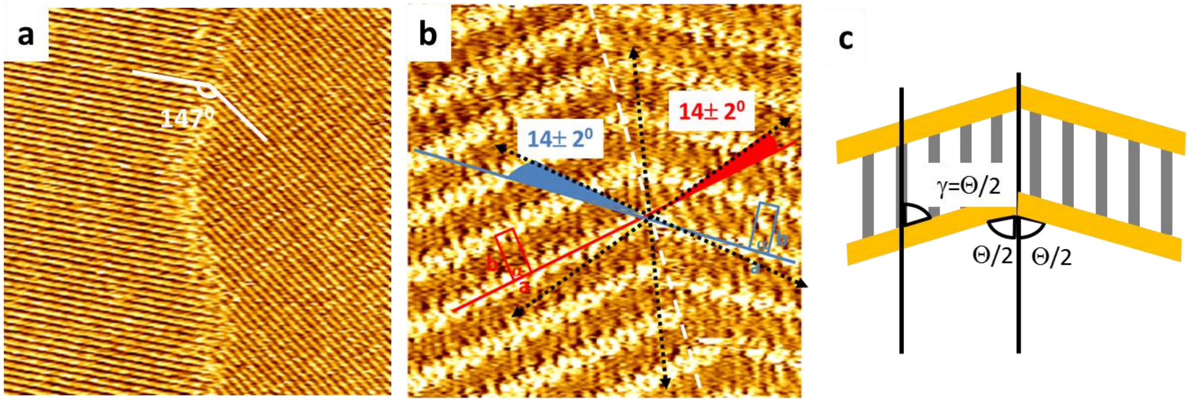

Figure 3.S2. (a) Large scale (127×127 nm^2, V_b = 700 mV, I_t = 0.3 nA) and (b) high resolution (25×25 nm^2, Vb = 1370 mV, I_t = 0.2 nA) STM images of PhC10-SAc at tetradecane/HOPG interface, showing the interdomain angle and the angles between the lamellar axis of PhC10-SAc domains (blue and red lines) and the main crystallographic axis of HOPG (black dotted lines). (c) Schematic presentation of relationship between the interdomain angle and the tilt γ of the alkyl chains vs the direction of the lamellae: $\gamma = \Theta/2$.

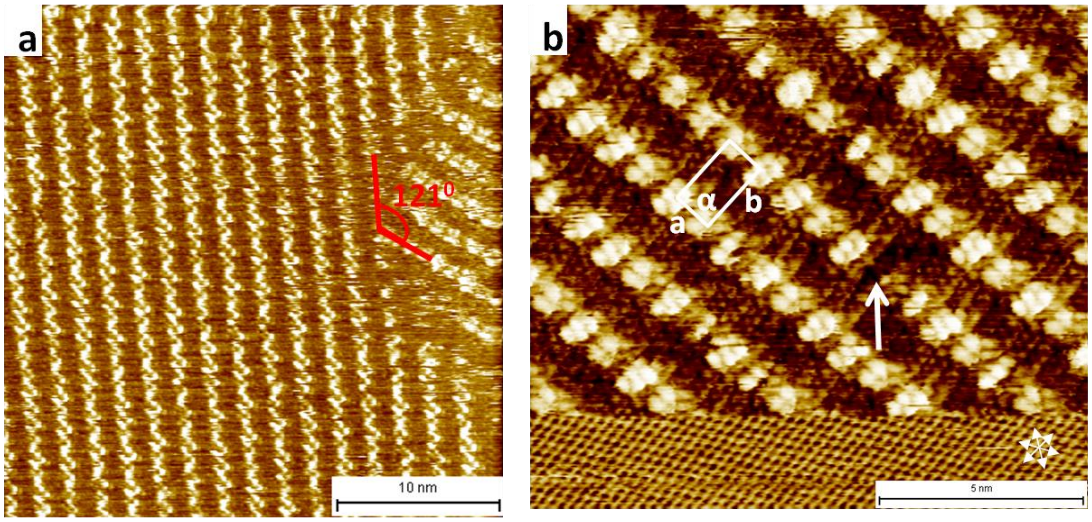

Figure 3.S3. (a) Large scale STM image (V_b = 800mV, I_t = 0.2 nA) of PhC10-SH SAMN. (b) High resolution STM image (V_b = 800 mV, I_t = 0.2 nA) showing PhC10-SH SAMN and underlying HOPG lattice ($\mathrm{V_b}$ is switched to 50mV in the bottom part of the image); white box shows the unit cell: (a =0.95 ± 0.05 nm; b = 2 ± 0.1 nm; 89 ± 1°); the white arrow points to one missed molecule.

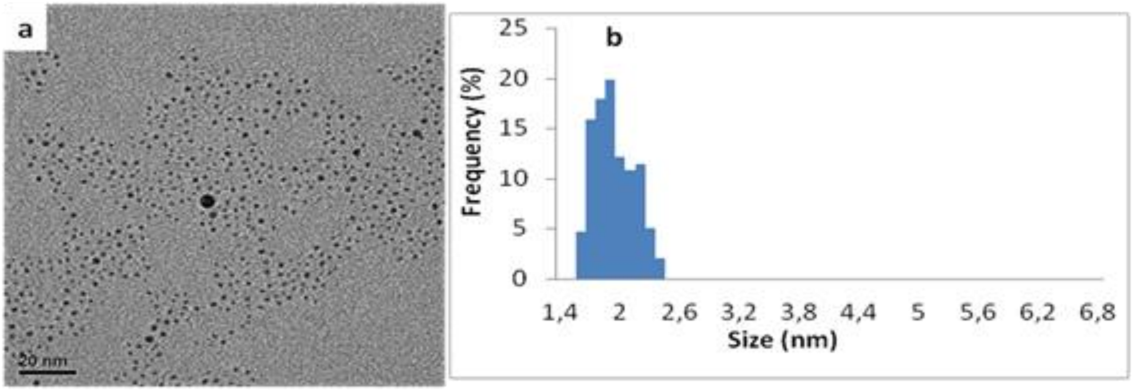

Figure 3.S4. C12-AuNPs: (a) TEM image and (b) analysis of size distribution.

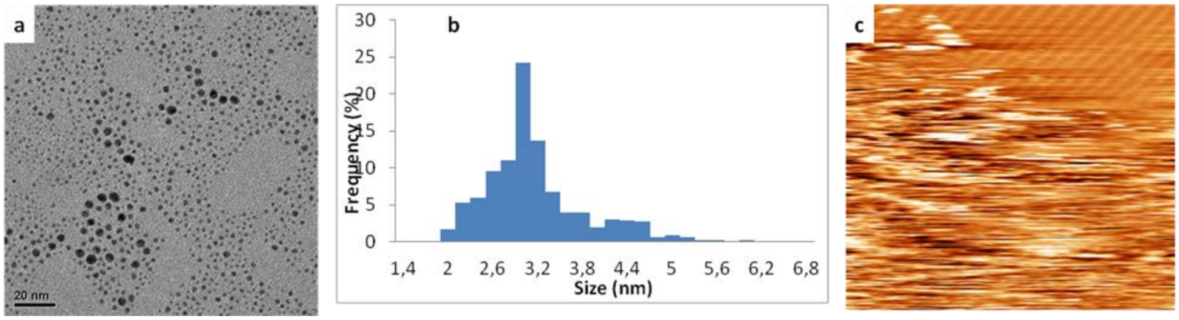

Figure 3.S5. C12-AuNP with high polydispersity: (a) TEM image, (b) analysis of size distribution, (c) STM image of disordered AuNP at tetradecane/ PhC10-SAc /HOPG interface (62 × 62 nm^2, V_b = 1200 mV, I_t = 0.08 nA).

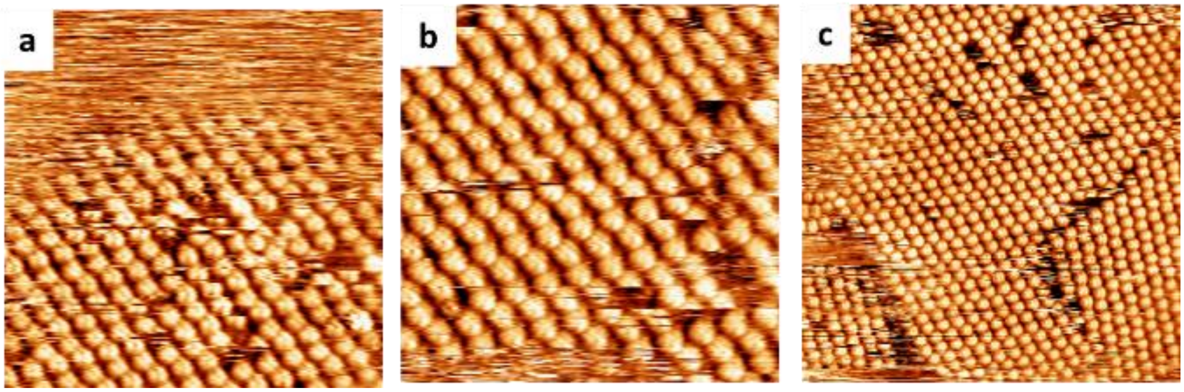

Figure 3.S6. STM images of C12-AuNP self-assembly at tetradecane/PhC10-SAc modified HOPG interface: (a) 60 ×60 nm^2, V_b = 900 mV, I_t = 0.05 nA; (b) 47.3 ×47.3 nm^2, V_b = 1600 mV, I_t = 0.18 nA; (c) 100 ×100 nm^2, V_b = 900 mV, I_t = 0.15 nA.

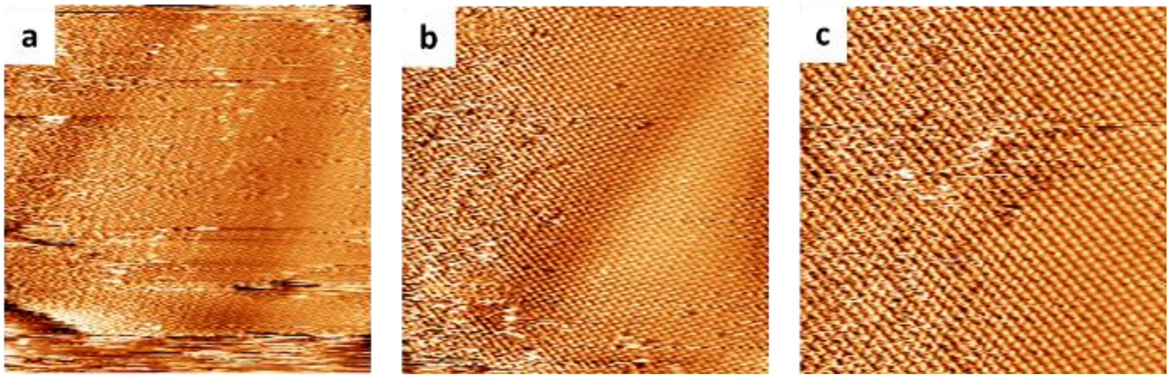

Figure 3.S7. STM images of large assemblies of C12-AuNP at tetradecane/ PhC10 /HOPG interface: (a) 300 ×300 nm^2 ;V_b = 900 mV, I_t = 0.05 nA; (b) 200 ×200 nm^2 ; V_b = 500 mV, I_t = 0.1 nA; (c) 130 ×130 nm^2, V_b = 900 mV, I_t = 0.15 nA.

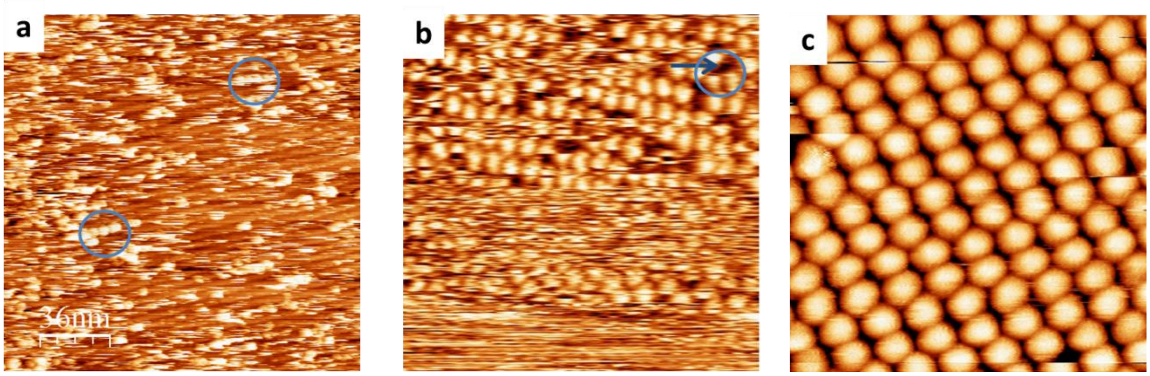

Figure 3.S8. Sequence of STM images showing different stages of C12-AuNP assembly at tetradecane/ PhC10-SAc /HOPG interface: (a) 80×80 nm^2; V_b = 800 mV, I_t = 0.08 nA; (b) 60×60 nm^2; V_b = 800 mV, I_t = 0.08 nA; (c) 34×34 nm^2, V_b = 700 mV, I_t = 0.1 nA.

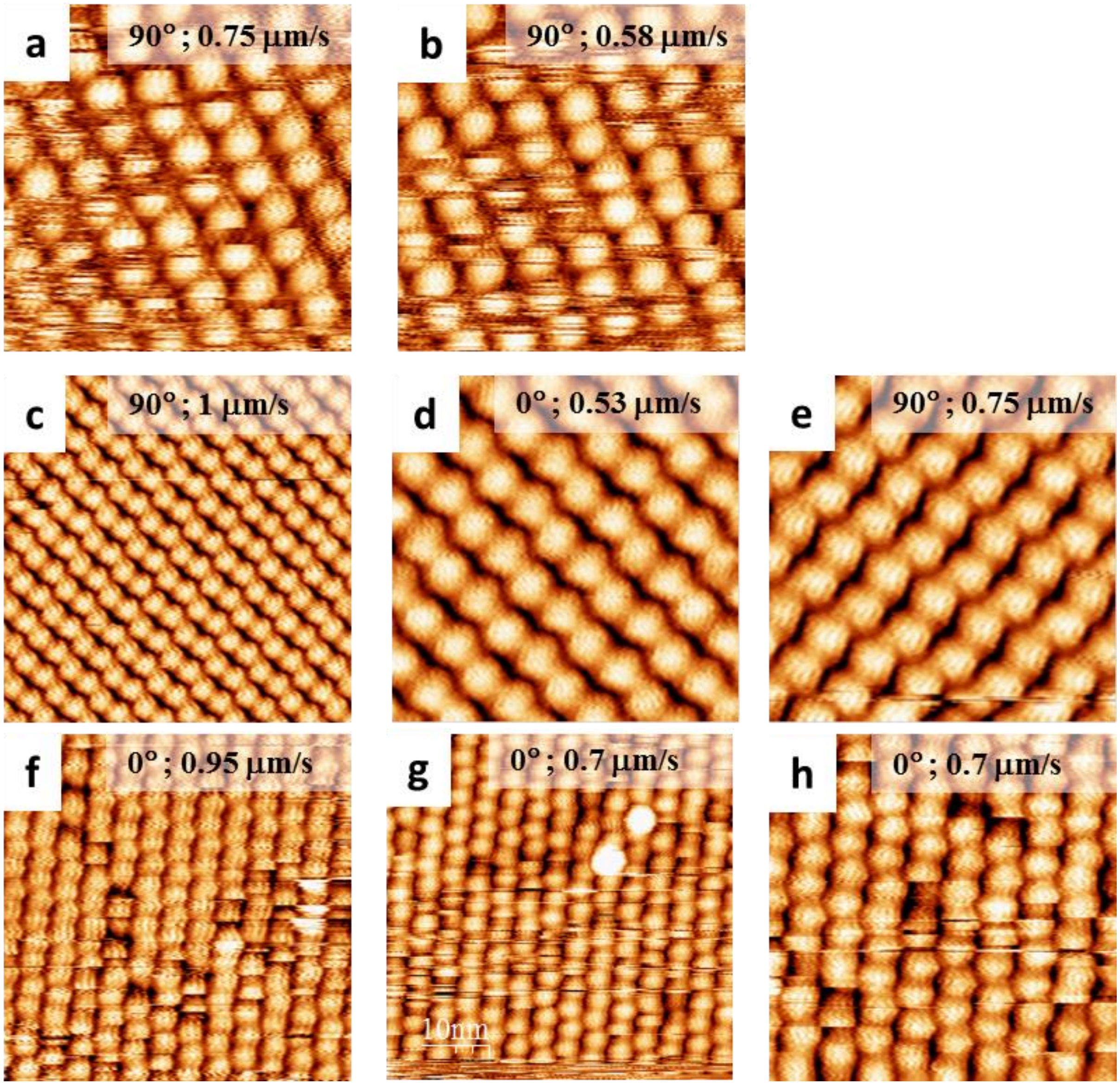

Figure 3.S9. STM images of C12-AuNP at (a,b) tetradecane/PhC10-SAc and (c–h) tetradecane/PhC10 interface showing ripples on AuNP surface. The surface was imaged at 0° or 90° scanning angles and different scanning speed (0.5–1 μm/s, see insets). The average ripple spacing are: (a) 0.61 nm, (b) 0.59 nm, (c) 0.73, (d) 0.59 nm, (e) 0.68 nm, (f) 0.72 nm, (g) 0.66 nm, (h) 0.71 nm. Other scanning conditions: (a) 27.9×27.9 nm^2; V_b = 600 mV, I_t = 0.12 nA; (b) 27.9×27.9 nm^2; V_b = 600 mV, I_t = 0.12 nA); (c) 47.6×47.6 nm^2; V_b = 500 mV, I_t = 0.1 nA; (d) (25.5×25.5 nm^2 , V_b = 900 mV, I_t = 0.15 nA); (e) 25.5×25.5 nm^2 , V_b = 900 mV, I_t = 0.15 nA; (f) 47.9 ×47.9 nm^2; V_b = 800 mV, I_t = 0.12 nA; (g) 51×51 nm^2; V_b = 600 mV, I_t = 0.12 nA; (h) 34×34 nm^2 , V_b = 600 mV, I_t = 0.12 nA).

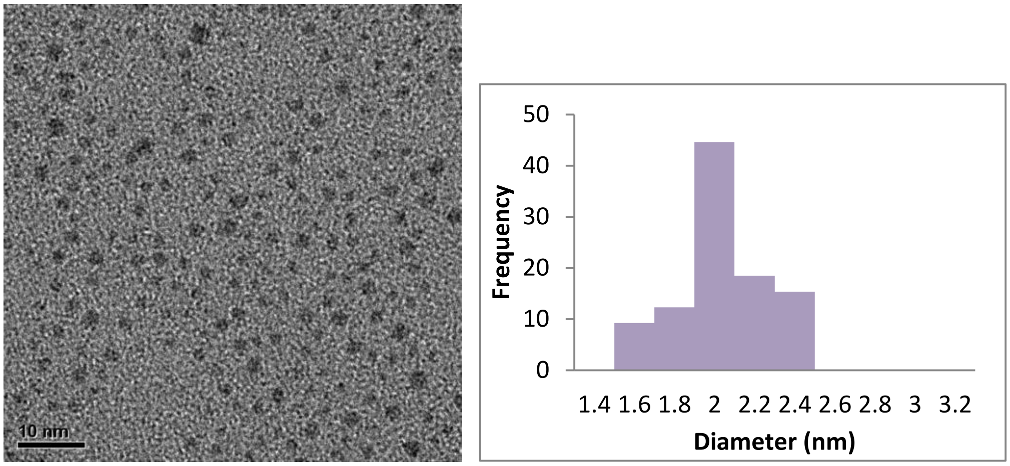

Figure 3.S10. C8-AuNP: (a) TEM image and (b) analysis of size distribution.

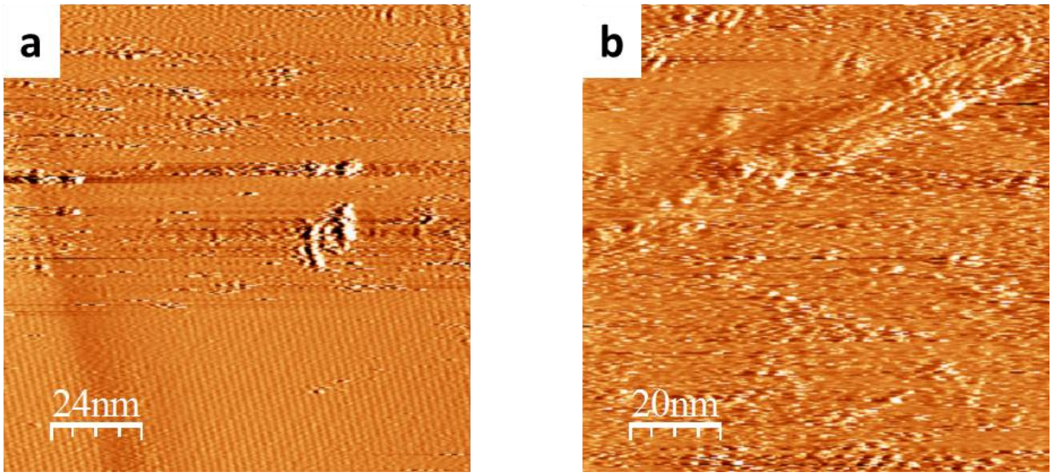

Figure 3.S11. STM images of C8-AuNP in tetradecane at (a) PhC10/HOPG and (b) PhC18/HOPG surfaces (no assembly and little absorption was observed). Scanning conditions: (a) 120×120 nm^2, V_b = 900 mV, I_t = 0.2 nA; (b) 100×100 nm^2, V_b = 900 mV, I_t = 0.2 nA.

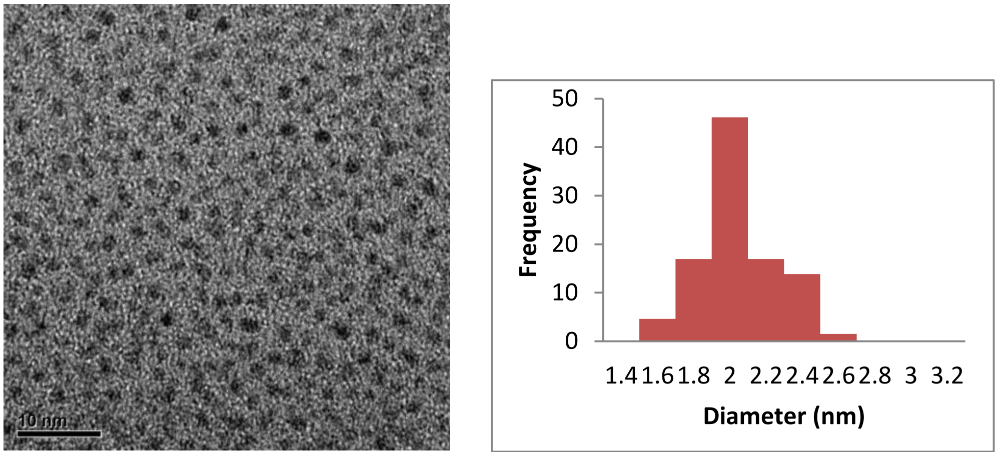

Figure 3.S12. C18-AuNP: (a) TEM image and (b) analysis of size distribution.

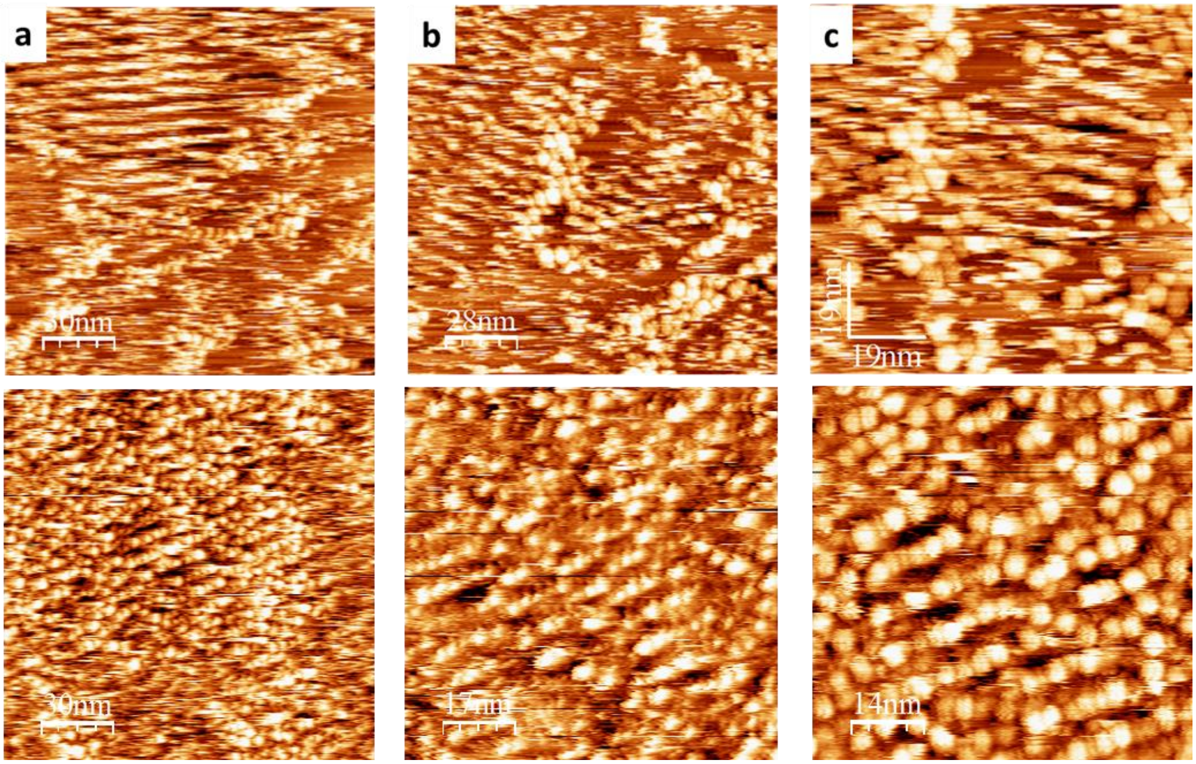

Figure 3.S13. STM images of C18-AuNP self-assembly at tetradecane/ PhC18 /HOPG interface. The measured distance between two adjacent rows of AuNP is 6.6±0.4nm, which is close to ≈6.5±0.2 nm diameter of the C18-AuNP with fully extended ligand (1.94 ± 0.21 nm metal core plus twice the length of the octadecanethiol ligand, 2×2.28 nm). Scanning conditions: (a) V_b = 1600 mV, I_t = 0.17 nA; (b) V_b = 1700 mV, I_t = 0.27 nA; (c) V_b = 1100 mV, I_t = 0.29 nA.

Table 3.S1. Statistical data for unit cell parameters measured from STM images.

	Unit cell param.	Image 1	Image 2	Image 3	Image 4	Image 5	**Average**	**Sdev**
PhC10-SAc	a, nm	1.90	2.17	2.03	2.1	2.1	**2.06**	**0.10**
	b, nm	0.97	1.06	1.05	1.03	0.98	**1.01**	**0.04**
	α, °	86	85	85	86	86	**85.6**	**0.5**
PhC10	a, nm	1.77	1.83	1.8	1.8	1.79	**1.80**	**0.02**
	b, nm	0.99	0.99	0.96	1.03	0.98	**0.99**	**0.03**
	α, °	79	79	79	81	80	**79.6**	**0.9**
PhC18	a, nm	2.69	2.73	2.64	2.61	2.83	**2.70**	**0.08**
	b, nm	1.09	0.97	0.99	0.97	0.94	**0.99**	**0.05**
	α, °	86	85	87	85	82	**85.0**	**1.9**
AuNP @ PhC10-SAc	a, nm	6.29	6.10	5.97	6.28	5.91	**6.11**	**0.17**
	b, nm	4.01	4.15	4.13	4.08	4.06	**4.09**	**0.06**
	α, °	71	67	66	67	66	**67.4**	**2.1**
AuNP @ PhC10	a, nm	6.38	6.09	6.02	5.89	6.15	**6.12**	**0.18**
	b, nm	3.89	3.89	3.74	3.97	4.00	**3.89**	**0.10**
	α, °	76	73	74	73	71	**73.4**	**1.80**

Chapter 4: Adsorption of C_{60} on Top of Benzenethiol and Pentafluorobenzenethiol SAMs

4.1 Abstract

Understanding the structural organization and growth of organic molecules at a self-assembled monolayer (SAM)-liquid interface is important for achieving high performance SAM based electronic devices. C_{60} adsorption onto benzenethiol (BT) pentafluorobenzenethiol (PFBT), and octanethiol (C8SH) SAM modified Au(111) was studied using STM at a liquid-solid interface. A continuous film of C_{60} molecules forms two orders of magnitude faster ($k = 3.3 \pm 0.2\times10^{-7}\ s^{-1}$) on PFBT compared to BT ($1.1 \pm 0.3\times10^{-9}\ s^{-1}$) and C8SH SAMs ($k = 9.5 \pm 1.2\times10^{-9}\ s^{-1}$). In BT and C8SH cases, randomly distributed C_{60} aggregates are observed. Close inspection of the C_{60} film reveals a multilayer with an hexagonal close packed $(2\sqrt{3} \times 2\sqrt{3})R30°$ structure for the top two layers. The difference in C_{60} growth behavior is proposed to originate from the differing orientation of the dipole moments of BT and PFBT SAMs.

4.2 Introduction

Self-assembled monolayers prepared from thiol-terminated molecules have been successfully used for tailoring the physical and chemical properties of metals, oxides, and semiconductors[1,2,3] for a range of application including electrochemical sensors,[4] surfaces patterning,[5] friction and lubrication control,[6] and protective coatings.[7] Amongst other properties, SAMs offer an efficient means to tune the work function of an electrode, reducing the charge injection barriers between the electrode and the organic thin film, and improving the morphology of the subsequent thin film semiconductor. For this reason, SAMs have become an integral part of many organic semiconducting devices including organic light emitting diodes (OLEDs) and field-effect transistors (OFETs).[8,9,10]

Alkanethiols with different chain lengths[11] and their fluorinated derivatives[12] have been used to modify the surface potential of metal substrates. However, the large band gap of the aliphatic thiols (> 5 eV) limits the charge transport across the resulting SAMs, leading to decreased device performance.[13] On the other hand, because of their delocalised π orbitals and relatively small band gap (<4.5 eV), aromatic thiols have been particularly effective in facilitating charge transfer across SAMs.

By changing the surface energy of a substrate, SAMs can alter the morphology and the interfacial organization of the organic semiconducting material allowing the fabrication of high-performance FET.[14] Furthermore, the surface dipole created by SAMs has been used to tune the energy level alignment at metal/organic semiconductor interface.[15,16] For instance, benzenethiol (BT, molecular dipole moment $\mu = 1.06$ D) and pentafluorobenzenethiol (PFBT, $\mu = 1.55$ D) induce a shift of the Au work function of −0.94 eV and +0.8 eV, respectively. Of particular interest is the alignment of the Fermi energy of an electrode with the LUMO of n-type organic semiconductors, which otherwise requires use of environmentally unstable low work-function electrodes for efficient electron injection.

The special structural and electronic properties of Buckminsterfullerene (C_{60}) make it a valuable material for a number of applications including single molecule[17] and thin film organic electronic devices.[18,19] Much effort has been devoted to understand and control the assembly of C_{60}, since it is key to optimizing the performance of C_{60} thin-film-based applications such as solar cells.[20,21] Consequently, the molecular orientation and supramolecular organization of C_{60} monolayers on metal (Au[22,23,24] Ag,[25,26] Cu[27,28]), inorganic (Si[29,30], GaAs,[31] Ge[32]) as well as organic (porphyrins,[33] oligothiophenes,[34,35] pentacene[36]) semiconductors have been extensively studied. In contrast, adsorption of C_{60} onto organothiols has been rarely explored. Vapor deposition of C_{60} on alkanethiol SAMs showed the formation of close packed islands[37] or one-dimensional chains[38] that were suggested to be residing on top of the SAM molecules. It was recently suggested that C_{60} molecules penetrate octanethiol[39] and 11-phenoxyundecanethiol SAMs[40] by forming islands (chains, hexagonal and cubic close packed domains) that are intermixed with the thiol molecules.

Surprisingly, adsorption of C_{60} onto aromatic SAMs such BT and PFBT has not yet been reported, although these SAMs, as mentioned above, are of particular interest in molecular electronic devices.

In this work, the structural properties of BT and PFBT SAMs formed on Au(111) and the kinetics of the subsequent C_{60} adsorption are investigated by performing an *in-situ* STM experiment at the liquid-solid interface. Using X-ray photoelectron spectroscopy (XPS) we demonstrate that, in contrast to a previous reports, [39,40] the thiol molecules are not displaced during

C_{60} adsorption from solution but instead form an adlayer on top of the SAM. STM characterization reveals both slight structural differences between BT and PFBT SAMs and dramatically different abilities to direct the adsorption of C_{60} molecules from solution.

4.3 Results and discussion

4.3.1 Self-assembly of PFBT and BT on Au(111)

The electronic properties of BT and PFBT SAMs, especially the surface potential, are closely related to their structural order and molecular coverage.[41,42] The study of the structure and molecular orientation of these SAMs thus provides an opportunity to investigate the effect of different dipole moments within SAMs on the morphology of subsequent organic layers.

The self-assembly of BT and PFBT on Au (111) has been extensively studied using various analytical techniques.[43,44,45,46,47,48,49,50,51,52,53,54] For instance, STM characterization of BT adsorption at room temperature reveals either completely disordered SAM or small ordered domains (less than 15 nm^2).[50] Long range ordered BT and PFBT SAMs with different structural lattices (Table 4.S1) have been observed under specific preparation conditions (long incubation time of 190 h[51] , elevated temperature of 75 °C,[52,53] exchange with a pre-adsorbed cyclohexanethiol SAMs[54]). Such a dependence of the SAM structure on the preparation mode and a variety of contradictory reports complicates comparisons between BT and PFBT SAMs, and justifies further experiment performed under identical conditions.

Fig. 4.1 shows a representative STM image of SAMs prepared by immersion of Au(111) in ethanol solutions of BT and PFBT (1 mM) for 18 h at 60 °C. Large scale STM images of BT and PFBT SAMs at the air-solid interface show structural domains consisting of ordered molecular-size features. Within these domains, one can distinguish pits and islands with an apparent STM height of ~±2.4 Å which corresponds to the height of a monoatomic Au(111) layer. These features have been previously observed on both aliphatic and aromatic SAMs and were attributed to the relaxation of the herringbone reconstruction of Au(111) and the release of Au adatoms. The mobility of these adatoms determines whether islands or pits are preferentially formed. In the PFBT case, large islands were observed due to the low mobility of adatoms which assemble into islands instead of diffusing to the step edges, as for the BT SAM case.[55]

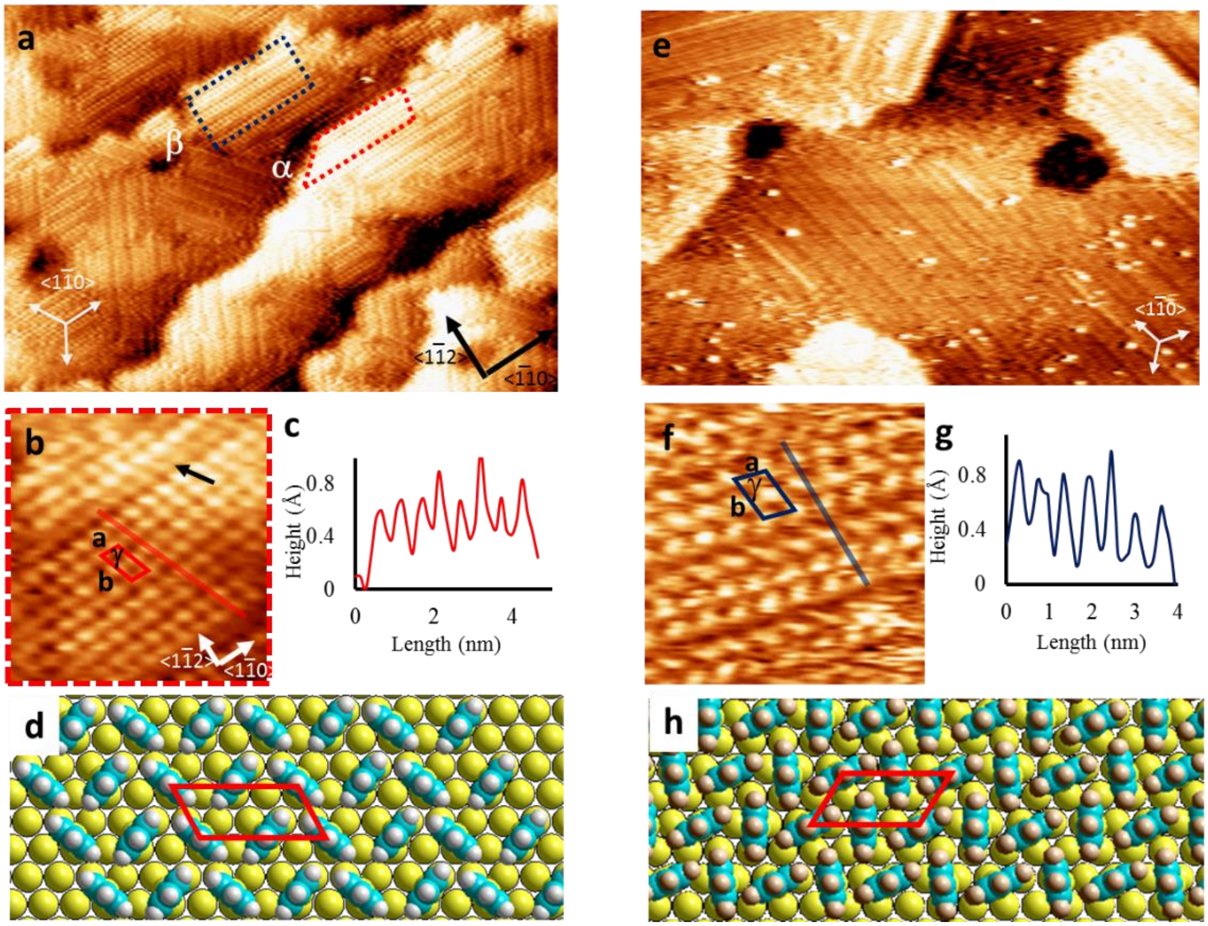

Figure 4.1. (a) Large scale STM image of BT SAMs on Au(111) (54×40 nm^2). The blue and red dashed rectangles highlight α and β phases. (b) High resolution STM image of α phase (7×7 nm^2), unit cell: a=0.54±0.05 nm, b=1.1±0.05, γ= 63±3°. (c) Cross-section height profile along the red line in (b). (d) Molecular model of α phase of BT SAM. (e) and (f) large scale (54×40 nm^2) and high resolution STM images (7×7 nm^2) of PFBT SAM, unit cell: a=0.58±0.05 nm, b=0.98±0.05 nm, γ= 64±4° respectively. (g) Cross-section height profile along the blue line in image (f). (h) Molecular model of PFBT SAM. (a,b) (V_b = 400 mV, I_t = 0.3 nA), (e,f) (V_b = 200 mV, I_t = 0.2 nA).

The BT and PFBT are resolved as bright spots forming parallel stripes oriented along one of the three preferential $\langle 1\bar{1}0\rangle$ directions reflecting the 3-fold symmetry of the underlying Au(111) (Fig. 4.1a,1e and 4.S3c). High resolution STM images of BT SAMs reveals the formation of two different phases, in a ~1:3 ratio, here referred to as the α phase and β phase (Figures 4.1b and 4.2a).

The α phase is described by an oblique unit that contains two molecules and has the parameters a=0.54±0.05 nm; b=1.1±0.05 γ= 63±3°. A comparison of the dimensions and orientation of the unit cell with the underlying Au(111) lattice suggests a $a_h(\sqrt{3} \times 2\sqrt{3})R30°$ commensurate structure, where a_h = 2.89 Å is the closest neighbour interatomic distance in the Au

[111] plane. The unit cell has been measured is consistent with a herringbone-like arrangement of BT molecules. This type of packing was frequently observed for aromatic thiols.[56,57,58,59]

In the β phase (Fig. 4.2), each 3rd stripe appears with a lower brightness (lower STM height) which results in a unit cell that contains three molecules and has the parameters of a=0.52±0.5 nm; b=1.5±0.1 nm, γ= 63±3°, suggesting a $a_h(\sqrt{3} \times 3\sqrt{3})R30°$ structure in comparison to the Au(111) lattice. The unit cells of the α and β phases are superimposable, having identical intermolecular distance of ~5 Å (√3a) (along the **a** and **b** directions of the unit cell) and differ only in the molecular contrast. The possible origin of this contrast difference could be Au reconstruction below the SAM or different degree of tilt of the phenyl rings. Occasionally, contrast switching that is randomly occurring between adjacent molecular rows or within the same row has been observed at the phase boundary (Fig. 4.S1).

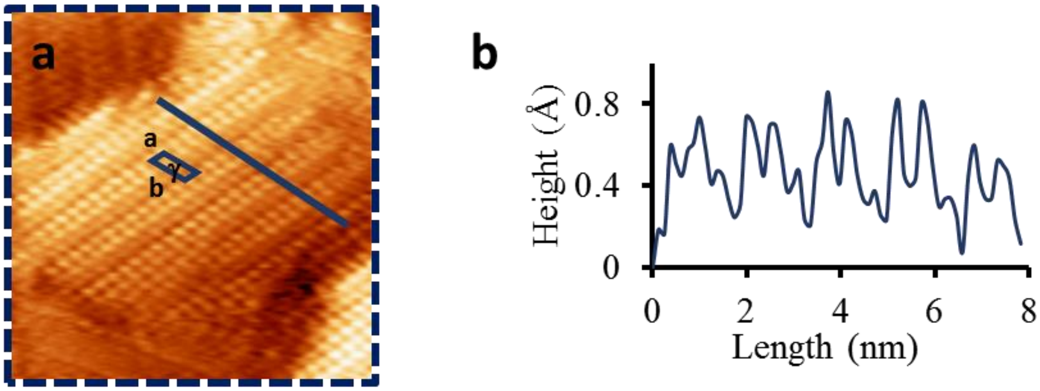

Figure 4.2. (a) High resolution STM image of the β phase of BT SAM (14×14 nm^2). Unit cell parameters are: a=0.52±0.05 nm; b=1.5±0.1 nm; γ= 63±3°. (b) Cross-section height profile along the blue line in image (a). V_b = 200 mV, I_t = 0.2 nA.

Overall, the measured lattices of BT SAM in the α and β phases are well described by a commensurate $(m\sqrt{3}\times n\sqrt{3})R30°$ structure (m and n are integers) commonly reported for arenethiol and alkanethiols on Au(111).[1,2,3]

High resolution STM imaging of PFBT SAMs provides the determination of a unit cell of a= 0.58±0.05 nm; b = 0.98 ±0.05 nm; γ = 62±2°, containing two non-equivalent molecules. This likely corresponds to the commensurate $a_h(2 \times 2\sqrt{3})R30°$ (Fig. 4.1f). In contrast to BT SAM, the herringbone-like arrangement of PFBT molecules is clearly identified from the high resolution STM image.

In summary, BT and PFBT molecules have similar lattices structure within experimental errors and differ mostly in their terminal atom (H/F) and the dipole moment. In the following section we study the effect of BT and PFBT SAMs in guiding the formation of well-ordered C_{60} molecular nanostructures.

4.3.2 Self- assembly of C_{60} on SAM-modified gold.

Figures 4.3, 4.4**,** and 4.S2 show sequential STM images following the addition of a C_{60} solution in phenyloctane (~1 mM) on BT, PFBT, and C8SH SAMs, respectively.

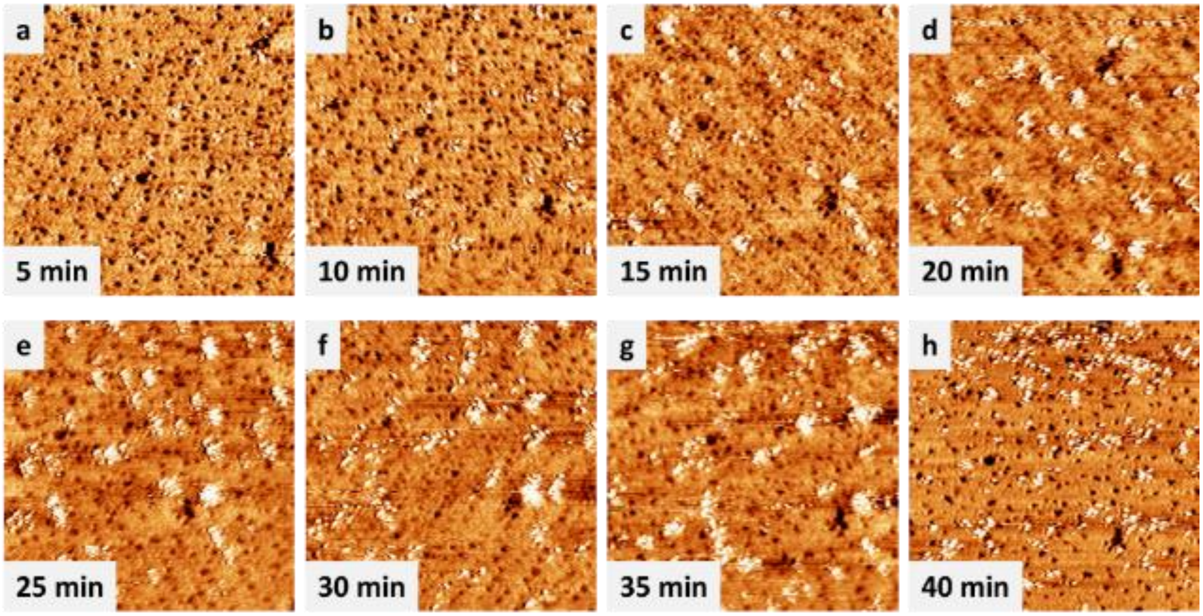

Figure 4.3. Sequential STM images (113×113 nm^2) recorded in 1 mM C_{60}/phenyloctane on the BT SAM modified Au(111). V_b = 400 mV, I_t = 0.2 nA.

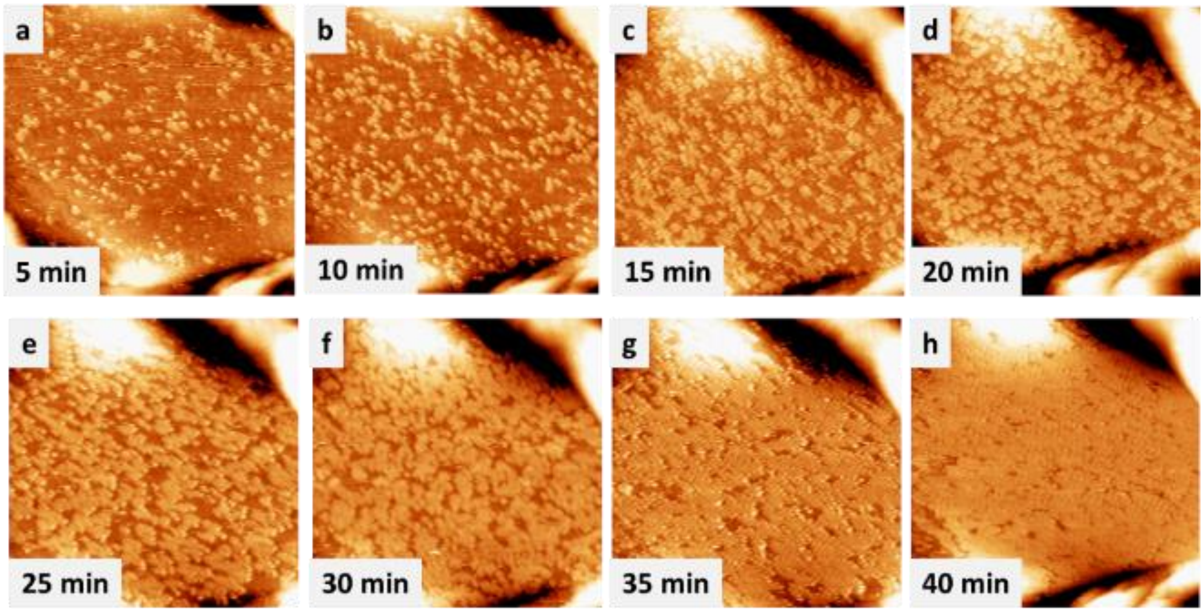

Figure 4.4. Sequence of STM images (94×94 nm^2) recorded in 1 mM C_{60}/phenyloctane on the PFBT SAM modified Au(111). V_b = 400 mV, I_t = 0.2 nA.

Adsorption of C_{60} on a BT SAM initially results in isolated bright islands with an apparent height of ca. 4 Å and a lateral size of ~1 nm, which could be attributed to individual fullerenes (Fig.4.3).[60,61] Their population increases with time and small aggregates of 2-5nm become visible after ~10 min. Similarly, only disordered aggregates of C_{60} have been observed on C8SH-Au (Fig. 4.S2, 4.S3).

However, the behaviour of C_{60} on PFBT SAM is very different: bright islands of 2-6 nm size are formed within 5 min and their size keeps increasing until a continuous film is formed within ~40 min. The analysis of the height profile of C_{60} on PFBT (Fig. 4.5) shows an apparent height 0.4 ± 0.1 nm, similar to the height measured for C_{60} on BT and C8SH SAMs (Fig. 4.S3). Occasional areas with a double height (0.9 ± 0.1 nm) can be reasonably attributed to two C_{60} layers.

Interestingly, inspection of the spatial distribution of C_{60} molecules in the second layer reveals that they are preferentially located at the edges of the underlying C_{60} islands, and their population decreases with time from ~30% at 15 min, to ~7% at 25 min, to ~1% at 35 min (Fig. 4.5). These observations suggest a mechanism where C_{60} monolayer formation is initiated by nucleation and growth of 2D islands in the submonolayer regime, then the subsequent C_{60} molecules adsorb either at the free area of the PFBT-Au substrate or on top of the pre-existing C_{60} islands where they diffuse to edges and cross the Ehrlich-Schwoebel barrier (step-edge barrier[62]) contributing to the complete formation of the monolayer. A similar layer-by-layer growth mechanism has been previously suggested for C_{60} multilayer formation.[63,64]

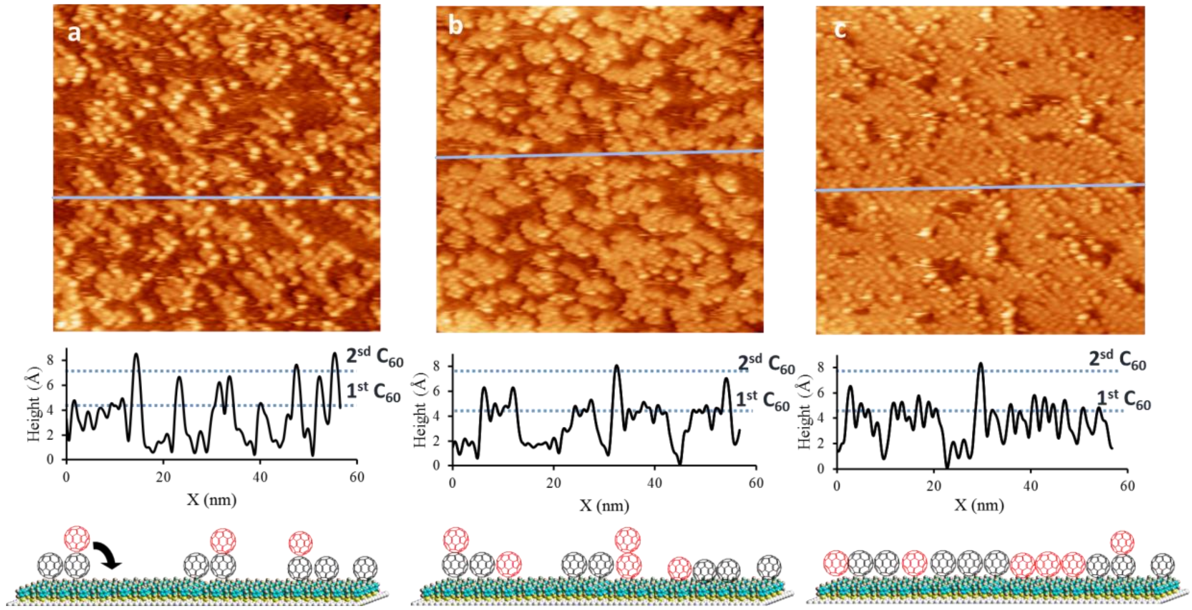

Figure 4.5. Surface profile recorded according to the blue line showing the evolution of the height of C_{60} molecules deposited on top of PFBT modified gold substrate. The acquisition time is (a) 15 minutes, (b) 25 minutes, (c) 35 minutes. 57×57 nm^2. V_b = 400 mV, I_t = 0.2 nA.

The analysis of the surface coverage vs time (Fig. 4.6) provides quantitative information on the growth kinetics of the C_{60} monolayer. The sigmoidal form of the obtained curve is consistent with the Kolmogorov–Johnson–Mehl–Avrami (KJMA)[65,66] kinetic model (Equation 4.1)

$$\theta(t) = 1 - e^{-kt^n} \tag{4.1}$$

Where $\theta(t)$ is surface coverage at time t and k is an observed rate constant which depends on both the nucleation and growth rate. The exponent n represents the dimensionality of the growth and the time dependence nucleation which was fixed at 2 considering 2D assembly under study, wherein nucleation proceeds rapidly to completion. This model, originally devised to describe phase transitions in metal alloys,[67,68] has been recently used to predict the kinetics of self-assembled monolayer formation by molecular exchange.[69,70,71]

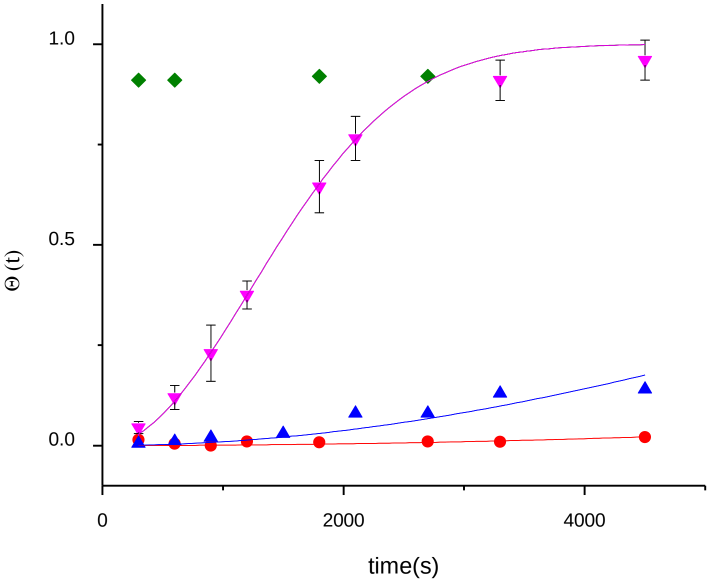

Figure 4.6. Evolution of molecular coverage of C_{60} adsorbed from 1mM solution in phenyloctane on bare Au(111)(◆), PFBT(▼), BT(●), and C8SH(▲) modified Au(111) substrate. Curves are fits to KJMA model.

A number of alternative kinetics models that are typically used for predicting the kinetics of SAM formation,[72] including Langmuir adsorption models, were considered but they cannot fit the observed sigmoidal shape of the binding isotherm. The better suitability of KJMA over Langmuir models is expected considering the slow nucleation process of C_{60} assembly[73]

Fitting the curves to the KJMA model leads to k of $3.3 \pm 0.2\times10^{-7}$ s^{-1}, $9.5 \pm 1.2\times10^{-9}$ s^{-1}, and $1.1 \pm 0.3\times10^{-9}$ s^{-1}, for PFBT, C8SH and BT, respectively. The much faster growth of C_{60} on PFBT SAMs (as compared to BT and C8SH) was somewhat unexpected considering the known lipophobic properties of fluoroorganic surfaces.

The measurement of water contact angle on BT and PFBT SAMs shows values (75 ± 2° and 80 ± 2° respectively) suggesting that the PFBT surface is slightly more hydrophobic than BT. Both SAMs show similarly lipophilicity as judged by the low wetting contact angle measured for phenyloctane (<10°). The high lipophilicity of PFBT was somewhat unexpected considering the known liphophobic properties of fluorocarbons (hexadecane contact angle of 71°)[74], although high wettability of perfluorobiphenyl-4,4’-dithiol has been previously reported.[75]

The accelerated growth of C_{60} film might be explained by the larger dipole moment of PFBT, leading to the induced dipole moment within the subsequent C_{60} layers.[41,76,77] Although C_{60} itself does not have any dipole (or higher multipoles), it is a highly polarizable molecule lending itself to dipole−induced dipole interactions. Previous studies reported the use of dipole-induced dipole moment interactions for growing molecular porphyrin wires on insulating surface.[78]

The observation of ordered C_{60} assembly only on top of PFBT SAM demonstrates the major contribution of C-F···C and C-F···π interactions in driven the growth and the formation C_{60} monolayer. The importance of these intermolecular interactions has been previously recognized, both in small molecules and in proteins.[79] For example, X ray crystallography characterization of fluorinated tetraphenylporphyrins-fullerenes cocrystals has shown the crucial role of C-F- C_{60} interaction in dictating the structure of the obtained cocrystal.[80]

Another important question is whether PFBT SAMs remain intact upon C_{60} adsorption. The published papers on C_{60} adsorption on top of thiol SAM modified Au(111) substrate contain contrasting interpretations of the observed STM images.[37,38,39,40] The initial studies assumed that C_{60} is residing on top of SAM,[37,38] while the direct adsorption on Au(111), with displacement of thiol molecules was invoked in the more recent works.[39,40] In both cases, no direct evidence for either adsorption mode were provided.

To address the issue of the fate of a SAM upon C_{60} adsorption, we have characterized PFBT SAMs before and after adsorption of C_{60} molecules using XPS (Fig. 4.7, Table 4.1). The reduction of the F1s, S2p, and Au4f peaks intensity was observed upon deposition of C_{60} molecules. In itself, it could originate from either overlayer adsorption (attenuating the ejected core electrons) as well as with direct on-Au(111) adsorption due to displacement of PFBT molecules. However, the unchanging ratios of F/Au and S/Au peak areas before and after C_{60} adsorption indicates that no displacement of PFBT took place (Table 4.1). Deconvolution of the C1s peak reveals two main peaks C-C at (285 eV) and C-F at (287 eV) in addition to a small broad peak at 289 eV likely attributed to traces of C=O. Consistent with the previous observations, the C-F/Au signal remains constant while C-C/Au increases upon C_{60} adsorption. Accordingly, we conclude that C_{60} forms an overlayer on top of the PFBT SAM.

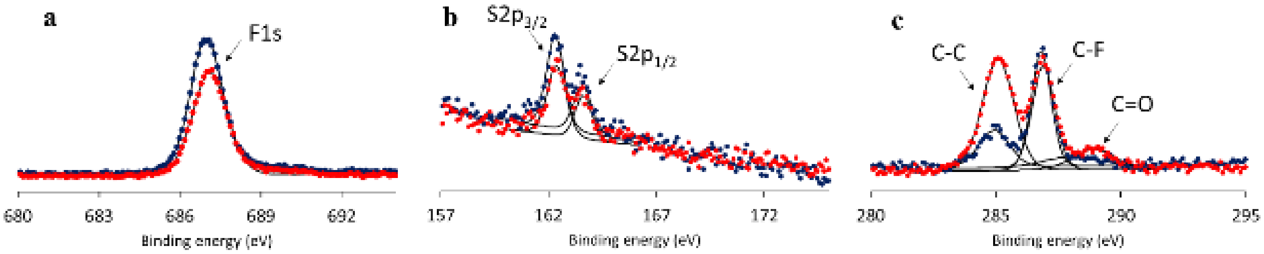

Figure 4.7. XPS spectra of (a) F1s, (b) S2p, and (c) C1s for PFBT (●) and C_{60}-PFBT (●) adlayers, respectively.

Table 4.1. Peak area ratios of PFBT and C_{60}/PFBT modified Au substrate.

	F/Au ($\times 10^{-3}$)	S/Au ($\times 10^{-3}$)	S/F ($\times 10^{-3}$)	C-C/Au ($\times 10^{-3}$)	C-F/Au ($\times 10^{-3}$)	C(total)/Au ($\times 10^{-3}$)
PFBT	60±3	4.2±0.1	71±5	5±1	10±1	17±1
C_{60}/PFBT	58±1	4.5±0.2	67±4	12±2	13±1	38±3

To explore the formation of C_{60} multilayers on PFBT SAM, further investigation of C_{60} assembly was performed after few hours of C_{60} solution deposition. As shown in Fig. 4.8, C_{60} multilayers (at least three apparent layers) have been formed likely due to the slow evaporation of the solvent. The apparent height difference between these layers was measured to be approximatively 1 Å. This is lower than the previous height measured (4 Å) for a C_{60} monolayer on top of PFBT (BT and C8SH). This low apparent height is likely attributed to the low tunneling current across organic multilayers as has been previously reported for alkali halides multilayers.[81] The C_{60} molecules in two apparent layers adopt a closely packed hexagonal lattice with a unit cell of a=b=1.0± 0.2 nm; α=60 ± 2° assigned to the $(2\sqrt{3} \times 2\sqrt{3})R30^0$ structure. Similar packing has also been observed for C_{60} adsorbed on bare gold at phenyloctane-Au interface (a=b=1.07± 0.1nm; α=63 ± 3°) (Fig. 4.S4).

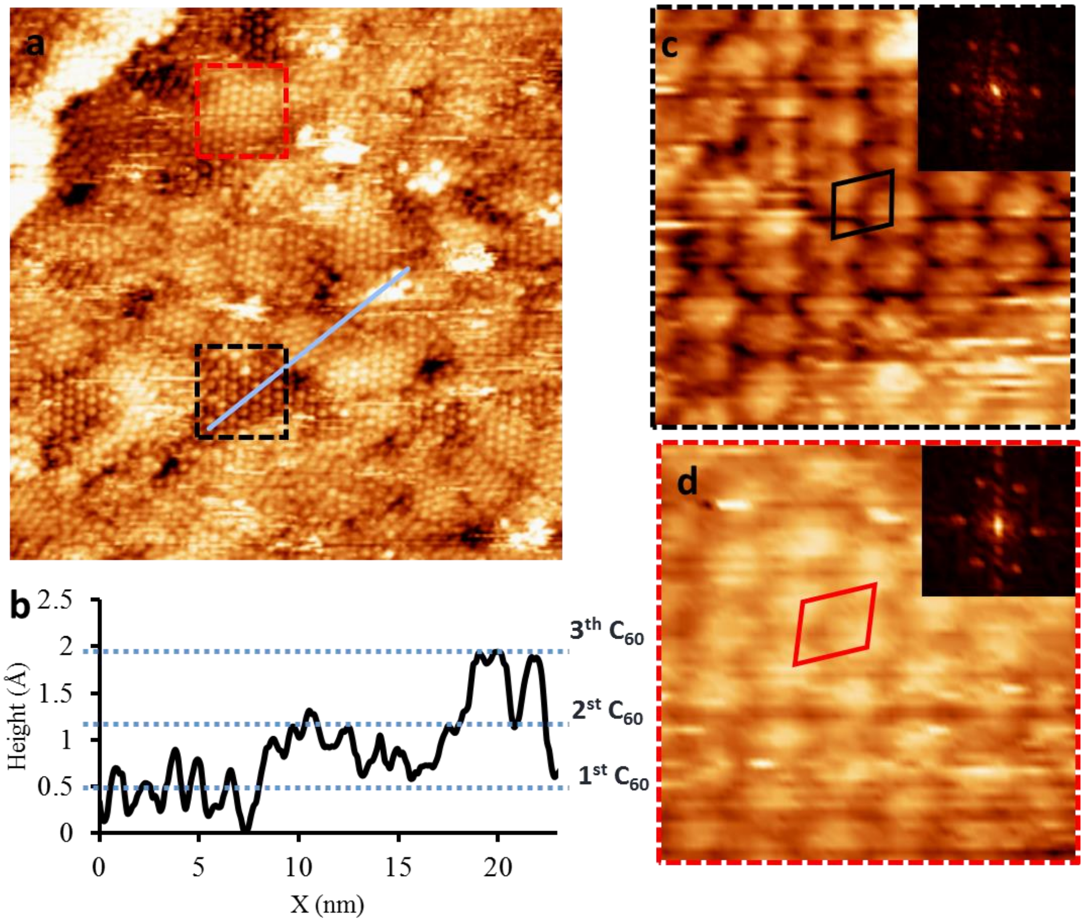

Figure 4.8. STM image showing the multilayer formation on top of PFBT-Au. The black and red boxes highlight the first and second layer respectively. 50×50 nm^2 (b) Surface profile recorded according to the blue line showing the first, second, and third C_{60} layer. (c) and (d) High resolution STM image of first and second monolayers showing the formation hexagonal close network (c) 6×6 nm^2 (d) 7×7 nm^2. Unit cell parameters are a=b=1.0± 0.2nm; α=60 ± 2^0. Inset Fast Fourier transform (FFT) images. V_b = 400 mV, I_t = 0.2 nA.

4.4 Conclusions

The packing of BT and PFBT on an Au(111) surface and subsequent adsorption of C_{60} have been investigated by STM at the liquid-solid interface. BT and PFBT molecules show similar lattice structures with respect to the surface normal. The inductive effect of the fluorine substituent in PFBT molecules induce a rapid growth of C_{60} multilayer on PFBT SAMs compared to BT and C8SH SAMs. These multilayers were shown by XPS to reside on top of the PFBT SAM and not within the SAM. STM characterisation reveals a close packed hexagonal lattice with a $(2\sqrt{3} \times 2\sqrt{3})R30^0$ structure of C_{60} layers. These results contribute to the fundamental understanding of molecular growth processe of organic semiconductors which is a prerequisite for optimizing the performance in thin film-based devices.

4.5 Experimental section

Preparation of the SAMs. Au(111) substrates with atomically flat terraces were prepared by thermal evaporation of gold onto freshly cleaved mica sheets preheated at 450 °C under a pressure of 10^{-7}-10^{-8} Pa. The SAMs of benzenthiol (BT) and pentafluorobenzenethiol (PFBT) were prepared by immersing the Au/mica in a 0.1mM EtOH (ACS reagent) solution of the corresponding thiols at 60 °C for 2 to 18 hours. After SAM formation, the samples were rinsed with pure EtOH, dried under a stream of ultrapure N_2 and imaged either at solid-air or solid-phenyloctane interface. Fullerene (C_{60}) molecules were dissolved in phenyloctane (Sigma-Aldrich, 98%) and used directly without further purification. A volume of 10 to 15 μL of 1mM phenyloctane solutions of C_{60} have been deposited on BT or PFBT-Au modified gold substrate. The resulting assembly has been investigated at liquid–solid interface.

Scanning tunneling microscopy (STM). All STM experiments were performed under ambient conditions using a Multimode8^{TM} equipped with a Nanoscope^{TM} V controller (Bruker, Santa Barbara, CA) and Nanoscope 8.15r3 software. The STM tips were mechanically cut from Pt/Ir wire (80/20, diameter 0.25 mm, Nanoscience). All STM-images were obtained in the constant current mode using an A scanner and low current STM converter by applying a tunneling current I_{set} of 70 to 400 pA and a sample bias V_{set} of -300 to 600 mV. Calibration of the piezoelectric positioners was verified by atomic resolution imaging of graphite. The raw images were processed from WSxM5.0 software.

X-ray photoelectron spectroscopy (XPS). XPS spectra were recorded on a ThermoFisher Scientific K-alpha instrument equipped with a monochromatic Al Kα X-ray source (1486.6 eV). Spectral energies were calibrated by setting the binding energy of Au $4f_{7/2}$ (84.0 eV). The peak-fitting procedure was performed using the Thermo Avantage software (version 4.60).

Density Functional Theory Calculations. The DFT calculations were performed by Dr. Olexandr Voznyy using GGA + empirical (Grimme) van der Waals. The adsorption energy has been calculated for C_{60} placed on top of the herringbone structure of BT and PFBT SAMs.

References

---

[1] Love, J. C.; Estroff, L. A.; Kriebel, J. K.; Nuzzo, R. G.; Whitesides, G. M.Self-Assembled Monolayers of Thiolates on Metals as a Form of Nanotechnology. *Chem. Rev.* **2005**, *105*, 1103–1170.

[2] Smith, R. K.; Lewis, P. A.; Weiss, P. S. Patterning Self-Assembled Monolayers. *Prog. Surf. Sci.* **2004**, *75*, 1– 68.

[3] Vericat, C.; Vela, M. E.; Benitez, G.; Carro, P.; Salvarezza, R. C.Self-Assembled Monolayers of Thiols and Dithiols on Gold: New Challenges for a Well-Known System. *Chem. Soc. Rev.* **2010**, *39*, 1805–1834.

[4] Gooding, J. J.; Mearns, F.; Yang, W.; Liu, J. Self-Assembled Monolayers into the 21st Century: Recent Advances and Applications. *Electroanalysis* **2003**, *15*, 81–96.

[5] Xia, Y.; Whitesides, G. M. Soft Lithography. *Angew. Chem., Int. Ed.* **1998**, *37*, 550–575.

[6] Lio, A.; Charych, D. H.; Salmeron, M. Comparative Atomic Force Microscopy Study of the Chain Length Dependence of Frictional Properties of Alkanethiols on Gold and Alkylsilanes on Mica. *J. Phys. Chem. B* **1997**, *101*, 3800–3805.

[7] Scherer, J.; Vogt, M. R.; Magnussen, O. M.; Behm, R. J. Corrosion of Alkanethiol-Covered Cu(100) Surfaces in Hydrochloric Acid Solution Studied by in-Situ Scanning Tunneling Microscopy. *Langmuir* **1997**, *13*, 7045–7051.

[8] Campbell, I.; Rubin, S.; Zawodzinski, T.; Kress, J.; Martin, R.; Smith, D.; Barashkov, N.; Ferraris, J. P Controlling Schottky Energy Barriers in Organic Electronic Devices using Self-Assembled Monolayers. *J. Phys. Rev. B.* **1996**, *54*, 14321–14324.

[9] Meijer, E. J.; de Leeuw, D. M.; Setayesh, S.; van Veenendaal, E.; Huisman, B. H.; Blom, P. W. M.; Hummelen, J. C.; Scherf, U.; Klapwijk, T. M. Solution-Processed Ambipolar Organic Field-Effect Transistors and Inverters. *Nat. Mater.* **2003**, *2*, 678–682.

[10] de Boer, B.; Hadipour, A.; Mandoc, M. M.; van Woudenbergh, T.; Blom, P. W. M. Tuning of Metal Work Functions with Self-Assembled Monolayers. *Adv. Mater.* **2005**, *17*, 621–625.

[11] Evans, S. D.; Ulman A. Surface potential studies of alkyl-thiol monolayers adsorbed on gold. *Chem. Phys. Lett*. **1990**, *170*, 462−466.

[12] Alloway, D. M.; Hofmann, M.; Smith, D. L.; Gruhn, N. E.; Graham, A. L.; Colorado, R.; Wysocki, V. H.; Lee, T. R.; Lee, P. A.; Armstrong, N. R. Interface Dipoles Arising from Self-Assembled Monolayers on Gold: UV−Photoemission Studies of Alkanethiols and Partially Fluorinated Alkanethiols. *J. Phys. Chem. B* **2003**, *107*, 11690−11699.

[13] Bock, C.; Pham, D. V.; Kunze, U.; Käfer, D.; Witte, G.; Wöll, C. Improved morphology and charge carrier injection in pentacene field-effect transistors with thiol-treated electrodes. *J. Appl. Phys*. **2006**, *100*, 114517.

---

[14] Gundlach, D. J.; Royer, J. E.; Park, S. K.; Subramanian, S.; Jurchescu, O. D.; Hamadani, B. H.; Moad, A. J.; Kline, R. J.; Teague, L. C.; Kirillov, O.; Richter, C. A.; Kushmerick, J. G.; Richter, L. J.; Parkin, S. R.; Jackson T. N.; Anthony, J. E. Contact-Induced Crystallinity for High-Performance Soluble Acene-Based Transistors and Circuits. *Nat. Mater.* 2008, *7*, 216–221.

[15] Hong, J.-P.; Park, A.-Y.; Lee, S.; Kang, J.; Shin, N.; Yoon, D. Y. Tuning of Ag Work Functions By Self-Assembled Monolayers of Aromatic Thiols For an Efficient Hole Injection For Solution Processed Triisopropylsilylethynyl Pentacene Organic Thin Film Transistors. *Appl. Phys. Lett.* **2008,** *92*, 143311–143314.

[16] Reichenbaecher, K.; Suess, H. I.; Hulliger, J. Fluorine in Crystal Engineering–the Little Atom that Could. *Chem. Soc. Rev.* **2005**, *34*, 22–30.

[17] Park, H.; Park, J.; Lim, A.; Anderson, E.; Alivisatos, A.; McEuen, P. Nanomechanical oscillations in a single-C_{60} transistor. *Nature* **2000**, *407*, 57–60.

[18] Yu, G.; Gao, J.; Hummelen, J. C.; Wudl, F.; Heeger, A. J.Polymer Photovoltaic Cells: Enhanced Efficiencies via a Network of Internal Donor-Acceptor Heterojunctions. *Science* **1995**, *270*, 1789– 179.

[19] Mutolo, K. L.; Mayo, E. I.; Rand, B. P.; Forrest, S. R.; Thompson, M. E.Enhanced Open-Circuit Voltage in Subphthalocyanine/C_{60} Organic Photovoltaic Cells. *J. Am. Chem. Soc.* **2006**, *128*, 8108–8109.

[20] Campoy-Quiles, M.; Ferenczi, T.; Agostinelli, T.; Etchegoin, P. G.; Kim, Y.; Anthopoulos, T. D.; Stavrinou, P. N.; Bradley, D. D. C.; Nelson, J. Morphology Evolution via Self-Organization and Lateral and Vertical Diffusion in Polymer:Fullerene Solar Cell Blends. *Nat. Mater.* **2008**, *7*, 158–164.

[21] Li, Z.; Wong, H. C.; Huang, Z.; Zhong, H.; Tan, C. H.; Tsoi, W. C.; Kim, J. S.; Durrant, J. R.; Cabral, J. T. Performance Enhancement of Fullerene-Based solar Cells by Light Processing. *Nat. Commun.* **2013**, *4*, 2227.

[22] Wilson, R. J.; Meijer, G.; Bethune, D. S.; Johnson, R. D.; Chambliss, D. D.; de Vries, M. S.; Hunziker, H. E.; Wendt, H. R. Imaging C_{60} Clusters on a Surface Using a Scanning Tunnelling Microscope. *Nature* **1990**, *348*, 621–622.

[23] Altman, E. I.; Colton, R. Determination of the orientation of C_{60} adsorbed on Au(111) and Ag(111). *J. Phys. Rev. B.* **1993**, *48*, 18244–18249.

[24] Altman, E. I.; Colton, R. J. Interaction of C_{60} with the Au(111) $23\times\sqrt{3}$ reconstruction. *J. Vac. Sci. Technol., B.* **1994**, *12*, 1906–1909.

[25] Sau, J. D.; Neaton, J. B.; Choi, H. J.; Louie, S. G.; Cohen, M. L. Electronic Energy Levels of Weakly Coupled Nanostructures: C_{60}-Metal Interfaces. *Phys. Rev. Lett.* **2008**, *101*, 026804.

[26] Altman, E. I.; Colton, R.J. Determination of the orientation of C_{60} adsorbed on Au(111) and Ag(111). *Phys Rev, B* **1993**, *48*, 18244–18249.

---

[27] Hebard, A. F.; Ruel, R. R.; Eom, C. B. Charge transfer and surface scattering at Cu-C_{60} planar interfaces. *Phys. Rev. B* **1996**, *54*, 14052–14060.

[28] Larsson, J. A.; Elliott, S. D.; Greer, J. C.; Repp, J.; Meyer, G.; Allenspach, R. Orientation of individual C_{60} molecules adsorbed on Cu(111): Low-temperature scanning tunneling microscopy and density functional calculations. *Phys. Rev. B* **2008**, *77*, 115434.

[29] Yao, X.; Ruskell, T. G.; Workman, R. K.; Sarid, D.; Chen, D., Scanning tunneling microscopy and spectroscopy of individual C_{60} molecules on Si(100)-(2 × 1) surfaces. *Surf. Sci.* **1996,** *366,* 3,743–749.

[30] Hou, J. G.; Jinlong, Y.; Haiqian, W.; Qunxiang, L.; Changgan, Z.; Hai, L.; Wang, B.; Chen, D. M.; Qingshi, Z., Identifying molecular orientation of individual C_{60} on a Si(111)-(7 × 7) surface. *Phys. Rev. Lett.* **1999,** *83,* 3001–3004.

[31] Li, Y. Z.; Patrin, J. C.; Chander, M.; Weaver, J. H.; Chibante, L. P. F.; Smalley, R. E., Ordered overlayers of C_{60} on GaAs(110) studied with scanning tunneling microscopy. *Science* **1991,** *252*, 547–548.

[32] Kristin, R.; Wirth, K. R.; Zegenhagen, J. STM study of the adsorption of single C_{60} molecules on the Ge(111)-c(2 × 8) surface. *Surf. Sci.* **1996**, *351*, 13–23.

[33] Bonifazi, D.; Spillmann, H.; Kiebele, A.; de Wild, M.; Seiler, P.; Cheng, F.; Güntherodt, H.-J.; Jung, T.; Diederich, F., Supramolecular Patterned Surfaces Driven by Cooperative Assembly of C_{60} and Porphyrins on Metal Substrates. *Angew. Chem., Int. Ed.* **2004,** *43*, 4759–4763.

[34] Mena-Osteritz, E.; Bäuerle, P., Complexation of C_{60} on a Cyclothiophene Monolayer Template. *Adv. Mater*. **2006**, *18*, 447–451.

[35] MacLeod, J. M.; Ivasenko, O.; Fu, C.; Taerum, T.; Rosei, F.; Perepichka, D. F., Supramolecular Ordering in Oligothiophene−Fullerene Monolayers. *J. Am. Chem. Soc.* **2009,** *131*, 16844–16850.

[36] Yang, Y.-C.; Chang, C.-H.; Lee, Y.-L., Complexation of Fullerenes on a Pentacene-Modified Au(111) Surface. *Chem. Mater.* **2007**, *19*, 6126–6130.

[37] Zeng, C. G.; Wang, H. Q.; Wang, B.; Yang, J. L.; Hou, J. G. Negative Differential-Resistance Device Involving Two C_{60} Molecules. *Appl. Phys. Lett.* **2000**, *77*, 3595–3597.

[38] Zeng, C. G.; Wang, B.; Li, B.; Wang, H. Q.; Hou, J. G. Self-Assembly of One-Dimensional Molecular and Atomic Chains Using Striped Alkanethiol Structures as Templates. *Appl. Phys. Lett.* **2001**, *79*, 1685–1687.

[39] Li, F.; Tang, L.; Zhou, W.; Guo, Q. Formation of Confined C_{60} Islands within Octanethiol Self-Assembled Monolayers on Au(111). *J. Phys. Chem. C.* **2009**, *113*, 17899–17903.

[40] Nakayama, M.; Kautz, N. A.; Wang, T.; Sibener, S. J. Formation of Rectangular Packing and One-Dimensional Lines of C_{60} on 11-Phenoxyundecanethiol Self-Assembled Monolayers on Au(111). *Langmuir* **2012**, *28*, 4694–4701.

---

[41] Schmidt, C.; Witt, A.; Witte, G. Tailoring the Cu(100) Work Function by Substituted Benzenethiolate Self-Assembled Monolayers. *J. Phys. Chem. A.* **2011**, *115*, 7234–7241.

[42] Hong, S.-Y.; Yeh, P.-C.; Dadap, J. I.; Osgood, R. M. Interfacial Dipole Formation and Surface-Electron Confinement in Low-Coverage Self-Assembled Thiol Layers: Thiophenol and p-Fluorothiophenol on Cu(111). *ACS Nano* **2012**, *6*, 10622–10631.

[43] Fuxen, C.; Azzam, W.; Arnold, R.; Witte, G.; Terfort, A.; Wöll, C. Structural Characterization of Organothiolate Adlayers on Gold: The Case of Rigid, Aromatic Backbones. *Langmuir* **2001**, *17*, 3689–3695.

[44] Tao, Y.-T.; Wu, C.-C.; Eu, J.-Y.; Lin, W.-L.; Wu, K.-C.; Chen, C.-H. Structure Evolution of Aromatic-Derivatized Thiol Monolayers on Evaporated Gold. *Langmuir* **1997**, *13*, 4018–4023.

[45] Yang, G. H.; Liu, G. Y.New Insights for Self-Assembled Monolayers of Organothiols on Au(111) Revealed by Scanning Tunneling Microscopy. *J. Phys. Chem. B* **2003**, *107*, 8746–8759.

[46] Dhirani, A.-A.; Zehner, W.; Hsung, R. P.; Guyot-Sionnest, P.; Sita, L.Self-Assembly of Conjugated Molecular Rods: A High-Resolution STM Study. *J. Am. Chem. Soc.* **1996**, *118*, 3319–3320.

[47] Wan, L.-J.; Terashima, M.; Noda, H.; Osawa, M. Molecular Orientation and Ordered Structure of Benzenethiol Adsorbed on Gold(111). *J. Phys. Chem. B.* **2000**, *104*, 3563–3569.

[48] Frey, S.; Stadler, V.; Heister, K.; Eck, W.; Zharnikov, M.; Grunze, M.; Zeysing, B.; Terfort, A. Structure of Thioaromatic Self-Assembled Monolayers on Gold and Silver. *Langmuir* **2001**, *17*, 2408–2415.

[49] Jung, H. H.; Won, Y. D.; Shin, S.; Kim, K. Molecular Dynamics Simulation of Benzenethiolate and Benzyl Mercaptide on Au(111). *Langmuir* **1999**, *15*, 1147–1154.

[50] Noh, J.; Park, H.; Jeong, Y.; Kwon, S. Structure and Electrochemical Behavior of Aromatic Thiol Self-Assembled Monolayers on Au(111). *Bull. Korean Chem. Soc.* **2006**, *27*, 403–406.

[51] Azzam, W.; Bashir, A.; Ulrich Biedermann, P.; Rohwerder, M.Formation of Highly Ordered and Orientated Gold Islands: Effect of Immersion Time on the Molecular Adlayer Structure of Pentafluorobenzenethiols (PFBT) SAMs on Au(111). *Langmuir* **2012**, *28*, 10192–10208.

[52] Kang, H.; Park, T.; Choi, I.; Lee, Y.; Ito, E.; Hara, M.; Noh, J. Formation of Large Ordered Domains in Benzenethiol Self-Assembled Monolayers on Au(111) Observed by Scanning Tunneling Microscopy. *Ultramicroscopy* **2009**, *109*, 1011–1014.

[53] Kang, H.; Lee, N.-S.; Ito, E.; Hara, M.; Noh, J. Formation and Superlattice of Long-Range-Ordered Self-Assembled Monolayers of Pentafluorobenzenethiols on Au(111). *Langmuir* **2010**, *26*, 2983–2985.

[54] Kang, H.; Lee, H.; Kang, Y.; Hara, M.; Noh, J. Two-Dimensional Ordering of Benzenthiol Self-Assembled Monolayers Guided by Displacement of Cyclohexanethiols on Au(111). *Chem. Commun.* **2008**, 5197–5199.

---

[55] Poirier, G. E. Mechanism of Formation of Au Vacancy Islands in Alkanethiol Monolayers on Au(111). *Langmuir* **1997**, *13*, 2019–2026.

[56] Kang, J. F.; Ulman, A.; Liao, S.; Jordan, R.; Yang, G.; Liu, G.-yu. Self-Assembled Rigid Monolayers of 4′-Substituted-4-mercaptobiphenyls on Gold and Silver Surfaces. *Langmuir* **2001**, *17*, 95–106.

[57] Käfer, D.; Witte, G.; Cyganik, P.; Terfort, A.; Wöll, C. A Comprehensive Study of Self-Assembled Monolayers of Anthracenethiol on Gold: Solvent Effects, Structure, and Stability. *J. Am. Chem. Soc.* **2006**, *128*, 1723–1732.

[58] Shaporenko, A.; Brunnbauer, M.; Terfort, A.; Grunze, M.; Zharnikov, M.Structural Forces in Self-Assembled Monolayers: Terphenyl-Substituted Alkanethiols on Noble Metal Surfaces. *J. Phys. Chem. B.* **2004**, *108*, 14462–14469.

[59] Yang, G. H.; Liu, G. Y. New Insights for Self-Assembled Monolayers of Organothiols on Au(111) Revealed by Scanning Tunneling Microscopy. *J. Phys. Chem. B.* **2003**, *107*, 8746–8759.

[60] Paßens, M.; Waser, R.; Karthäuser, S. Enhanced fullerene–Au(111) coupling in (2√3 × 2√3)R30° superstructures with intermolecular interactions. *Beilstein J. Nanotechnol.* **2015,** *6*, 1421–1431.

[61]. Pawlak, R.; Kawai, S.; Fremy, S.; Glatzel, T.; Meyer, E. High-Resolution Imaging of C_{60} Molecules Using Tuning-Fork-Based Non-contact Atomic Force Microscopy. *J. Phys.: Condens Matter* **2012**, *24*, 084005-1–084005-10.

[62] Bommel, S.; Kleppmann, N.; Weber, C.; Spranger, H.; Schäfer, P.; Novak, J.; Roth, S. V.; Schreiber, F.; Klapp, S. H. L.; Kowarik, S.Unravelling the Multilayer Growth of the Fullerene C_{60} in Real Time. *Nat. Commun.* **2014**, *5*, 5388–5395.

[63] Zhong, D.; Hirtz, M.; Wang, W.; Dou, R.; Chi, L.; Fuchs, H. Kinetics of Island Formation in Organic Film Growth. *Phys. Rev. B* **2008**, *77*, 113404-1–113404-4.

[64] Xiao, W. D.; Ruffieux, P.; Ait-Mansour, K.; Groning, O.; Palotas, K.; Hofer, W. A.; Groning,P.; Fasel, R. Formation of a Regular Fullerene Nanochain Lattice. *J. Phys. Chem. B.* **2006**, *110*, 21394–21398.

[65] Khawam, A.; Flanagan, D. R.Solid-State Kinetic Models: Basics and Mathematical Fundamentals. *J. Phys. Chem. B* **2006**, *110*, 17315–17328.

[66]Finney, E. E.; Finke, R. G.Is There a Minimal Chemical Mechanism Underlying Classical Avrami-Erofe'ev Treatments of Phase-Transformation Kinetic Data? *Chem. Mater.* **2009**, *21*, 4692–4705.

[67] Avrami, M. Kinetics of Phase Change. I. General Theory. *J. Chem. Phys*. **1939**, *7*, 1103−1112.

[68] Avrami, M. Kinetics of Phase Change. II. Transformation-Time Relations for Random Distribution of Nuclei. *J. Chem. Phys*. **1940**, *8*, 212−224.

[69] Saavedra, H. M.; Barbu, C. M.; Dameron, A. A.; Mullen, T. J.; Crespi, V. H.; Weiss, P. S. 1-Adamantanethiolate Monolayer Displacement Kinetics Follow a Universal Form *J. Am. Chem. Soc.* **2007**, *129*, 10741–10746.

---

[70] Wang, Y.; Zeiri, O.; Neyman, A.; Stellacci, F.; Weinstock, I. A. Nucleation and Island Growth of Alkanethiolate Ligand Domains on Gold Nanoparticles. *ACS Nano* **2012**, *6*, 629–640.

[71] Hohman, J. N.; Thomas, J. C.; Zhao, Y.; Auluck, H.; Kim, M.; Vijselaar, W.; Kommeren, S.; Terfort, A.; Weiss, P. S.Exchange Reactions between Alkanethiolates and Alkaneselenols on Au{111}. *J. Am. Chem. Soc.* **2014**, *136*, 8110–8121.

[72] Kassam, A.; Bremner, G.; Clark, B.; Ulibarri, G.; Lennox, R. B. Place Exchange Reactions of Alkyl Thiols on Gold Nanoparticles. *J. Am. Chem. Soc.* **2006**, *128*, 3476–3477.

[73] Liu, Y.; Shen, L. From Langmuir Kinetics to First- and Second-Order Rate Equations for Adsorption. *Langmuir* **2008**, *24*, 11625–11630.

[74] Bain, C. D.; Troughton, E. B.; Tao, Y. T.; Evall, J.; Whitesides, G. M.; Nuzzo, R. G.Formation of Monolayer Films by the Spontaneous Assembly of Organic Thiols from Solution onto Gold *J. Am. Chem. Soc.* **1989**, 111, 321– 335

[75] De Boer, B.; Meng, H.; Perepichka, D.F.; Zheng, J.; Frank, M. M.; Chabal, Y. J.; Bao, Z. Synthesis and Characterization of Conjugated Mono- and Dithiol Oligomers and Characterization of Their Self-Assembled Monolayers. *Langmuir* **2003**, *19*, 4272–4284

[76] Evans, S. D.; Ulman, A. Surface potential studies of alkyl-thiol monolayers adsorbed on gold *Chem. Phys. Lett.* **1990**, *170*, 462–466.

[77] Ford, W. E.; Gao, D.; Knorr, N.; Wirtz, R.; Scholz, F.; Karipidou, Z.; Ogasawara, K.; Rosselli, S.; Rodin, V.; Nelles, G.; von Wrochem, F. Organic Dipole Layers for Ultralow Work Function Electrodes. *ACS Nano* **2014**, *8*, 9173–9180.

[78] Maier, S.; Fendt, L.-A.; Zimmerli, L.; Glatzel, T.; Pfeiffer, O.; Diederich, F.; Meyer, E. Nanoscale Engineering of Molecular Porphyrin Wires on Insulating Surfaces. *Small* **2008,** *4,* 1115–1118.

[79] Saraogi, I.; Vijay, V. G.; Das, S.; Sekar, K.; Guru Row: T. N. C–halogen…π interactions in proteins: a database study. *Cryst. Eng*. 2003, 6, 69– 77.

[80] Olmstead, M. M.; Nurco, D. J. Fluorinated Tetraphenylporphyrins as Cocrystallizing Agents for $C_{60}$and C_{70} *Cryst. Growth Des.* **2006**, 6, 109–113.

[81] Hebenstreit, W.; Schmid, M.; Redinger, J.; Podloucky, R.; Varga, P. Bulk Terminated NaCl(111) on Aluminum: A Polar Surface of an Ionic Crystal? *Phys. Rev. Lett.* **2000**, *85*, 5376–5379.

Appendix Z

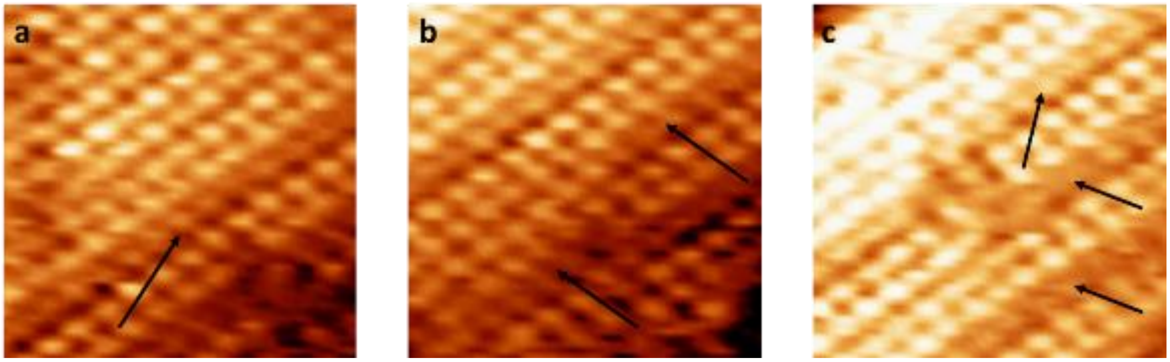

Figure 4.S1. High resolution STM image showing contrast switching in BT SAM. (6×6 nm^2).

Table 4.S1. Different unit cell parameters of BT SAM on Au (111) reported in the literature.

a (nm)	b(nm)	α (deg)	Suggested commensurate structure	Reference
1.04 ± 0.2	1.04 ± 0.2	60	$a(2\sqrt{3} \times 2\sqrt{3})$	[1]
1.65 ± 0.07	1.05 ± 0.07	84 ± 3	$a(3\sqrt{3} \times 2\sqrt{3})$	[2]
0.5±0.02	0.5±0.02	59±3	$a(\sqrt{3} \times \sqrt{3})$	[3]
1.04	1.29	81^0	$a(2\sqrt{3} \times 3\sqrt{3})$	[4]
0.57	1.23	23^0	$a(2\sqrt{3} \times 3\sqrt{3})$	[5]

---

[1] Wan, L.-J.; Terashima, M.; Noda, H.; Osawa, M.Molecular Orientation and Ordered Structure of Benzenethiol Adsorbed on Gold(111). *J. Phys. Chem. B* **2000**, *104*, 3563–3569.

[2] Käfer, D.; Bashir, A.; Witte, G. Interplay of Anchoring and Ordering in Aromatic Self-Assembled Monolayers. *J. Phys. Chem. C* **2007**, *111*, 10546-10551

[3] Jin, Q.; Rodriguez, J. A.; Li, C. Z.; Darici, Y.; Tao, N. J. Self-assembly of aromatic thiols on Au(111). *Surf. Sci.* **1999**, *425*, 101–111.

[4] Kang, H.; Park, T.; Choi, I.; Lee, Y.; Ito, E.; Hara, M.; Noh, J. Formation of Large Ordered Domains in Benzenethiol Self-Assembled Monolayers on Au(111) Observed by Scanning Tunneling Microscopy. *Ultramicroscopy* **2009**, *109*, 1011–1014.

[5] Kang, H.; Lee, H.; Kang, Y.; Hara, M.; Noh, J.Two-Dimensional Ordering of Benzenthiol Self-Assembled Monolayers Guided by Displacement of Cyclohexanethiols on Au(111) .*Chem. Commun.* **2008**, 5197–5199.

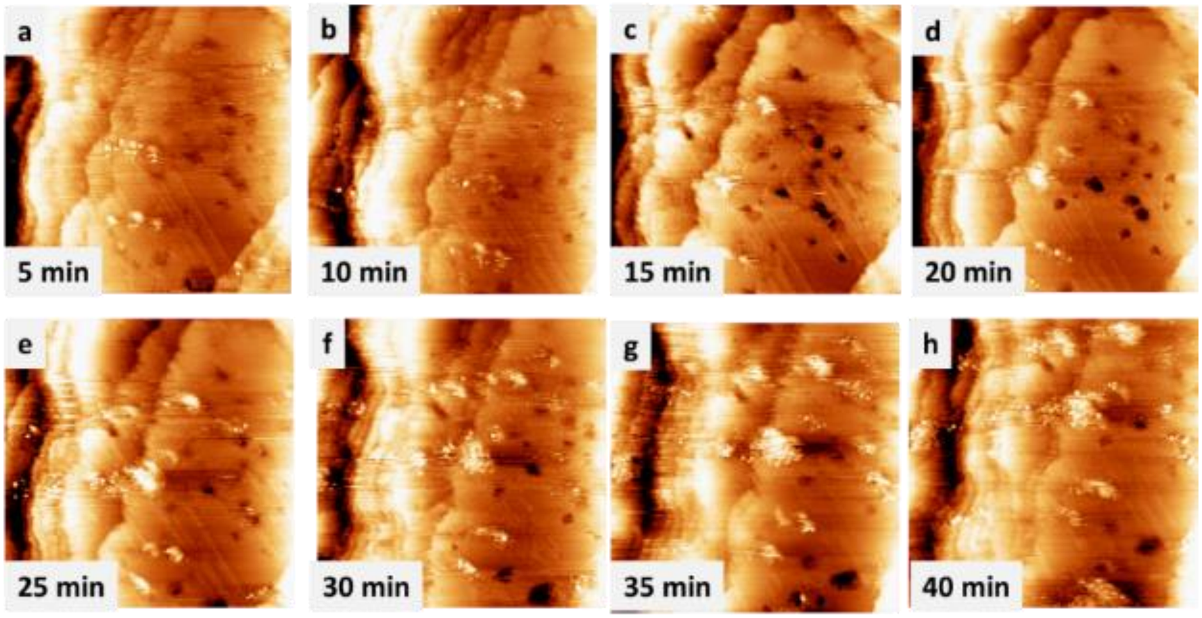

Figure 4.S2. Sequence of STM images recorded for C_{60} assembly on top of C8SH modified gold substrate at liquid-solid interface. Scanning parameters (a-h) 90×90 nm^2; V_b = 400 mV, I_t = 0.2 nA.

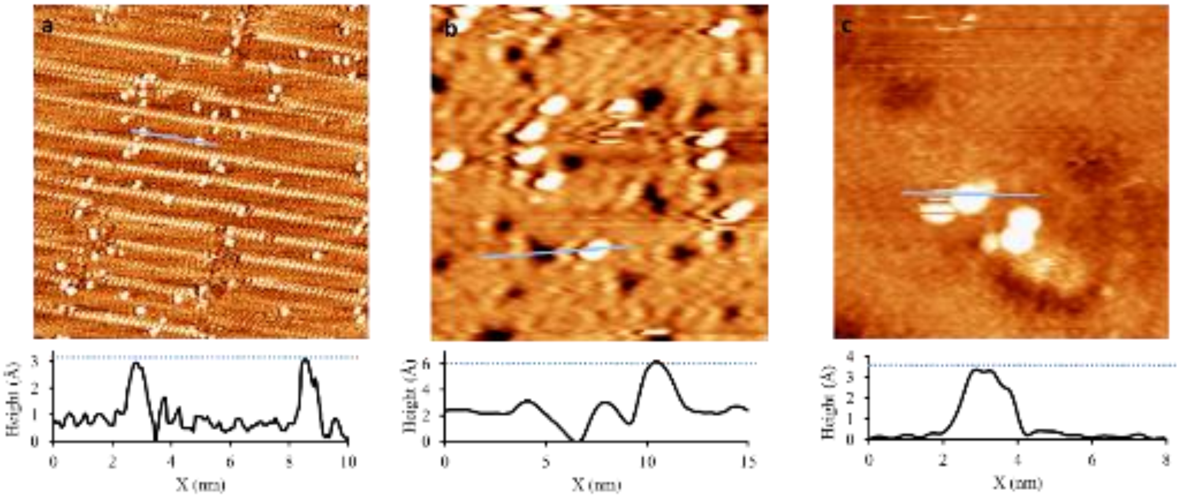

Figure 4.S3. Surface profile recorded according to the blue of C_{60} on top of (a) PFBT (6×6 nm^2), (b) BT , and (c) C8SH SAMs. (a) (35.5×35.5 nm^2), (b) (29.3×29.3 nm^2), (c) (17×17 nm^2) V_b = 400 mV, I_t = 0.2 nA.

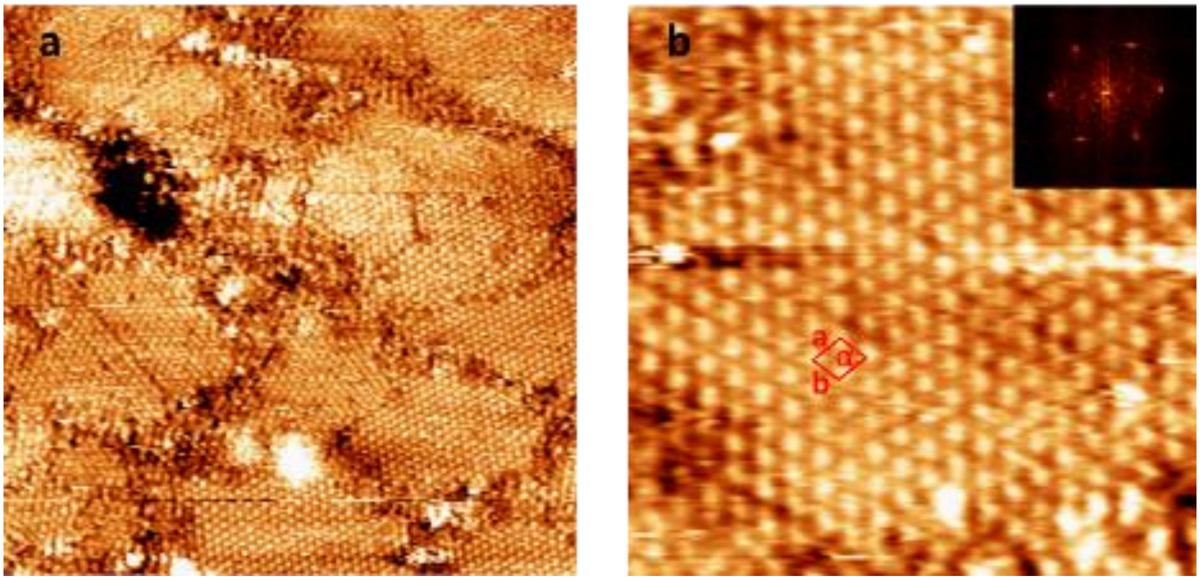

Figure 4.S4. STM image showing the formation hexagonal close network of C_{60} on top of bare gold. (a) 67×67 nm^2, (a) 21×21 nm^2. The unit cell is: a=b=1.07± 0.1nm; α=63 ± 4^0**.**

Table 4.S2. Fitting parameters using KJMA model of C_{60} growth on PFBT, BT, C8SH, and Au substrates

Model	KJMA			
Equation	y =1-exp(-K*(x^2))			
	K Value	Standard Error	Reduced Chi-Sqr	Adj. R-Square
PFBT	3.31×10^{-7}	1.7×10^{-8}	0.48002	0.99531
C8SH	1.1×10^{-9}	2.8×10^{-10}	4.58E-05	-0.23916
BT	9.5×10^{-9}	1.2×10^{-9}	6.02E-04	0.79042
Au	$> 1\times10^{-6}$	-	-	-

Chapter 5: Self-assembly of [C_{60}]Fullerene Multicarboxylic Acids on Au(111) and SAM Modified Au(111)

5.1 Abstract

The adsorption of C_{60} malonic acid derivatives ($C_{61}(CO_2H)_2$ and $C_{66}(CO_2H)_{12}$ on Au(111) and a pentafluorobenzenthiol SAM-modified Au substrate (PFBT-Au) has been investigated using scanning tunneling microscopy (STM) at a liquid-solid interface. On Au(111), C_{61}-$(CO_2H)_2$ forms an extended $(2\sqrt{3} \times 2\sqrt{3})R30°$ overlayer structure, driven primarily by the strong molecule-Au interactions. On a PFBT-Au substrate, only short clusters (predominantly dimers) engaging in the intermolecular hydrogen bonding are observed. Adsorption of $C_{66}(CO_2H)_{12}$ on an Au substrate generates an extended 2D molecular network where the molecular units are interconnected via hydrogen bonding. Similar to $C_{61}(CO_2H)_2$ a second monolayer has been observed at long immersion times. On a PFBT SAM- modified Au substrate, $C_{66}(CO_2H)_{12}$ forms 1D clusters as a result of intermolecular hydrogen bonding.

5.2 Introduction

Since its discovery in 1985,[1] C_{60} has attracted much attention owing to its intriguing electronic, magnetic, and chemical properties. There is renewed interest in using a C_{60}-based nanostructure as a component of organic photovoltaic cells,[2,3,4] field effect transistors,[5,6,7] and biochemical sensors[8,9]. Generally these applications require a transfer of C_{60} properties to the device surface using various chemical and physical methods [10]

In this respect, surface modification via facile molecular self-assembly provides a means to create complex structures and patterns of C_{60} molecules with sub-nanometer precision over an extended length scale.[11] Such structures are governed by a subtle interplay of intermolecular and molecule-substrate interactions.[12]

C_{60} itself self-assembles into hexagonal close packed (hcp) arrays when deposited on transition metal surfaces.[13,14,15] More complex fullerene architectures have been created by pre-patterning the substrate with a molecular template that accommodates individual C_{60} molecules, either through the host-guest interactions with a porous network (oligothiophene,[16,17] benzene di- and tri-carboxylic acids,[18] calix[8]arene,[19] PTCDI-melamine[20]) or the donor-acceptor interactions with SAMN of electron donating molecules (porphyrin,[21] perylene[22], coronene[23], and pentacene[24]). In these cases, the assembly is dominated by molecule-substrate interactions rather than intermolecular forces. On the other hand, strengthening intermolecular interactions via hydrogen bonds offers a high level of control over the molecular self-assembly process and provides a way toward programmable C_{60} supramolecular structures for potential application in molecular machines and optoelectronic devices.[25,26]

Despite the importance of hydrogen-bonding motifs for the design of supramolecular architectures, their application to 2D assemblies of fullerenes has been rarely reported.[27] Adsorption of phenyl-C_{61}-butyric acid methyl ester (PCBM) on Au(111) in UHV shows coverage-dependent behavior.[28] At low molecular coverage, PCBM self-assembles into 1D wires and 2D networks that grow preferentially at the fcc sites of Au(111) substrate. Increasing the molecular coverage supresses the effect of substrate and increases the contribution of intermolecular hydrogen bonds between PCBM tails groups, resulting in large 2D islands that span the surface of the substrate.[29] STM and low-energy electron diffraction (LEED) studies of C_{60}-functionalized malonic acid (C_{61}-$(CO_2H)_2$) adlayer on Au(111) reveal the formation of a hexagonal close packed structure that is ascribed to hydrogen bonding between CO_2H of neighbouring molecules. [30]

In this work, we explore the effect of intermolecular and molecule-substrate interactions on hydrogen-bonded fullerene derivatives. The assembly of multicarboxylic acid derivatives of C_{60} (C_{61}-$(CO_2H)_2$ and $C_{66}(CO_2H)_{12}$) on bare Au (111) and a pentafluorobenzenethiol (PFBT) modified Au (111) substrates (Scheme 5.1) is investigated at liquid-solid interface. On Au (111), STM reveals the formation of a hexagonal close packed structure of C_{61}-$(CO_2H)_2$ driven by molecular-substrate and weak intermolecular H-bonding, whereas C_{61}-$(CO_2H)_2$ adsorption shows a hydrogen bonded assembly. On PFBT modified Au, C_{61}-$(CO_2H)_2$ forms clusters with different sizes up to heptamers with the predominance of dimers, whereas $C_{66}(CO_2H)_{12}$ self-assembles mainly into longer clusters as a result of intermolecular hydrogen bonding.

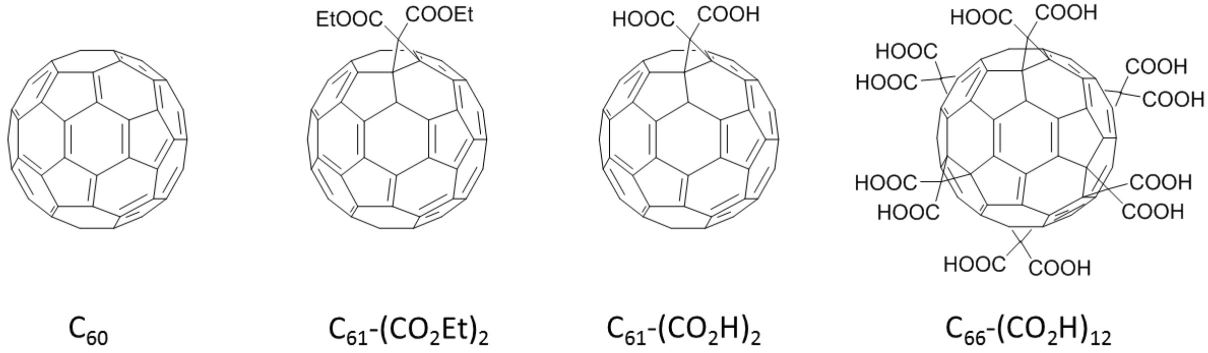

Scheme 5.1. Chemical structure of fullerene derivatives.

5.3 Results and Discussion

Fig. 5.1 shows a representative STM image of C_{61}-$(CO_2H)_2$ adlayer obtained at a liquid-solid interface after drop casting a saturated phenyloctane solution of C_{61}-$(CO_2H)_2$ onto Au(111). The individual molecules appear as featureless bright spots with a diameter of about 0.7 nm. This assignment is supported by the size of vacancies and admolecules in the monolayer, showing as dark and bright spots respectively, highlighted by circles in Fig. 5.1b.

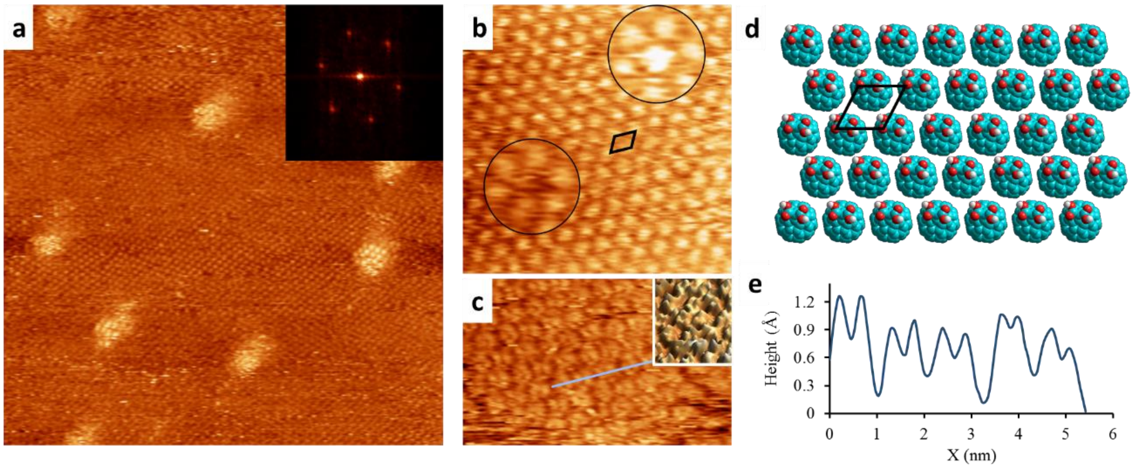

Figure 5.1. (a) Representative 76 × 76 nm^2 STM images of a C_{61}-$(CO_2H)_2$ monolayer at phenyloctane/Au (111). Inset: Fast Fourier Transform (FFT) showing the hexagonal structure of the monolayer. (b) STM image showing the unit cell: a=b=1±0.1 nm, $\alpha=60\pm3^0$. 21 × 21 nm. The circles highlight a missing and an admolecule in the C_{60} monolayer. (c) High resolution STM image showing the upper position of CO_2H groups of C_{61}-$(CO_2H)_2$ molecule (76 × 76 nm^2). Inset: 3D STM image showing CO_2H groups. (e) Cross section profile along the blue line in (d). Tentative model for a hexagonal close-packed C_{61}-$(CO_2H)_2$ molecules. (a,b) V_b = 600 mV, I_t = 0.2 nA; (c) V_b = 800 mV, I_t = 0.3 nA.

The high resolution STM image (Fig. 5.1b) and its 2D FFT (inset Fig. 5.1a) reveal a hexagonal close packed arrangement of C_{61}-$(CO_2H)_2$ with unit cell parameters of $a = b = 1\pm0.1$ nm, $\alpha=60\pm3°$, assigned to $(2\sqrt{3} \times 2\sqrt{3}\ )R30°$ overlayer structure. The same molecular packing has been reported for non-functionalized C_{60} adsorbed on Au(111) in ambient,[31] UHV[32,33] conditions, and at a liquid-solid interface[34,35] (Fig. 5.2).

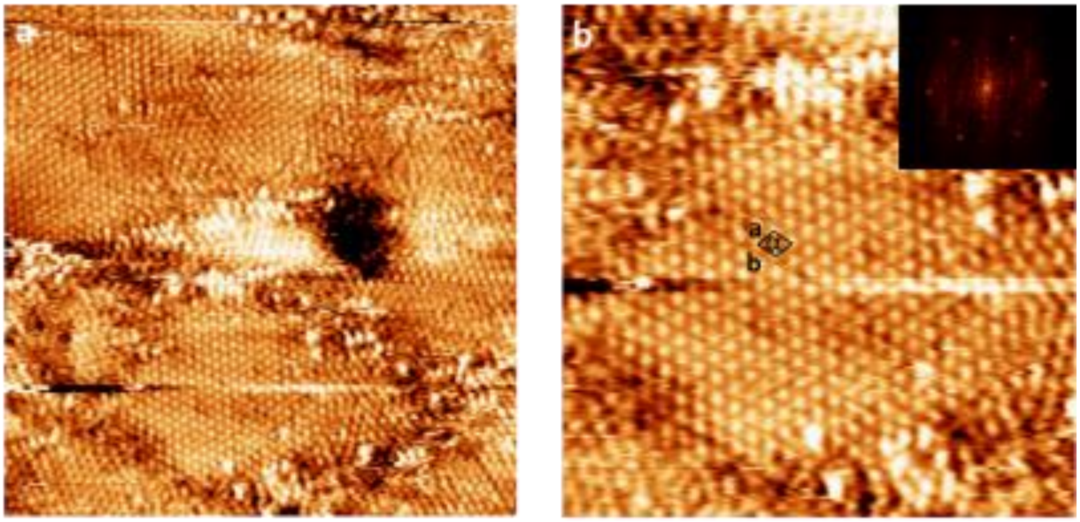

Figure 5.2. STM image showing the formation hexagonal close network of C_{60} on top of bare Au(111). (a) 60×60 nm^2, (a) 31×31 nm^2. The unit cell is: a=b=1.07± 0.1nm; $\alpha=63 \pm 4^{\circ}$**.** V_b = 700 mV, I_t = 0.3 nA.

At certain tunnelling conditions, pairs of higher brightness features have been resolved on top of C_{61}-$(CO_2H)_2$ (inset Fig. 5.1c and Fig. 5.1e). These features could likely be attributed to CO_2H groups, as previously observed by UHV STM.[36] It was earlier suggested that hexagonal close packed (hcp) C_{61}-$(CO_2H)_2$ assembly is driven by strong intermolecular hydrogen bonds between CO_2H groups of adjacent molecules. However, our molecular modeling (Fig. 5.3) shows that in the observed 2D structural lattice the mutual orientation of the CO_2H groups does not allow for continuous hydrogen bonding networks, although the molecules can pair via weak hydrogen bonding above the molecular 2D crystal plane (Fig. 5.3c,d).[37]

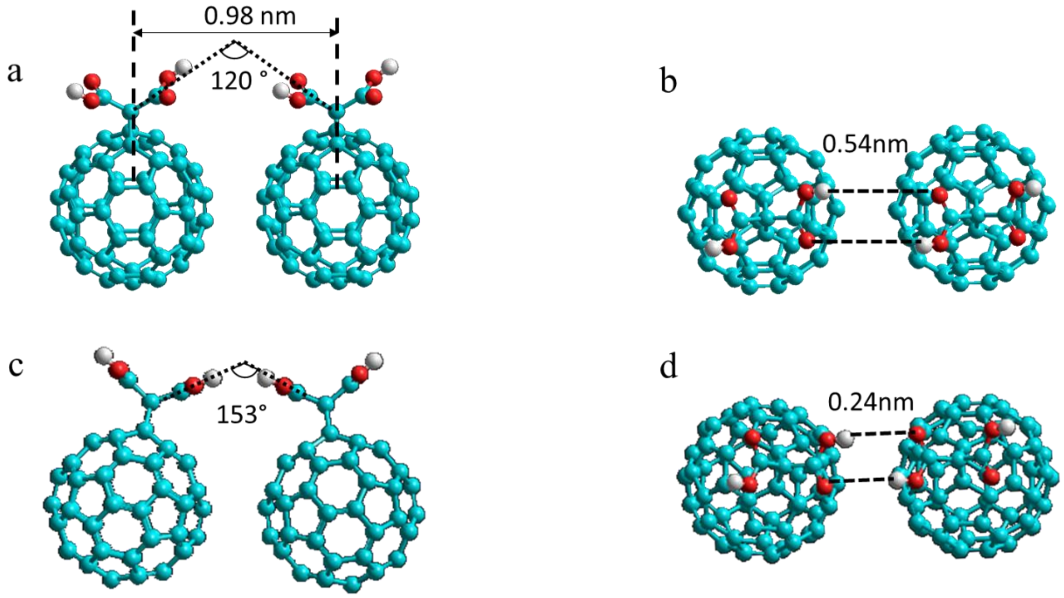

Figure 5.3. Side (a) and top view (b) of $C_{61}(CO_2H)_2$ dimer showing interplanar angle of 120° between CO_2H groups of adjacent molecules. Side (c) and top view (d) of $C_{61}(CO_2H)_2$ dimer interacting via $R^2_2(8)$ pairing of carboxylic groups.

It is noteworthy, that the free COOH groups of a C_{61}-$(CO_2H)_2$ adlayer might form hydrogen bonds with molecules of a second layer which probably explains the presence of small bright islands of C_{61}-$(CO_2H)_2$ perfectly aligned with first molecular layer (Fig. 5.4).

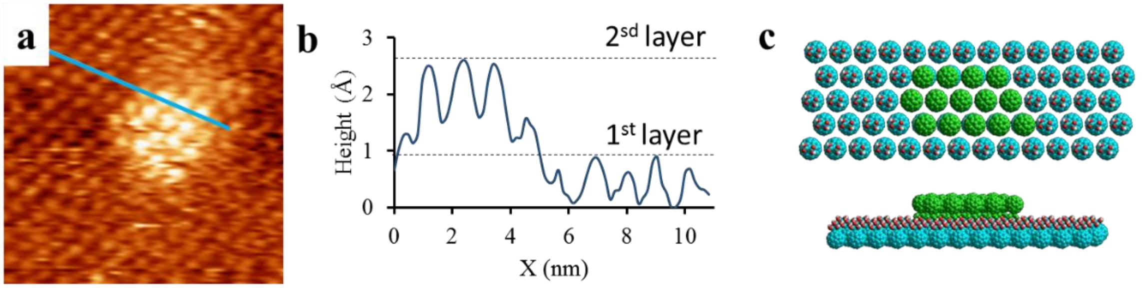

Figure 5.4. (a) STM image showing two layers of $C_{61}(CO_2H)_2$ molecules on Au(111) (15 × 15 nm^2). (b) Cross sectional profile along the blue line in (a). (c) Molecular model (top and side view) showing two layers. V_b = 600 mV, I_t = 0.2 nA.

Overall, these arguments suggest that the C_{61}-$(CO_2H)_2$ assembly is mainly driven by strong molecule-substrate binding with weaker van der Waals molecule-molecule interactions. The former was estimated both experimentally using temperature programmed desorption (TPD)[38] (~43 kcal/mol) and by DFT calculations (~31 kcal/mol)[39]. The nature of such interactions has been the subject of a number of studies. High resolution angle resolved photoemission[40], STM,[41,42] and DFT[43,44] calculations suggest a strong, covalent like character for the C_{60}-metal interaction. This was concluded from the observed hybridization between the d-states of the metal surface and the π-orbitals at the C_{60} cage, the significant charge transfer from the substrate to C_{60} (0.7 to 2 e^- per molecule,[45]), and the surface reconstruction upon fullerene adsorption.[46,47]

One way to weaken the C_{60}-substrate interaction is by passivating the surface of Au(111) with a monolayer of organothiols.[48,49,50,51] In the following, we explored the assembly of C_{61}-$(CO_2H)_2$ on Au(111) pre-modified with PFBT SAM, which has been previously (Chapter 4) shown to favorably interact with C_{60}. SAM of PFBT on Au(111) is characterized by rows of molecules oriented along $\langle 1\bar{1}0 \rangle$ direction of the underlying Au (111), forming a $(2 \times 2\sqrt{3})$ 2D crystal lattice with two standing up molecules per unit cell.[52] In contrast to Au(111) surface, adsorption of C_{61}-$(CO_2H)_2$ onto a PFBT-Au substrate at the solid-liquid interface did not yield a close-packed structure. Instead, a range of C_{61}-$(CO_2H)_2$ clusters, up to a heptamers are observed on the surface (Fig. 5.5).

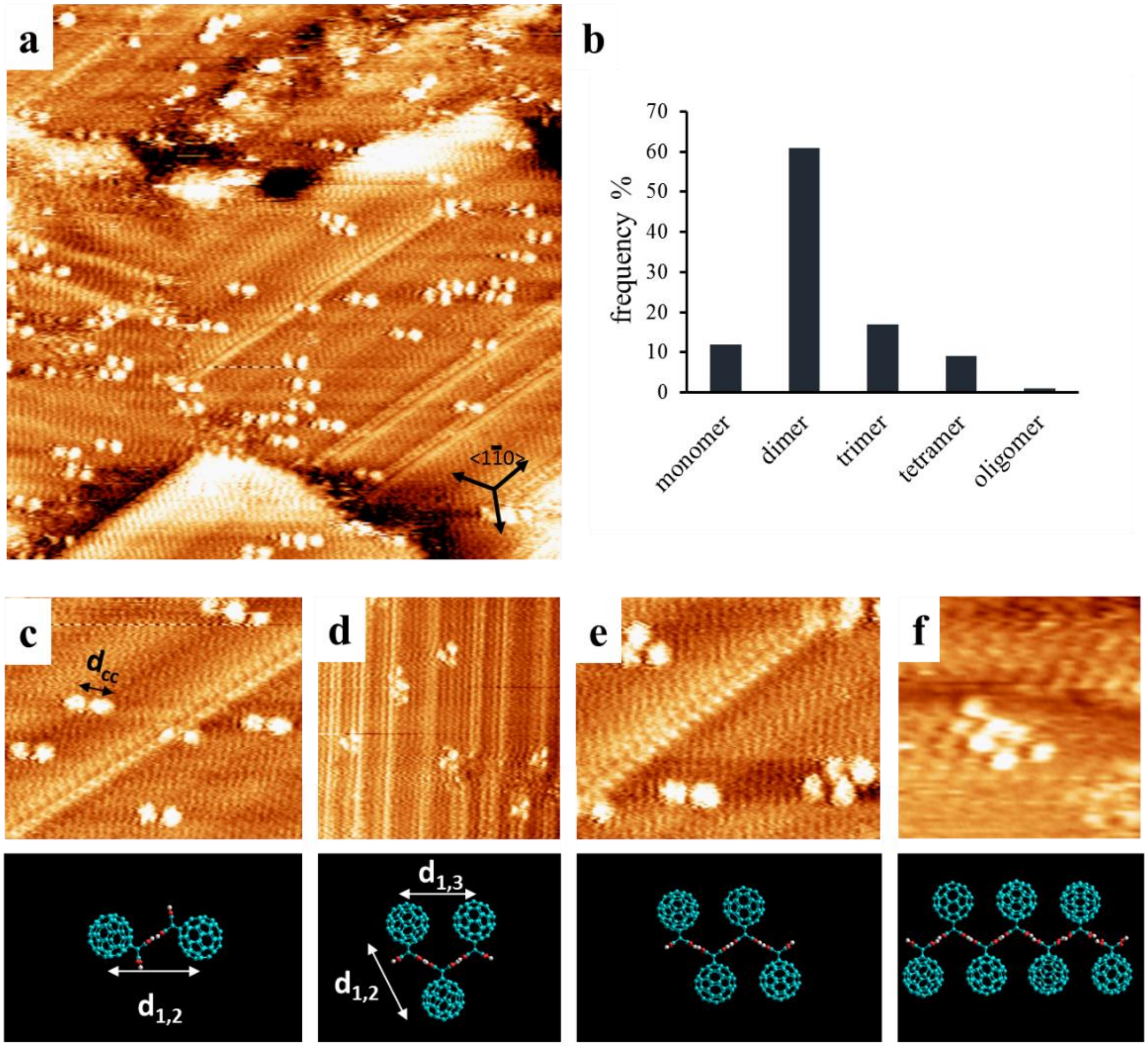

Figure 5.5. (a) Representative 40 × 40 nm^2 STM images of C_{61}-$(CO_2H)_2$ monolayer on PFBT/ Au(111). (b) Histogram of C_{61}-$(CO_2H)_2$ assembly distribution. STM image and corresponding molecular model of C_{61}-$(CO_2H)_2$ (c) dimers (14 × 11 nm^2) (d) trimers (27 × 31 nm^2), (e) tetramers (12 × 9 nm^2), and (f) heptamers (11 × 11 nm^2). $d_{1,2}$ and $d_{1,3}$ are center-to-center distances between the neighboring and each third molecule, respectively, in the $R^2_2(8)$ H bonded polymer of C_{61}-$(CO_2H)_2$. V_b = 800 mV, I_t = 0.15 nA.

Statistical analysis of STM images (Fig. 5.5b) reveals the predominance of dimers (60%). These nanostructures are remarkably immobile: no significant drift in their location was observed during STM scanning (Fig. 5.6a-c) suggesting their strong interaction with the substrate. An unexpectedly strong interaction has been previously observed for C_{60} on-PFBT SAM on Au (Chapter 4). It is noteworthy that the dimers align preferentially along the $\langle 1\bar{1}0 \rangle$ direction of Au (111). This alignment does not seem to be induced by scanning the STM tip, since no reorientation was observed upon the change of the scan direction (Fig. 5.6d,e).

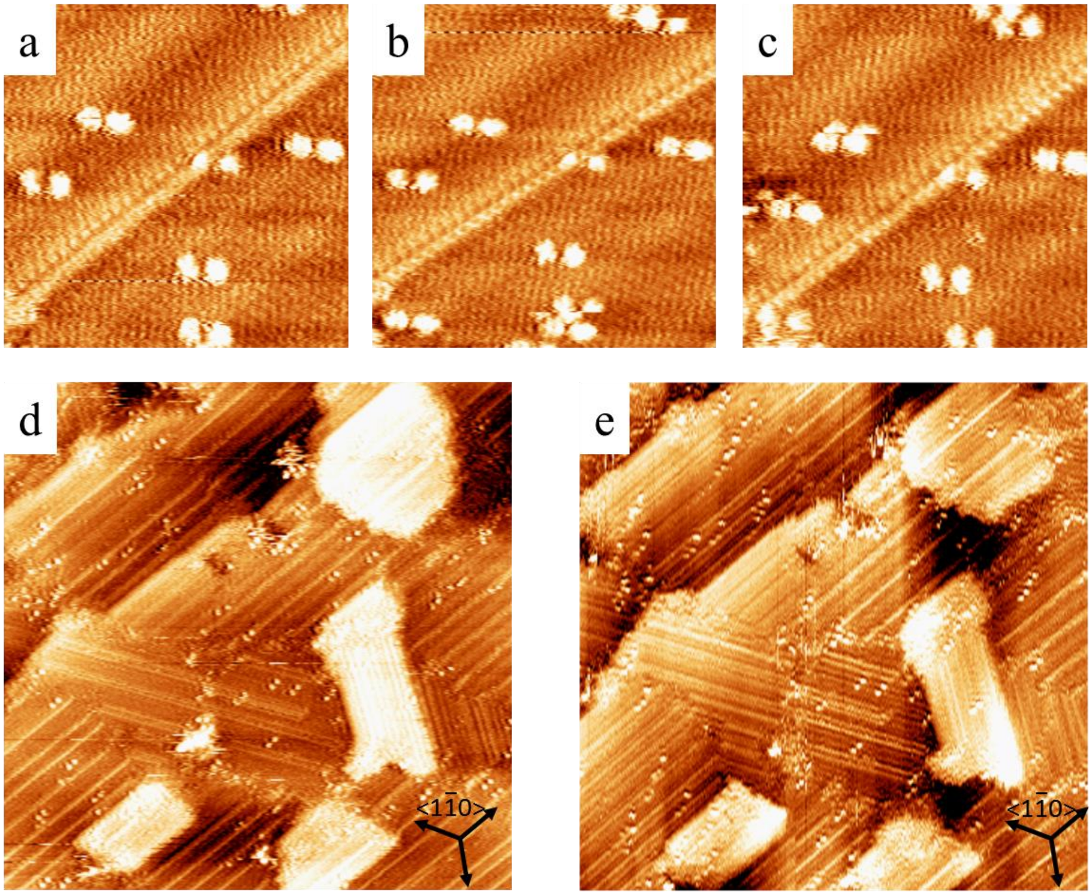

Figure 5.6. (a), (b), and (c) Consecutive STM images showing the stability of C_{61}-$(CO_2H)_2$ dimers. (13.8×13.8 nm^2). (d) and (e) a representative 81 × 81 nm STM image of C_{61}-$(CO_2H)_2$ dimers on PFBT/Au at 0° and 90° scanning angle respectively. V_b = 800 mV, I_t = 0.15 nA.

Analysis of the molecular separation in C_{61}-$(CO_2H)_2$ clusters shows two distinct distances: $d_{1,2}$ = 1.4 ± 0.2 nm, and $d_{2,3}$ = 1.2 ± 0.2 nm for the neighboring and each third molecules, respectively. This is consistent with a $d_{1,2}$ of 1.5 nm and a $d_{2,3}$ of 1.2 nm predicted by the molecular model of C_{61}-$(CO_2H)_2$ arrays interconnected through $R^2_2(8)$ hydrogen bonds (Fig. 5.5). In these structures, the molecules are stabilised by one $R^2_2(8)$ hydrogen bond as well as weak vdW interactions between each third molecules in the zigzag chain. An alternative mode of assembly of C_{61}-$(CO_2H)_2$ has also been considered but ruled out based on the very different modelled intermolecular separations (Fig. 5.7) .

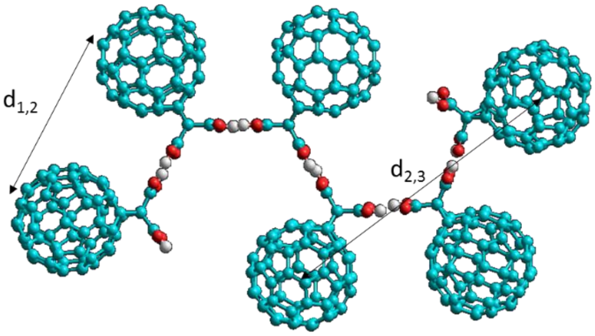

Figure 5.7. Molecular model of an alternative C_{61}-$(CO_2H)_2$ hexamer. $d_{1,2}$ = 1.2 nm; $d_{2,3}$ = 2.0 nm.

A control experiment with an ester of fullerene malonic acid (C_{61}-$(CO_2Et)_2$) derivative confirms the critical role that the hydrogen bonding plays in the observed assembly (Fig. 5.8). Upon adsorption of C_{61}-$(CO_2Et)_2$ onto PFBT-Au, only randomly distributed individual molecules are observed on the surface.

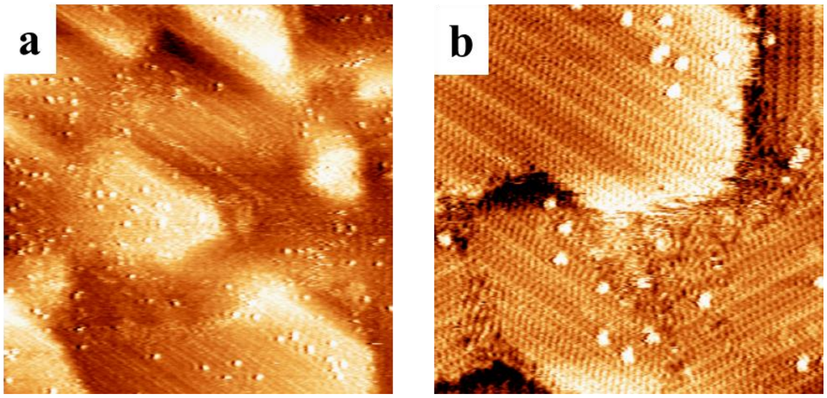

Figure 5.8. (a) Representative 70 × 70 nm^2 STM images of C_{61}-$(CO_2Et)_2$ on PFBT/Au. (b) High resolution STM image showing isolated C_{61}-$(CO_2Et)_2$ molecules. 31 × 31 nm^2. V_b = 700 mV, I_t = 0.15 nA

The above results highlight the importance of hydrogen bonding in the formation of C_{61}-$(CO_2H)_2$ clusters. However, as more molecules interconnect via hydrogen bonds, the frequency of the clusters formation decreases (60% dimers, 17% trimers, 9% tetramers, 1% heptamers). This trend indicates that the spontaneous self-assembly of C_{61}-$(CO_2H)_2$ into small clusters is more favorable. A plausible explanation might be the free rotation of dimers compared to longer cluster which would increase the entropy of molecules and also might enable a more favorable enthalpy of interaction. The incorporation of molecules within PFBT SAMs through partial replacement of thiol molecules could also explain the favorable formation of dimers which would cause less strain within SAM than longer clusters.

As a bidentate H-bonding building block (two $R^2_2(8)$ synthons), C_{61}-$(CO_2H)_2$ can only assemble into 1D chains. In order to create 2D molecular networks using hydrogen bonding we employed of $C_{66}(CO_2H)_{12}$ molecule with six malonic acid moieties aligned in the three orthogonal space directions (Fig. 5.9).

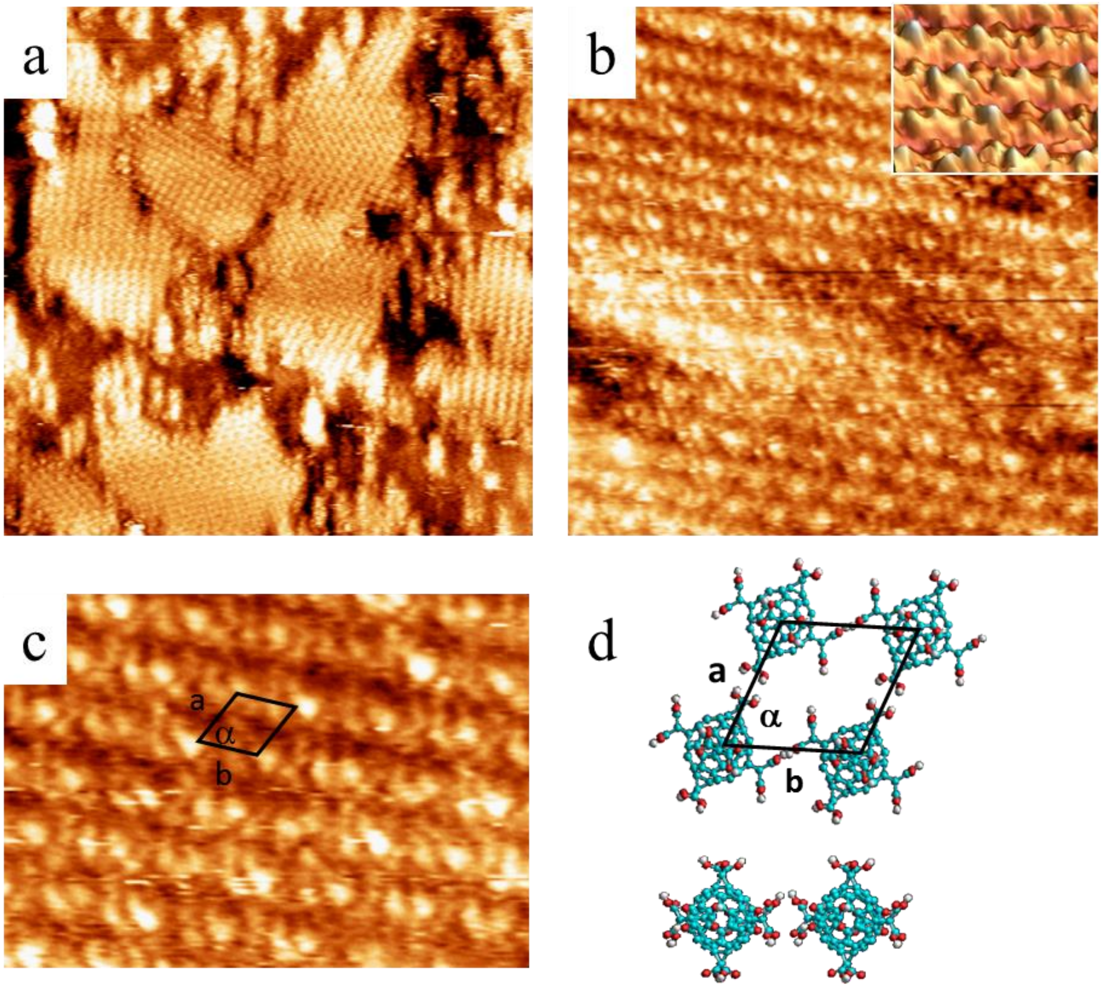

Figure 5.9. (a) Representative 80 × 80 nm^2 STM images showing domains of a C_{66} $(CO_2H)_{12}$ monolayer on Au (111). (b) STM image showing one domain of C_{66}-$(CO_2H)_{12}$ (20 × 20 nm^2). Inset 3D STM image showing the upper $-CO_2H$ groups. 6 × 6 nm^2 (c) High resolution STM image showing the oblique unit cell. $a=b=1.5\pm0.2$ nm, $\alpha=72\pm3°$. 10 × 10 nm^2. (d) Tentative model (top and side view) for close-packed C_{66}-$(CO_2H)_{12}$ molecules. Unit cell. $a=b=1.5$nm, $\alpha=68°$ (Top and side view). V_b = 800 mV, I_t = 0.15 nA.

Adsorption of C_{66}-$(CO_2H)_{12}$ onto Au(111) from a saturated phenyloctane solution results in the spontaneous formation of a 2D molecular structure with a domain size ranging from 20 to

60 nm (Fig. 5.9a). A zoom-in of these domains reveals two bright protrusions on top of each molecule, as was observed for C_{61}-$(CO_2H)_2$, and attributed to CO_2H groups. The 2D SAMN of C_{66}-$(CO_2H)_{12}$ is characterized by an oblique unit cell that contains one molecule and has the parameters of a=b=1.5±0.2 nm, α=72±3°, which is different from the hexagonal close-packed arrangement observed for C_{61}-$(CO_2H)_2$. Based on the high resolution STM images (Fig. 5.9c), a tentative molecular packing model is proposed (Fig. 5.9d). This model shows a unit cell a=b=1.5 nm, α=68° which is consistent with experimental results. The molecules are assembled into oblique structure in which each molecule is connected to two neighboring molecules through strong $R^2_2(8)$ hydrogen bonds of two CO_2H groups along **b** direction of unit cell. Thus formed H bonded supramolecular lines are held together by less favorable hydrogen bond contacts of four other CO_2H groups along **a** direction. The model also suggests that two other CO_2H groups in the ab plane are precluded from H bonding by the geometry of the network. Due to the four fold symmetry of C_{66}-$(CO_2H)_{12,}$ two CO_2H groups per molecule might favorably interact with Au(111). The interaction of CO_2H groups with Au substrate has been previously reported for the standing up phase of trimesic acid (TMA) on Au(111).[53,54] Finally, the remaining two CO_2H groups are pointing away from the substrate enabling a potential binding of a second layer. Indeed, as shown in Fig. 5.10, after 18h of Au immersion in C_{66}-$(CO_2H)_{12}$ solution the growth of a second layer has been observed. Disordered aggregates in addition to well-ordered islands that include few defect sites have been clearly distinguished in the second layer. Based on the cross sectional profile, a molecular packing where C_{66}-$(CO_2H)_{12}$ assemble are on top of each other has been suggested which is similar to C_{61}-$(CO_2H)_2$ bilayer.

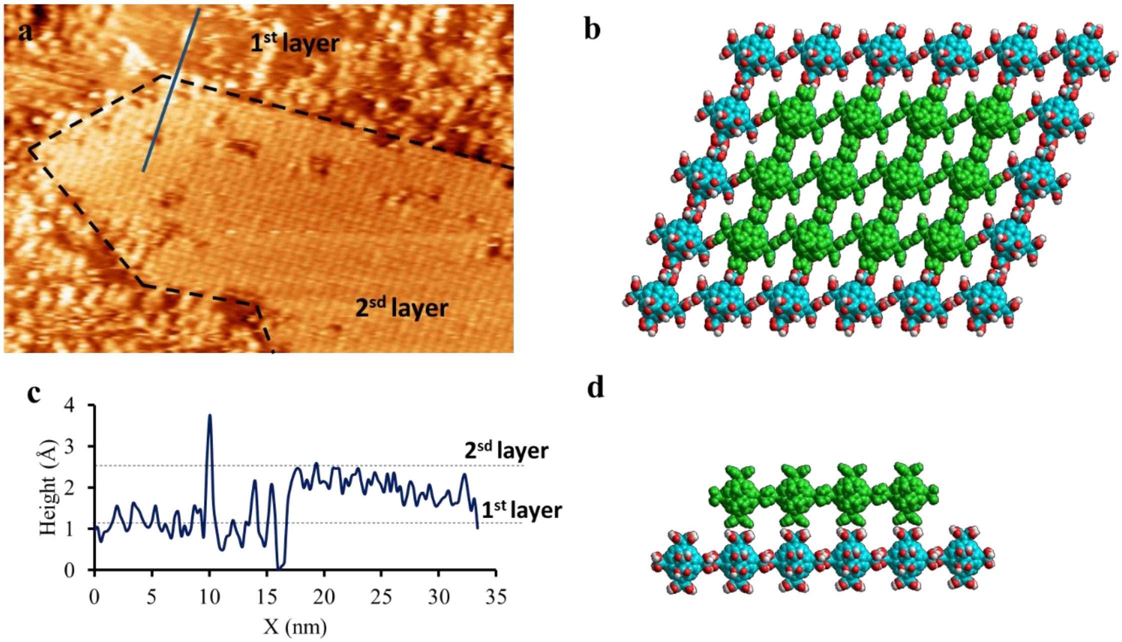

Figure 5.10. (a) STM image showing two layers of $C_{66}(CO_2H)_{12}$ molecules on Au(111) (90 × 57 nm^2). (b) (d) Molecular model (Top and side view) showing two layers. Unit cell. a=b=1.5nm, α=68°. (c) Cross sectional profile along the blue line in (a). V_b = 1000 mV, I_t = 0.15 nA.

The STM image of $C_{66}(CO_2H)_{12}$ molecules adsorption onto a PFBT-Au substrate at the solid-liquid interface reveals individual molecules that are aggregated into clusters (Fig. 5.11a) or aligned as dimers or tetramers on top of PFBT stripes (Fig. 5.11b). An interparticle distance $d_{1,2}$ of ~1.5nm has been measured for $C_{66}(CO_2H)_{12}$ rows suggesting their interconnection via hydrogen bonds. The possibility of SAM penetration and intermixing of $C_{66}(CO_2H)_{12}$ with PFBT molecules might explain the lack of formation of ordered 2D monolayers on this substrate.

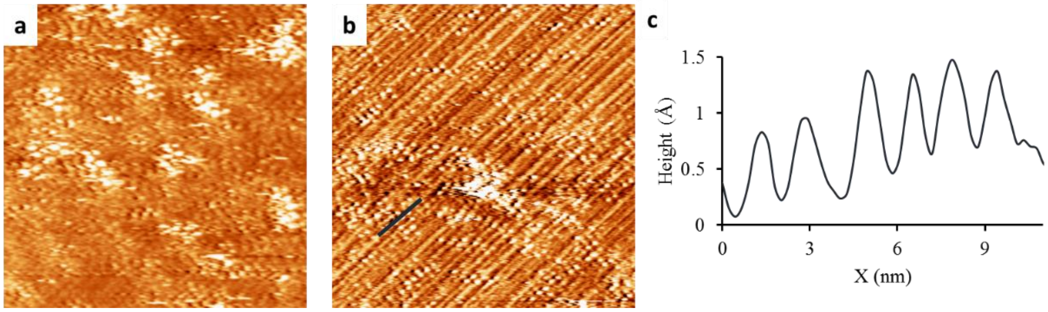

Figure 5.11. (a) STM images showing a C_{66}-$(CO_2H)_{12}$ adlayer on PFBT/Au (111). (b) STM image showing one domain of C_{66}-$(CO_2H)_{12}$ .60 × 60 nm^2. (c) Cross sectional profile along the blue line in (b). V_b = 800 mV, I_t = 0.2 nA.

5.4 Conclusions

The directionality, selectivity and relatively high bond strength of intermolecular hydrogen bonding have been exploited for the formation of mono and bilayers of [C_{60}]fullerene multicarboxylic acids derivatives (C_{61}-$(CO_2H)_2$ and $C_{66}(CO_2H)_{12}$). The resulting monolayer structures (dimers, oblique, hexagonal) were shown to depend on the number and position of carboxylic functionalities. A close packed monolayer structure is obtained upon adsorption of C_{61}-$(CO_2H)_2$ onto Au(111). The CO_2H groups are pointing away from the surface which suggests that the monolayer is mainly driven by molecule-substrate interaction. In this case, the hydrogen bonds do not contribute significantly to stabilization of the monolayer but likely participate in the growth of a second layer. On PFBT modified Au substrate, C_{61}-$(CO_2H)_2$ form hydrogen bonded 1D clusters. $C_{66}(CO_2H)_{12}$ which have six malonic acid oriented in three different directions form a hydrogen bonded 2D molecular network onto Au (111) and 1D clusters on top of the PFBT modified Au substrate. This study highlights the important role of intermolecular hydrogen bonding in the formation of supramolecular nanostructures of fullerene derivatives which is of great interest for application in areas such as catalysis, gas storage, and drug release.

5.5 Experimental part

Fullerene derivatives C_{61}-$(CO_2Et)_2$, C_{61}-$(CO_2H)_2$, and $C_{66}(CO_2H)_{12}$ were prepared according to literature.[55,56,57]

Au(111) substrates with atomically flat terraces were prepared by thermal evaporation of gold onto freshly cleaved mica sheets preheated at 450 °C under a pressure of 10^{-7}-10^{-8} Pa. The SAMs of pentafluorobenzenethiol (PFBT) were prepared by immersing the Au/mica in a 0.1mM EtOH (ACS reagent) solution of the corresponding thiols at 60 ^{0}C for 2 to 18 hours. After SAM formation, the samples were rinsed with pure EtOH and dried under a stream of ultrapure N_2. Fullerene derivatives were dissolved in phenyloctane (Sigma-Aldrich, 98%) and used directly without further purification. A volume of 10 to 15 μL of saturated phenyloctane solutions of C_{60} have been deposited on bare Au(111) or on PFBT-Au substrate. The resulting assembly have been investigated at a liquid–solid interface.

All STM experiments were performed at liquid-solid interface using Multimode8^{TM} equipped with a Nanoscope^{TM} V controller (Bruker, Santa Barbara, CA) and Nanoscope 8.15r3 software. The STM tips were mechanically cut from Pt/Ir wire (80/20, diameter 0.25 mm, Nanoscience). All STM-images were obtained in the constant current mode using an A scanner and low current STM converter by applying a tunneling current I_{set} of 70 to 400 pA and a sample bias V_{set} of -300 to 600 mV. Calibration of the piezoelectric positioners was verified by atomic resolution imaging of graphite. The raw images were processed from WSxM5.0 software.

The geometry optimizations of C_{61}-$(CO_2H)_2$ and C_{66}-$(CO_2H)_{12}$ were performed using HyperChem 8.0 software (from Hypercube Inc.), applying the MM+ force field with the Polak-Ribiere gradient optimization algorithm until a root-mean-square gradient convergence criterion of 0.001 kcal Å^{-1} mol^{-1} is reached.

References

---

[1] Kroto, H.W.; Heath, J. R.; Obrien, S. C.; Curl, R. F.; Smalley, R. E.C_{60}: Buckminsterfullerene. *Nature* **1985**, *318*,162– 163.

[2] Sariciftci, N. S.; Smilowitz, L.; Heeger, A. J.; Wudl, F. Photoinduced Electron Transfer from a Conducting Polymer to Buckminsterfullerene. *Science* **1992**, *258*, 1474– 1476.

[3] Yu, G.; Gao, J.; Hummelen, J.C.; Wudl, F.; Heeger, A. J. Polymer Photovoltaic Cells: Enhanced Efficiencies via a Network of Internal Donor-Acceptor Heterojunctions. *Science* **1995**, *270*, 1789– 1791

[4] Heeger, A. J. 25th Anniversary Article: Bulk Heterojunction Solar Cells: in the Mechanism of Operation. *Adv. Mater.* **2014**, *26*, 10– 28.

[5] Haddon, R. C.; Perel, A. S.; Morris, R. C.; Palstra, T. T. M.; Hebard, A. F.; Fleming, R. M. C_{60} Thin Film Transistors. *Appl. Phys. Lett.* **1995**, *67*, 121– 123.

[6] Dodabalapur, A.; Katz, H. E.; Torsi, L.; Haddon, R. C. Organic Heterostructure Field-Effect Transistors. *Science* **1995**, *269*, 1560– 1562.

[7] Wang, C.; Dong, H.; Hu, W.; Liu, Y.; Zhu, D. Semiconducting π-Conjugated Systems in Field-Effect Transistors: A Material Odyssey of Organic Electronics. *Chem. Rev.* **2011**, *112*, 2208– 2267.

[8] Goyal, R. N.; Gupta, V. K.; Bachheti, N.; Sharma, R. A. Electrochemical Sensor for the Determination of Dopamine in Presence of High Concentration of Ascorbic Acid Using a Fullerene-C_{60} Coated Gold Electrode. *Electroanalysis* **2008**, *20*, 757–764.

[9] Griese, S.; Kampouris, D. K.; Kadara, R. O.; Banks, C. E. A Critical Review of the Electrocatalysis Reported at C_{60} Modified Electrodes. *Electroanalysis* **2008**, *20*, 1507–1512.

[10] Bonifazi, D.; Enger, O.; Diederich, F. Supramolecular [60]Fullerene Chemistry on Surfaces. *Chem. Soc. Rev.* **2007**, *36*, 390– 414.

[11] Sanchez, L.; Otero, R.; Gallego, J. M.; Miranda, R.; Martin, N. Ordering Fullerenes at the Nanometer Scale on Solid Surfaces. *Chem. Rev.* **2009**, *109*, 2081– 2091.

[12] Barth, J. V.; Costantini, G.; Kern, K. Engineering Atomic and Molecular Nanostructures at Surfaces. *Nature* **2005**, *437*, 671– 679.

[13] Altman, E. I.; Colton, R. J. Nucleation, growth, and structure of fullerene films on Au(111). *Surf. Sci.* **1992**, *279*, 49– 67.

[14] Altman, E. I.; Colton, R. J. The interaction of C_{60} with noble metal surfaces. *Surf. Sci.* **1993**, 295, 13– 33

[15] Altman, E. I.; Colton, R. J. Determination of the orientation of C_{60} adsorbed on Au(111) and Ag(111). *Phys. Rev. B.* **1993**, 48, 18244

---

[16] Mena-Osteritz, E.; Bäuerle, P. Complexation of C_{60} on a Cyclothiophene Monolayer Template. *Adv. Mater*. **2006**, *18*, 447–451.

[17] MacLeod, J. M.; Ivasenko, O.; Fu, C.; Taerum, T.; Rosei, F.; Perepichka, D. F. Supramolecular Ordering in Oligothiophene Fullerene Monolayers. *J. Am. Chem. Soc*. **2009**, *131*, 16844– 16850.

[18] Stepanow, S.; Lingenfelder, M.; Dmitriev, A.; Spillmann, H.; Delvigne, E.; Lin, N.; Deng, X. B.; Cai, C. Z.; Barth, J. V.; Kern, K. Steering Molecular Organization and Host–Guest Interactions Using Two-Dimensional Nanoporous Coordination Systems. *Nat. Mater.* **2004**, *3*, 229– 233.

[19] Pan, G.; Liu, J.; Zhang, H.; Wan, L.; Zheng, Q.; Bai, C. Configurations of a Calix[8]arene and a C_{60}/Calix[8]arene Complex on a Au(111) Surface. *Angew. Chem., Int. Ed.* **2003**, *42*, 2747– 2751.

[20] Theobald, J. A.; Oxtoby, N. S.; Phillips, M. A.; Champness, N. R.; Beton, P. H. Controlling Molecular Deposition and Layer Structure with Supramolecular Surface Assemblies. *Nature* **2003**, *424*, 1029– 1031.

[21] Bonifazi, D.; Spillmann, H.; Kiebele, A.; de Wild, M.; Seiler, P.; Cheng, F. Y.; Güntherodt, H. J.; Jung, T.; Diederich, F. Supramolecular Patterned Surfaces Driven by Cooperative Assembly of C-60 and Porphyrins on Metal Substrates. *Angew. Chem., Int. Ed.* **2004**, *43*, 4759– 4763.

[22] Yoshimoto, S.; Tsutsumi, E.; Fujii, O.; Narita, R.; Itaya, K. Effect of Underlying Coronene and Perylene Adlayers for [60]Fullerene Molecular Assembly. *Chem. Commun.* **2005**,1188– 1190.

[23] Yoshimoto, S.; Tsutsumi, E.; Narita, R.; Murata, Y.; Murata, M.; Fujiwara, K.;Komatsu, K.; Ito, O.; Itaya, K. Epitaxial Supramolecular Assembly of Fullerenes Formed by Using a Coronene Template on a Au(111) Surface in Solution. *J. Am. Chem. Soc.* 2007, *129*, 4366– 4376.

[24] Yang, Y.-C.; Chang, C.-H.; Lee, Y.-L.Complexation of Fullerenes on a Pentacene-Modified Au(111) Surface. *Chem. Mater.* **2007**, 19, 6126– 6130.

[25] Sanchez, L.; Martín, N.; Guldi, D. M. Hydrogen Bonding Motifs in Fullerene Chemistry. *Angew. Chem., Int. Ed.* **2005**, *44*, 5374– 5382.

[26] Zhang, E.-Y.; Wang, C.-R. Fullerene self-assembly and supramolecular nanostructures. *Curr. Opin. Colloid Interface Sci.* **2009**, *14*, 148–156.

[27] Otero, R.; Gallego, J. M.; de Parga, A. L. V.; Martin, N.; Miranda, R.Molecular Self-Assembly at Solid Surfaces *Adv. Mater.* **2011**, 23, 5148– 5176

[28] Ecija, D.; Otero, R.; Sánchez, L.; Gallego, J. M.; Wang, Y.; Alcamí, M.; Martín, F.; Martín, N.; Miranda, R. Crossover Site-Selectivity in the Adsorption of the Fullerene Derivative PCBM on Au(111) *Angew. Chem., Int. Ed.* **2007**, *46*, 7874.

[29] Wang, Y.; Alcamí, M.; Martín, F. Understanding the Supramolecular Self-Assembly of the Fullerene Derivative PCBM on Gold Surfaces *ChemPhysChem* **2008**, 9, 1030– 1035

---

[30] Matsumoto, M.; Inukai, J.; Yoshimoto, S.; Takeyama, Y.; Ito, O.; Itaya, K. Two-Dimensional Network Formation in the C_{60} Malonic Acid Adlayer on Au(111) *J. Phys. Chem. C*, **2007**, *111*,13297– 13300

[31] Jehoulet, C.; Obeng, Y. S.; Kim, Y. T.; Zhou, F. M.; Bard, A. J.Electrochemistry and Langmuir Trough Studies of C_{60} and C_{70} Films. *J. Am. Chem. Soc.* **1992**, *114*, 4237–4247.

[32] Wilson, R. J.; Meijer, G.; Bethune, D. S.; Johnson, R. D.; Chambliss, D. D.; de Vries, M. S.; Hunziker, H. E.; Wendt, H. R. Imaging C_{60} Clusters on a Surface Using a Scanning Tunnelling Microscope. *Nature* **1990**, *348*, 621−622.

[33] Sakurai, T.; Wang, X.-D.; Xue, Q. K.; Hasegawa, Y.; Hashizume, T.; Shinohara, H. Scanning Tunneling Microscopy Study of Fullerenes. *Prog. Surf. Sci.*, **1996**, *51*, 263– 408.

[34] Katsonis, K.; Marchenko, A.; Fichou. D. Dynamics and spectroscopy of single C_{60} molecules adsorbed on Au(1 1 1) at the liquid-solid interface. *J. Photochem. Photobiol. A: Chem.* **2003**. *158*, 101-104.

[35] Katsonis, N.; Marchenko, A.; Fichou, D. Dynamics and spectroscopy of single C_{60} molecules adsorbed on Au(111) at the liquid/solid interface. *Synth. Met.* **2003**, *137*, 1453-1455.

[36] Matsumoto, M.; Inukai, J.; Yoshimoto, S.; Takeyama, Y.; Ito, O.; Itaya, K. Two-Dimensional Network Formation in the C_{60} Malonic Acid Adlayer on Au(111). *J. Phys. Chem. C* 2007, *111*, 13297– 13300.

[37] Wood, P. A.; Allen, F. H.; Pidcock, E.Hydrogen-Bond Directionality at the Donor H Atom-Analysis of Interaction Energies and Database Statistics. *CrystEngComm* **2009**, *11*, 1563–1571.

[38] Tzeng, C. T.; Lo, W. S.; Yuh, J. Y.; Chu, R. Y.; Tsuei, K. D. Photoemission, Near-Edge x-ray-Absorption Spectroscopy, and Low-Energy Electron-Diffraction Study of C_{60} on Au(111) Surfaces. *Phys. Rev. B* **2000**, *61*, 2263–2272.

[39] Li, H.; Pussi, K.; Hanna, K.; Wang, L.-L.; Johnson, D.; Cheng, H. P.; Shin, H.; Curtarolo, S.;Moritz, W.; Smerdon, J.; McGrath, R.; Diehl, R. Surface Geometry of C_{60} on Ag(111)**.** *Phys. Rev. Lett.* **2009**, *103*, 056101– 1–4.

[40] Z.-X.; Greber, T.; Osterwalder, J. Electronic Structure at the C_{60}/Metal Interface: An Angle-Resolved Photoemission and First-Principles Study. *Phys. Rev. B.* **2008**, *77*, 075134.

[41] Silien, C.; Pradhan, N. A.; Ho, W.; Thiry, P. A. Influence of Adsorbate-Substrate Interaction on the Local Electronic Structure of C_{60} Studied by Low-Temperature STM *Phys. Rev. B.* **2004**, *69*, 115434.

[42] Lu, X.; Grobis, M.; Khoo, K. H.; Louie, S. G.; Crommie, M. F. Charge Transfer and Screening in Individual C_{60} Molecules on Metal Substrates: a Scanning Tunneling Spectroscopy and Theoretical Study *Phys. Rev. B.* **2004**, *70*, 115418.

[43] Wang, L.-L.; Cheng, H.-P. Rotation, Translation, Charge Transfer, and Electronic Structure of C_{60} on Cu(111) Surface. *Phys. Rev. B.* **2004**, *69*, 045404.

[44] Wang, L.-L.; Cheng, H.-P. Density Functional Study of the Adsorption of a C_{60} Monolayer on Ag(111) and Au(111) Surfaces. *Phys. Rev. B.* **2004**, *69*, 165417.

---

[45] Lu, X.; Grobis, M.; Khoo, K. H.; Louie, S. G.; Crommie, M. F. Charge Transfer and Screening in Individual C_{60} Molecules on Metal Substrates: a Scanning Tunneling Spectroscopy and Theoretical Study .*Phys. Re*v. *B.* **2004**, *70*, 115418.

[46] Pai, W. W., Hsu, C.-L., Lin, M. C., Lin, K. C., and Tang, T. B. Structural Relaxation of Adlayers in the Presence of Adsorbate-Induced Reconstruction: C_{60}/Cu(111). *Phys. Rev. B.* **2004**, *69*,125405.

[47] Hinterstain, M., Torrelles, X., Felici, R., Rius, J., Huang, M., Fabris, S., Fuess, H., and Pedio, M. Looking Underneath Fullerenes on Au(110): Formation of Dimples in the Substrate. *Phys. Rev. B.* **2008**, *77*, 153412.

[48] Franke, K. J.; Schulze, G.; Henningsen, N.; Fernández-Torrente, I.; Pascual, J. I.; Zarwell, S.; Rück-Braun, K.; Cobian, M.; Lorente, N. Reducing the Molecule-Substrate Coupling in C_{60}-Based Nanostructures by Molecular Interactions. *Phys. Rev. Lett.* **2008**, *100*, 036807.

[49] Zeng, C. G.; Wang, H. Q.; Wang, B.; Yang, J. L.; Hou, J. G. Negative Differential-Resistance Device Involving Two C_{60} Molecules. *Appl. Phys. Lett.* **2000**, *77*, 3595– 3597.

[50] Zeng, C. G.; Wang, B.; Li, B.; Wang, H. Q.; Hou, J. G. Self-Assembly of One-Dimensional Molecular and Atomic Chains Using Striped Alkanethiol Structures as Templates. *Appl. Phys. Lett.* **2001**, *79*, 1685–1687.

[51] Nakayama, M.; Kautz, N. A.; Wang, T.; Sibener, S. J. Formation of Rectangular Packing and One-Dimensional Lines of C_{60} on 11-Phenoxyundecanethiol Self-Assembled Monolayers on Au(111) .*Langmuir* **2012**, *28*, 4694– 4701.

[52] Azzam, W.; Bashir, A.; Ulrich Biedermann, P.; Rohwerder, M.Formation of Highly Ordered and Orientated Gold Islands: Effect of Immersion Time on the Molecular Adlayer Structure of Pentafluorobenzenethiols (PFBT) SAMs on Au(111), *Langmuir* **2012**, *28*, 10192– 10208.

[53] Su, G. J.; Zhang, H. M.; Wan, L. J.; Bai, C. L.; Wandlowski, T. Potential-Induced Phase Transition of Trimesic Acid Adlayer on Au(111). *J. Phys. Chem. B.* **2004**, *108*, 1931–1937.

[54] Li, Z.; Han, B.; Wan, L. J.; Wandlowski, T. Supramolecular Nanostructures of 1,3,5-Benzene-Tricarboxylic Acid at Electrified Au(111)/0.05 M H_2SO_4 Interfaces: An in Situ Scanning Tunneling Microscopy Study. *Langmuir* **2005**, *21*, 6915– 6928.

[55] A. Hirsch, I. Lamparth, H. R. Karfunkel. Fullerene Chemistry in Three Dimensions: Isolation of Seven Regioisomeric Bisadducts and Chiral Trisadducts of C_{60} and Di(ethoxycarbonyl)methylene. *Angew. Chem. Int. Ed. Engl.* **1994**, *33*, 437–438.

[56] A. Hirsch, I. Lamparth, T. Grösser, H. R. Karfunkel. Regiochemistry of Multiple Additions to the Fullerene Core: Synthesis of a Th-Symmetric Hexakis adduct of C_{60} with Bis(ethoxycarbonyl)methylene. *J. Am. Chem. Soc.* **1994**, *116*, 9385–9386.

---

[57] I. Lamparth, C. Maichle-Mössmer, A. Hirsch. Reversible Template-Directed Activation of Equatorial Double Bonds of the Fullerene Framework: Regioselective Direct Synthesis, Crystal Structure, and Aromatic Properties of *Th*-$C_{66}(COOEt)_{12}$. *Angew. Chem. Int. Ed. Engl.* **1995**, *34*, 1607–1609.

Chapter 6: Conclusions and future work

6.1 Conclusions

Molecular self-assembly offers an attractive approach for constructing ordered molecular structures for nanopatterning applications. By taking advantage of the hierarchical order of physisorbed monolayers and the enhanced stability offered by chemisorbed molecules, robust and/or versatile 2D molecular networks were formed, and explored for templating AuNPs and C_{60} nanostructures. An important part of this work was the design and the assembly of building blocks through various intermolecular and molecule-substrate interactions on HOPG and Au substrates. The balance between these interactions was found to determine the packing, orientation, and stability of the resulting molecular monolayers.

This was shown first for the SAM formed from tridentate thiol molecules on Au(111) (Chapter 2).This synthetically versatile molecular motif is based on a benzene ring substituted with three methylthiol groups in alternation with three different alkyl chains (methyl, ethyl, dodecyl). The STM, XPS, and electrochemical characterizations of these SAMs reveal a dependence of the surface density and molecular orientation on the size of the alkyl substituents. Indeed, SAMs of Me_3-BTMT exhibits the highest molecular density of the three molecules studied but the lowest ratio of substrate-bound/free thiol, suggesting a preferential standing-up orientation with only one thiol group interacting with the surface. In contrast, the bulkier ethyl substituents in Et_3-BTMT favour a lying down orientation on the surface, yielding a SAM with a higher degree of chemisorption. Finally, ODe_3-BTMT predominantly adsorbs in a lying down orientation where almost all its thiol groups bond to the gold substrate. This orientation is mainly driven by the vdW interactions between the alkoxy chains and the gold, and between themselves. As a whole, these findings demonstrate a method for controlling the packing density, conformational order, and stability of SAMs by tailoring the structures of multifunctional alkanethiol adsorbates. This in turn opens the door to new uses for SAMs in surface engineering applications.

The possibility of tailoring the interplay between the molecule-substrate and intermolecular interactions was also demonstrated for physisorbed SAMN (Chapter 5). Tuning the molecule-Au interaction was demonstrated using a PFBT modified Au substrate. The directionality and selectivity of intermolecular hydrogen bonding drives the assembly of mono and bilayers of [C_{60}]fullerene multicarboxylic acid derivatives (C_{61}-$(CO_2H)_2$ and $C_{66}(CO_2H)_{12}$). The resulting structures (dimer, oblique, hexagonal) were shown to depend on the number and position of carboxylic functionalities and the nature of the surface. This study highlights the important role of the fullerene structure and intermolecular interactions in the self-assembly process.

The use of physisorbed monolayers for nanopatterning applications was demonstrated. SAMN of a *p*-dialkoxybenzene derivatives has been used as template for directing the two dimensional assembly of thiol-capped AuNPs at liquid-solid interface. The lamellar molecular adlayer acts as a sticky template, enabling the adsorption of AuNPs. Notably, the structural information of the monolayer is transferred to the AuNP assembly, which leads to superlattices with a non-centrosymmetric unit cell. This templating effect is primarily driven by van der Waals interactions between the alkyl chains of NP ligands and those of the underlying molecular template, and the efficiency of assembly is highest when the alkyl chains on the NP and substrate surfaces are of similar lengths. The resulting immobilization of AuNP in the ordered monolayer on HOPG enables high-resolution STM imaging of the internal structure of AuNPs in the liquid environment. Achieving the efficient 2D-templating effect at a solid-liquid interface opens the way for directing the self-organization of a variety of nanomaterials (other metal nanoparticles, quantum dots, etc.) under dynamic equilibrium conditions.

Using X-ray photoelectron spectroscopy (XPS) we demonstrate that, in contrast to previous reports, the thiol adsorbates are not displaced during C_{60} adsorption from solution but instead form an adlayer on top of the SAM. STM characterization reveals both slight structural differences between BT and PFBT SAMs and dramatically different abilities to direct the adsorption of C_{60} molecules from solution.

Chemisorbed monolayers of BT and PFBT were formed on Au(111) and explored for directing the organization and growth of C_{60} molecules. Similar structural properties of BT and PFBT SAMs but different templating effects were observed. The *in situ* STM investigation of C_{60} layer growth kinetic reveals a faster (>100X) multilayer formation on PFBT compared to BT and C8SH SAMs. C_{60} multilayers are located on top of PFBT SAM as shown by XPS. STM characterisation reveals a $(2\sqrt{3} \times 2\sqrt{3})R30°$ structure of these multilayers. The insights gained in this study demonstrates the importance of controlling the growth process at a SAM-semiconductor interface for producing high performance thin film-based devices.

6.2 Future work

Overall, the combination of SAMs with SAMN offers considerable design flexibility and precise control of the structural properties and functionalities of molecular monolayer. Exploring these monolayers for patterning inorganic nanostructures is still at an early stage. The next step will be to investigate new morphologies of mono- and polymetallic nanosized inorganic structures such as Au nanorods or Au-Pt nanoparticles. Patterning such nanostructures is of great interest in a range of applications, such as in electronic devices, catalysis, sensing, and energy conversion.

Further understanding of the nature of C_{60} growth onto SAMs and extending this study to more semiconductor nanoparticles will allow for the formation of well-controlled films that have great potential in constructing low-cost electronic devices such as organic solar cells and field effect transistors.

The formation of these molecular networks and inorganic nanostructures onto more versatile substrates such as graphene is expected to promote the development of graphene-based flexible electronics with novel properties. Moreover, it represents a promising method for functionalization of graphene without compromising its electronic properties.